

THÈSE

En vue de l'obtention du

DOCTORAT DE L'UNIVERSITÉ DE TOULOUSE

Délivré par :

Institut National Polytechnique de Toulouse (INP Toulouse)

Discipline ou spécialité :

Micro-ondes, Électromagnétisme et Optoélectronique

Présentée et soutenue par :

Mme LI WU

le jeudi 17 décembre 2015

Titre :

CONTRIBUTION A L'ETUDE MULTI-PHYSIQUE DU CHAUFFAGE DE MILIEUX POREUX PAR ENERGIE RADIOFREQUENCE INTERMITTENTE DANS UNE CELLULE COAXIALE

Ecole doctorale :

Génie Electrique, Electronique, Télécommunications (GEET)

Unité de recherche :

Laboratoire Plasma et Conversion d'Energie (LAPLACE)

Directeur(s) de Thèse :

M. JUNWU TAO

M. JEAN LOUIS LACOUT

Rapporteurs :

M. KAMA HUANG, SICHUAN UNIVERSITY

M. LIONEL ESTEL, INSA ROUEN

Membre(s) du jury :

Mme PATRICIA ARLABOSSE, ECOLE NLE SUP DES MINES ALBI CARMAUX, Président

M. JEAN-FRANCOIS ROCHAS, WAVES CONCEPT, Membre

M. JEAN LOUIS LACOUT, INP TOULOUSE, Membre

M. JUNWU TAO, INP TOULOUSE, Membre

Contribution to the multi-physics study of porous media heated intermittently by RF energy in a coaxial cell

Li WU

Acknowledgements

This PhD study is accomplished in laboratory of Laplace, ENSEEIHT, Toulouse University. It is a result of support and assistance by many people. I wish to express my gratitude to them for their contributions.

Firstly, I would like to thank Laplace for receiving me to do PhD here.

I would like to address my hearty gratitude particularly to my supervisors, Professor Junwu TAO in Laplace-ENSEEIHT of Toulouse University and Professor Jean-Louis LACOUT in CIRIMAT-ENSIACET of Toulouse University, for guiding me through my PhD research. They are very knowledgeable and patient, which set good examples for me in the future. Their support, advices, help, encouraging and friendship during my study will be always appreciated and remembered.

I should admit that it is my great honor to have Prof. Kama HUANG from Sichuan University, China and Prof. Lionel ESTEL from LSPC-INSA Rouen in my committee. I appreciate their precious time for examining my dissertation even though their schedules are quite full.

I would also like to express my sincere gratitude to Madame Patricia ARLABOSSE from MINES Albi-Carmaux and M. Jean François ROCHAS from Société WAVES CONCEPTE to accept to be the examiner and attend my defense.

My deep appreciation also goes to Dr. Tan-Hoa VUONG and Prof. Jacque DAVID in our group for their help during these three years, especially for their help in doing experiments and realizing the direct power coupler and impedance adaptation circuit. My gratitude goes equally to Prof. Serge LEFEUVRE, Aron RAMIS and Christina from Midival for their help during the preparation of my experiment.

The infrared camera is provided by another group--CS in our laboratory of LAPLACE. I should thank particularly Mr. Didier FLUMIAN for his generously lending the infrared camera to me and guiding us how to use the infrared camera.

I wish to thank the family of Prof. TAO, the wife of Prof. Jean-Louis LACOUT and Madame Zhongxia HU. They all treat me like a family member, which makes me feel like that I stay with family and help me get through the suffering of home sick.

I also want to take this opportunity to thank all my friends in China and in France. They are always willing to listen to my grumbles and give me a hand whenever I need help. Their concerns and supports always give me the energy to overcome difficulties. My gratitude equally goes to my friends and labmates: Yalei HOU, Xiaolan TANG, Dan LI, Huacheng ZHU, Junqing LAN, Yang YANG, Priscilia DAQUIN, Caroline GIRARD, Jammal RAMMAL, Jingyi WANG, Wencong ZHANG and so on for their kindly help and friendship.

Last but not least, I would like to express my deepest appreciation and thanks to my family. They are always available and ready to help me when I need their support. They comfort me when I am sad or home sick. They are all inclusive of me even though when I am capricious and stubborn. It is their unconditional patience, love and support that get me through this long endeavors.

Résumé

Avec l'explosion économique et démographique, le besoin en matériaux poreux tels que la nourriture, le bois ou la brique connait une croissance telle que leur commerce est très actif dans le monde entier. La déshydratation des milieux poreux étant l'une des plus importantes et stables méthodes pour leur préservation, il est parfois nécessaire d'utiliser cette méthode pour stocker, transporter et mieux utiliser ces matériaux. Depuis la Seconde Guerre Mondiale, il existe des méthodes de chauffage RF dans bien des domaines. Bien que beaucoup de nouvelles technologies de chauffage sont devenues extrêmement importantes du point de vue commercial et très largement utilisées, le chauffage RF est préféré aux autres moyens de chauffage pour plusieurs raisons: 1) le résultat est plus rapide, nécessitant un moindre temps pour atteindre la température désirée; 2) le chauffage radiofréquence peut être spatialement plus uniforme que les méthodes conventionnelles de chauffage; 3) le chauffage par radiofréquences peut être allumé ou éteint instantanément; 4) il est plus efficace pour un grand volume de nourriture; 5) l'investissement nécessaire est moindre, etc. Cependant on trouve très peu d'information sur le chauffage radiofréquence pour la déshydratation des matériaux poreux dans la littérature. Par conséquent, il est intéressant d'étudier les interactions entre les radiofréquences et les milieux poreux.

Afin d'améliorer le taux d'énergie radiofréquence utilisé, cette thèse propose une cavité coaxiale pour étudier le cycle de chauffage radiofréquence d'une pomme de terre dans différents états : solide, liquide et gazeux. Dans un premier temps nous avons étudié les mécanismes de transport de masse et de chaleur dans le milieu poreux sans radiofréquence sur le modèle d'une brique 1D à l'aide d'un code Matlab. Les résultats de simulation ont été comparés qualitativement avec ceux du papier de référence. A partir de ce modèle, nous avons construit et simulé un modèle 2D axisymétrique avec le chauffage radiofréquence périodique d'une pomme de terre. L'équation de Landau et Lifshitz, Looyenga a été utilisées pour prédire le changement de permittivité effective dans la simulation car il est difficile d'obtenir une donnée précise pour un milieu poreux. La salinité de l'échantillon chauffé (qui est une caractéristique très importante) a été estimée. Les effets de différentes périodes, hauteurs de l'échantillon et puissances de la distribution en température ont été étudiés et analysés. Nous avons également mené des expériences similaires pour mesurer les changements de température durant le processus de chauffage. Tous les résultats de simulations sont comparés qualitativement avec les résultats mesurés.

De même nous avons effectué des analyses de sensibilité et en avons conclu quelques suggestions concernant l'amélioration des effets du chauffage. A partir de ces suggestions, nous avons proposé un nouveau modèle de chauffage radiofréquence afin de s'affranchir des défauts du modèle précédent.

Mots clés: Chauffage radiofréquence par intermittence, milieux poreux, permittivité effective, l'équation de Landau et Lifshitz, Looyenga, salinité, cellule coaxiale

Abstract

With the rapid growth of economic and population explosion, the demands for porous media such as foods, woods and bricks enlarge so wildly that their trades are busy around the world. To be stored, transported and utilized better, dehydration of porous media is necessary since drying is one of the most important and stable methods for preserving materials.

After World War two, possible RF heating in many domains was suggested. Even though a lot of novel heating technologies have become extremely commercially important and been widely used, RF heating is preferred to the other heating means for several significant reasons: 1) it is rapid and requires less time to come up to the desired process temperature; 2) radio frequency heating may be relatively spatially more uniform than conventional heating; 3) radio frequency heating systems can be turned on or off instantly; 4) it is better for large, thick food; 5) it requires lower investment costs, and so on. However, little information on radio frequency heating for commercial drying of porous media is available in the published literature. Therefore, it will be interesting to research the interaction between RF and porous media.

This thesis, to improve the use ratio of RF energy further, proposed a coaxial cell to research RF cycling heating potato with different phases: solid, liquid and gas. The mechanism of mass and heat transport in the porous media without RF energy was studied first by solving the governing equations of 1D brick model with Matlab codes. The calculated results compared qualitatively with those in the reference paper. Based on that model, an axisymmetric 2D model with periodically RF heating potato was built and simulated. Landau and Lifshitz, Looyenga equation was employed to predict the effective permittivity change in the simulation since it is difficult to get the accurate measurement data of porous media. The salinity of heated sample- a very important parameter of the mixing rule-was estimated. The effects of different process period, variation of height of sample and power on the temperature distributions were studied and analyzed. Corresponding experiments were also conducted to measure the temperature change during the heating process. All the simulated results compared qualitatively with the measured ones.

Sensitivity analysis was also done and some suggestions on the improvement of heating effect were concluded. Based on the suggestions, a new RF heating model was proposed to overcome the drawbacks of our previous model.

Key words: RF intermittently heating, porous media, effective permittivity, Landau and Lifshitz, Looyenga equation, salinity, coaxial cell

Table of contents

Acknowledgements I
Résumé III
Abstract V
List of figures XI
List of tables XVII
Nomenclature XIX
Chapter 1 Introduction and objectives 1
Reference of chapter 1 5
Chapter 2 Theoretical basis and applications 7
2.1 Disciplines employed for researching the mass and heat flow in porous media 7
2.1.1 Simple models of moisture transport in porous media 7
2.1.2 More generalized models for multiphases transport in porous media 7
2.1.3 Applications of the multiphase flow models to conventional heating 10
2.2 Mechanism of microwave and RF in the heating 11
2.2.1 Brief introduction of polarizations 11
2.2.2 Brief introduction of effective permittivity 13
2.3 Mathematical modeling and applications of RF heating porous media 16
2.3.1 Mathematical equations 16
2.3.2 Applications of RF heating 17
2.4 Intermittent heating 19
Reference of chapter 2 23
Chapter 3 Numerical research on multiphase transfer under convective heating 29
3.1 Theoretical preparation 29
3.1.1 Assumptions 29
3.1.2 Equilibrium state variables and vapor pressure 30
3.1.3 Mass and heat conservation equations 33
3.1.4 Initial and boundary conditions 39
3.2 Numerical solutions 41
3.2.1 Introduction of the used finite difference method 41
3.2.2 Discretization for the governing equations 43
3.2.3 Discretization of the boundary 46
3.2.4 Assembly of matrix 49
3.2.5 The calculated results and discussion 51
3.3 Calculated results and discussions 53

3.4 Conclusion 60
Reference of chapter 3 61
Chapter 4 Measurement of effective permittivity of potato Agata 63
4.1 Effective permittivity of agricultural products 64
4.1.1 Impact factors of permittivity 64
4.1.2 Dielectric mixture equations 67
4.2 Measurement techniques of effective permittivity 71
4.2.1 Common measurement techniques 72
4.2.2 Measurement developed in LAPLACE 76
4.3 Estimate the salinities of researched material 80
4.3.1 Measurement preparation 80
4.3.2 Measuring the input impedance of partially loaded cell 84
4.3.3 Estimated results 85
4.4 Discussion and conclusion 89
Reference of chapter 4 91
Chapter 5 A 2D axisymmetric model of RF intermittently heating potato 95
5.1 Schematic of 2D axisymmetric model 95
5.2 The governing equations 96
5.2.1 Maxwell's equation 97
5.2.2 Momentum conservation equation 97
5.2.3 Mass conservation equation 98
5.2.4 Heat conservation equation 98
5.2.5 Phase change 99
5.2.6 Initial and boundary conditions 100
5.3 Input parameters 100
5.3.1 Specific heat capacity 101
5.3.2 Capillary diffusivity of liquid water 101
5.3.3 Permeability of water and gas 102
5.3.4 The permittivity of potato during the processing 103
5.4 The experiment 108
5.4.1 Material and preparation 108
5.4.2 The implement of experiment 109
5.5 Comparison of results and discussion 110
5.5.2 Comparison of temperature profiles of intermittent heating 112
5.5.3 Simulated pressure tendency 120
5.5.4 Simulated of moisture profiles 126

5.6 Conclusion 128
Reference of chapter 131
Chapter 6 Sensitivity analysis and optimizations 133
6.1 Sensitivity analysis 133
6.1.1 Effect of different RF power 133
6.1.2 Effect of mass transfer coefficient 136
6.1.3 Effect of heat transfer coefficient 139
6.1.4 Effect of water intrinsic permeability 142
6.1.5 Effect of water saturation 145
6.1.6 Effect of porosity 148
6.1.7 Effect of height of sample 151
6.1.7 Effect of different location of the potato sample 154
6.2 The optimization of the RF heating model 156
6.3 Conclusion 158
Reference of chapter 6 159
Chapter 7 Conclusions and future work 161
List of publications 165

List of figures

Figures in chapter 2:

Figure 2.1 Schematic of mechanism of RF heating

Figure 2.2 Intermittent heating modes: (a) step-wise, (b) step-up, (c) step-down

Figures in chapter 3:

Figure 3.1 Schematic of porous media

Figure 3.2 Representative element volume of porous media

Figure 3.3 Schematic of 1D brick

Figure 3.4 Schematic of discretization method

Figure 3.5 Sketch for the Crank-Nicolson scheme

Figure 3.6 Discretization of the calculation domain

Figure 3.7 Flow chart of calculation

Figure 3.8 Pressures of 61 nodes vs 21 nodes

Figure 3.9 Pressures of 61 nodes vs 41 nodes

Figure 3.10 Pressures of 61 nodes vs 81 nodes

Figure 3.11 Pressures of 61 nodes vs 101 nodes

Figure 3.12 Saturations of 61 nodes vs 21 nodes

Figure 3.13 Saturations of 61 nodes vs 41 nodes

Figure 3.14 Saturations of 61 nodes vs 81 nodes

Figure 3.15 Saturations of 61 nodes vs 101 nodes

Figure 3.16 Temperatures of 61 nodes vs 21 nodes

Figure 3.17 Temperatures of 61nodes vs 41 nodes

Figure 3.18 Temperatures of 61 nodes vs 81 nodes

Figure 3.19 Temperatures of 61 nodes vs 101 nodes

Figure 3.20 Calculated temperatures by Matlab

Figure 3.21 Temperatures in reference paper

Figure 3.22 Calculated saturations by Matlab

Figure 3.23 Saturations in reference paper

Figure 3.24 Calculated pressures by Matlab

Figure 3.25 Pressures in reference paper

Figures in chapter 4:

Figure 4.1 Schematic of transmission line measurement system
Figure 4.2 Schematic of open-end probe measurement system
Figure 4.3 Schematic of free space measurement system
Figure 4.4 Schematic of resonant cell measurement system
Figure 4.5 Schematic of coaxial cell
Figure 4.6 Schematic of coaxial cell connected with conical transition
Figure 4.8 Picture of two transitions mounted head tail
Figure 4.9 Photos of the cutting equipment
Figure 4.10 Photos of the cut sample
Figure 4.11 Comparisons of measured data of potato samples placed at different locations
Figure 4.12 Comparisons of fitted measured data of potato samples placed at different locations
Figure 4.13 Comparisons of simulated data of potato samples placed at different locations
Figure 4.14 Comparison of measured data of potato samples with different height
Figure 4.15 Simulated input impedances with different inner diameter of annular samples
Figure 4.16 Measured input impedances with different inner diameter of annular samples
Figure 4.17 Equivalent circuit of the whole measured system
Figure 4.18 Picture of equipment for measurement
Figure 4.19 Comparison of measured and simulated input impedance: (a) real part, (b) imaginary part
Figure 4.20 Comparison of measured and simulated effective permittivity: (a) real part, (b) imaginary part
Figure 4.21 Measured data of Russett Burbank potato by Nelson

Figures in chapter 5:

Figure 5.1 Schematic of 2D axisymmetric model
Figure 5.2 Simple flow chart of simulation
Figure 5.3 Schematic of effective permittivity updation
Figure 5.4 Temperature of cross-section after 12th heating: sample doesn't touch inner conductor (left); sample doesn't touch outer conductor (middle); sample touches both conductors (right)
Figure 5.5 Photos of the cutting equipment and cut sample

Figure 5.6 Schematic of the experiment setup
Figure 5.7 Positions of two points for measuring temperature: height of sample is 57mm (left); height of sample is 45mm (right)
Figure 5.8 Temperature changes of point 1
Figure 5.9 Temperature changes of point 2
Figure 5.10 Comparison of temperatures of sample after processing 15 cycles (inside)
Figure 5.11 Comparison of temperatures of sample after processing 15 cycles (outside surface)
Figure 5.12 Temperature changes of point 1
Figure 5.13 Temperature changes of point 2
Figure 5.14 Comparison of temperatures of sample after processing 25 cycles (inside)
Figure 5.15 Comparison of temperatures of sample after processing 25 cycles (side surface)
Figure 5.16 Temperature changes of point 1
Figure 5.17 Temperature changes of point 2
Figure 5.18 Comparison of temperatures of sample after processing 16 cycles (inside)
Figure 5.19 Comparison of temperatures of sample after processing 16 cycles (side surface)
Figure 5.20 Samples without (left) and with (right) transformation
Figure 5.21 Temperature changes of point 1
Figure 5.22 Temperature changes of point 2
Figure 5.23 Comparison of temperatures of sample after processing 20 cycles (inside)
Figure 5.24 Comparison of temperatures of sample after processing 20 cycles (side surface)
Figure 5.25 Pressure change of point 1(left) and distribution (right) after processing 15 cycles
Figure 5.26 Pressure change of point 1(left) and distribution (right) after processing 25 cycles
Figure 5.27 Pressure change of point 1(left) and distribution (right) after processing 16 cycles
Figure 5.28 Pressure change of point 1(left) and distribution (right) after processing 20 cycles
Figure 5.29 Cross-sectional distribution of temperature (left) and pressure (right) after processing 15 cycles
Figure 5.30 Cross-sectional distribution of temperature (left) and pressure (right) after processing 25 cycles
Figure 5.31 Cross-sectional distribution of temperature (left) and pressure (right) after processing 16 cycles
Figure 5.32 Cross-sectional distribution of temperature (left) and pressure (right) after processing 20 cycles
Figure 5.33 Average moisture content (left) and distribution (right) after processing 15 cycles
Figure 5.34 Average moisture content (left) and distribution (right) after processing 25 cycles

Figure 5.35 Average moisture content (left) and distribution (right) after processing 16 cycles
Figure 5.36 Average moisture content (left) and distribution (right) after processing 20 cycles

Figures in chapter 6:

Figure 6.1 Comparison of pressures of point 1
Figure 6.2 Comparison of moisture contents
Figure 6.3 Comparison of average temperatures
Figure 6.4 Comparison of temperatures of point 1
Figure 6.5 Comparison of water concentration distributions of different slices of samples heated by different powers: 50W (left), 100W (middle), 150W (right)
Figure 6.6 Comparison of temperature distributions of different slices of samples heated by different powers: 50W (left), 100W (middle), 150W (right)
Figure 6.7 Comparison of temperatures of point 1
Figure 6.8 Comparison of average temperatures
Figure 6.9 Comparison of moisture contents
Figure 6.10 Comparison of pressures of point 1
Figure 6.11 Comparison of water concentration distributions of different slices of samples heated by different values of h_m: 0.004*m/s* (left), 0.008*m/s* (middle), 0.012 *m/s* (right)
Figure 6.12 Comparison of temperature distributions of different slices of samples heated by different values of h_m: 0.004 (left), 0.008 (middle), 0.012 (right)
Figure 6.13 Comparison of temperatures of point 1
Figure 6.14 Comparison of average temperatures
Figure 6.15 Comparison of moisture contents
Figure 6.16 Comparison of pressures of point 1
Figure 6.17 Comparison of water concentration distributions of different slices of samples heated by different values of h_t: 10 (left), 20 (middle), 100 (right).
Figure 6.18 Comparison of temperature distributions of different slices of samples heated by different values of h_t: 10 (left), 20 (middle), 100 (right)
Figure 6.19 Comparison of temperatures of point 1
Figure 6.20 Comparison of average temperatures
Figure 6.21 Comparison of moisture contents
Figure 6.22 Comparison of pressures of point 1

Figure 6.23 Comparison of water concentration distributions of different slices of samples heated by different values of $k_{in,w}$: 1e-15 (left), 1e-16 (middle), 1e-17 (right)
Figure 6.24 Comparison of temperature distributions of different slices of samples heated by different values of $k_{in,w}$: 1e-15 (left), 1e-16 (middle), 1e-17 (right)
Figure 6.25 Comparison of temperatures of point 1
Figure 6.26 Comparison of average temperatures
Figure 6.27 Comparison of pressures of point 1
Figure 6.28 Comparison of water concentration distributions of different slices of samples heated by different values of S_w: 0.6 (left), 0.9 (middle), 0.96 (right)
Figure 6.29 Comparison of temperature distributions of different slices of samples heated by different values of S_w: 0.6 (left), 0.9 (middle), 0.96 (right)
Figure 6.30 Comparison of temperatures of point 1
Figure 6.31 Comparison of average temperatures
Figure 6.32 Comparison of pressures of point 1
Figure 6.33 Comparison of temperature distributions of different slices of samples heated by different values of ϕ: 0.85 (left), 0.88 (middle), 0.9 (right)
Figure 6.34 Comparison of water concentration distributions of different slices of samples heated by different values of ϕ: 0.85 (left), 0.88 (middle), 0.9 (right)
Figure 6.35 Comparison of temperatures of point 1
Figure 6.36 Comparison of average temperatures
Figure 6.37 Comparison of moisture contents
Figure 6.38 Comparison of pressures of point 1
Figure 6.39 Comparison of temperature distributions of different slices of samples heated by different values of heights: 57mm (left), 45mm (middle), 28.5mm (right)
Figure 6.40 Comparison of water concentration distributions of different slices of samples heated by different values of heights: 57mm (left), 45mm (middle), 28.5mm (right)
Figure 6.41 Comparison of temperatures of point 1
Figure 6.42 Comparison of average temperatures
Figure 6.43 Comparison of moisture contents
Figure 6.44 Comparison of pressures of point 1
Figure 6.45 Comparison of temperatures of point 1
Figure 6.46 Comparison of average temperatures
Figure 6.47 Comparison of moisture contents

Figure 6.48 Comparison of pressures of point 1
Figure 6.49 Comparison of water concentration distributions of different slices of samples heated by different values of positions: 20mm (left), 40mm (middle), 60mm (right)
Figure 6.50 Comparison of temperature distributions of different slices of samples heated by different values of positions: 20mm (left), 40mm (middle), 60mm (right)
Figure 6.51 Schematic of new model

List of tables

Table 2.1 Frequencies assigned by FCC for industrial, scientific and medical use

Table 2.2 Some successful applications of RF heating foods

Table 2.3 Research findings of stepwise intermittent heating food products

Table 3.1 Input parameters of 1D brick model

Table 4.1 Effect of the dielectric properties of salt, fat and free water with frequency and temperature

Table 4.2 General comparison of dielectric property measurement systems

Table 4.3 Effective permittivities of measured samples

Table 4.4 Comparison of measured average and simulated effective permittivity

Table 5.1 Input parameters of potato in the simulation

Table 6.1 Increasing of temperature, pressure e and moisture loss under different power levels

Table 6.2 Comparison of moisture content losses of different S_w

Table 6.3 Comparison of moisture losses of different ϕ

Nomenclature

Latin Symbol :

Symbol	Description
a	Radius, (m)
b_i	Coefficients in finite differential equations
C	Molar density of gas mixture, (kg/mol)
C_p	Specific heat, $(J/(kg \cdot K))$
c	Mass concentration, $(kg\ /\ m^3)$
c_i	Coefficients in finite differential equations
D_c	Binary diffusivity of air and vapor, (m^2/s)
$D_{eff,g}$	Effective gas diffusivity in moist materials, (m^2/s)
D_{eff}	Effective diffusivity in moist materials, (m^2/s)
D_w	Capillary diffusivity, (m^2/s)
$\vec{E}$	Electric field intensity, (V/m)
f	Frequency, $(1/s)$
$\vec{H}$	Magnetic field intensity, $(N/(m \cdot A))$
Δh_{vap}	Enthalpy of vaporization, (J/kg)
h_t	Heat transfer coefficient on open boundary,$(W/(m^2 \cdot K))$
h_m	Mass transfer coefficient on open boundary, (m/s)
I	Volumetric evaporation term, $(kg/(m^3 \cdot s))$
i	Point number in x-axis; symbol of imaginary part

K	Evaporation rate constant, (1/s)
K_i	Coefficients in differential equations
k	Boltzmann constant, (J/K)
k_t	Thermal conductivity, $(W/(m \cdot K))$
k_{in}	Intrinsic permeability, (m^2)
$k_{in,w}$	Liquid intrinsic permeability at very wet stage, (m^2)
$k_{in,g}$	Gas intrinsic permeability at very dry stage, (m^2)
$k_{r,g}$	Gas relative permeability, dimensionless
$k_{r,w}$	Water relative permeability, dimensionless
k_{eff}	Effective thermal conductivity, $(W/(m \cdot K))$
$\vec{j}$	Mass diffusive flux, $(kg/(m^3 \cdot s)))$
j	Symbol of imaginary part
M	Molecular weight, $(kg/kmol)$
M	Moisture content (d.b.)
N	Normality of the solution
P	Total pressure, (Pa)
P_0	Initial pressure, (Pa)
p_v	Partial pressure of vapor, (Pa)
p_a	Partial pressure of air, (Pa)
p_c	Capillary pressure, (Pa)
p	Polarization
q_{surf}	Heat flow on the boundary, (W/m^2)

Q	Volumetric heat source term, (W/m^3)
R	Universal gas constant, $(J/\ (kmol\ \cdot K))$
R_v	Vapor gas constant, $(J/(kg\cdot\ K))$
R_a	Air gas constant, $(J/(kg\cdot\ K))$
t	Heating time, (s)
V	Volume, (m^3)
ΔV	Representative element volume
$\vec{m}$	Convective flux, $(kg/(m^2\cdot s)))$
$\vec{n}$	Total flux, $(kg/(m^2\cdot s)))$
n	Time point
S	Salinity
S_w	Liquid saturation
S_g	Gas saturation
S_0	Initial saturation
S_{11}	Reflection coefficient
T	Temperature, (K)
T_0	Initial temperature, (K)
$\vec{u}$	Velocity, $(\mathrm{m/s})$
χ_i	Molar fraction
x	X-axis
Δx	Mesh size of space
Δt	Time increment

Z	Input impedance, (Ω)
Z_0	Characteristic impedance, (Ω)
Z_{meas}	Measured input impedance of total system, (Ω)
Z_{ech}	Input impedance of loaded cell, (Ω)

Greek symbols:

Symbol	Description
α	Empirical spread of relaxation times
ρ	Density, (kg/m^3)
ϕ	Porosity
μ	Viscosity, $(Pa \cdot s)$
ω_v	Mass fraction of vapor
ω_a	Mass fraction of air
μ_0	Permeability of free space
ε	Permittivity
ε_0	Permittivity of free space
ε_r	Relative permittivity
ε_r'	Dielectric constant
ε_r''	Dielectric loss
ε_∞	Permittivity under extremely high frequency
ε_s	Static permittivity at zero frequency

λ	Latent of vapor, (J/kg)
ω	Angular frequency, $(1/s)$
$(\rho C_p)_{eff}$	Effective heat capacity of the moist materials, (J/m^3)
ρ_{eff}	Apparent density, (kg/m^3)
$\rho_{v,0}$	Ambient vapor density, (kg/m^3)
σ	Surface tension, (N/m); ionic conductivity
τ	Relaxation time, (s)
μ	Dynamic viscosity, $(Pa \cdot s)$; static conductivity
υ	Volume fraction

Subscripts and superscripts:

Symbol	Description
a	Air
v	Vapor
g	Gas
w	water
amb	Ambient
s	Solid matrix
eff	Effective
$1,2,3\cdots$	Different substances
0	Atmosphere
l	Load

$'$	Real part
$''$	Imaginary part
$*$	Conjugate

Abbreviation:

Symbol	Description
SC	Short circuit
OC	Open circuit
Re	Real part
Im	Imagianry part

Chapter 1 Introduction and objectives

A porous medium is characterized by a partitioning of the total volume into solid matrix and pore space, with the latter being filled by one or more fluids. Many natural substances such as rocks and soil (e.g. petroleum reservoirs), biological tissues (e.g. wood, bones), a lot of foods and man-made materials such as cements and ceramics can be considered as porous media. They are important and can be seen everywhere in our everyday life, research field and industrial applications.

With the development of economic and population explosion, more and more porous media such as foods, woods and bricks are needed and their trades are more frequently around the world. To be stored, transported and utilized better, dehydration of porous media is necessary since drying is one of the most important and stable methods for preserving materials because most of the water inside them has been removed.

Before, most of the drying based on the conventional heating such as steam, hot water, hot air or a combination of any of them which have been used almost since human being learnt how to use fire. These kinds of heating methods are mature and applied everywhere if dehydration is needed. However, the energy source of conventional heating only can heat the surfaces of the treated materials directly. It causes food molecules to react largely from the surface inward, so that successive layers heat in turn, leading to a temperature gradient that can burn the outside of the material while the interior is rare. Since the interior temperatures and moistures of samples can be changed only by the heat conduction from surfaces, these drying processes require enormous time, energy and cost due to high latent heat of water. Moreover, the traditional methods may be easier to cause the problems to environment. Nowadays, human development faces a profound crisis of energy sources and environment. Therefore, it is a must to find the high efficient methods to treat the vast porous media. Advanced drying techniques and equipment are therefore necessary to reduce energy consumption and drying time. To improve this situation, a lot of new methods have been investigated for drying porous media: freeze drying, air oven drying, vacuum drying, RF and microwave drying, to name a few [1][2][3][4][5].

Radio and microwave heating are preferred to the other heating means for the primary reason that they are rapid and require less time to come up to the desired process temperature, which

can approach the benefits of high temperature-short time processing. This is particularly true for solid and semi-solid foods that depend on the slow thermal diffusion process in conventional heating [6]. It has been proven that radio frequency and microwave heating may be relatively spatially more uniform than conventional heating [7], however, heating uniformity is hard to predict.

Many researchers focus on microwave drying a large range of porous media in different domains, and there have been numerous articles until today with relative parameters widely available. However, very little information on radio frequency heating for commercial drying of porous media is available in the published literature and much fewer commercial facility for this purpose could be located than microwave, despite RF heating applications in the food industry have been recognized since the 1940s [8][9], and despite the many strengths it owns. Our quantitative understanding is still limited even though the existence of periodical summaries in comprehensive reviews [5].

What's more, even though that there exist some drawbacks for RF heating comparing to microwave heating such as less RF sources in the market, relatively lower heating efficiency, RF heating still could be an attractive alternative over microwave heating for processing porous media. It has been reported that RF heating could be an attractive alternative over MW heating for processes of porous media due to its several advantages such as better for large, thick food, lower investment costs, easier to understand and control and so on [5][10]. Laycock, Piyasena and Mittal also reported that RF heating at 27.12 MHz could serve to reduce cooking times by up to 90% in whole, minced and comminuted beef [11]. Therefore, it is very interesting and necessary to research RF processing porous materials. However, researchers indicated that RF heating may also lead to uneven temperature distribution with the existence of hot spot or thermal runaway [12]. Fortunately, these problems might be improved by another advantage of RF heating.

The other advantage of radio frequency heating systems is that they can be turned on or off instantly. The merits of intermittent drying have been well established for a variety of materials with or without electromagnetic energy [13][14]. Periodically heating reportedly results in greater depth of heating than continuous heating for the same total input energy. Furthermore, RF intermittently heating, comparing to continuous application of power, leads to more uniform temperature distribution within the sample [15]. This can improve product

quality and process efficiency [16] and be a potential alternative solution for hot spot and thermal runaway.

Therefore, RF heating presents a promising prospective. In this thesis, I try to propose a model of RF intermittently heating porous media. To achieve more uniform temperature distribution and lower the computation requirement, a coaxial cell is employed as the heating equipment. As mentioned above, many researchers focus on microwave drying, therefore, the information about key parameter that determines the interaction between RF and materials-effective permittivity- is rare. Therefore, a method for estimating the effective permittivity of porous media is also proposed. Potato is chosen as the researched object because its structure parameters are available in literatures.

The objects of my thesis are to:

1) Investigate the interaction between RF and porous media, studying how the mass and heat transfer inside the sample during RF heating.
2) Propose a multi-physics model for radio frequency heating porous media by coaxial cell.
3) Develop an experimental system to measure the distribution on temperature and moisture change to check the simulation results and optimize the simulation model.
4) Study and analyze which parameters having strong impacts on the heating effects.
5) Try to improve the RF heating system.

Organization of this dissertation:

Chapter 2: Briefly introduce the mathematical background about conventional and RF heating porous media. The mechanism of how RF heats materials and its applications are also addressed.

Chapter 3: Study the definitions and relations of the parameters describing porous media. The heat and mass transfer in the porous media of a 1D model of brick under conventional heating is investigated to further understand the mechanism of multiphase flow of porous media. The calculated results are analyzed and compared.

Chapter 4: Study the knowledge of effective permittivity of porous media and choose Landau and Lifshitz, Looyenga equation to predict the effective permittivity of potato. To estimate the salinity of potato-a very important parameter for the mixing rule, the coaxial cell is employed

to measure the input impedance of loaded cell. A COMSOL combining Matlab code is developed to estimate the salinity of potato samples by comparing the measure and corresponding simulated input impedances under different frequencies. Another COMSOL combined Matlab code is used to double check the estimated salinity.

Chapter 5: Based on the mathematical model in chapter 3, the Maxwell's equations are coupled with them to simulate the model of RF intermittently heating potato sample in the coaxial cell. The effective permittivity is predicted by Landau and Lifshitz, Looyenga equation with our estimated salinity. Four different cases of simulations are conducted. Corresponding experiments are also carried out. The simulated and measured results are compared and analyzed.

Chapter 6: Sensitivities of several important parameters in the RF heating porous media model are studied. These analyses are focus on the impacts of variations of parameters on the changes of temperature, pressure distributions and moisture losses of the processed materials. Some improvements of heating effect are provided. Aimed at overcoming the problems existed in our model, another idea of RF heating porous media is briefly presented.

Chapter 7: Conclude what I have done and the points that may be helpful for the research of RF heating other kinds of porous media. Prospective works are also listed.

Reference of chapter 1

[1] C. D., Clary, S. J., Wang, & V. E., Petrucci, "Fixed and incremental levels of microwave power application on drying grapes under vacuum," *Journal of Food Science*, vol.70, no.5, pp. 344-349, 2005.

[2] Cui, Z.W., Li, C.Y., Song, C.F., Song, Y.,. "Combined microwave-vacuum and freeze-drying of carrot and apple chips," *Dry. Technol.,* vol.26, no.12, pp. 1517–1523, 2008.

[3] Bai-Ngew, S., Therdthai, N., Dhamvithee, P., "Characterization of microwave vacuum-dried durian chips," *J. Food Eng.*, vol.104, pp.114–122, 2011.

[4] M. Zhang, J. Tang, A.S. Mujumdar and S. Wang, "Trends in microwave-related drying of fruits and vegetables," *Trends in Food Science & Technology*, vol. 17, pp. 524-534, 2006.

[5] Punidadas Piyasena, Chantal Dussault, Tatiana Koutchma, H. S. Ramaswamy, and G. B. Awuah, "Radio frequency heating of foods: principles, applications and related properties—A review," *Critical Reviews in Food Science and Nutrition*, vol.43, no.6, pp.587–606, 2003.

[6] U.S. Department of Health and Human Services "Kinetics of Microbial Inactivation for Alternative Food Processing Technologies," *A report of the Institute of Food Technologists for the Food and Drug Administration of the U.S. Department of Health and Human Services*, http://www.fda.gov/Food/FoodScienceResearch/SafePracticesforFoodProcesses/ucm100250.htm.

[7] Datta, A. K. and Hu, W., "Quality optimization of dielectric heating processes," *Food Technol.* vol. 46, no.12, pp.53-56, 1992.

[8] Anonymous, "Radio frequency ovens increase productivity and energy efficiency," *Prepared Foods*, September, pp. 125, 1993.

[9] McCormick, R, "Dielectric heat seeks low moisture applications," *Prepared Foods*, September, pp.139–140, 1988.

[10] Joseph P. Kerry and John F. Kerry, "Processed meats: improving safety, nutrition and quality," *Wood head publishing limited*, pp. 645, 2011.

[11] L. Laycock, P. Piyasena, G.S.Mittal, "Radio frequency cooking of ground, comminuted and muscle meat products," *meat science*, vol. 65, no.3, pp. 959-965, 2003.

[12] Zhang, L., Lyng, J. G., & Brunton, N. P. , "Effect of radio frequency cooking on the texture, colour and sensory properties of a large diameter communited meat product," *Meat Science*, vol.68 , no.2, pp.257–268, 2004.

[13] N. N. Grinchik, P. V. Akulich, A. L. Adamovich, P. S. Kuts, and S. P. Kundas, "Modeling of nonisothermal heat and moisture transfer in capillary-porous media in periodic microwave heating," *J. Engineering Physics and Thermophysics,* vol.80, no. 1, pp. 1-10, 2007 .

[14] I. Farkas, Z. Rendik, "Intermittent thin layer corn drying," *Drying Technology*, vol.15, no.6–8, pp. 1951–1960, 1997.

[15] H. W. Yang, S. Gunasekaran, "Comparison of temperature distribution in model food cylinders based on Maxwell's equations and Lambert's law during pulsed microwave heating," *J. Food Engineering*, vol.64, no.4, pp. 445–453, 2004.

[16] S. Gunasekaran, "Pulsed microwave-vacuum drying of food materials," *Drying Technology*, vol.17, no.3, pp. 395–412, 1999.

Chapter 2 Theoretical basis and applications

2.1 Disciplines employed for researching the mass and heat flow in porous media

2.1.1 Simple models of moisture transport in porous media

The effective diffusivity is introduced in the description of moisture loss in conventional drying. This coefficient considers all the effects of possible mechanisms of transport of moisture in both the liquid and vapor gas phases.

$$\frac{\partial M}{\partial t} = \nabla(D_{eff}\nabla M) \tag{2-1}$$

Where M is the total moisture content. D_{eff} indicates the effective diffusivity whose value in most researches is obtained from fitting experimental data to the solution of the same equation.

The heat transfer equation is employed to govern the heat transport inside the material:

$$(\rho C_p)_{eff}\frac{\partial T}{\partial t} = \nabla\left(k_{eff}\nabla T\right) + I \tag{2-2}$$

$(\rho C_p)_{eff}$ presents an effective parameter whose meaning is provided in the next section. I is the rate of internal evaporation which is approximated by Tong et al. [1] as:

$$I = \lambda\rho_d\frac{\partial M}{\partial t} \tag{2-3}$$

However, this equation assumes that all of the moisture change at any location contributes to latent heat at that location, which is physically unrealistic. Ni et al. [2] also propose a different but simple assumption regarding evaporation term and the corresponding equations. However, it still has its limitations.

2.1.2 More generalized models for multiphases transport in porous media

Luikov developed a theory for porous media in 1975 which became famous and was applied in the study of other researchers [3]. Based on the phenomenological theory of non-

equilibrium thermo dynamic, he derived the heat transfer equation and mass conservation equation of liquid water. The temperature, moisture content and gas pressure were chosen as primary variables. The final equations were:

$$\frac{\partial T}{\partial t} = K_{11}\nabla^2 T + K_{12}\nabla^2 M + K_{13}\nabla^2 P \tag{2-4}$$

$$\frac{\partial M}{\partial t} = K_{21}\nabla^2 T + K_{22}\nabla^2 M + K_{23}\nabla^2 P \tag{2-5}$$

$$\frac{\partial P}{\partial t} = K_{31}\nabla^2 T + K_{32}\nabla^2 M + K_{33}\nabla^2 P \tag{2-6}$$

The advantages of this model are: 1) the convective flows of gas and capillary flow are taken into consideration; 2) these equations are parallel, which is favorable to find the analytical solution for some simple cases. Unfortunately, this model also has several serious drawbacks. Because all the flux formulas are based on phenomenology, the physical interpretation is not very clear. The phase conversion factor—ratio of water transport in the vapor phase to water transport in the liquid phase, is treated as a constant and employed in this theory. Even though its utilization can simplify the model solution, the assumed value of phase conversion factor really makes the solution semi-empirical. What's more, the gas diffusion is not described in diffusion transport and liquid bulk flow is not described in convective transport. Although the theory is used in some works to calculate the relative effects of various parameters on the solution, it is not applied widely today due to these disadvantages.

To overcome those shortcomings existed in Luikov's model and provide a better theory, Whitaker developed a set of heat and mass transfer equations for porous media based on mechanism [4]. Firstly, he derived the heat transfer equation and each phase's mass conservation equation. Then he volume averaged different phases. Rigorous study for the transition from the individual phase at the "microscopic" level to representative average volume at the "macroscopic" level provided the fundamental and convincing basis for this theory. To achieve these equations, some assumptions were taken, like: 1) Darcy's law was valid for this model; 2) temperatures of these three phases were equivalent; 3) Fickian diffusion and filtrational flow motived gas transport; 4) only capillary flow existed in the liquid transport while the effect of gas pressure was assumed negligible; 5) the structure of porous media was rigid and there was no bound water inside. The final equations are shown below:

$$(\rho C_p)_{eff}\frac{\partial T}{\partial t} + \left(\rho_w C_{pw}\overrightarrow{u_w} + \rho_g C_{pg}\overrightarrow{u_g}\right)\nabla T = \nabla\left(k_{eff}\nabla T\right) - \lambda I \tag{2-7}$$

$$\frac{\partial}{\partial t}\left(\varepsilon_g \rho_v\right) + \nabla\left(\rho_v\overrightarrow{u_g}\right) = \nabla\left(\rho_g D_{eff,g}\nabla\left(\frac{\rho_v}{\rho_g}\right)\right) + I \tag{2-8}$$

$$\frac{\partial}{\partial t}\left(\varepsilon_g \rho_a\right) + \nabla\left(\rho_a\overrightarrow{u_g}\right) = \nabla\left(\rho_g D_{eff,g}\nabla\left(\frac{\rho_a}{\rho_g}\right)\right) \tag{2-9}$$

$$\frac{\partial}{\partial t}(\varepsilon_w \rho_w) + \nabla(\rho_w\overrightarrow{u_w}) = -I \tag{2-10}$$

Compared to the theory of Luikov, the physics of this model is better understood. The hypotheses are clear and reasonable, and the parameters are well-defined. Whitaker has also applied his theory to the case study [5][6].

Besides the two theories presented above, Bories et al. [7], Moyne and Degiovanni [8], Plumb et al. [9], Nasrallah et al. [10], H. Ni et al. [11] also developed their own governing equations in research. Their equations were similar to those of Whitaker's. Although they did not always discuss the phase averaging explicitly, much of the steps and assumption in Whitaker's model were implied in these formulations. Among them, S. Ben Nasrallah cited a lot of works conducted previously and theoretically studied the heat and mass transfer during the drying of porous media. His model was drawn from the work of Whitaker [4] and leaded to a very comprehensive set of equations with three variables—temperature, moisture content and pressure. The conservation equations for vapor, liquid water, gaseous mixture and heat in the porous medium were written, respectively, as:

$$\frac{\partial \rho_v}{\partial t} + \frac{\partial}{\partial x}\left(\rho_v\overrightarrow{u_v} - \rho_g D_{eff,g}\frac{\partial}{\partial x}\left(\frac{\rho_v}{\rho_g}\right)\right) = I \tag{2-11}$$

$$\frac{\partial \rho_w}{\partial t} + \frac{\partial}{\partial x}\left(\rho_w\overrightarrow{u_w}\right) = -I \tag{2-12}$$

$$\frac{\partial \rho_g}{\partial t} + \frac{\partial}{\partial x}\left(\rho_g\overrightarrow{u_g}\right) = I \tag{2-13}$$

$$\frac{\partial}{\partial t}\left(\overrightarrow{\rho C_p}T\right) + \frac{\partial}{\partial x}\left(\rho_w C_{p,w}\overrightarrow{u_w}T + \sum_{j=v,a}\rho_j C_{p,j}\overrightarrow{u_j}T\right) = \frac{\partial}{\partial x}\left(k_{eff}\frac{\partial T}{\partial x}\right) - \Delta h_{vap}^{\circ} I \tag{2-14}$$

Where

$$\Delta h_{vap}^{\circ} = \Delta h_{vap} + (C_{p,w} - C_{p,v})T \tag{2-15}$$

$$\overline{\rho C_p} = \rho_s C_{p,s} + \rho_w C_{p,w} + \rho_v C_{p,v} + \rho_a C_{p,a} \quad (2\text{-}16)$$

This model is employed successfully to research the heat and mass transport in the porous materials. In my research, the model of S. Ben Nasrallah is utilized to study how mass and heat transport in 1D brick for better understanding the mechanism of flows in porous media with convection heating.

2.1.3 Applications of the multiphase flow models to conventional heating

Almost all the models for multiphase flow in porous media can be classified into two groups according to whether the researchers developed their equations based on phenomenological observation (Luikov) or mechanistic consideration (Whitaker). For the Luikov system, Robbins and Ozisik [12] decoupled Luikov's equations to get analytic solution and further studied the effect of various dimensionless parameters on drying in constant gas pressure. Irudayara and Wu [13][14] solved 1D and 2D Luikov's equations by finite element method. R.N. Pandey et al. developed a novel technique that provided complete and satisfactory solutions to Luikov system to specified initial and surface conditions [15]. His new method was applied to obtain the temperature and moisture distributions during contact drying of a moist porous sheet. A number of pairs of complex conjugate roots were evaluated and a set of bench mark results was obtained. L.B. Dantas et al. estimated dimensionless parameters of Luikov's system for heat and mass transfer in capillary porous media [16]. They also examined the effects of the heating process, more specifically the heat flux magnitude and the heating time period, on the accuracy of the estimated parameters. F. Nadi et al. developed a two-dimensional model to simulate coupled heat and mass transfer in apple under vacuum drying based on Luikov's equations. A parametric study was also carried out to determine the effects of heat and mass transfer coefficients on temperature and moisture content distributions inside apple during vacuum drying. A comparison between the theoretical predictions and a set of experimental results reported in the literature showed very good agreement [17].

Even though the Luikov system is accepted by many researchers, the mechanistic formulation of Whitaker's model is more widely used. Wei et al. studied conventional heating 1D cylindrical model with Whitaker's theory [18]. The finite difference method as well as central difference method was adopted to discretize time and space component of the equations. A similar set of equations was solved with a method of finite differences based on the notion of

control domain by Nasrallah and Perré in 1988 [10]. They used a non-uniform mesh with centered space difference and fully implicit time differencing with upwinding for the convective term. Models of brick and softwood treated in 1D slab coordinates were studied during conventional heating with their deduced formulas. Later, Perré and Moyne [19] extended this work to solve the governing equations of 2D rectangular softwood model. They took the bound water into account for conventional heating of softwood that was treated as hygroscopic and anisotropic material. Boukadida and Nasrallah [20] followed similar formulation and analyzed the heat and mass transfer in 2D model of clay brick. For more general application, Phillip Gibson deduced a set of nonlinear partial differential equations to describe the coupled energy and mass transport inside hygroscopic porous media, particularly with reference to textile materials in woven, nonwoven, and laminated forms [21]. The basis for the set of governing equations was Whitaker's comprehensive theory for mass and energy transport through porous media. Ilic and Turner [22] assumed that the porous media was consisted of wet and dry zones with moving boundary and applied separate equations in each zone. Turner and Perré compared the model developed by Perré and his coworkers with that developed by Turner and his coworkers [23]. The final forms of equations were slightly different in the two models although the underlying physics were exactly the same. They compared their 2D codes for conventional drying of wood and concluded reasonable qualitative agreement between them. P. Perré and J. Passard proposed a physical and mechanical model to predict the stress field in wood [24]. Two examples were proposed, which allowed the importance of the mechanical characterization to be exhibited. Following this work, R. Rémond et al. proposed a model able to simulate heat and mass transfer and mechanical behaviour of a wooden board during processing [25].

2.2 Mechanism of microwave and RF in the heating

2.2.1 Brief introduction of polarizations

The radio frequency spectrum covers a broad band of frequencies from 3kHz to 300MHz. The microwave that is similar to RF in heating behaviors embraces the higher range between 300MHz and 3000GHz. RF heating or MW heating is an innovative technique that bases on electro-technologies. Both of them are known as dielectric heating that is a process in which a high frequency alternating electric field (radio wave or electromagnetic radiation) heats a dielectric material. Unlike the conventional heating method that energy is transferred from the

heat source to the processed material due to the great temperature gradient, RF and microwave can generate heat within the product directly because of the frictional interaction between molecules (i.e., volumetric heating).

Owing to congested bands of microwave and RF already being used for communication purposes, only a limited number of bands are allocated for industrial, scientific and medical applications. The bands in the USA assigned by the Federal Communications Commission (FCC) are listed below. It is worth-noticing that frequencies of 433.896MHz and 2375MHz are also available for use outside USA.

Table 2.1 Frequencies assigned by FCC for industrial, scientific and medical use

	Frequency
Radio frequency	13.56MHz ± 6.68kHz
	27.12MHz ± 160kHz
	40.68MHz ± 20kHz
Microwave	915MHz ± 13MHz
	2450MHz ± 50MHz
	5800MHz ± 75MHz
	24125MHz ± 125MHz

In all the materials, there exist either free or bound charges. The interaction between tested materials and EM field causes motion of the bound charges. This effect is named polarization which can be classified as ionic, orientation, atomic and electronic polarization. Movement of ions in the media under the impact of EM field is called ionic polarization. It is strongly temperature dependent typically predominant effect when frequency is lower than 1GHz [26].

In RF heating system, the RF generator creates an alternating electric field between two electrodes. The heated material locates between the electrodes where the alternating energy causes polarization, the molecules in the material continuously reorienting themselves to face opposite pole.

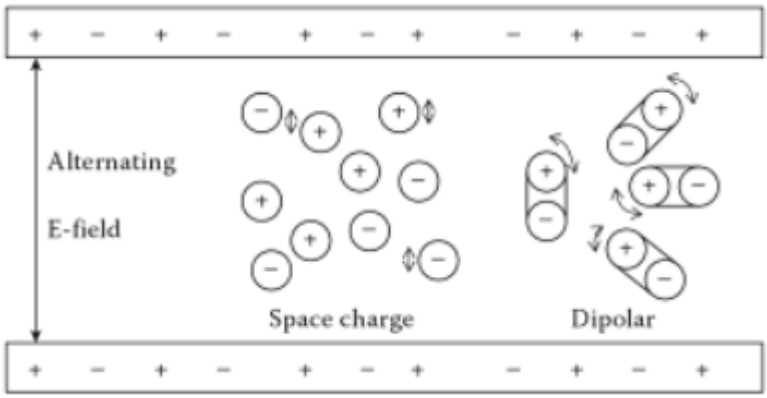


Figure 2.1 Schematic of mechanism of RF heating

Microwave doesn't have sufficient energy to cause ionization [26]. Electric polarization occurs in atoms, in which electrons can be displaced with respect to the nucleus. This polarization exists in all the materials with varying degrees. The materials are almost lossless if only the electric polarization and atomic polarization are present.

Orientation polarization is the most significant one among all the possible forms of energy loss mechanisms when the frequency is above 1 GHz. It is present widely in many dielectric materials. The presence of moisture or water causes dielectric heating due to the dipolar nature of water. During electromagnetic heating, when the high frequency alternating electric field is incident on the water molecules, the permanently polarized dipolar molecules try to realign themselves with the electric field. Since the polarity changes rapidly, this realignment occurs million times per second and causes internal friction of colliding neighboring molecules resulting in the volumetric heating of the material. This effect is also temperature dependent while the electric and atomic polarizations are irrelevant to the temperature. At microwave frequencies, dipole polarization is the most important mechanism for energy transfer at the molecular level. Water is chiefly responsible for the MW heating due to dominant dipolar interaction with microwave comparing to other components of the materials. Microwave heating might also occur due to the oscillatory migration of ions in the food which generates heat in the presence of a high frequency oscillating electric field [27].

2.2.2 Brief introduction of effective permittivity

The relationship between the permittivity and polarization is then described as:

$$\vec{p} = (\varepsilon_r - 1)\varepsilon_0 \vec{E} \tag{2-17}$$

The relative permittivity is a measure of the polarizing effect of external electric field. Polarization of the electric charge in which the rotational motion is restricted leads to a time lag between the electric field and the polarization. This time lag is known as relaxation time and proportional to the dissipation energy within the material.

For heat to be generated inside the materials, MW or RF must penetrate into the samples. The permittivity quantifies the capacitive and conductive components of the materials. The term "permittivity" implies the relative complex permittivity here, i.e., the permittivity of a material relative to free space, often termed the complex dielectric constant. It is often expressed as:

$$\varepsilon_r = \varepsilon_r' - i\varepsilon_r'' \tag{2-18}$$

Where ε_r' is the dielectric constant and ε_r'' is the dielectric loss factor. The dielectric constant is associated with the capability for energy storage in the electric field in the material, and the loss factor presents energy dissipation in the material or the conversion from electric energy to heat energy. Here, all loss mechanisms, due to dipole relaxation and ionic conduction, are included in the dielectric loss factor ε_r''.

2.2.2.1 Factors influencing dielectric property

Several factors like EM frequency, temperature, density, compositions and their volume fractions, have the impacts on dielectric properties of biomass.

As discussed above, the substances can be heated due to the polarization mechanisms. Variations of frequencies may cause different times of rotation or collide among molecules, generating diverse heat levels. Nelson indicated that the dielectric properties vary significantly with the change of frequencies for most of the materials [28]. Debye equation can calculate the permittivity of water that exists commonly in the biomass for a wide range of frequencies [29].

The effect of temperature on the dielectric properties mainly lies on its ability to change the dielectric loss factor. There is no analytical expression to be used in Debye's equation to estimate the variations of dielectric properties when changing temperatures [26][30]. The dielectric loss factor may increase or decrease with increasing of temperature [26].

The bulk density is vital for the granular materials as they entrap air in the voids. Comparing to the liquid water, air has a much lower dielectric loss factor. In highly granular and low bulk density materials, since their amounts of air with low loss factor are very high, the dielectric loss factors overall decrease. This will ultimately stunting the heating rate in EM field.

Water is the dominant component for many porous media. Its dielectric property is very high comparing to the other constitutes. Wang et al. summarized that water content in the materials largely determined the dielectric properties of the whole substances [31].

2.2.2.2 Measurement and mixing rules for dielectric properties

The methods to determine the dielectric properties of materials can be grouped into resonant and non-resonant methods. The resonant methods are relatively more accurate than the non-resonant methods. However, both of these two kinds of methods have their advantages and disadvantages and find their applications in the real world. The most commonly used techniques for permittivity measurement at the microwave frequencies include open-ended probe methods, transmission line methods, resonant cell methods and free space methods using horn waveguides, time domain reflectometry methods and so on [32][33][34].

However, for some materials, machining of samples to exact dimensions required for dielectric properties measurement is difficult. What's more, its measurements might be easy to do, but to provide the exact dielectric properties for porous materials is a difficult undertaking. It is hard to obtain the uniform temperature and moisture distribution in the porous sample due to its inhomogeneous structure, which may lead to inaccurate measurement. Besides, since the permittivity depends on several factors that are correlated with each other, it is impossible to measure the relation between dielectric property with one factor while maintain the other parameters unchangeable. Therefore, mixing rules seems to be an interesting alternative approach since it is reported that mixing rules approximate the properties to an extent of being used in real world work [35].

The dielectric properties play a key role for the interaction of EM field and materials. The information about dielectric properties and how we estimate the permittivity of sample used in our research are detailed in chapter 4.

2.3 Mathematical modeling and applications of RF heating porous media

The interaction mechanisms of radio frequency heating are quite similar to those of microwave heating. Therefore, the principles of microwave heating are generally applicable to radio frequency, which makes it easier to research and understand the interaction between RF and porous media.

2.3.1 Mathematical equations

Modeling of EM heating porous media has been achieved generally in two ways. One is to divide the entire heating into periods and to simplify the governing equations in each period of time [36]. The other is to simultaneously solve these fully coupled equations for the entire heating process [37][38]. The former may not need much computer capability but require many assumption and simplification which restrict its more general use. The latter takes advantages of the powerful capability of computer to provide more accurate and more general predictions [39]. For the recent researches, most of the models adapt the latter method to study the interaction between EM and treated materials. The governing equations consist of mass and heat transfer equations developed based on Whitaker's system and the Maxwell's equations [38].

$$\nabla \times \vec{E} = -j\omega\mu_0\vec{H} \tag{2-19}$$

$$\nabla \times \vec{H} = j\omega\varepsilon_0\varepsilon_r\vec{E} \tag{2-20}$$

$$\frac{\partial}{\partial t}(\phi\rho_w S_w) + \nabla\cdot(\overrightarrow{u_w}\rho_w) - \nabla\cdot(D_c\nabla(\phi\rho_w S_w)) = -I \tag{2-21}$$

$$\frac{\partial}{\partial t}\left(\phi\rho_g S_g\right) + \nabla\cdot\left(\rho_g\overrightarrow{u_g}\right) = I \tag{2-22}$$

$$\frac{\partial}{\partial t}\left(\phi\rho_g S_g\omega_v\right) + \nabla\cdot\left(\overrightarrow{u_g}\rho_g\omega_v\right) = \nabla\cdot\left(\phi S_g\frac{C_g^2}{\rho_g}M_a M_v D_{eff,g}\nabla x_v\right) + I \tag{2-23}$$

$$\rho_{eff}C_{p,eff}\frac{\partial T}{\partial t} + \nabla\cdot\left(\left(\rho C_p\vec{u}\right)_{fluid}T\right) = \nabla\cdot\left(k_{eff}\nabla T\right) - \lambda I + Q \tag{2-24}$$

This set of equations will be utilized in our model for studying RF drying potato sample in chapter 5.

2.3.2 Applications of RF heating

The birth of electromagnetic induction technology dates back to 1831[40]. Many RF applications have been demonstrated throughout the history of electromagnetism. After World War two, possible RF heating in many domains were suggested. Food is one of the dominant treated objects. Here in this section, a brief introduction of RF heating application in research and industry will be presented. Since potato is chosen as the example in our research, this introduction will place particular emphasis on the applications of RF heating foods.

The application of RF heating has a long history, for the early work with RF heating of foods (porous media) can be dated back to the 1940s [41][42]. These early efforts attempted to apply RF energy to cook various processed meat products, to heat bread, to dehydrate and blanch vegetables, etc. [43][44]. However, the work resulted in very few commercial installations in the 1940s, primarily due to the high overall operating costs associated with using RF energy. By the 1960s, studies on the application of RF energy in foods focused mainly on thawing frozen products. Several commercial lines emerged [45]. Demeczky [46] successfully showed that juices (peach, quince and orange) in bottles moving on a conveyer belt through an RF applicator had better bacteriological and organoleptic qualities comparing to those treated by conventional thermal methods. In the late 1980s, RF energy found its commercial applications in the food industry for post-bake drying of cookies and crackers [47] [48]. Such RF systems have been recognized to be 70% efficient in removing moisture while only 10% efficiency with conventional ovens [49]. The use of RF heating resulted in reduced energy consumption and improved product quality, both considered great advantages over the traditional baking oven. During the 1990s, due to increased food safety requirements, great attention has been given to the use of RF energy for pasteurization and sterilization of meat products [50]. It has been reported that RF heating could be particularly suitable for heat processing cured whole meat products like hams because the principle mode of heating occurs via ionic depolarization [51]. Solvated ions are particularly plentiful in hams since curing salts have been added in the preparation, making a much stronger RF absorption ability and quicker increasing of temperature. In the past, RF heating had been applied to the pasteurization of sausage meat emulsions [52]and cured hams [53]. Tulip International AS Denmark and APV has even found commercial application with the development of a method for the continuous production of cooked meats.

More recently, Laycock, Piyasena, and Mittal [54] reported that RF heating at 27.12 MHz could serve to reduce cooking time by up to 90% in whole, minced and comminuted beef. Unfortunately, the eating quality and particularly the texture of some products were adversely affected. However, limited information about impact of poor quality of meat products processed by this method is available aside from the research of Laycock (2003). Researchers have proved that this technology is undoubtedly capable for fast and efficient pasteurisation of meat products [54][55][56]. Much of the past work on RF pasteurization of meat products has involved the application of RF to uncased meats [52][54][55]. This kind of method could reduce packaging costs for processors, however, at the same time, it increased the risk of post process contamination and potentially reduced yield due to juice losses from unpackaged hot products. Post-cooking temperature profiles of meat emulsions presented in recent work by Zhang, Lyng, and Brunton suggested that uneven temperature distributions were possible in RF cooked meat products [56].

In the area of sterilization, continuous flow aseptic processing and packaging systems have largely replaced conventional thermal treatments. Such a concept is essentially a success story for easy flow liquid products. Scrapped surface heat exchangers have come to the rescue while processing viscous products. For particulate products, aseptic processing is still questionable due to uncertainties associated with particle residence time distribution and associated heat transfer. The primary advantage of improved uniformity of heating was shown for in-package sterilization of foods in large packages using radio frequency at 27.12 MHz, although enhanced edge heating continued to be an issue [57]. However, the lack of knowledge about the dielectric properties of various foods as functions of composition, temperature, and frequency has restricted the optimum design of RF heating system [42]. Commercial radio frequency heating systems for the purpose of food sterilization are not known to be in use, although they have been researched over the years [53][50][57].

RF heating has also been used to control pest-insects, fungi, and pathogens in food grains. Many laboratory RF systems working at frequency of 27.12MHz are developed to eradicate the harmful insects in wheat [58][59], rice grains [60], corn [61] and barley seeds [62]. All the researches have good results in controlling insects. Some of the successful applications of RF processing foods are listed in table 2.2. Besides the research and applications in foods, RF heating finds their applications in other domains. Zhenhu HU et al. used radio frequency to pretreat switchgrass with catalytic alkali (NaOH), which gained higher yield [63]. Drying of woods, ceramic and fiberglass with RF are also widely applied in industry.

Table 2.2 Some successful applications of RF heating foods

Process	Frequency (MHz)	Food Items	References
Thawing frozen food	14-17	Eggs, fruits, vegetables	Cathcart et al. 1947
	36-40	Fish	Jason and Sanders, 1962
	36-40	Meat	Sanders, 1966
Tempering	10-300	Meat	Experimental station, Parma, Italy, 1997
Post-baking drying	27.12	Cookies, crackers, snack foods	Radio frequency Co., MA, Mermelstein, 1988
Pasteurization	9	Meats	Pircon et al., 1953
	60	Cured hams	Bengtsson et al., 1970
	27	Sausage emulsion	Houben et al., 1994
Cooking	13.56	Ham	Tulip international, 1995
Roasting	60	Cocoa beans	Electrotechnology application center, PA, Cresko, Anantheswaran, 1998

2.4 Intermittent heating

The operating condition of a drying process can be monitored in order to reduce the operating cost by changing air flow rate, humidity, temperature or operating pressure, individually or in tandem [26]. Several modes of operating conditions on powers are possible. They are stepwise with equal intervals or with varying intervals, step-up and step-down profiles, shown in Figure 2.2.

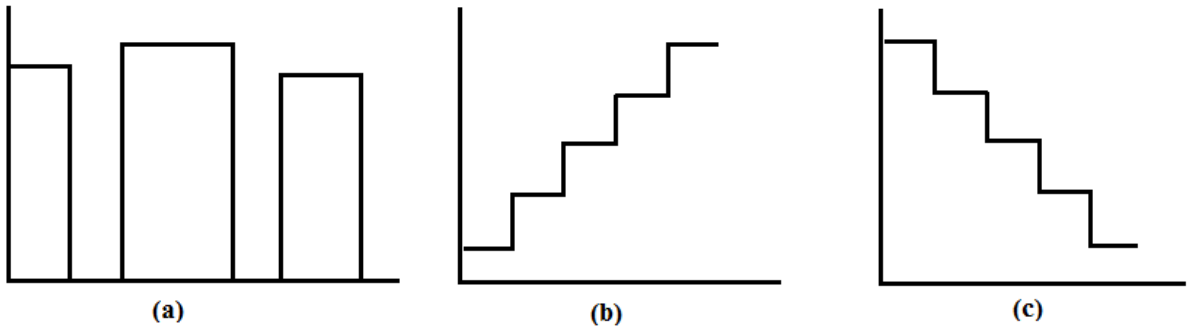


Figure 2.2 Intermittent heating modes: (a) step-wise, (b) step-up, (c) step-down

These kinds of heating modes can be used to obtain high energy efficiency without subjecting the product beyond its permissible temperature and pressure limits while maintaining a high moisture loss rate. Some intermittent dryings have distinctive active and non-active drying. The period of time when the heat input is stopped is called non-active drying or tempering. During each non-active heating period, internal moisture within the drying materials redistributes and the moisture gradient decreases. Reduction of the moisture gradient has a beneficial effect that can lead to more homogeneous temperature distribution and prevent crack formation. Furthermore, migration of moisture from interior to the surface of treated material during tempering allows the drying rate in the following active drying to be increased dramatically.

Owning to the advantage that RF source could be turned on or off instantly, it is very easy to implement the stepwise change operation to the RF heating system. It is noteworthy that various modes of intermittent heating are possible. In my dissertation, the stepwise is adopted since its application can minimize energy loss. The merits of stepwise intermittent drying have been well established for a variety of materials with or without microwave energy [64] [65]. Some other recent research findings on stepwise intermittent heating summarized by Jatindra K. Sahu are selected to show further the advantages of periodically heating [26].

Table 2.3 Research findings of stepwise intermittent heating food products

Researched product	Findings
Guava pieces	Minimize degradation of ascorbic acid content
Pasta	Long tempering period at higher temperature was needed to ensure better product quality of pasta
Solid byproducts from olive oil extraction	Longer period can redistribute internal moisture and level moisture content of interior surface, leading to higher moisture loss
Rough rice	Tempering at 45 Celsius degrees for 2 hours gave better milling recovery, head rice ratio, grain hardness, degree of whiteness and cracked grains ratio; while tempering at 60 Celsius degrees have better rough rice quality

Banana slices	Performances of drying kinetics and color degradation

Periodically heating reportedly results in greater depth of heating than continuous heating for the same total input energy. Furthermore, microwave or RF intermittently heating, comparing to continuous application of power, leads to more uniform temperature distribution within the sample [66]. This can improve product quality and process efficiency [67].

Reference of chapter 2

[1] Tong, C. H. "Microwave heating of baked dough products with simultaneous heat and moisture transfer," *PhD Thesis, University of Wisconsin*, 1988.

[2] Ni, H., A. K. Datta and R. Parmeswar. "Prediction of moisture loss and its relation to heating uniformity in microwaved foods," *Proceedings of 29th Microwave Power Symposium*, Chicago, IL,1994.

[3] Luikov, A. V., "Systems of differential equations of heat and mass transfer in capillary-porous bodies (review)," *Int. J. Heat Mass Transfer*, vol.18, no.1-A, pp.1-13, 1975.

[4] Whitaker, S. "Simultaneous heat, mass and momentum transfer in porous media: a theory of drying," *Adv. Heat Transfer*, vol.13, pp.119-203,1977.

[5] Whitaker S. and Chou W., "Drying granular porous media-Theory and experiment," *Drying technology*, vol. 1, P3, 1983.

[6] S. Chen and S. Whitaker, "Moisture distribution during constant rate drying period for unconsolidated porous media: Failure of the diffusion theory," in Mujumdar, *A. S. (ed.), Drying 86*, vol.1,pp. 39-48, Hemisphere, Washington D. C., 1986,

[7] S. Bories, G. Bacon and M. Recan, "Experimental and numerical study of coupled heat and mass transfer in porous materials," *Proc. 4th Int. Drying Symp.*, Kyoto, pp. 159-164. 1984.

[8] C. Moyne and A. Degiovanni, "Importance of gas phase momentum equation in drying above the boiling point of water," *Proc. 4th Inl. Drying Symp.*, Kyoto ,1984.

[9] O. A. Plumb, G. A. Spolek and B, A. Olmstead, "Heat and mass transfer in wood during drying," *Int. J. Heat Mass Transfer* vol.28, pp. 1669-1678, 1985.

[10] S.Ben Nasrallah and P. Perre, "Detailed study of a model of heat and mass transfer during convective drying of porous media," *Int. J. Heat Mass Transfer*, vol. 31, no. 5, pp. 957-967, 1988.

[11] H. Ni, A.K. Datta, K. E. Torrance, "Moisture transport in intensive microwave heating of biomaterials: a multiphase porous media model," *Int. J. Heat Mass Transfer*, vol. 42, pp.1501-1512, 1999.

[12] Robbins, M. C. and M. N. Ozisik., "Analysis of drying in capillary-porous planar media," *Drying Technology*, vol.6, no.4, pp.579-599, 1988.

[13] Irudayaraj, J. and Y. Wu., "Finite element analysis of coupled heat, mass, and pressure transfer in porous biomaterials," *Numerical Heat Transfer: Part A*, vol.26, pp. 337-350,1994.

[14] Irudayaraj, J. and Y.Wu., "Analysis and application of Luikov's heat, mass, and pressure transfer model to a capillary porous media," *Drying Technology*, vol.14,no.3-4, pp.803-824, 1996.

[15] R.N. Pandey, S.K. Srivastava, M.D. Mikhailov, "Solutions of Luikov equations of heat and mass transfer in capillary porous bodies through matrix calculus: a new approach," *Int. J. Heat Mass Transfer*, vol. 42, pp. 2649-2660, 1999.

[16] L.B. Dantas, H.R.B. Orlande, R.M.Cotta, "Estimation of dimensionless parameters of Luikov's system for heat and mass transfer in capillary porous media," *Int. J. Therm. Sci.*, vol.41 pp.217–227, 2002.

[17] F. Nadi, G. H. Rahimi, R. Younsi, T. Tavakoli, and Z. Hamidi-Esfahani, "Numerical Simulation of Vacuum Drying by Luikov's Equations," *Drying Technology*, vol.30, pp.197–206, 2012.

[18] Wei, C. K., H. T. Davis, E. A. Davis and J. Gordan., "Heat and mass transfer in water-laden sandstone: convective heating," *AIChE J.*, vol.31, no.8, pp.1338-1348,1985.

[19] Perre, P.and C. Moyne., "Processes related to drying, part II: use of the same model to solve transfers both in saturated and unsaturated porous media," *Drying Technology,* vol.9, no.5, pp.1153-1179, 1991.

[20] Boukadida, N. and S. B. Nasrallah., "Two dimensional heat and mass transfer during convective drying of porous media," *Drying Technology*, vol.13,no.3, pp. 661-694,1995.

[21] Phillip Gibson, "Technical report Natick/TR -951004, United States Army Natick research," *development and engineering center Natick*, Massachusetts 01760-5000, 1994.

[22] Ilic, M. and I. W. Turner. "Convective drying of a consolidated slab of wet porous material," *Int. J. Heat Mass Transfer*, vol.32,no.1, pp. 2351-2362,1989.

[23] Turner, I. W. and P. Perré. "A comparison of the drying simulation codes which are used for the modeling of two- dimensional wood drying processes," *Drying Technology*, vol.13, no.3, pp.695-735,1995.

[24] P. Perré and J. Passard, "A physical and mechanical model able to predict the stress field in wood over a wide range of drying conditions," *Drying technology*, vol. 22, nos. 1 & 2, pp. 27–44, 2004.

[25] R. Rémond, J. Passard, P. Perré, "The effect of temperature and moisture content on the mechanical behaviour of wood: a comprehensive model applied to drying and bending," *European Journal of Mechanics - A/Solids,* vol.26, no. 3, pp.558–572, 2007.

[26] Jatindra K. Sahu, "Introduction to advanced food process engineering," *CRC press, Taylor & Francis Group*, pp.645, 2014.

[27] A.K. Datta and P. Michael Davidson, "Microwave and radio frequency processing," *J. food science-supplement*, pp.32-41, 2000.

[28] Nelson, S.O., "Measurement of microwave dielectric properties of particulate materials," *Journal of food engineering*, vol.21, pp.365-384, 1994.

[29] Datta, A.K. and Ramaswamy, C.A., "Microwave technology for food applications," *Marcel Dekker*, New York, 2001.

[30] Buffer, C.R., "Microwave cooking and processing: engineering fundamentals for a food scientist," *Van Nostran Reinhold*, New York, 1993.

[31] Wang, Y., Wig, T. D., Tang, J. and Hallberg, L. M., "Dielectric properties of foods relevant to RF and microwave pasteurization and sterilization," *Journal of food engineering*, vol.57, pp.257-268 , 2003.

[32] S. O. Nelson, "Dielectric property measurement techniques and applications," *Transactions of the ASAE*, vol. 42, no. 2, pp.523-529,1999.

[33] M.S. Venkatesh, G.S.V. Raghavan, "An overview of dielectric properties measuring techniques," *Canadian biosystems engineering*, vol. 47, 7.51-7.30, 2005.

[34] Udo Kaatze, "Techniques for measuring the microwave dielectric properties of materials," *Metrologia,* vol. 47, pp. S91-S113, 2010.

[35] Ari Sihvola, "Mixing rules with complex dielectric coefficients," *Subsurface Sensing Technologies and Applications*, vol. 1, no. 4, pp.393-415, 2000.

[36] Perkins RM, "The heat and mass transfer characteristics of boiling point drying using radio frequency and microwave electromagnetic fields," *Int J Heat and Mass Transfer*, vol. 23, pp. 687-695, 1980.

[37] Ayappa KG, Davis HT, Crapiste G, Davis EA, Gordon J; "Microwave heating: an evaluation of power formulations," *Chemical Engineering Science*, vol. 27, pp.1005-1016, 1991.

[38] Vineet Rakesh and Ashim K. Datta, Jeffrey H. Walton, Kathryn L. McCarthy and Michael J. McCarthy, "Microwave combination heating: coupled electromagnetics-multiphase porous media modeling and MRI experimentation," *AIChE Journal*, vol.58, no. 4, pp. 1262-1278, 2012.

[39] Haitao Ni, "Multiphase moisture transport in porous media under intensive microwave heating," *A dissertation of Cornell University*, 1997.

[40] S.L. Semiatin and S. Zinn, "Elements of Induction heating: Design, Control, and Applications," *Electric Power Research Institute*, Inc. 1988, pp. 3.

[41] Anonymous. "Radio frequency ovens increase productivity and energy efficiency," *Prepared Foods*, September:125, 1993.

[42] Punidadas Piyasena, Chantal Dussault, Tatiana Koutchma, H. S. Ramaswamy, and G. B. Awuah, "Radio frequency heating of foods: principles, applications and related properties—A review," *Critical Reviews in Food Science and Nutrition*, vol.43, no.6, pp.587–606, 2003.

[43] Moyer, J. C. and Stotz, E., "The blanching of vegetables by electronics," *Food Technology*, vol.1, pp. 252–257, 1947.

[44] Victor Falguera and Albert Ibarz, "Juice processing: Quality, safety and value-added opportunities," *CRC press, Taylor& Francis group,*2014.

[45] Jason, A. C. and Sanders, H. R., "Dielectric thawing of fish. Experiments with frozen herrings. Experiments with frozen white fish," *Food Technology*, vol.16, no.6, pp.101–112, 1962.

[46] Demeczky, M., "Continuous pasteurization of bottled fruit juices by high frequency energy," *Proceedings of IV International Congress on Food Science and Technology, vol. IV*, pp.11–20, 1974.

[47] RICE, J., "RF technology sharpens bakery's competitive edge," *Food Proc*., vol.6, pp.18-24, 1993.

[48] MERMELSTEIN, N. H., "Microwave and radio frequency drying," *Food Technology*, vol.52, no.11, pp.84-86, 1998.

[49] Mermelstein, N. H., "Interest in radio frequency heating heats up," *Food Technology*, vol.51,no.10, pp.94–95,1997.

[50] HOUBEN, J., SCHOENMAKERS. L., van PU'ITEN, E., van ROON, P. and KROL, B., "Radio-frequency pasteurization of sausage emulsions as a continuous process," *J. Micro. Power & Electromagnetic Energy*, vol.26, no.4, pp.202-205, 1991.

[51] Ryyna¨nen, S., "The electromagnetic properties of food materials: A review of the basic principles," *Journal of Food Engineering*, vol.26, pp.409–429.,1995.

[52] Houben, J., Schoenmakers, L., van Putten, E., van Roon, P., & Krol, B., "Radio-frequency pasteurization of sausage emulsions as a continuous process," *J. Micro. Power & Electromagnetic Energy*, vol.26, no.4, pp.202–205, 1991.

[53] Bengtsson, N. E., Green, W., & Del Valle, F. R., "Radio frequency pasteurization of cured hams," *Journal of Food Science*, vol.35, pp.681–687, 1970.

[54] L. Laycock, P. Piyasena, G.S.Mittal, "Radio frequency cooking of ground, comminuted and muscle meat products," *meat science*, vol.65, no.3, pp.959-965, 2003.

[55] van Roon, P. S., Houben, J. H., Koolmees, P. A., van Vilet, T., & Krol, B., "Mechanical and microstructural characteristics of meat doughs, either heated by a continuous process in a radio frequency field or conventionally in a waterbath," *Meat Science*, vol.38, no.1, pp.103–116,1994.

[56] Zhang, L., Lyng, J. G., & Brunton, N. P., "Effect of radio frequency cooking on the texture, colour and sensory properties of a large diameter communited meat product," *Meat Science*, vol.68, no.2, pp.257–268, 2004.

[57] Wig, T., Tang, J., Younce, F., Hallberg, L., Dunne, C. P. and Koral, T., "Radio frequency sterilization of military group rations," *AIChE Annual Meeting*,1999.

[58] Nelson S.O., "Possibilities for controlling stored grain insects with radio frequency energy," *J. Micro. Power & Electromagnetic Energy*, vol.7, no.3, pp.231-239,1972.

[59] Nelson S.O., "Insect-control studies with microwaves and other radio frequency energy," *Bulletin of the entomological society of America*, vol.19, no.3, pp.157-163, 1973.

[60] Janhang P., Krittigammas N., Lucke W., Vearasilp S., "Using radio frequency heat treatment to control seed-borne Trichoconis padwickii in rice seed (Oryza sativa L.),"

Conference on international agricultural research for development, Stuttgart-Honenheim, Germany, 2005.

[61] Vasanachalorn P., Janhang P., Krittigamas N., Von Horsten D., Lucke W., "Radio frequency heat treatment to eradicate Fusarium semitectum in corn grain (Zea Mays)," *Agricultural science journal,* vol.37, no.5, pp.180-182 , 2006.

[62] George B. Awuah, Hosahalli S. Ramaswamy, Juting Tang, "Radio-Frequency heating in food processing: Principles and applications," *CRC Press, Taylor & Francis Group*, 2014.

[63] Zhenhu Hu, Yifen Wang, Zhiyou Wen, "Alkali (NaOH) Pretreatment of Switchgrass by Radio Frequency-based Dielectric Heating," *Appl Biochem Biotechnol*, vol.148, pp.71-81, 2008.

[64] N. N. Grinchik, P. V. Akulich, A. L. Adamovich, P. S. Kuts, and S. P. Kundas, "Modeling of nonisothermal heat and moisture transfer in capillary-porous media in periodic microwave heating," *Journal of Engineering Physics and Thermophysics*, vol.80, no.1, pp.1-10, 2007.

[65] I. Farkas, Z. Rendik, "Intermittent thin layer corn drying," *Drying Technology*, vol.15, no.6–8, pp.1951–1960,1997.

[66] H. W. Yang, S. Gunasekaran, "Comparison of temperature distribution in model food cylinders based on Maxwell's equations and Lambert's law during pulsed microwave heating," *Journal of Food Engineering*, vol.64, no.4, pp.445–453, 2004.

[67] S. Gunasekaran, "Pulsed microwave-vacuum drying of food materials," *Drying Technology*, vol.17, no.3, pp.395–412,1999.

Chapter 3 Numerical research on multiphase transfer under convective heating

To understand the mechanism of RF heating porous media better, the disciplines describing the mass and heat transfer in materials under convective heating are studied first. Several researchers have developed heat and mass transfer equations for porous media starting from conservation equations and mechanistic flux models [1][2][3][4][5]. In this paper, the formulas presented in S. Ben Nasrallah's article [2] are employed to study the mass and heat transfer in 1D brick model with convective heating.

3.1 Theoretical preparation

3.1.1 Assumptions

A schematic of constitution of porous media [6] is revealed by Figure 3.1. Three phases are included in this model: solid, liquid water, vapor and air. To arrive at the governing equations, several important assumptions are needed and listed as following:

1) All the phases are continuous. Even though that the liquid may be discontinuous when its saturation level is lower than a certain value [7], the primary goal of this chapter is to know better the moisture transport during a short heating time, the substance won't be dried to the level that the liquid becomes disconnected. Therefore, this assumption is tenable for our research.
2) The temperatures in the three phases are equal. The hypothesis is widely utilized in convective heating [2][3][7] and microwave heating [8][9][10].
3) Both the vapor and air behave like the ideal gas [2][7][10].
4) The Reynolds number is small and Darcy' law is valid for describing the convective flow of gas and liquid phases.
5) The convective flow due to the gradient in total gas pressure and capillary pressure due to the gradient of capillary force contribute to the liquid movement.

6) Evaporation/condensation is distributed throughout the food domain instead of being a surface phenomenon.
7) The effective thermal conductivity is proportional to the mass content of each phase [3] [11][12] [13].
8) Mass transfer coefficient that quantifies the convective moisture loss is independent of the surface conditions [2][3].
9) The porous media is assumed isotropic for simplify the model, although it is not always true for porous materials, especially for biomass.
10) Shrinkage of the sample during the heating time is not considered because the structure of the sample is stiff.
11) Gravity is ignored. The sample size is small so that the effect of difference in height is insignificant.

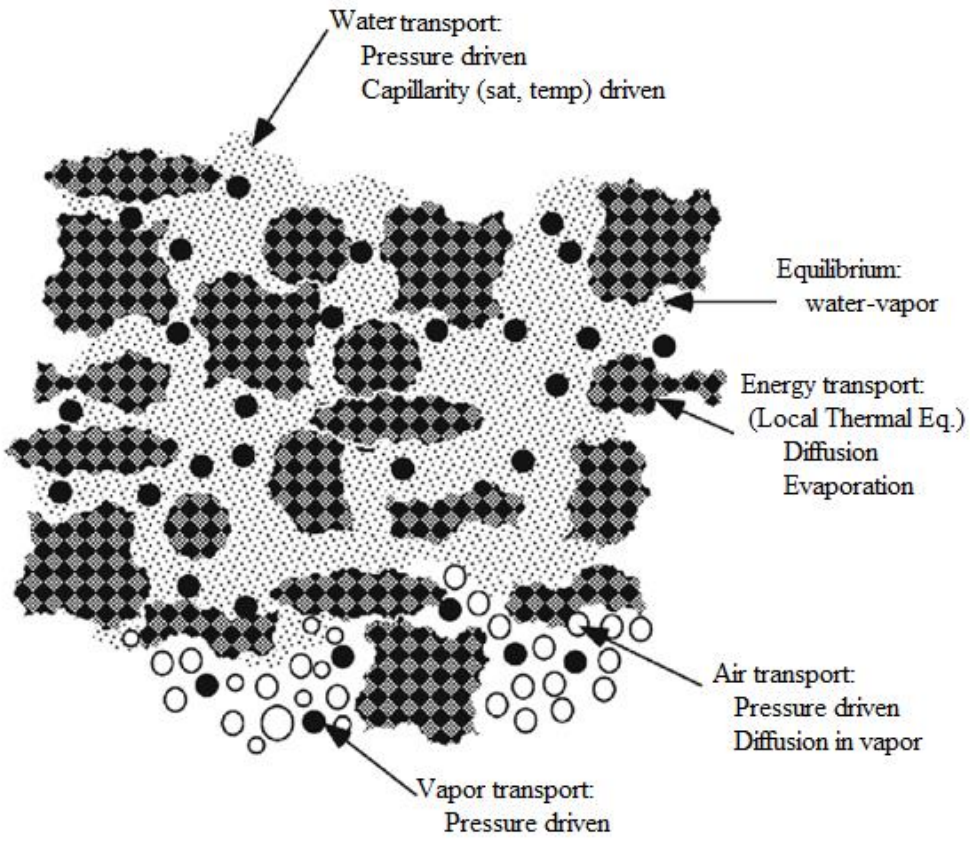


Figure 3.1 Schematic of porous media

3.1.2 Equilibrium state variables and vapor pressure

Rahman [14] listed several different porosity definitions (apparent porosity, open pore porosity, closed pore porosity, bulk porosity and total porosity) in the context of foods (hygroscopic porous media). But all of these porosity definitions did not separate liquid water from the solid matrix, and are only defined in terms of the gas porosity as seen in Figure 3.2b. Figure 3.2 provides a schematic of representative element volume of porous media. It is the smallest volume over which a measurement can be made that will yield a value representative of the whole. The derivations of the formulas below are all based on the representative element volume, all of which are applicative to describe behaviors of the macro-scale porous media.

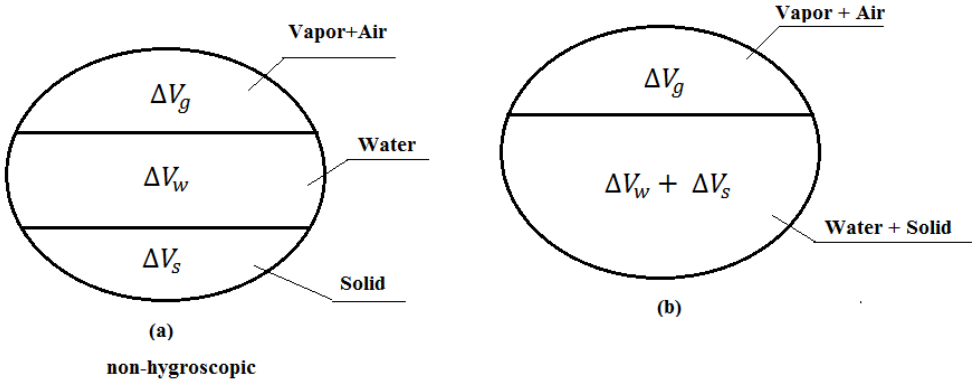


Figure3.2 representative element volume of porous media

Actually, the porosity of porous media should describe the fraction of void space in the material, where the void may contain, for example, air or water. For the non-hygroscopic porous media, the three phases are separated and the porosity is defined as the volume fraction occupied by gas and liquid due to the phases inside are clearly separated. Therefore, we adapt the definitions and equations analogous to those well-established in non-hygroscopic porous media for all the porous models and calculate the vapor and air concentration from gas volume fraction, liquid concentration from water volume fraction [5]. Since we have made the assumption that the sample won't shrink, the representative element volume in porous media can be described as:

$$\Delta V = \Delta V_g + \Delta V_s + \Delta V_w \tag{3-1}$$

Then porosity can be defined as

$$\phi = \frac{\Delta V_g + \Delta V_w}{\Delta V} \tag{3-2}$$

Saturations of liquid and gas are listed respectively

$$S_w = \frac{\Delta V_w}{\Delta V_w + \Delta V_g} = \frac{\Delta V_w}{\phi \Delta V} \tag{3-3}$$

$$S_g = \frac{\Delta V_g}{\Delta V_w + \Delta V_g} = \frac{\Delta V_g}{\phi \Delta V} \tag{3-4}$$

$$S_w + S_g = 1 \tag{3-5}$$

Since the air and vapor don't react with each other, the total pressure exerted is equal to the sum of the partial pressure of the individual gases according to Dalton' Law.

$$P = p_v + p_a \tag{3-6}$$

The mass densities of vapor and air can be deduced from the ideal gas law in molar form:

$$p_v \Delta V_g = \frac{m_v}{M_v} RT \tag{3-7}$$

$$p_a \Delta V_g = \frac{m_a}{M_a} RT \tag{3-8}$$

Where m_i (i=a, v) indicates the mass of air and vapor, respectively; M_i (i=a, v) the molar mass of air and vapor. R is the ideal gas constant and T the temperature.

Introducing density $\rho = {}^{m}/_{V}$, we get the densities of air, vapor and their mixture

$$\rho_v = \frac{m_v}{\Delta V_g} = \frac{p_v M_v}{RT} = \frac{p_v}{R_v T} \tag{3-9}$$

$$\rho_a = \frac{m_a}{\Delta V_g} = \frac{p_a M_a}{RT} = \frac{p_a}{R_a T} \tag{3-10}$$

$$\rho_g = \frac{m_v + m_a}{\Delta V_g} = \rho_a + \rho_v \tag{3-11}$$

Where $R_v = {}^{R}/_{M_v}$, $R_a = {}^{R}/_{M_a}$.

The molar density of the gas mixture is

$$C = \frac{P}{RT} \tag{3-12}$$

In the similar way, the mass concentrations of air, vapor and liquid water are

$$c_v = \frac{m_v}{\Delta V} = \frac{p_v S_g \phi}{R_v T} = \frac{p_v (1-S_w)\phi M_v}{RT} \tag{3-13}$$

$$c_a = \frac{m_a}{\Delta V} = \frac{p_a S_g \phi}{R_a T} = \frac{p_a (1-S_w)\phi M_a}{RT} \tag{3-14}$$

$$c_g = c_a + c_v \tag{3 -15}$$

$$c_w = \rho_w \phi S_w \tag{3-16}$$

Below listing another two important variables, one is the moisture content, which is defined by the mass fraction of mass of liquid water to that of solid matrix:

$$M = \frac{\phi S_w \rho_w}{(1-\phi)\rho_s} \tag{3-17}$$

The other one is the vapor pressure, which demonstrates the liquid's evaporation rate. Generally, the change of equilibrium vapor pressure can be divided into three stages characterized by moisture content ranges. When the material is very wet, the vapor pressure varies non-linearly with temperature according to Clausius-Clapeyron equation for both hygroscopic and non-hygroscopic porous materials. Then, as the material dries, surface tension on the liquid by the smaller pores starts to hold the liquid more tightly and thereby lessen the vapor pressure. The variation in this section can be described by the Kelvin equation. With the materials getting even drier, several forces such as London-Van der Waals force, double layers force, short range forces and Hydrogen bonding become important [15], leading to a more sharply reduction of vapor pressure comparing with only the effect of capillary pores. It is in this range that isotherm relationships are indispensable.

The change process of vapor pressure is complicated and hard to describe theoretically. Fortunately, measurements have been done for food continuously from very wet stage to very dry stage. The whole curve is referred to as isotherm relationship [7] which is a function of temperature, moisture content and the type of material,

$$p_v = p_{sat}(T) a_w(M) \tag{3-18}$$

p_{sat} is the vapor pressure of free water, M is the moisture content.

3.1.3 Mass and heat conservation equations

A schematic of the 1D brick model is shown in Figure 3.3, which is in the form of a flat porous slab. The left side of the slab is exposed to an air flux with fixed velocity, temperature and relative humidity. The energy and moisture convect with the outer space from this side. The other side is adiabatic and impervious, where the energy and moisture flux is zero.

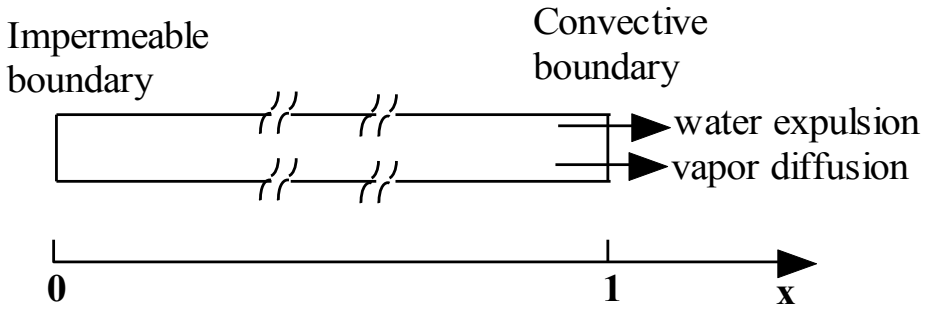


Figure 3.3 Schematic of 1D brick

During the convective heating, there are diffusive transports of vapor and air, capillary pressure driven liquid transport and total gas pressure driven flows of air, vapor and water.

Diffusion is the net movement of a substance (e.g., an atom, ion or molecule) from a region of high concentration to a region of low concentration. This is also referred to as the movement of a substance down a concentration gradient. Therefore, the diffusive fluxes can be written in term of mole concentration fractions [7].

$$\overrightarrow{Ja} = -\frac{C^2}{\rho} M_a M_v D_{eff,g} \nabla x_a \tag{3-19}$$

$$\overrightarrow{Jv} = -\frac{C^2}{\rho} M_a M_v D_{eff,g} \nabla x_v \tag{3-20}$$

$$x_i = \frac{p_i}{P_{amb}} \quad i = a, v \tag{3-21}$$

$D_{eff,g}$ is the effective gas diffusivity in the porous media. P_{amb} is the ambient pressure. The reason for choosing the gradient of the molar fraction rather than the gradient of the mass fraction as the driving force is that the molar fraction is directly related to the partial pressures of air, vapor, and the total pressure. The employment of mole fraction will make the subsequent derivations much simpler.

The convective flux is described by Darcy's Law. Since the effect of capillary pressure is included as a diffusion term, velocity of each phase due to total gas pressure is given by:

$$\overrightarrow{u_i} = -\frac{k_{r,i}k_{in,i}}{\mu_i}\nabla P \tag{3-22}$$

Where i stands for water, air and vapor. The components of air and vapor share the same velocity. $k_{r,i}$ and $k_{in,i}$ are the relative and intrinsic permeability of different phases, respectively.

The mass fluxes of air and vapor based on the total cross-section are written as:

$$\overrightarrow{m_a} = -\rho_a \frac{k_{r,a}k_{in,a}}{\mu_a}\nabla P \tag{3-23}$$

$$\overrightarrow{m_v} = -\rho_v \frac{k_{r,v}k_{in,v}}{\mu_v}\nabla P \tag{3-24}$$

The total fluxes of air and vapor consist of the diffusion and convective flux

$$\overrightarrow{n_a} = -\rho_a \frac{k_{in,g}k_{r,g}}{\mu_g}\nabla P - \frac{C^2}{\rho_g} M_a M_v D_{eff,g}\nabla x_a \tag{3-25}$$

$$\overrightarrow{n_v} = -\rho_v \frac{k_{in,g}k_{r,g}}{\mu_g}\nabla P - \frac{C^2}{\rho_g} M_a M_v D_{eff,g}\nabla x_v \tag{3-26}$$

The flux of water is:

$$\overrightarrow{n_w} = -\rho_w \frac{k_{in,w}k_{r,w}}{\mu_w}\nabla p_w \tag{3-27}$$

Substituting the above formulas into equation (3-25), we can further deduce it as :

$$\overrightarrow{n_a} = -\frac{p_a M_a}{RT}\frac{k_{in,g}k_{r,g}}{\mu_g}\nabla P - \left(\frac{P}{RT}\right)^2 \frac{1}{\frac{p_v M_v + p_a M_a}{RT}} M_a M_v D_{eff,g}\nabla\left(\frac{p_a}{P}\right) \tag{3-28}$$

$$= -\frac{p_a M_a}{RT}\frac{k_{in,g}k_{r,g}}{\mu_g}\nabla P - \left(\frac{P}{RT}\right)^2 \frac{RT}{p_v M_v + p_a M_a} M_a M_v D_{eff,g}\nabla\left(1 - \frac{p_v}{P}\right)$$

$$= -\frac{p_a M_a}{RT}\frac{k_{in,g}k_{r,g}}{\mu_g}\nabla P + \frac{1}{RT}\frac{1}{p_v M_v + p_a M_a} M_a M_v D_{eff,g}(P\nabla p_v - p_v\nabla P)$$

$$= -\frac{p_a M_a}{RT}\frac{k_{in,g}k_{r,g}}{\mu_g}\nabla P + \frac{1}{RT}\frac{1}{p_v M_v + p_a M_a} M_a M_v D_{eff,g}\left(P\frac{\partial p_v}{\partial S_w}\nabla S_w + P\frac{\partial p_v}{\partial T}\nabla S_w - p_v\nabla P\right)$$

Similarly, the total fluxes of vapor and water are:

$$\overrightarrow{n_v} = -\frac{p_v M_v}{RT}\frac{k_{in,g}k_{r,g}}{\mu_g}\nabla P - \left(\frac{P}{RT}\right)^2 \frac{1}{\frac{p_v M_v + p_a M_a}{RT}} M_a M_v D_{eff,g}\nabla\left(\frac{p_v}{P}\right) \tag{3-29}$$

$$= -\frac{p_v M_v}{RT}\frac{k_{in,g}k_{r,g}}{\mu_g}\nabla P - \frac{1}{RT}\frac{1}{p_v M_v + p_a M_a} M_a M_v D_{eff,g}(P\nabla p_v - p_v \nabla P)$$

$$= -\frac{p_v M_v}{RT}\frac{k_{in,g}k_{r,g}}{\mu_g}\nabla P - \frac{1}{RT}\frac{1}{p_v M_v + p_a M_a} M_a M_v D_{eff,g}\left(P\frac{\partial p_v}{\partial S_w}\nabla S_w + P\frac{\partial p_v}{\partial T}\nabla S_w - p_v \nabla P\right)$$

$$\overrightarrow{n_w} = -\rho_w \frac{k_{in,w}k_{r,w}}{\mu_w}\nabla p_w \tag{3-30}$$

$$= -\rho_w \frac{k_{in,w}k_{r,w}}{\mu_w}\nabla(P - p_c)$$

$$= -\rho_w \frac{k_{in,w}k_{r,w}}{\mu_w}(\nabla P - \frac{\partial p_c}{\partial S_w}\nabla S_w - \frac{\partial p_c}{\partial T}\nabla T)$$

3.1.3.1 Vapor mass conservation equation

$$\frac{\partial c_v}{\partial t} + \nabla \cdot \overrightarrow{n_v} = I \tag{3-31}$$

I is the phase change, which will be introduced later.

Like the total flux, the first term on the left side of the equation is developed further here:

$$\frac{\partial c_v}{\partial t} = -\frac{p_v \phi M_v}{RT}\frac{\partial S_w}{\partial t} + \frac{(1-S_w)\phi M_v}{R}\frac{\partial}{\partial t}\left(\frac{p_v}{T}\right) \tag{3-32}$$

$$= -\frac{p_v \phi M_v}{RT}\frac{\partial S_w}{\partial t} + \frac{(1-S_w)\phi M_v}{R}\frac{\partial}{\partial t}\left(\frac{1}{T}\frac{\partial p_v}{\partial S_w}\frac{\partial S_w}{\partial t} + \frac{\partial T}{\partial t}\left(\frac{T\partial p_v/\partial T - p_v}{T^2}\right)\right)$$

Combining equations (3-29) and (3-32), it is clear that vapor mass conservation equation is a formula of variables of water saturation S_w, temperature T and total gas pressure P. Equation (3-32) can be written in form as below:

$$K_{4v}\frac{\partial S_w}{\partial t} + K_{5v}\frac{\partial T}{\partial t} + K_{6v}\frac{\partial P}{\partial t} = \nabla(K_1 \nabla S_w) + \nabla(K_2 \nabla T) + \nabla(K_3 \nabla P) + I \tag{3-33}$$

3.1.3.2 Water mass conservation equation

$$\frac{\partial c_w}{\partial t} + \nabla \cdot \overrightarrow{n_w} = -I \tag{3-34}$$

$$\frac{\partial c_w}{\partial t} = \phi \rho_w \frac{\partial S_w}{\partial t} \tag{3-35}$$

To balance the number of equations solved and the unknown variables, equation (3-31) is added with (3-34), eliminating the phase change I.

$$\frac{\partial c_v}{\partial t} + \nabla \cdot \overrightarrow{n_v} + \frac{\partial c_w}{\partial t} + \nabla \cdot \overrightarrow{n_w} = 0 \tag{3-36}$$

The simple form of three unknown variables is given by:

$$K_4 \frac{\partial S_w}{\partial t} + K_5 \frac{\partial T}{\partial t} + K_6 \frac{\partial P}{\partial t} = \nabla(K_1 \nabla S_w) + \nabla(K_2 \nabla T) + \nabla(K_3 \nabla P) \tag{3-37}$$

$$K_1 = \frac{M_a M_v D_{eff,g}}{RT(p_v M_v + p_a M_a)} P \frac{\partial p_v}{\partial S_w} - \rho_w \frac{k_{in,w} k_{r,w}}{\mu_w} \frac{\partial p_c}{\partial S_w}$$

$$K_2 = \frac{M_a M_v D_{eff,g}}{RT(p_v M_v + p_a M_a)} P \frac{\partial p_v}{\partial T} - \rho_w \frac{k_{in,w} k_{r,w}}{\mu_w} \frac{\partial p_c}{\partial T}$$

$$K_3 = -\frac{M_a M_v D_{eff,g}}{RT(p_v M_v + p_a M_a)} p_v + \rho_w \frac{k_{in,w} k_{r,w}}{\mu_w} + \frac{p_v M_v}{RT} \frac{k_{in,g} k_{r,g}}{\mu_g} \tag{3-38}$$

$$K_4 = -\frac{p_v \phi M_v}{RT} + \frac{(1 - S_w)\phi M_v}{RT} \frac{\partial p_v}{\partial S_w} + \phi \rho_w$$

$$K_5 = \frac{(1 - S_w)\phi M_v}{R} \left(\frac{T^{\partial p_v}/_{\partial T} - p_v}{T^2}\right)$$

$$K_6 = 0$$

3.1.3.3 Air mass conservation equation

$$\frac{\partial c_a}{\partial t} + \nabla \cdot \overrightarrow{n_a} = 0 \tag{3-39}$$

$$\frac{\partial c_a}{\partial t} = \frac{\phi M_a}{R}\left[-\frac{\partial S_w}{\partial t}\frac{P - p_v}{T} + (1 - S_w)\frac{\partial}{\partial t}\left(\frac{P - p_v}{T}\right)\right] + \frac{(1 - S_w)\phi M_a}{RT}\frac{\partial P}{\partial t} \tag{3-40}$$

$$= \frac{\phi M_a}{R}\left[-\frac{P - p_v}{T}\frac{\partial S_w}{\partial t} + (1 - S_w)\left(\frac{\partial}{\partial S_w}\left(\frac{P - p_v}{T}\right)\frac{\partial S_w}{\partial t} + \frac{\partial}{\partial T}\left(\frac{P - p_v}{T}\right)\frac{\partial T}{\partial t}\right)\right] + \frac{(1 - S_w)\phi M_a}{RT}\frac{\partial P}{\partial t}$$

$$= \frac{\phi M_a}{R}\left[-\frac{P - p_v}{T}\frac{\partial S_w}{\partial t} + (1 - S_w)\left(-\frac{1}{T}\frac{\partial p_v}{\partial S_w}\frac{\partial S_w}{\partial t} + \left(-\frac{P}{T^2} - \frac{\partial}{\partial T}\left(\frac{p_v}{T}\right)\right)\frac{\partial T}{\partial t}\right)\right] + \frac{(1 - S_w)\phi M_a}{RT}\frac{\partial P}{\partial t}$$

$$= -\frac{\phi M_a}{R}\left(\frac{P - p_v}{T} + \frac{(1 - S_w)}{T}\frac{\partial p_v}{\partial S_w}\right)\frac{\partial S_w}{\partial t} - \frac{\phi M_a (1 - S_w)}{R}\left(\frac{P}{T^2} + \frac{\partial}{\partial T}\left(\frac{p_v}{T}\right)\right)\frac{\partial T}{\partial t}\right) + \frac{(1 - S_w)\phi M_a}{RT}\frac{\partial P}{\partial t}$$

The simple form of three unknown variables is given by:

$$K_{10} \frac{\partial S_w}{\partial t} + K_{11} \frac{\partial T}{\partial t} + K_{12} \frac{\partial P}{\partial t} = \nabla(K_7 \nabla S_w) + \nabla(K_8 \nabla T) + \nabla(K_9 \nabla P) \tag{3-41}$$

$$K_7 = -\frac{M_a M_v D_{eff,g}}{RT(p_v M_v + p_a M_a)} P \frac{\partial p_v}{\partial S_w}$$

$$K_8 = -\frac{M_a M_v D_{eff,g}}{RT(p_v M_v + p_a M_a)} P \frac{\partial p_v}{\partial T}$$

$$K_9 = \frac{M_a M_v D_{eff,g}}{RT(p_v M_v + p_a M_a)} p_v + \frac{k_{in,g} k_{r,g}}{\mu_g} \frac{p_a M_a}{RT} \tag{3-42}$$

$$K_{10} = -\frac{\phi M_a}{R}\left(\frac{P - p_v}{T} + \frac{(1 - S_w)}{T}\frac{\partial p_v}{\partial S_w}\right)$$

$$K_{11} = -\frac{(1 - S_w)\phi M_v}{R}\left(\frac{P}{T^2} + \frac{T^{\partial p_v}/_{\partial T} - p_v}{T^2}\right)$$

$$K_{12} = \frac{(1 - S_w)\phi M_v}{RT}$$

3.1.3.4 Heat transfer equation

$$\frac{\partial}{\partial t}(\rho_{eff} C_{p,eff} T) + \nabla \cdot \left(\left(\rho C_p \vec{u}\right)_{fluid} T\right) = \nabla \cdot \left(k_{eff} \nabla T\right) - \lambda I \tag{3-43}$$

Where λ is the enthalpy of evaporation, k_{eff} the effective thermal conductivity.

$$\rho_{eff} = (1 - \phi)\rho_s + \phi(S_w \rho_w + S_g \rho_g) \tag{3-44}$$

$$C_{p,eff} = x_s C_{p,s} + x_w C_{p,w} + x_g(\omega_v C_{p,v} + \omega_a C_{p,a}) \tag{3-45}$$

$$k_{eff} = (1 - \phi)k_{t,s} + \phi(S_w k_{t,w} + S_g(\omega_v k_{t,v} + \omega_a k_{t,a})) \tag{3-46}$$

Using the water mass conservation equation to replace phase change I, the final form of equation (3-43) is

$$K_{16}\frac{\partial S_w}{\partial t} + K_{17}\frac{\partial T}{\partial t} + K_{18}\frac{\partial P}{\partial t} = -\nabla \cdot \left(\left(\rho C_p \vec{u}\right)_{fluid} T\right) + \nabla(K_{13}\nabla S_w) + \nabla(K_{14}\nabla T) + \nabla(K_{15}\nabla P) \tag{3-47}$$

$$K_{13} = \lambda \rho_w \frac{k_{in,w} k_{r,w}}{\mu_w} \frac{\partial p_c}{\partial S_w}$$

$$K_{14} = k_{eff} + \lambda \rho_w \frac{k_{in,w} k_{r,w}}{\mu_w} \frac{\partial p_c}{\partial T} \tag{3-48}$$

$$K_{15} = \lambda \rho_w \frac{k_{in,w} k_{r,w}}{\mu_w}$$

$$K_{16} = -\lambda \rho_w \phi$$

$$K_{17} = (\rho C_p)_{eff}$$

$$K_{18} = 0$$

3.1.4 Initial and boundary conditions

3.1.4.1 Initial conditions

Initially, the pressure throughout the sample is equal to the ambient pressure. As mentioned above in the assumptions, the temperatures of liquid water, air, vapor and solid are the same and set to a certain value. The water saturation is also uniform at the starting point. Thus, the initial conditions for the 1D brick under convective heating are listed as:

$$S_w = S_0$$

$$T = T_0 \tag{3-49}$$

$$P = P_{amb}$$

3.1.4.2 Boundary conditions

Two kinds of boundary conditions are needed in this model. The left side is the convective boundary where heat, moisture, gas are exchanged with the surrounding space. The right one is insulated boundary, from which the porous media isn't affected by the ambient environment.

Insulated boundary:

On the insulated boundary, the fluxes of heat, moisture and air are null, i.e.

$$\overrightarrow{n_w} = 0$$

$$\overrightarrow{n_v} = 0 \tag{3-50}$$

$$\overrightarrow{n_a} = 0$$

$$k_{eff} \frac{\partial T}{\partial t} + \lambda \rho_w \overrightarrow{u_w} = 0$$

Adding $\overrightarrow{n_w}$ and $\overrightarrow{n_v}$, the simple form equations describing insulated boundary are obtained:

$$-K_1\nabla S_w - K_2\nabla T - K_3\nabla P = 0$$

$$-K_7\nabla S_w - K_8\nabla T - K_9\nabla P = 0 \qquad (3\text{-}51)$$

$$-k_{eff}\nabla T = 0$$

Convective boundary:

Mass transfer on the surface is assumed to be in equilibrium with the surrounding which means that all mass flux reaching the boundary from inside is convected away immediately. Regardless of volumetric evaporation present inside, surface evaporation occurs simultaneously which means that there is liquid flux crossing the boundary and vaporizing instantly. The surface evaporation only affects the boundary mass and heat flux and is determined based on the surface area covered by the liquid. Because it contacts the surrounding directly, the pressure of convective is assumed to equal the ambient pressure during the whole heating process.

$$\overrightarrow{n_w} = \phi S_w\,(\rho_v - \rho_{v,0})h_m$$

$$\overrightarrow{n_v} = \phi S_g\,(\rho_v - \rho_{v,0})h_m \qquad (3\text{-}52)$$

$$P = P_{amb}$$

$$k_{eff}\frac{\partial T}{\partial t} + \lambda\rho_w\overrightarrow{u_w} = h_t(T_{amb} - T)$$

Where h_m is the mass transfer coefficient, h_t the heat transfer coefficient. $\rho_{v,0}$ and T_{amb} denote the ambient vapor density and temperature. $\rho_w\overrightarrow{u_w} = \overrightarrow{n_w}$, which is replaced by equation (3-34) to be consistent with the final differential equations. Therefore, we get

$$-K_1\nabla S_w - K_2\nabla T - K_3\nabla P = \phi(\frac{p_v M_v}{RT} - \rho_{v0})h_m$$

$$P = P_{amb} \qquad (3\text{-}53)$$

$$-K_{13}\nabla S_w - K_{14}\nabla T - K_{15}\nabla P = (T - T_{amb})h_t$$

In the next section, finite difference methods are applied to discretize and solve the multiphase equations first—equation (3-37), (3-41) and (3-47). Then the discretization process is provided in detail. The calculated results are compared with those shown in the reference paper at last.

3.2 Numerical solutions

3.2.1 Introduction of the used finite difference method

Finite difference method was used to discretize the governing equations with central difference in space and the Crank-Nicolson (C-N) scheme in time.

Crank Nicolson method, developed by John Crank and Phyllis Nicolson in the mid 20th century, is a finite difference method used for numerically solving the heat equation and similar partial differential equations [16]. It is implicit in time and unconditionally stable for diffusion equations [17].

Now we take one-dimension diffusion equation as an example to show how the Crank Nicolson method works. For 1D model, the length of the sample is assumed to be L and processing time T. Divide [0, L] into I intervals indexed by i=1, 2, …, I, and [0, T] into N equally space intervals indexed by n=1, 2, …, N, shown in Figure 3.1. The length of each interval in space is Δx and Δt in time. The partial derivatives are centered around time grid point $n + 1/2$ (the red point) [18][19].

$$\frac{\partial T}{\partial t} = \frac{\partial}{\partial x}\left(D(x)\frac{\partial T}{\partial x}\right) \tag{3-54}$$

Let's centered difference $D(x)\frac{\partial T}{\partial x}$ at $x_{i+1/2}$ and $x_{i-1/2}$ first (the green point). Then use these two expressions to find a centered difference formula for the entire expression at x_i (the purple point).

$$\frac{\partial}{\partial x}\left(D(x)\frac{\partial T}{\partial x}\right) = \frac{D_{i+\frac{1}{2}}\left(\frac{\partial T}{\partial x}\right)_{i+\frac{1}{2}}^{n+\frac{1}{2}} - D_{i-\frac{1}{2}}\left(\frac{\partial T}{\partial x}\right)_{i-\frac{1}{2}}^{n+\frac{1}{2}}}{\Delta x}$$

$$= \frac{D_{i+\frac{1}{2}}(T_{i+1}-T_i)^{n+\frac{1}{2}} - D_{i-\frac{1}{2}}(T_i-T_{i-1})^{n+\frac{1}{2}}}{\Delta x^2} \tag{3-55}$$

Next, we take care of the time derivative. The T at time point $n + \frac{1}{2}$ is replaced by the average of that at the around two time points n and $n + 1$.

$$T^{n+\frac{1}{2}} = \frac{T^{n+1}+T^n}{2} \tag{3-56}$$

Substituting equation (3-56) into (3-55), we get

$$\frac{T_i^{n+1}-T_i^n}{\Delta t}=\frac{D_{i+\frac{1}{2}}\left(T_{i+1}^{n+1}-T_i^{n+1}+T_{i+1}^n-T_i^n\right)-D_{i-\frac{1}{2}}\left(T_i^{n+1}-T_{i-1}^{n+1}+T_i^n-T_{i-1}^n\right)}{2(\Delta x)^2} \tag{3-57}$$

Put all the variables at time level $n+1$ at the left side of the equation, and all the ones at time level n at the right side. To simplify the problems, D is set to same time level of its following variable.

$$-D_{i-\frac{1}{2}}^{n+1}T_{i-1}^{n+1}+\left(\frac{2(\Delta x)^2}{\Delta t}+D_{i+\frac{1}{2}}^{n+1}+D_{i-\frac{1}{2}}^{n+1}\right)T_i^{n+1}-D_{i+\frac{1}{2}}^{n+1}T_{i+1}^{n+1} \tag{3-58}$$

$$=D_{i-\frac{1}{2}}^{n}T_{i-1}^{n}+\left(\frac{2(\Delta x)^2}{\Delta t}-D_{i+\frac{1}{2}}^{n}-D_{i-\frac{1}{2}}^{n}\right)T_i^{n}+D_{i+\frac{1}{2}}^{n}T_{i+1}^{n}$$

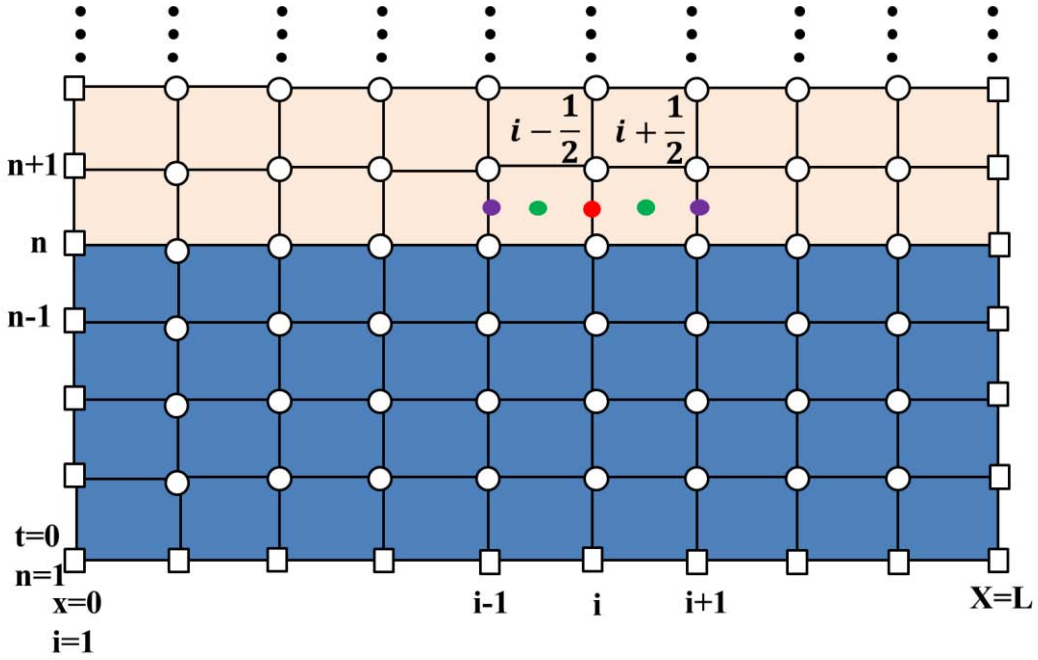


Figure3.4 Schematic of discretization method

The sketch for the Crank-Nicolson scheme for diffusion equation:

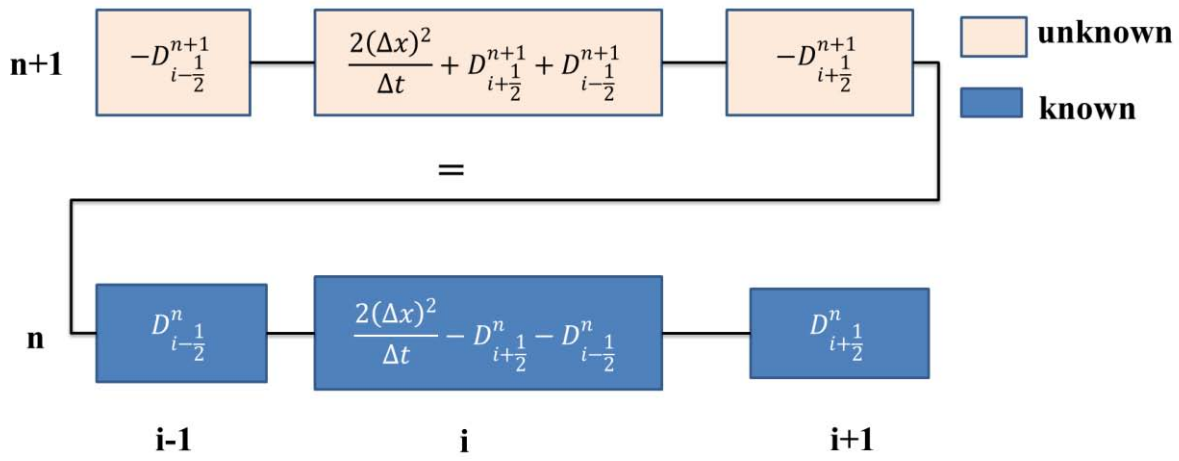


Figure 3.5 Sketch for the Crank-Nicolson scheme

It is apparent that the variables in future cannot individually be written as simple linear combinations of those in present, but are simultaneously determined as the solution to this system of linear equations. However this system has a very convenient structure, which can be assembled in matrix and solved easily.

3.2.2 Discretization for the governing equations

The same deducing process described in section 3.2.1 is employed to disperse the governing equations. A uniform mesh with N+1 nodes is used to discretize equations.

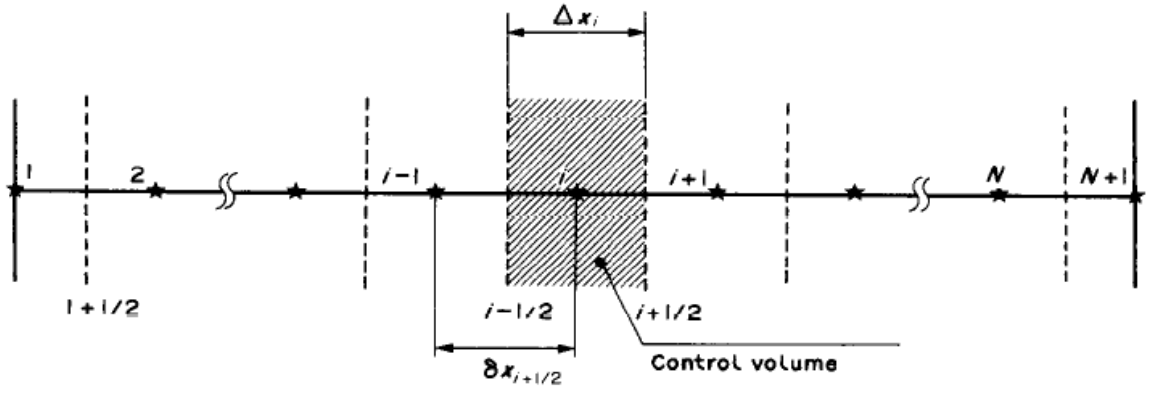


Figure 3.6 Discretization of the calculation domain

For equation (3-37), the coefficients at the left side are at time $n+\frac{1}{2}$ and point i, i.e. that should be written in the form: $K_i^{n+\frac{1}{2}}$. After being discretized, equation (3-37) becomes:

$$b_1 S_{w,i-1}^n + b_2 T_{i-1}^n + b_3 P_{i-1}^n + b_4 S_{w,i}^n + b_5 T_i^n + b_6 P_i^n + b_7 S_{w,i+1}^n + b_8 T_{i+1}^n + b_9 P_{i+1}^n$$
$$= c_1 S_{w,i-1}^{n+1} + c_2 T_{i-1}^{n+1} + c_3 P_{i-1}^{n+1} + c_4 S_{w,i}^{n+1} + c_5 T_i^{n+1} + c_6 P_i^{n+1} + c_7 S_{w,i+1}^{n+1} + c_8 T_{i+1}^{n+1} + c_9 P_{i+1}^{n+1} \quad (3\text{-}59)$$

Where c_i ($i = 1, 2, \dots, 9$) is the coefficient of future variable. b_i ($i = 1, 2, \dots, 9$) is that of present variable. For this equation,

$$c_1 = \frac{K_{1,i-1/2}^{n+1}}{2(\Delta x)^2} \qquad c_2 = \frac{K_{2,i-1/2}^{n+1}}{2(\Delta x)^2}$$

$$c_3 = \frac{K_{3,i-1/2}^{n+1}}{2(\Delta x)^2} \qquad c_4 = -\frac{K_{1,i-1/2}^{n+1} + K_{1,i+1/2}^{n+1}}{2(\Delta x)^2} - \frac{K_{4,i}^{n+1/2}}{\Delta t}$$

$$c_5 = -\frac{K_{2,i-1/2}^{n+1} + K_{2,i+1/2}^{n+1}}{2(\Delta x)^2} - \frac{K_{5,i}^{n+1/2}}{\Delta t} \qquad c_6 = -\frac{K_{3,i-1/2}^{n+1} + K_{3,i+1/2}^{n+1}}{2(\Delta x)^2} - \frac{K_{6,i}^{n+1/2}}{\Delta t}$$

$$c_7 = \frac{K_{1,i+1/2}^{n+1}}{2(\Delta x)^2} \qquad c_8 = \frac{K_{2,i+1/2}^{n+1}}{2(\Delta x)^2}$$

$$c_9 = \frac{K_{3,i+1/2}^{n+1}}{2(\Delta x)^2} \qquad b_1 = -\frac{K_{1,i-1/2}^{n}}{2(\Delta x)^2}$$

$$b_2 = -\frac{K_{2,i-1/2}^{n}}{2(\Delta x)^2} \qquad b_3 = -\frac{K_{3,i-1/2}^{n}}{2(\Delta x)^2}$$

$$b_4 = \frac{K_{1,i-1/2}^{n} + K_{1,i+1/2}^{n}}{2(\Delta x)^2} - \frac{K_{4,i}^{n+1/2}}{\Delta t} \qquad b_5 = \frac{K_{2,i-1/2}^{n} + K_{2,i+1/2}^{n}}{2(\Delta x)^2} - \frac{K_{5,i}^{n+1/2}}{\Delta t}$$

$$b_6 = \frac{K_{3,i-1/2}^{n} + K_{3,i+1/2}^{n}}{2(\Delta x)^2} - \frac{K_{6,i}^{n+1/2}}{\Delta t} \qquad b_7 = -\frac{K_{1,i+1/2}^{n}}{2(\Delta x)^2}$$

$$b_8 = -\frac{K_{2,i+1/2}^{n}}{2(\Delta x)^2} \qquad b_9 = -\frac{K_{3,i+1/2}^{n}}{2(\Delta x)^2}$$

Similarly, the equation (3-41) is:

$$b_{10} S_{w,i-1}^n + b_{11} T_{i-1}^n + b_{12} P_{i-1}^n + b_{13} S_{w,i}^n + b_{14} T_i^n + b_{15} P_i^n + b_{16} S_{w,i+1}^n + b_{17} T_{i+1}^n + b_{18} P_{i+1}^n$$
$$= c_{10} S_{w,i-1}^{n+1} + c_{11} T_{i-1}^{n+1} + c_{12} P_{i-1}^{n+1} + c_{13} S_{w,i}^{n+1} + c_{14} T_i^{n+1} + c_{15} P_i^{n+1} + c_{16} S_{w,i+1}^{n+1} + c_{17} T_{i+1}^{n+1} + c_{18} P_{i+1}^{n+1} \quad (3\text{-}60)$$

$$c_{10} = \frac{K_{7,i-1/2}^{n+1}}{2(\Delta x)^2} \qquad c_{11} = \frac{K_{8,i-1/2}^{n+1}}{2(\Delta x)^2}$$

$$c_{12}=\frac{K_{9,i-1/2}^{n+1}}{2(\Delta x)^2} \qquad c_{13}=-\frac{K_{7,i-1/2}^{n+1}+K_{7,i+1/2}^{n+1}}{2(\Delta x)^2}-\frac{K_{10,i}^{n+1/2}}{\Delta t}$$

$$c_{14}=-\frac{K_{8,i-1/2}^{n+1}+K_{8,i+1/2}^{n+1}}{2(\Delta x)^2}-\frac{K_{11,i}^{n+1/2}}{\Delta t} \qquad c_{15}=-\frac{K_{9,i-1/2}^{n+1}+K_{9,i+1/2}^{n+1}}{2(\Delta x)^2}-\frac{K_{12,i}^{n+1/2}}{\Delta t}$$

$$c_{16}=\frac{K_{7,i+1/2}^{n+1}}{2(\Delta x)^2} \qquad c_{17}=\frac{K_{8,i+1/2}^{n+1}}{2(\Delta x)^2}$$

$$c_{18}=\frac{K_{9,i+1/2}^{n+1}}{2(\Delta x)^2} \qquad b_{10}=-\frac{K_{7,i-1/2}^{n}}{2(\Delta x)^2}$$

$$b_{11}=-\frac{K_{8,i-1/2}^{n}}{2(\Delta x)^2} \qquad b_{12}=-\frac{K_{9,i-1/2}^{n}}{2(\Delta x)^2}$$

$$b_{13}=\frac{K_{7,i-1/2}^{n}+K_{7,i+1/2}^{n}}{2(\Delta x)^2}-\frac{K_{10,i}^{n+1/2}}{\Delta t} \qquad b_{14}=\frac{K_{8,i-1/2}^{n}+K_{8,i+1/2}^{n}}{2(\Delta x)^2}-\frac{K_{11,i}^{n+1/2}}{\Delta t}$$

$$b_{15}=\frac{K_{9,i-1/2}^{n}+K_{9,i+1/2}^{n}}{2(\Delta x)^2}-\frac{K_{12,i}^{n+1/2}}{\Delta t} \qquad b_{16}=-\frac{K_{7,i+1/2}^{n}}{2(\Delta x)^2}$$

$$b_{17}=-\frac{K_{8,i+1/2}^{n}}{2(\Delta x)^2} \qquad b_{18}=-\frac{K_{9,i+1/2}^{n}}{2(\Delta x)^2}$$

For equation (3-47), the convective term in energy equation $\nabla\cdot\left(\left(\rho C_p\vec{u}\right)_{\text{fluid}}T\right)$ is ignored because it is much smaller than the latent heat 2. Therefore, its final form is:

$$\begin{aligned}&b_{19}S_{w,i-1}^{n}+b_{20}T_{i-1}^{n}+b_{21}P_{i-1}^{n}+b_{22}S_{w,i}^{n}+b_{23}T_{i}^{n}+b_{24}P_{i}^{n}+b_{25}S_{w,i+1}^{n}+b_{26}T_{i+1}^{n}+b_{27}P_{i+1}^{n}\\&=c_{19}S_{w,i-1}^{n+1}+c_{20}T_{i-1}^{n+1}+c_{21}P_{i-1}^{n+1}+c_{22}S_{w,i}^{n+1}+c_{23}T_{i}^{n+1}+c_{24}P_{i}^{n+1}+c_{25}S_{w,i+1}^{n+1}+c_{26}T_{i+1}^{n+1}+c_{27}P_{i+1}^{n+1}\end{aligned} \quad (3\text{-}61)$$

$$c_{19}=\frac{K_{13,i-1/2}^{n+1}}{2(\Delta x)^2} \qquad c_{20}=\frac{K_{14,i-1/2}^{n+1}}{2(\Delta x)^2}$$

$$c_{21}=\frac{K_{15,i-1/2}^{n+1}}{2(\Delta x)^2} \qquad c_{22}=-\frac{K_{13,i-1/2}^{n+1}+K_{13,i+1/2}^{n+1}}{2(\Delta x)^2}-\frac{K_{16,i}^{n+1/2}}{\Delta t}$$

$$c_{23}=-\frac{K_{14,i-1/2}^{n+1}+K_{14,i+1/2}^{n+1}}{2(\Delta x)^2}-\frac{K_{17,i}^{n+1/2}}{\Delta t} \qquad c_{24}=-\frac{K_{15,i-1/2}^{n+1}+K_{15,i+1/2}^{n+1}}{2(\Delta x)^2}-\frac{K_{18,i}^{n+1/2}}{\Delta t}$$

$$c_{25}=\frac{K_{13,i+1/2}^{n+1}}{2(\Delta x)^2} \qquad c_{26}=\frac{K_{14,i+1/2}^{n+1}}{2(\Delta x)^2}$$

$$c_{27}=\frac{K_{15,i+1/2}^{n+1}}{2(\Delta x)^2} \qquad b_{19}=-\frac{K_{13,i-1/2}^{n}}{2(\Delta x)^2}$$

$$b_{20}=-\frac{K_{14,i-1/2}^{n}}{2(\Delta x)^2} \qquad b_{21}=-\frac{K_{15,i-1/2}^{n}}{2(\Delta x)^2}$$

$$b_{22}=\frac{K_{13,i-1/2}^{n}+K_{13,i+1/2}^{n}}{2(\Delta x)^2}-\frac{K_{16,i}^{n+1/2}}{\Delta t} \qquad b_{23}=\frac{K_{14,i-1/2}^{n}+K_{14,i+1/2}^{n}}{2(\Delta x)^2}-\frac{K_{17,i}^{n+1/2}}{\Delta t}$$

$$b_{24}=\frac{K_{15,i-1/2}^{n}+K_{15,i+1/2}^{n}}{2(\Delta x)^2}-\frac{K_{18,i}^{n+1/2}}{\Delta t} \qquad b_{25}=-\frac{K_{13,i+1/2}^{n}}{2(\Delta x)^2}$$

$$b_{26}=-\frac{K_{14,i+1/2}^{n}}{2(\Delta x)^2} \qquad b_{27}=-\frac{K_{15,i+1/2}^{n}}{2(\Delta x)^2}$$

Where $K_{i\pm 1/2}=(K_i \pm K_{i+1})/2,\ K^{n+1/2}=(K^n+K^{n+1})/2$.

3.2.3 Discretization of the boundary

The insulated boundary:

$$b_1' S_{w,1}^n + b_2' T_1^n + b_3' P_1^n + b_4' S_{w,2}^n + b_5' T_2^n + b_6' P_2^n$$
$$= c_1' S_{w,1}^{n+1} + c_2' T_1^{n+1} + c_3' P_1^{n+1} + c_4' S_{w,2}^{n+1} + c_5' T_2^{n+1} + c_6' P_2^{n+1} \qquad (3\text{-}62)$$

$$c_1^{'}=-\frac{K_{1,1+1/2}^{n+1}}{2\Delta x}-\frac{K_{4,1}^{n+1/2}\Delta x}{2\Delta t} \qquad c_2^{'}=-\frac{K_{2,1+1/2}^{n+1}}{2\Delta x}-\frac{K_{5,1}^{n+1/2}\Delta x}{2\Delta t}$$

$$c_3^{'}=-\frac{K_{3,1+1/2}^{n+1}}{2\Delta x}-\frac{K_{6,1}^{n+1/2}\Delta x}{2\Delta t} \qquad c_4^{'}=\frac{K_{1,1+1/2}^{n+1}}{2\Delta x}$$

$$c_5^{'}=\frac{K_{2,1+1/2}^{n+1}}{2\Delta x} \qquad c_6^{'}=\frac{K_{3,1+1/2}^{n+1}}{2\Delta x}$$

$$b_1^{'}=\frac{K_{1,1+1/2}^{n}}{2\Delta x}-\frac{K_{4,1}^{n+1/2}\Delta x}{2\Delta t} \qquad b_2^{'}=\frac{K_{2,1+1/2}^{n}}{2\Delta x}-\frac{K_{5,1}^{n+1/2}\Delta x}{2\Delta t}$$

$$b_3^{'} = \frac{K_{3,1+1/2}^{n}}{2\Delta x} - \frac{K_{6,1}^{n+1/2}\Delta x}{2\Delta t} \qquad b_4^{'} = -\frac{K_{1,1+1/2}^{n}}{2\Delta x}$$

$$b_5^{'} = -\frac{K_{2,1+1/2}^{n}}{2\Delta x} \qquad b_6^{'} = -\frac{K_{3,1+1/2}^{n}}{2\Delta x}$$

$$b_7' S_{w,1}^{n} + b_8' T_1^{n} + b_9' P_1^{n} + b_{10}' S_{w,2}^{n} + b_{11}' T_2^{n} + b_{12}' P_2^{n}$$

$$= c_7' S_{w,1}^{n+1} + c_8' T_1^{n+1} + c_9' P_1^{n+1} + c_{10}' S_{w,2}^{n+1} + c_{11}' T_2^{n+1} + c_{12}' P_2^{n+1} \quad (3\text{-}63)$$

$$c_7^{'} = -\frac{K_{7,1+1/2}^{n+1}}{2\Delta x} - \frac{K_{10,1}^{n+1/2}\Delta x}{2\Delta t} \qquad c_8^{'} = -\frac{K_{8,1+1/2}^{n+1}}{2\Delta x} - \frac{K_{11,1}^{n+1/2}\Delta x}{2\Delta t}$$

$$c_9^{'} = -\frac{K_{9,1+1/2}^{n+1}}{2\Delta x} - \frac{K_{12,1}^{n+1/2}\Delta x}{2\Delta t} \qquad c_{10}^{'} = \frac{K_{7,1+1/2}^{n+1}}{2\Delta x}$$

$$c_{11}^{'} = \frac{K_{8,1+1/2}^{n+1}}{2\Delta x} \qquad c_{12}^{'} = \frac{K_{9,1+1/2}^{n+1}}{2\Delta x}$$

$$b_7^{'} = \frac{K_{7,1+1/2}^{n}}{2\Delta x} - \frac{K_{10,1}^{n+1/2}\Delta x}{2\Delta t} \qquad b_8^{'} = \frac{K_{8,1+1/2}^{n}}{2\Delta x} - \frac{K_{11,1}^{n+1/2}\Delta x}{2\Delta t}$$

$$b_9^{'} = \frac{K_{9,1+1/2}^{n}}{2\Delta x} - \frac{K_{12,1}^{n+1/2}\Delta x}{2\Delta t} \qquad b_{10}^{'} = -\frac{K_{7,1+1/2}^{n}}{2\Delta x}$$

$$b_{11}^{'} = -\frac{K_{8,1+1/2}^{n}}{2\Delta x} \qquad b_{12}^{'} = -\frac{K_{9,1+1/2}^{n}}{2\Delta x}$$

$$b_{13}' S_{w,1}^{n} + b_{14}' T_1^{n} + b_{15}' P_1^{n} + b_{16}' S_{w,2}^{n} + b_{17}' T_2^{n} + b_{18}' P_2^{n} \quad (3\text{-}64)$$

$$= c_{13}' S_{w,1}^{n+1} + c_{14}' T_1^{n+1} + c_{15}' P_1^{n+1} + c_{16}' S_{w,2}^{n+1} + c_{17}' T_2^{n+1} + c_{18}' P_2^{n+1}$$

$$c_{13}^{'} = \frac{K_{16,1}^{n+1/2}\Delta x}{2\Delta t} \qquad c_{14}^{'} = -\frac{k_{eff}^{n+1}}{\Delta x} + \frac{K_{17,1}^{n+1/2}\Delta x}{2\Delta t}$$

$$c_{15}^{'} = \frac{K_{18,1}^{n+1/2}\Delta x}{2\Delta t} \qquad c_{16}^{'} = 0$$

$$c_{17}^{'} = \frac{k_{eff}^{n+1}}{\Delta x} \qquad c_{18}^{'} = 0$$

$$b_{13}^{'} = \frac{K_{16,1}^{n+1/2}\Delta x}{2\Delta t} \qquad b_{14}^{'} = \frac{k_{eff}^{n}}{\Delta x} + \frac{K_{17,1}^{n+1/2}\Delta x}{2\Delta t}$$

$$b_{15}^{'} = \frac{K_{18,1}^{n+1/2}\Delta x}{2\Delta t} \qquad b_{16}^{'} = 0$$

$$b_{17}^{'} = -\frac{k_{eff}^{n}}{\Delta x} \qquad b_{18}^{'} = 0$$

Open boundary :

$$b_1'' S_{w,N}^n + b_2'' T_N^n + b_3'' P_N^n + b_4'' S_{w,N+1}^n + b_5'' T_{N+1}^n + b_6'' P_{N+1}^n + \phi(\left(\frac{p_v M_v}{RT}\right)_1^n - \rho_{v0}) h_m \qquad (3\text{-}65)$$

$$= c_1'' S_{w,N}^{n+1} + c_2'' T_N^{n+1} + c_3'' P_N^{n+1} + c_4'' S_{w,N+1}^{n+1} + c_5'' T_{N+1}^{n+1} + c_6'' P_{N+1}^{n+1}$$

$$c_1^{"} = -\frac{K_{1,N+1/2}^{n+1}}{2\Delta x} \qquad c_2^{"} = -\frac{K_{2,N+1/2}^{n+1}}{2\Delta x}$$

$$c_3^{"} = -\frac{K_{3,N+1/2}^{n+1}}{2\Delta x} \qquad c_4^{"} = \frac{K_{1,N+1/2}^{n+1}}{2\Delta x} + \frac{K_{4,N+1}^{n+1/2}\Delta x}{2\Delta t}$$

$$c_5^{"} = \frac{K_{2,N+1/2}^{n+1}}{2\Delta x} + \frac{K_{5,N+1}^{n+1/2}\Delta x}{2\Delta t} \qquad c_6^{"} = \frac{K_{3,N+1/2}^{n+1}}{2\Delta x} + \frac{K_{6,N+1}^{n+1/2}\Delta x}{2\Delta t}$$

$$b_1^{"} = \frac{K_{1,N+1/2}^{n}}{2\Delta x} \qquad b_2^{"} = \frac{K_{2,N+1/2}^{n}}{2\Delta x}$$

$$b_3^{"} = \frac{K_{3,N+1/2}^{n}}{2\Delta x} \qquad b_4^{"} = -\frac{K_{1,N+1/2}^{n}}{2\Delta x} + \frac{K_{4,N+1}^{n+1/2}\Delta x}{2\Delta t}$$

$$b_5^{"} = -\frac{K_{2,N+1/2}^{n}}{2\Delta x} + \frac{K_{5,N+1}^{n+1/2}\Delta x}{2\Delta t} \qquad b_6^{"} = -\frac{K_{3,N+1/2}^{n}}{2\Delta x} + \frac{K_{6,N+1}^{n+1/2}\Delta x}{2\Delta t}$$

$$P_{N+1}^{n+1} = P_{amb} \qquad (3\text{-}65)$$

$$b''_{13}S^n_{w,N} + b''_{14}T^n_N + b''_{15}P^n_N + b''_{16}S^n_{w,N+1} + b''_{17}T^n_{N+1} + b''_{18}P^n_{N+1} + (T^n_1 - T_{amb})h_t$$

$$= c''_{13}S^{n+1}_{w,N} + c''_{14}T^{n+1}_N + c''_{15}P^{n+1}_N + c''_{16}S^{n+1}_{w,N+1} + c''_{17}T^{n+1}_{N+1} + c''_{18}P^{n+1}_{N+1} \qquad (3\text{-}66)$$

$$c''_{13} = -\frac{K^{n+1}_{13,N+1/2}}{2\Delta x} \qquad c''_{14} = -\frac{K^{n+1}_{14,N+1/2}}{2\Delta x}$$

$$c''_{15} = -\frac{K^{n+1}_{15,N+1/2}}{2\Delta x} \qquad c''_{16} = \frac{K^{n+1}_{13,N+1/2}}{2\Delta x} + \frac{K^{n+1/2}_{16,N+1}\Delta x}{2\Delta t}$$

$$c''_{17} = \frac{K^{n+1}_{14,N+1/2}}{2\Delta x} + \frac{K^{n+1/2}_{17,N+1}\Delta x}{2\Delta t} \qquad c''_{18} = \frac{K^{n+1}_{15,N+1/2}}{2\Delta x} + \frac{K^{n+1/2}_{18,N+1}\Delta x}{2\Delta t}$$

$$b''_{13} = \frac{K^{n}_{13,N+1/2}}{2\Delta x} \qquad b''_{14} = \frac{K^{n}_{14,N+1/2}}{2\Delta x}$$

$$b''_{15} = \frac{K^{n}_{15,N+1/2}}{2\Delta x} \qquad b''_{16} = -\frac{K^{n}_{13,N+1/2}}{2\Delta x} + \frac{K^{n+1/2}_{16,N+1}\Delta x}{2\Delta t}$$

$$b''_{17} = -\frac{K^{n}_{14,N+1/2}}{2\Delta x} + \frac{K^{n+1/2}_{17,N+1}\Delta x}{2\Delta t} \qquad b''_{18} = -\frac{K^{n}_{15,N+1/2}}{2\Delta x} + \frac{K^{n+1/2}_{18,N+1}\Delta x}{2\Delta t}$$

3.2.4 Assembly of matrix

To see what we did more clearly and make the algorithm more efficient, we define a matrix B to assemble the coefficients of present variables in the left side of the equations in section 3.2.2 and 3.2.3, a matrix C for the coefficients of future variables. Because the calculated domain has N+1 grid points, and each point is described by three equations with three unknown variables, all of the matrixes have 3N+3 rows. The relationship between these matrixes is like this:

$$[b]_{m,m}\begin{bmatrix} S_{w,1}^{n} \\ T_1^{n} \\ P_1^{n} \\ \vdots \\ \vdots \\ S_{w,N+1}^{n} \\ T_{N+1}^{n} \\ P_{N+1}^{n} \end{bmatrix}_{m,1} + \begin{bmatrix} 0 \\ 0 \\ 0 \\ \vdots \\ \vdots \\ \phi((\frac{p_v M_w}{RT})_1^n - \rho_{v0})h_m \\ P_{amb} \\ (T_1^n - T_{amb})h_t \end{bmatrix}_{m,1} = [c]_{m,m}\begin{bmatrix} S_{w,1}^{n+1} \\ T_1^{n+1} \\ P_1^{n+1} \\ \vdots \\ \vdots \\ S_{w,N+1}^{n+1} \\ T_{N+1}^{n+1} \\ P_{N+1}^{n+1} \end{bmatrix}_{m,1}$$

The values of variables at time level $n+1$ can be easily obtained by inverting matrix C. Unfortunately, inverting a matrix is computationally expensive. To avoid this inconvenience and guarantee the accuracy of the solution, Gauss elimination is employed when we actually implement this in Matlab.

To make the calculation process more clear, a flow chart is provided below. There are three subroutines (initial.m, calka.m and matcal.m) in our code. Initial.m is for loading in all the initial values for the model. Calka.m is for updating all the parameters and calculating the coefficients for the matrix while matcal.m tries to assemble the coefficients for the matrixes and solve the problem.

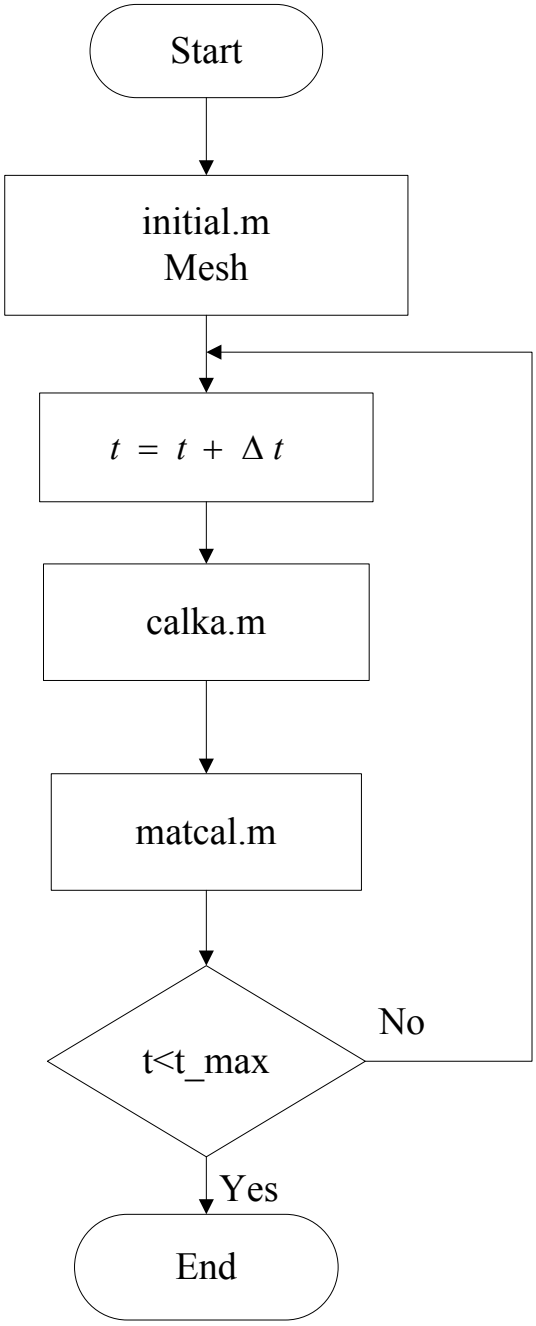


Figure 3.7 Flow chart of calculation

3.2.5 The calculated results and discussion

Since conventional heating has been studied in the past and it is expected to be simpler than RF heating, conventional heating is first studied as a prelude to better understanding of RF heating. Calculations for conventional heating were performed for clay brick for the input data shown in Table 3.1.

3.2.5.1 The input parameters

The input parameters of the 1D model are mainly cited from an article of S. Ben Nasrallah [2].

Table 3.1 Input parameters of model

Parameter	Symbol	Value	Source
Porosity	ϕ	0.26	[2]
Viscosity($P_a \cdot s$)			[2]
Water	μ_w	5.468e-4	
Vapor and air	μ_g	1.8e-5	
Intrinsic permeability(m^2)			[2]
Water	$k_{in,w}$	2.5e-14	
Vapor and air	$k_{in,g}$	2.5e-14	
Relative permeability			[2]
Water	$k_{r,w}$	$[(S_w - 0.09)/0.91]^3, S_w > 0.09$ $0, S_w < 0.09$	
Vapor and air	$k_{r,g}$	$1 - 1.1S_w, < 1/1.1$ $0, S_w > 1/1.1$	
Binary diffusivity(m^2/s)	$D_{eff,g}$	2.6e-6	[2]
Specific heat capacity($J/(kg \cdot K)$)			[2]
Water	C_{pw}	4180	
Solid	C_{ps}	879	
Vapor	C_{pv}	2062	
Air	C_{pa}	1006	
Thermal conductivity($W/(m \cdot K)$)			[2]
Water	$k_{t,w}$	0.57	
Solid	$k_{t,s}$	1.442	
Vapor	$k_{t,v}$	0.026	
Air	$k_{t,a}$	0.026	
Density(kg/m^3)			[2]
Water	ρ_w	1000	
Solid	ρ_s	2600	

Vapor	ρ_v	Ideal gas law	
Air	ρ_a	Ideal gas law	
Heat transfer coefficient($W/(m^2 \cdot K)$)	h_t	15	[2]
Mass transfer coefficient(m/s)	h_m	0.014	[2]
Ambient pressure (P_a)	P_{amb}	101325	[2]
Ambient temperature(K)	T_{amb}	360.15	[2]
Evaporation rate constant(1/s)	K	10	[2]
Latent heat of vaporization(J/kg)	λ	2.26e6	[2]
Vapor pressure(P_a)	p_v	$p_{sat}\exp(-2\sigma M_v/r\rho_w RT)$	[2]
Capillary pressure(P_a)	p_c	$\sqrt{\phi/k_{in,w}}\,\sigma J(S_w)$	[2]
Initial condition			[2]
Pressure(P_a)	P_0	101325	
Water saturation	S_0	0.9	
Temperature (K)	T_0	320.15	

Where

$$\sigma = 0.1212 + 1.67e-4T \tag{3-67}$$

$$J(S_w) = 0.364\left(1-\exp\left(-40(1-S_w)\right)\right) + 0.221(1-S_w) + 0.005/(S_w - 0.08) \tag{3-68}$$

$$\log(r) = 2.16e-2 + 43.8S_w - 253.5S_w^2 + 794.54S_w^3 - 1333.7S_w^4 + 1111S_w^5 - 352.5S_w^6 - 1 \tag{3-69}$$

$$p_{sat} = 3170 * \exp(4800 * (T - 293.15)/(293.15T)) \tag{3-70}$$

3.3 Calculated results and discussions

To balance the calculation cost and accuracy, different discretization is applied: the calculated domain is divided by 21 nodes, 41 nodes, 61 nodes, 81 nodes and 101 nodes, respectively.

Their results are compared to find the best mesh. The solid lines represent the results of 61 nodes and the dot lines denote those of the other nodes.

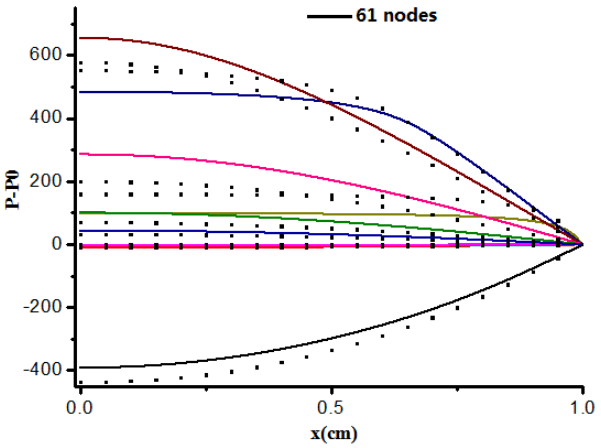


Figure 3.8 Pressures of 61 nodes vs 21 nodes

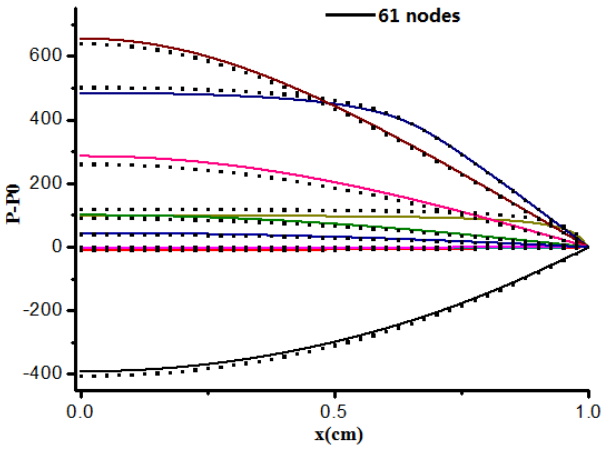


Figure 3.9 Pressures of 61 nodes vs 41 nodes

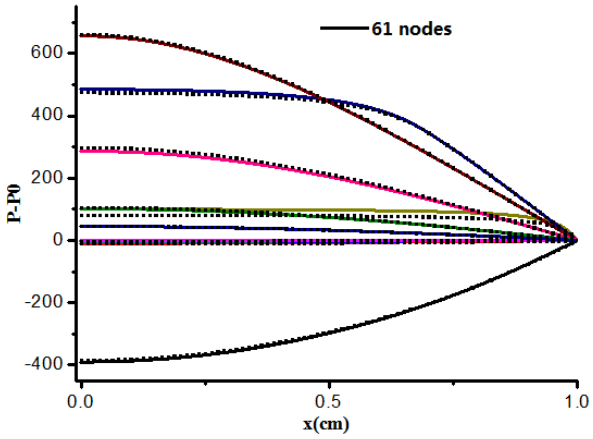


Figure 3.10 Pressures of 61 nodes vs 81 nodes

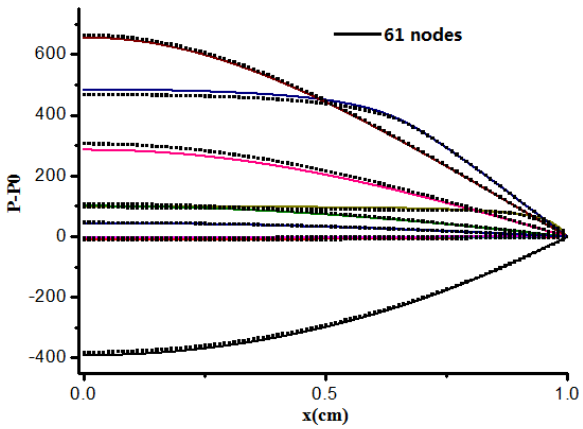


Figure 3.11 Pressures of 61 nodes vs 101 nodes

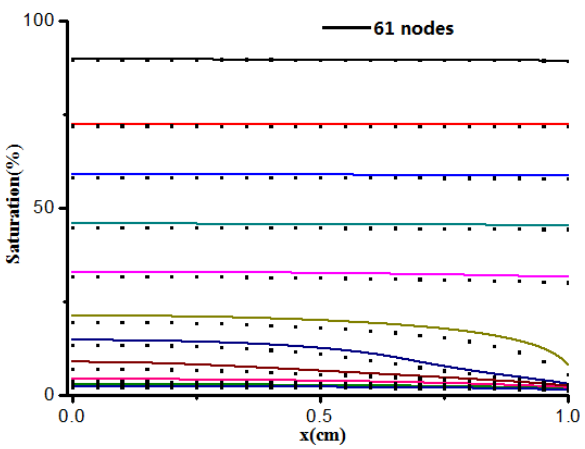


Figure 3.12 Saturations of 61 nodes vs 21 nodes

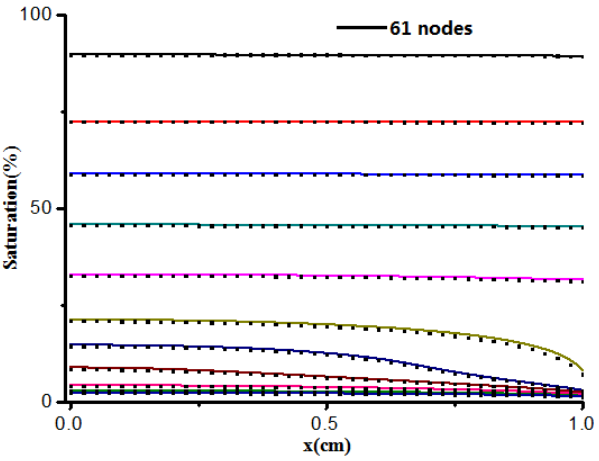


Figure 3.13 Saturations of 61 nodes vs 41 nodes

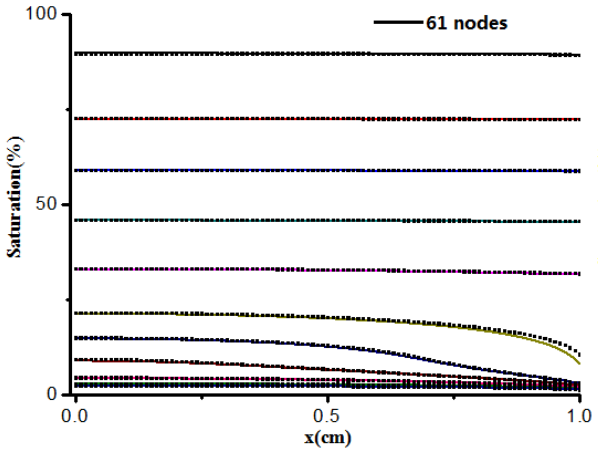


Figure 3.14 Saturations of 61 nodes vs 81 nodes

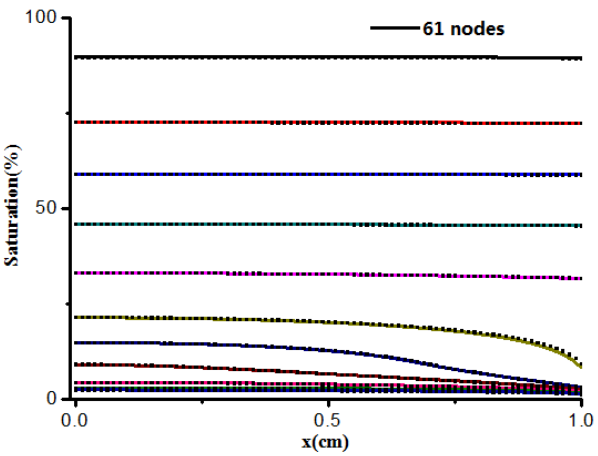


Figure 3.15 Saturations of 61 nodes vs 101 nodes

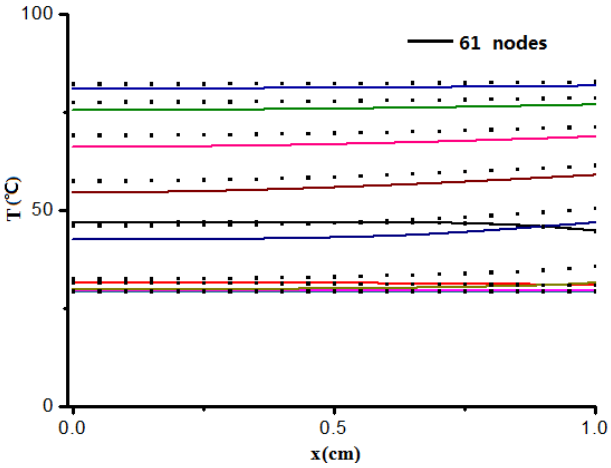


Figure 3.16Temperatures of 61 nodes vs 21 nodes

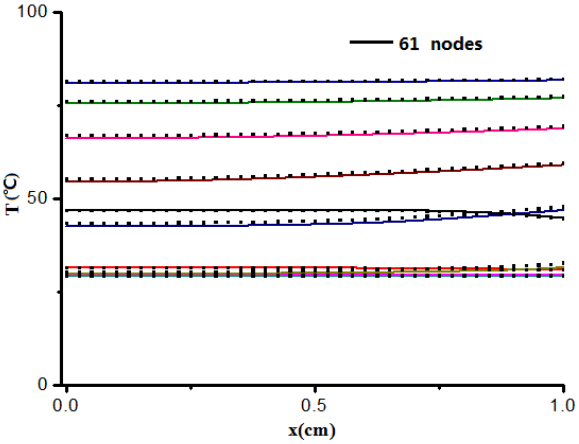


Figure 3.17 Temperatures of 61nodes vs 41 nodes

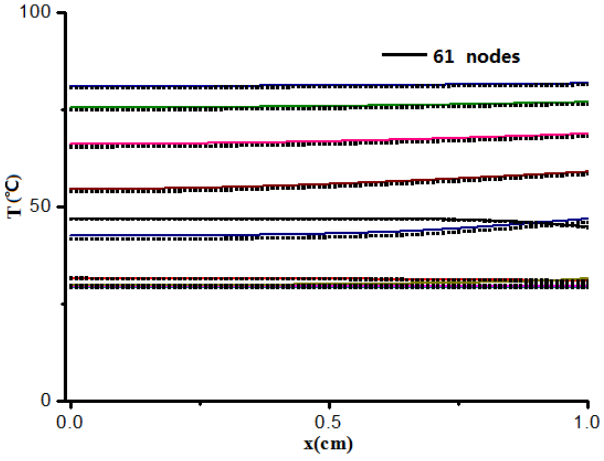


Figure 3.18 Temperatures of 61 nodes vs 81 nodes

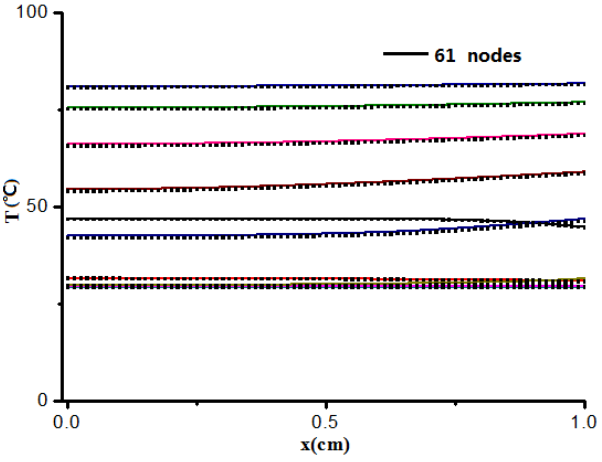


Figure 3.19 Temperatures of 61 nodes vs 101nodes

From the above comparisons, it is obvious that when the mesh is coarse, the distinctions between its consequences and those of 61 nodes are relatively large. The closer the number of grids is to 61, the smaller the distinction is. When the mesh is finer than the presupposed mesh, the values of results obtained are almost the same as those of 61 nodes. Therefore, the 1D model is equally discretized into 60 sections. The calculation results are then compared with those shown in the reference paper, revealing below.

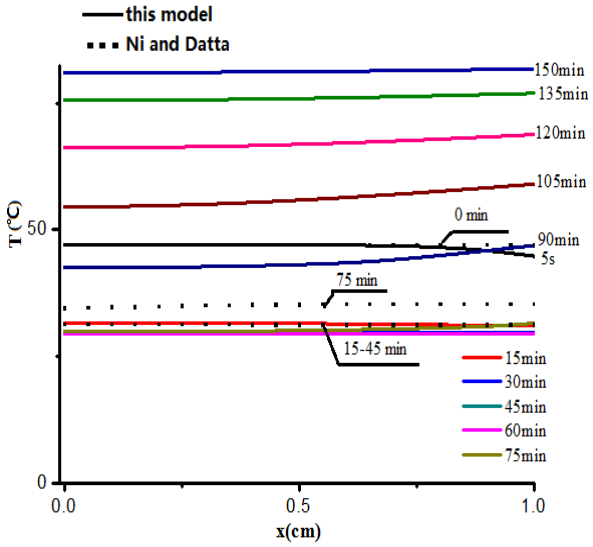


Figure 3.20 Calculated temperatures by Matlab

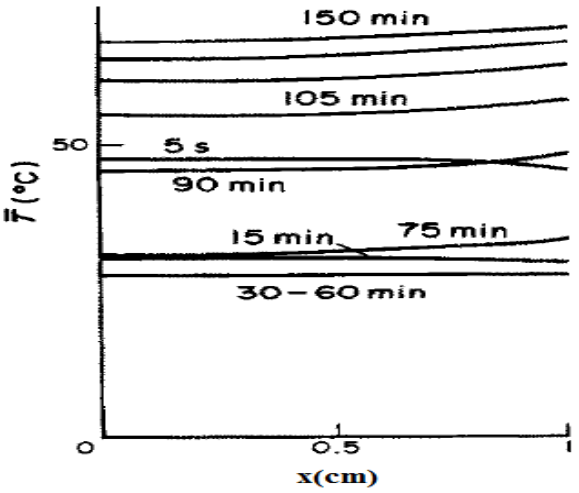


Figure 3.21 Temperatures in reference paper

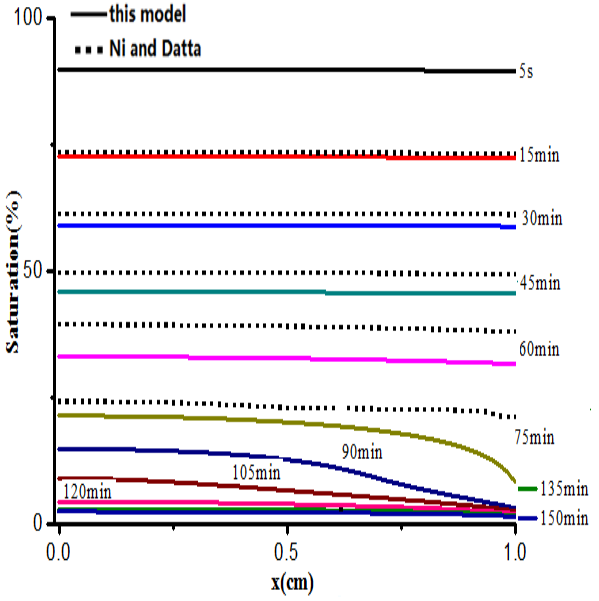


Figure 3.22 Calculated saturations by Matlab

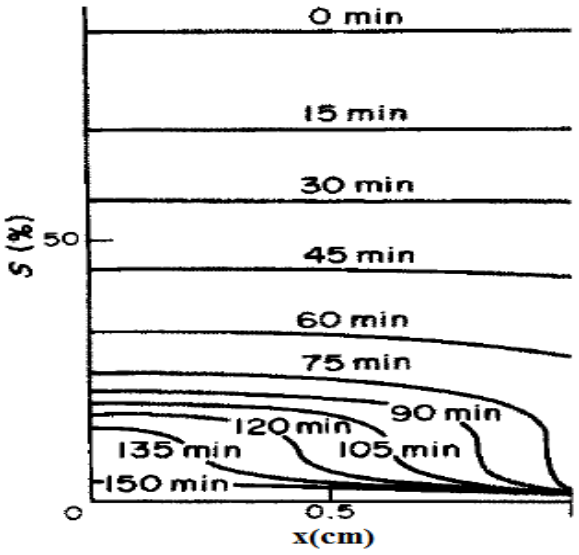
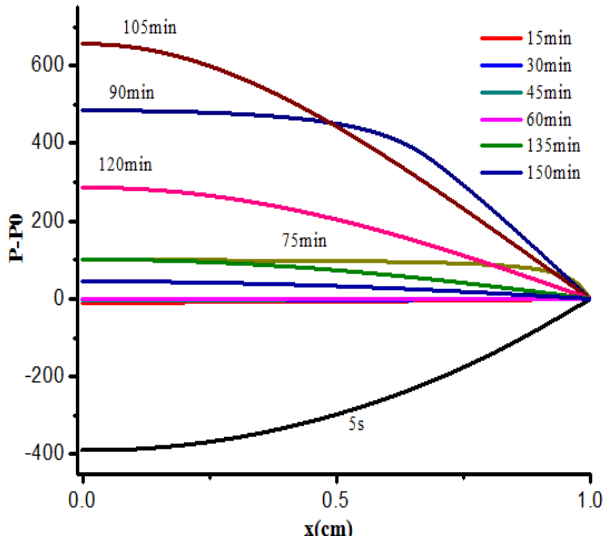


Figure 3.23 Saturations in reference paper



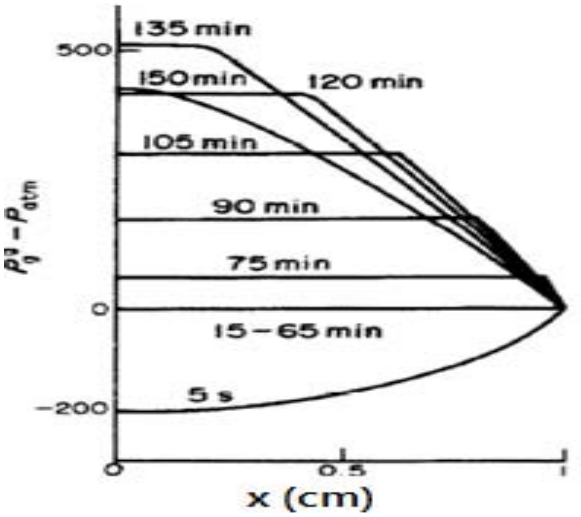


Figure 3.24 Calculated pressures by Matlab

Figure 3.25 Pressure in reference paper

Figure 3.21, 3.23 and 3.25 reveal the reference temperature, saturation and pressure, respectively. The mechanisms involved in drying process are analyzed first for each variable combined with its profiles and theory. Comparisons of consequences will be provided later.

Temperature profile:

At the beginning of drying, when the initial water content is sufficient, evaporation starts across the interface once the surface meets a higher ambient temperature, leading to a lower temperature at the open surface (the curve at 5s). The moisture gradient and temperature gradient drive the water inside the sample to be evaporated out, which makes the brick lose more heat. Even though ambient environment will supply the power (i.e. heat) for the surface due to convection, it is smaller than the lost energy. So the temperature consistently drops down from the open boundary to the insulated one. Temperature of the whole porous media approaches uniform when the drying is stable. This process is called period of constant drying rate. During this transition phase, the flow of vapour being negligible in the core of the medium, evaporation only takes place at the surface. It is reported that the higher the initial temperature is, the greater the drying rate [2].

As the drying continuing, more and more liquid is evaporated. When the liquid becomes discontinuous, the liquid migration stops (pendular state). The surface temperature starts to increase now because evaporation is very weak and the heat conducted from outside due to the high thermal conductivity coefficient of the sample becomes relatively larger. Conversely to the constant drying rate period, the drying rate decreases and temperature rises throughout

the media. This is the decreasing drying rate period, during which the evaporation propagates a zone in which the gradient of moisture content is very high (drying front) towards the impervious surface of the slab.

Pressure profile:

As the pressure has a strong relation with the temperature gradient, from the profile of temperature distribution, it is seen that initially the pressure peak is near the open surface. This is due to the evaporation being mostly near the surface from a much higher temperature, combined with the boundary pressure set at the atmospheric pressure. Later on, when the temperature of the sample achieves uniform, the pressure at each point equilibrates. During this period of constant drying rate, the increase in the volume of gas carried by liquid extraction tends to subject the medium to partial vacuum. The pressure persists is the capillary pressure.

As the temperature increasing, gas migration generated by diffusion inside the sample can not be expelled in time and the drying front moves towards interior from the open boundary, arising the vapor pressure on the drying front. A pressure gradient is observed between the front and the convective surface (Figure 3.25). Between the drying front and the impervious surface, a slight convection of the gas phase and the rise in temperature cause the pressure to level out at the value of drying front. The value of this pressure becomes even more important as the drying rate increases and as the permeability of the gaseous phase weakens. When the front reaches the impervious surface, the entire porous medium is in the hygroscopic zone. The pressure of the gaseous phase decreases and it will approach the ambient pressure when the front reaches the insulated boundary [2].

Profile of saturation:

The initial saturation corresponds to a moisture content of 0.9. The evaporation starts at the open surface first, then the gradient of moisture drive the liquid to the surface and evaporated. Because the sample is short and the initial water is continuous and sufficient, the saturation drops very fast but uniform throughout the sample (curves of 0-30min). For small values of T, the slope of the saturation curve is weak. When the drying front starts to move inward, the gas migration inside is blocked while that on the interface is still evaporated, causing the curve of saturation slightly drops at the right end.

Later, due to the rise of the surface temperature and pressure gradient, the moisture content decreases notably at the surface of the medium. However, the inside moisture drops slowly, because of a much reduced capillary diffusivity in these regions, which is the characteristics of diffusion controlled moisture transport, as can be seen in drying of brick [3]. As the front separates from the interface, the steepness in the moisture content profile becomes smaller. When the front reaches left surface, moisture content approaches the equilibrium moisture content.

Comparison of the results

Comparing the corresponding distributions of saturation, temperature and pressure, it is obvious that the calculated results agree qualitatively with those shown in the reference paper, with the change trend and values being almost the same. Ni and Datta have calculated the same model with the similar methods and provided part of their results in a published paper [5]. To double check the accuracy of our calculated results, the consequences obtained by Ni and Datta are also revealed in Figure 3.20 and 3.22. One can observe that the results in these two figures are very close. It is worth noticing that our calculated data are a little closer to those shown by Nasrallah comparing to the results shown by Ni and Datta.

However, we should also notice that there still exist some differences between our and Nasrallah's results. Water saturation near the surface predicted by our model is more gradual than theirs and there exist a few discrepancies in the pressures. The reasons that cause the difference between calculated results and the referenced ones are perhaps: 1) the mesh employed in the paper differs from that used in the reference paper. In our paper, the uniform grid is employed while the reference paper applied non-uniform mesh with denser grids near the open boundary; 2) the reference paper used centered space difference and fully implicit time differencing with upwind differencing for the convective term in energy equation; our research, however, didn't utilize another special method but Crank-Nicolson method to discretize the convective term; 3) when calculating coefficients of the equations, in treatment of the future terms in coefficient between us and Nasrallah during the solving process may be different, leading to tiny discrepancies for the calculated results and the reference ones.

3.4 Conclusion

In this chapter, the assumptions used in the research and the basic theory definitions are presented first. Porous media is treated as the composition of three phases: gas, liquid and solid. The disciplines describing the mass and heat transfer in materials under convective heating of 1D brick are then studied. Finite difference method was used to discretize the governing equations with central difference in space and the Crank-Nicolson (C-N) scheme in time. The calculated results compare qualitatively with those shown in articles of S. Ben Nasrallah [2] and Haitao Ni [5]. The accuracy of the relations of different parameters and assumptions are verified.

Based on the theories used in the 1D model, Maxwell's equations are added and coupled with the governing equations of the previous model to study the interaction of RF and porous media. Because it is not easy to shape brick in certain forms and its parameters under RF heating are not provided completely, we decide to use potato to further our research. In order to check the accuracy of the simulation model of RF heating potato, experiments are implemented. This part of work will be detailed in chapter 5.

Reference of chapter 3

[1] M. A. Stanish, G. S. Schajer, Ferhan Kayihan, "A mathematical model of drying for hygroscopic porous media," *AIChE journal*, vol.32, no.8, pp. 1301-1311, 1986.

[2] S. Ben Nasrallah and P. Perré, "Detailed study of a model of heat and mass transfer during convective drying of porous media," *Int. J. Heat Mass Transfer*, vol. 31, no. 5, pp.957-967, 1988.

[3] Ilic, M. and I. W. Turner., "Convective drying of a consolidated slab of wet porous material," *Int. J. Heat Mass Transfer,* vol.32, no.1, pp.2351-2362, 1989.

[4] Chen, P. and D. Pei., "A mathematical model of drying processes," *Int. J. Heat Mass Transfer*, vol.32, no.2, pp.297-310, 1989.

[5] H. Ni, A.K. Datta, K.E. Torrance, "Moisture transport in intensive microwave heating of biomaterials: a multiphase porous media model," *Int. J. Heat Mass Transfer*, vol. 42, pp.1501-1512, 1999.

[6] A. K. Datta, "Porous media approaches to studying simultaneous heat and mass transfer in food processes. I: Problem formulations," *Journal of Food Engineering*, vol.80, pp.80–95, 2006.

[7] Haitao Ni, "Multiphase moisture transport in porous media under intensive microwave heating," *a dissertation of Cornell University*, 1997.

[8] Constant, T., C. Moyne and P. Perré., "Drying with internal heat generation: theoretical aspects and application to microwave heating," *AIChE J.*, vol.42, no.2, pp.359-368, 1996.

[9] N. N. Grinchik, P. V. Akulich, A. L. Adamovich, P. S. Kuts, and S. P. Kundas, "Modeling of nonisothermal heat and moisture transfer in capillary-porous media in periodic microwave heating," *Journal of Engineering Physics and Thermophysics*, vol.80, no.1, pp.1-10, 2007.

[10] Vineet Rakesh and Ashim K. Datta, Jeffrey H. Walton, Kathryn L. McCarthy and Michael J. McCarthy, "Microwave combination heating: coupled electromagnetics-multiphase porous media modeling and MRI experimentation," *AIChE Journal*, vol.58, no.4, pp. 1262-1278, 2012.

[11] Whitaker, S., "Simultaneous heat, mass and momentum transfer in porous media: a theory of drying," *Adv. Heat Transfer*, vol,13, pp.119-203, 1977.

[12] Wei, C. K., H. T. Davis, E. A. Davis and J. Gordan, "Heat and mass transfer in water-laden sandstone: convective heating," *AIChE J.*, vol.31, no.8, pp.1338-1348,1985.

[13] Alexander Warning, Ashish Dhall, Diana Mitrea, Ashim K. Datta, "Porous media based model for deep-fat vacuum frying potato chips," J*ournal of Food Engineering*, vol.110, pp.428–440, 2012.

[14] Rahman, S., "Food Properties Handbook," *CRC Press, Inc.*, Boca Raton, FL. 1995.

[15] Contreras Medellin, R., "Hot air and microwave drying of deformable and rigid porous media," *PhD Thesis*, University of Minnesota, 1987.

[16] Crank-Nicolson method, *Wikipedia*, http://en.wikipedia.org/wiki/Crank%E2%80%93Nicolson_method.

[17] Thomas, J. W., "Numerical Partial Differential Equations: Finite Difference Methods," *Texts in Applied Mathematics* ***22***. Berlin, New York: Springer-Verlag. ISBN 978-0-387-97999-1, 1995.

[18] Gerald Recktenwald, "Crank Nicolson Solution to the Heat Equation," *ME 448/548 Notes*, *Portland State University Department of Mechanical Engineering*.

[19] Lab.8, "Implicit methods: the crank-nicolson algorithm," http://www.dynamicearth.de/compgeo/Tutorial/Day2/cranknicholson.pdf, pp.45-51.

Chapter 4 Measurement of effective permittivity of potato Agata

Previously, the mechanism of heat and mass transfer of porous media under convective heating is studied with 1D brick as an example. The behaviors of temperature, saturation and pressure are analyzed and their accuracies are proved. Based on that model, potato is chosen to further research the interaction mechanism between RF and porous media, due to potato is easy to get, to shape and its parameters are provided relatively completely. The key parameter of RF/MW heating materials model--effective permittivity--is addressed in detail in this chapter.

The term "permittivity" implies the relative complex permittivity, i.e., the permittivity of a material relative to free space, often termed the complex dielectric constant, which is expressed as $\varepsilon_r = \varepsilon_r' - i\varepsilon_r''$, where ε_r' is the dielectric constant and ε_r'' is the dielectric loss factor. The dielectric constant is associated with the capability for energy storage in the electric field in the material, and the loss factor presents energy dissipation in the material or the conversion from electric energy to heat energy. Here, all loss mechanisms, both those due to dipole relaxation and ionic conduction, are included in the dielectric loss factor ε_r'' [1].

The permittivities or dielectric properties of materials are of major significance in determining how electromagnetic energy in the radio-frequency and microwave range interacts with materials. In considering the potential use of selective radio frequency (RF) dielectric heating porous media—taking potato as an example, the need has been evident for data on permittivity of potato. Until nowadays, some researchers have measured the effective permittivity of many agricultural products and materials [1][2]. However, most of the measurements are taken under microwave frequency. Limited data on the permittivity of potato under RF have appeared in the literature [3]. What's more, even though there exist the effective permittivity of potato under RF, the measured data is those of Russett Burbank potato produced in USA [3]. No data about effective permittivity of Agata-a kind of potato sample available in Toulouse market and used in our research-are provided. Therefore, it is necessary to obtain the effective permittivity of Agata.

Permittivity of porous media is supposed to be a function of temperature, frequency and moisture content which are correlative to each other. The variation of any one would change the others. It is almost impossible to check the relation between one factor and effective permittivity without disturbing the other factors. What's more, its measurements might be done, but to provide the exact dielectric properties for porous materials is a difficult undertaking. It is hard to obtain the uniform temperature and moisture distribution in the porous sample due to its inhomogeneous structure, leading to inaccurate measurement. For some materials, machining of samples to exact dimensions required for dielectric properties measurement is also difficult. Therefore, mixing rules seem to be an interesting alternative approach since it is reported that mixing rules approximate the properties to an extent of being used in real world work [4].

Below, we will study the impacts of each factor plays on the effective permittivity first, then choose one mixing rule to describe the change of dielectric property of potato Agata in our research.

4.1 Effective permittivity of agricultural products

Normally, the dielectric properties of foods are relative to several factors. For hygroscopic materials like potatoes, water moisture is the dominant factor on determining dielectric property. There have been reports indicating that the dielectric properties depend on the frequencies, temperature, compositions and their volume fraction, and provided the corresponding change tendencies [2][5][6][7][8].

4.1.1 Impact factors of permittivity

4.1.1.1 Frequency dependence

Since the definition of dielectric property is based on the polarization of molecule and their efforts to reorient influenced by the alternating electric field, the dielectric properties of most materials vary with frequency, with the exception of some extremely low-loss materials. If the frequency is extremely high, no mechanical system can react and respond to the change of the electric field. The permittivity under this condition is presented by ε_∞. In the similar way, the static permittivity at zero frequency is termed as ε_s. Debye proposed a mathematical formula

to describe the interaction between dielectric properties of pure polar materials and frequency with ε_∞ and ε_s.

$$\varepsilon = \varepsilon_\infty + \frac{\varepsilon_s - \varepsilon_\infty}{1 + i\omega\tau} \tag{4-1}$$

Where ω is the angular frequency, τ is the relaxation time, the period associated with the time for the dipoles to revert to random orientation when the electric field is removed.

At very low and very high frequencies, the permittivities are both real and constant. At intermediate frequencies, the dielectric constant undergoes dispersion while the dielectric loss has the maximum loss at the frequency of $\omega = 1/\tau$ due to the dissipation of the electric field.

In fact, only few materials of interest consist of pure polar materials with a single relaxation time, most of materials have multi relaxation times even distribution of relaxation times. Therefore, the original Debye equation has been modified to better describe the frequency-dependent behavior of materials.

$$\varepsilon = \varepsilon_\infty + \frac{\varepsilon_s - \varepsilon_\infty}{1 + (i\omega\tau)^{1-\alpha}} \tag{4-2}$$

α is the empirical spread of relaxation times, which takes on values between 0 and 1.

4.1.1.2 Temperature dependence

The dielectric properties of materials are also relative to temperature. As frequency increases, the molecules will distance themselves from each other, then return to their normal orientation in a short time. Debye has used the assumed spherical molecules with radius of a, viscosity of η in the solution to study the dependence of relaxation time with temperature. He developed an equation to describe the single relaxation time, as shown below:

$$\tau = 4\pi a^3 \eta / kT \tag{4-3}$$

Where τ is relaxation time, T is the temperature in Kelvin, k is Boltzmann constant.

This equation shows clearly that the relaxation time is reversely proportional to temperature, that's said, the relaxation time decreases with increasing temperature. At the same time, the loss factor peak will shift to higher frequencies. Thus the dielectric constant will increase when temperature rises and the dielectric loss may either increase or decrease, depending on whether the frequency is higher or lower than the relaxation frequency [2][7].

N. E. Bengtsson and P. O. Risman [9] have measured the dielectric constants and dielectric losses of several food products under different temperatures at frequency of 2.8 GHz. The measured data show that the dielectric constants ascend sharply around 0 °C and then decrease as temperature increasing except for the salted food such as cooked ham. The dielectric losses of these materials show the same change tendencies.

Generally, the food composition consists of dipolar and ionic materials and their dielectric loss compose of dipolar loss and ionic loss. The increase in temperature will decrease the dipolar dielectric loss but in the case of ionic loss, dielectric loss will increase if the temperature increases [7]. The variation of dielectric loss of salty material is different because its loss factor consists of dipolar and ionic loss.

4.1.1.3 Density dependence

Density is another parameter that affects the dielectric properties. This is especially notable for particulate dielectric materials, like pulverized or granular materials. To understand better the density dependence of effective permittivity of particulate material, relationships between the dielectric properties of solids and those of air-particle mixtures, are needed.

For some materials, it is hard to shape the material to the exact dimension required for permittivity measurement. The need of relationships for converting dielectric properties of constituents in the sample to that of the whole material arises. Here, a relationship of dielectric properties of granular with density can be shown, for example, for a two phase mixture:

$$\sqrt{\varepsilon_{eff}} = \upsilon_1\sqrt{\varepsilon_1} + \upsilon_2\sqrt{\varepsilon_2} \tag{4-4}$$

Where ε_{eff} is the effective permittivity of the mixture, υ_1 and υ_2 are the volume fraction of each constituent in the mixture. ε_1 and ε_2 indicate the complex permittivity of each composition. More equations and details will be presented later.

4.1.1.4 Composition dependence

Dielectric properties of food products are relative to those of their compositions. Most food materials contain of carbohydrate, moisture, fat, protein, salt and so on. Free water and salt are two major components in the food composition that give the high effect on the dielectric property in the microwave spectrum. The complex interaction of every component in the food

composition that affects the dielectric property can be modeled using the dielectric model presented in [7] and [10]. Some researchers have suggested the other modeling methods such as multiple linear regressions, partial least square regression and artificial neural network to model the dielectric properties and the complex interaction between each component in the food composition.

Table 4.1 Effects of the dielectric properties of salt, fat and free water with frequency and temperature [7][11]

Component	Effects on dielectric property	
	Frequency	Temperature
Salt	ε'' increases with decreasing frequency at low frequency ε' decreases with increasing frequency	ε'' increases with increasing temperature ε' increases with increasing frequency
Fat	ε'' and $\varepsilon'$are constant at microwave frequency	ε'' and $\varepsilon'$are constant with temperature
Free water	ε'' increases at relaxation frequency ε' decreases with increasing frequency	ε'' and ε'decrease with increasing temperature

Datta and O.S. Nelson [11] have studied and summarized respectively the effects of temperature and frequency on the dielectric properties of salt, fat and free water. Their effective permittivity will affect that of the whole sample. However, in our research, we assume that all the salt is dissolved into the free water and carbohydrate, fat and protein are treated as solid. That is, the potato sample consists of salty water, solid and gas. Its dielectric property is decided by the three components.

4.1.2 Dielectric mixture equations

Until now, many different dielectric mixture equations have been proposed to predict the effective permittivity of mixtures [2][12][13][14][15][16]. Some of them will be presented below with two components.

For the notations employed below, ε_{eff} represents the effective permittivity of the mixture, ε_1 is the permittivity of the medium where particles with permittivity of ε_2 are dispersed. v_1 and v_2 are their corresponding volume fractions, which satisfy a relation $v_1 + v_2 = 1$.

Complex refractive index equation

$$(\varepsilon_{eff})^{1/2} = v_1(\varepsilon_1)^{1/2} + v_2(\varepsilon_2)^{1/2} \tag{4-5}$$

Landau & Lifshitz, Looyenga equation

$$(\varepsilon_{eff})^{1/3} = v_1(\varepsilon_1)^{1/3} + v_2(\varepsilon_2)^{1/3} \tag{4-6}$$

Bottcher equation

$$\frac{\varepsilon_{eff}-\varepsilon_1}{3\varepsilon_{eff}} = v_2 \frac{\varepsilon_2-\varepsilon_1}{\varepsilon_2+2\varepsilon_{eff}} \tag{4-7}$$

Bruggeman-Hanai equation

$$\frac{\varepsilon_{eff}-\varepsilon_2}{\varepsilon_1-\varepsilon_2}\left[\frac{\varepsilon_1}{\varepsilon_{eff}}\right]^{1/3} = 1 - v_2 \tag{4-8}$$

Rayleigh equation

$$\frac{\varepsilon_{eff}-\varepsilon_1}{\varepsilon_{eff}+2\varepsilon_1} = v_2 \frac{\varepsilon_2-\varepsilon_1}{\varepsilon_2+2\varepsilon_1} \tag{4-9}$$

Lichtenecker equation

$$\ln \varepsilon_{eff} = v_1 ln\varepsilon_1 + v_2 ln\varepsilon_2 \tag{4-10}$$

To evaluate the performance of these different methods for estimating effective permittivity of mixtures, all these mixing equations were tested in similar measurements on two plastic materials which could be measured in both solid and pulverized forms [17][18]. For these two plastic materials, one lossless and the other one with loss factor similar to grain, the Refractive Index and Landau and Lifshitz, Looyenga equations generally were found to give the best results. The error in predicting ε' for the lossless material was within l%, and the Landau and Lifshitz, Looyenga equation which was closest for the lossy plastic was 4%.

Other texts were also conducted with wheat and wheat flour [19][20], coal [18][19], coal and limestone and their mixtures [21][22]. The similar conclusions can be drawn that Landau & Lifshitz, Looyenga equation and Refractive Index equation seems to be more accurate than other mixture equations. Stuart O. Nelson also indicated that Landau & Lifshitz, Looyenga equation was a bit superior to the Refractive Index equation in fitting the data for both the whole-kernel wheat and the ground wheat [2]. Furthermore, D. C. DUBE mentioned that the LLL equation was probably the best equation in the literature yielding accurate enough dielectric constant (within 3%) for non-lossy and lossy materials [12]. Enis Tuncer has explicitly shown that the LLL expression could be applied to describe the dielectric properties of powdered and porous systems [23]. In summary, the Landau and Lifshitz, Looyenga mixture equation appears to be the recommended choices for practical use with mixtures. Therefore, we decide to use the LLL equation to predict the effective permittivity change in our model.

4.1.2.1 Landau & Lifshitz, Looyenga equation

As mentioned above, the potato sample consists of salty water, solid and gas. Its dielectric property is given by:

$$\varepsilon_{r,eff}^{1/3} = v_w \varepsilon_{r,w}^{1/3} + v_s \varepsilon_{r,s}^{1/3} + v_g \varepsilon_{r,g}^{1/3} \tag{4-11}$$

Where $\varepsilon_{r,eff}$ is the relative effective permittivity of potato sample, $\varepsilon_{r,w}$, $\varepsilon_{r,s}$, $\varepsilon_{r,g}$ present respectively the relative permittivity of salty water, solid and gas. v_w, v_s, v_g are the corresponding volume fraction.

Since liquid is the dominant constituent in the potato, the effective permittivity of saline water is critical in determining the dielectric property of the whole sample. It varies with frequency, temperature, salinity of the liquid and its behavior can be calculated from the most general form of Debye expression [24][25]:

$$\varepsilon_{r,w} = \varepsilon_\infty + \frac{\varepsilon_s - \varepsilon_\infty}{1 + (j\omega\tau)^{1-\alpha}} - j\frac{\sigma}{\omega\varepsilon_0} \tag{4-12}$$

Where $\omega = 2\pi f$ is the radian frequency with f in hertz, $\varepsilon_0 = 8.854e-12\ F/m$ is the permittivity of free space, ε_s and ε_∞ are respectively the static and high-frequency dielectric constants of the solute, σ the ionic conductivity of the dissolved salts in mho/m, α an

empirical parameters describing the distribution of relaxation times. Among all these parameters in Debye equation, ε_s, α and σ, τ are functions of temperature and salinity.

In order for equation (4-12) to be of practical computational value to the user, the specific dependence must be derived from experimental results utilizing regression fits to the data. Stogryn, Klein and Swift have respectively proposed their models to predict the dependence. D. H. Gadani et al. have measured the dielectric property of salty water under different frequency and salinity. The measured data is in good agreement with those calculated by Stogryn model as well as Klein and Swift model [27]. In our research, the Stogryn model is chosen to describe the dielectric property of saline water in potato sample.

4.1.2.2 Stogryn model [26][27]

According to Stogryn model, the values of ε_s and relaxation time τ as functions of temperature and normality are given by:

$$\varepsilon_s(T,N) = \varepsilon_s(T,0)a(N) \tag{4-13}$$

$$2\pi\tau(T,N) = 2\pi\tau(T,0)b(N,T) \tag{4-14}$$

Where T is temperature of water in ℃, N the normality of the solution.

$$a(N) = 1 - 0.2551N + 5.151 \times 10^{-2}N^2 - 6.889 \times 10^{-3}N^3 \tag{4-15}$$

$$b(N) = 0.1463 \times 10^{-2}NT + 1 - 0.04896N - 0.02967N^2 + 5.644 \times 10^{-3}N^3 \tag{4-16}$$

$$\varepsilon_s(T,0) = 87.74 - 0.40008T + 9.398 \times 10^{-4}T^2 + 1.41 \times 10^{-6}T^3 \tag{4-17}$$

The relaxation time for pure water is obtained then:

$$2\pi\tau(T,0) = 1.1109 \times 10^{-10} - 3.824 \times 10^{-12}T + 6.938 \times 10^{-14}T^2 - 5.096 \times 10^{-16}T^3 \tag{4-18}$$

The normality N can be calculated from salinity S as:

$$N = S(1.707 \times 10^{-2} + 1.205 \times 10^{-5}S + 4.058 \times 10^{-9}S^2) \tag{4-19}$$

S is the salinity in parts per thousand ($0 \leq S \leq 260$). For NaCl solutions the ionic conductivity is given by:

$$\sigma_{NaCl}(T,N) = \sigma_{NaCl}(25,N)[1 - 1.962 \times 10^{-2}\Delta + 8.08 \times 10^{-5}\Delta^2 - \Delta N(3.02 \times 10^{-5} + 3.922 \times 10^{-5}\Delta + N(1.721 \times 10^{-5} - 6.584 \times 10^{-6}\Delta))] \quad (4\text{-}20)$$

Where $\Delta = 25 - T$, and

$$\sigma_{NaCl}(25,N) = N[10.394 - 2.3776N + 0.68258N^2 - 0.13538N^3 + 1.0086 \times 10^{-2}N^4] \quad (4\text{-}21)$$

For the value of ε_∞ used in this model, Stogryn pointed out that there was no evidence showing that ε_∞ depends on the salinity. Even though that there is some evidence proving that ε_∞ may slightly depend on temperature, the situation is far from clear enough. The two data sets which addressed its temperature dependency conflicted with each other, with one stating that ε_∞ increased with increasing temperature while the other claiming the opposite change tendency [24][26][28]. He finds that the best fit for high frequency is achieved when ε_∞ is assumed to be a constant with value of 4.9. The estimated experimental uncertainty in ε_∞ is around $\pm 20\%$, which, however, contributes negligible errors for the effective permittivity of saline water. Therefore, ε_∞ is assigned as 5 in the calculation.

Unfortunately, the salinity of potato Agata, which plays a critical role in determining the permittivity of mixture, is unknown. Therefore, we have to find out a way to estimate the salinity of potato sample.

Some researchers have predicted the salinity of several kinds of materials by measuring the dielectric property of these samples and finding the correlation between salt content and permittivity [29][30]. Inspired by these articles, we decide to measure the S parameters of the whole system under different frequencies and obtain the corresponding input impedances. The salinity of potato Agata is estimated later by comparing the measured and corresponding simulated input impedances.

4.2 Measurement techniques of effective permittivity

There exist many methods to measure the dielectric property. The most commonly used techniques for permittivity measurement at the microwave frequencies include open-ended probe methods, transmission line methods, resonant cell methods and free space methods using horn waveguides, time domain reflectometry methods and so on [6][7][31][32][33][34]. Each of these measurement techniques can be designed to operate in a specific microwave

frequency range. Based on the existed techniques, a modified one-port coaxial cell is developed for the measurement. In this section, a brief overview of the dominant techniques and our measured model is presented.

4.2.1 Common measurement techniques

4.2.1.1Transmission/Reflection line method

The transmission line is an ordinary method to measure the complex permittivity of materials, which involves placing a sample in a section of waveguide or coaxial line and measuring the two-port scattering parameters with a vector network analyzer. The measurement is restricted to the dominant mode and frequency range. Calibration must be carried before doing the measurements. Reflected and transmitted signals are obtained and conversed to complex dielectric parameters. In most cases, this method requires the sample under test to be machined into a slab or annular geometry so that it can fit tightly into the waveguide or coaxial line. Liquids and viscous-fluid type food can be also measured with this method by using a sample holder. However, it is very important not to capture air on the surface of the Perspex windows or within the coaxial cell when measuring liquids. Surface contact between the windows and particulate materials can also lead to irregularities in the measured data [35].

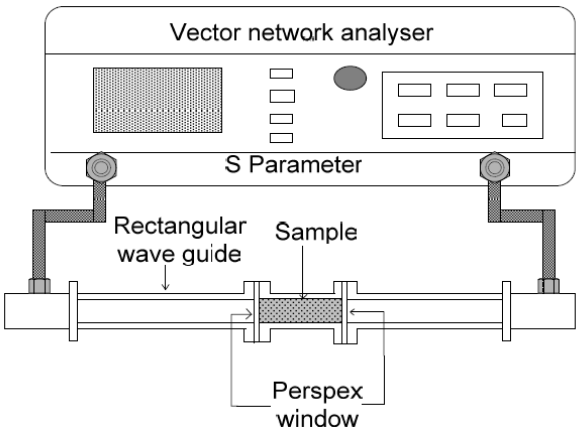


Figure 4.1 Schematic of transmission line measurement system

4.2.1.2 Open-ended probe method

The open-ended probe method is pioneered by Stuchly and Stuchly to circumvent many disadvantages of the transmission line measurement technique [36]. It has been used by

many researchers for years as a non-destructive testing method [37][38][39] [40]. In this method, the probe is pressed against a specimen or immersed into the liquids for measuring the reflection and determining the permittivity. For some special cases like in-vivo measurement of biological specimens, it is not possible to cut out of the sample of a material because the material characteristics may change. Therefore, with this method the sample can be placed in close contact with the probe without causing any changes in the material characteristics.

Besides, without strict requirement of the sample preparation, the open-ended probe measurement provides good accuracy for the measured complex permittivity of high loss materials. But care must be exercised with this technique because errors are introduced at very low and very high frequencies, as well as for low values of dielectric constant and loss factor. It is very important to ensure that there are no air bubbles on the interface between the coaxial probe surface and the liquid. This method only measures the local permittivity of the liquid as the electromagnetic field only propagates a fraction of a wavelength into the liquid. Therefore, it is important that the liquid or sample is homogeneous. Otherwise, this method is not suitable for solids or particulates.

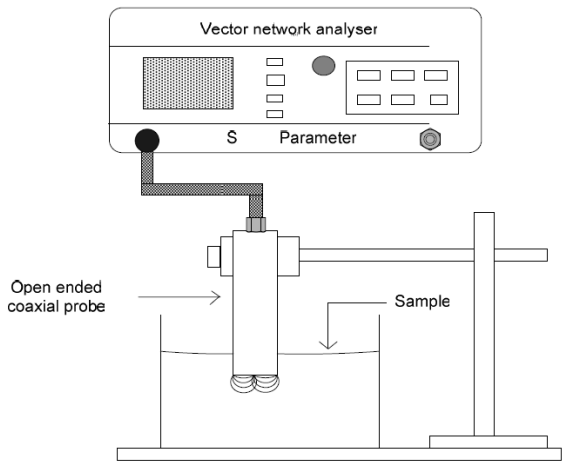


Figure 4.2 Schematic of open-end probe measurement system

4.2.1.3 Free space method

Of the available measurement means, free space technique is also categorized as non-destructive and contact-less measuring methods. Since it doesn't have a special preparation for the sample, it is particularly suitable for materials with high temperature or

inhomogeneous dielectrics or measurements in hostile environments. The free space measurement system often utilizes two antennas placed facing each other, with antennas connecting to the vector network analyzer. The sample is put between these two antennas and the attenuation and phase shift of the signal are measured to calculate the complex permittivity.

It has been reported that multiple reflections, mismatches, diffraction effects and parasitic interference from the immediate environment are accounted for the errors [31][41]. To enhance the measurement accuracy, special attention must be paid to the choice of the radiating elements, the design of the sample holder, the sample geometry and location between the two antennas.

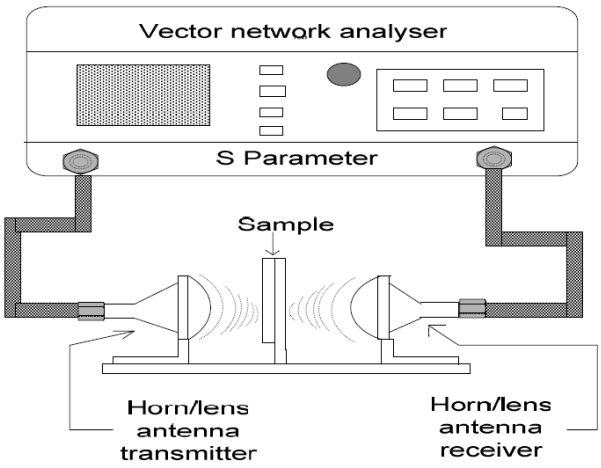


Figure 4.3 Schematic of free space measurement system

4.2.1.4 Resonant cell method

Resonant measurements are the most accurate methods of obtaining permittivity and permeability. It can be constructed and loaded a relatively low loss, small scale sample. The mechanism of this approach is based on the perturbation of resonant frequency and Q factor of the cell by the complex permittivity of sample. To determine the dielectric properties of the material, the resonant frequency and Q factor of the cell with and without sample are respectively measured. Then the complex permittivity of the sample can be calculated from the resonant frequency and Q factor of empty and filled cell, the volume of sample and empty cell [7][42].

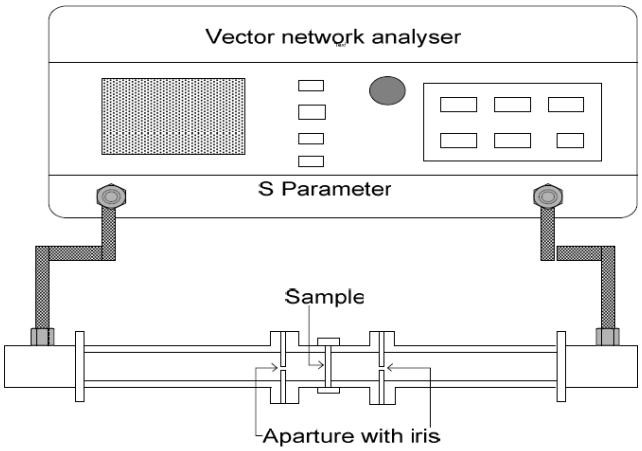


Figure 4.4 Schematic of resonant cell measurement system

This technique is recommended to measure the complex permittivity of a low loss material. As the cell is so sensitive to load variations, it has rigid requests on the sample preparation [43]. What's more, the resonant cell technique is not suited to on-line measurements as the sample has to be prepared and carefully loaded into the resonator structure.

To show the features and advantages of each method, a table is offered below:

Table 4.2 General comparison of dielectric property measurement systems [7][31]

	Transmission line	Open-ended probe	Resonant cell	Free space
Frequency	Restricted to waveguide bands	Broad band	single	Restricted to waveguide bands
Sample preparation	destructive/ hard	Non-destructive easy	Destructive hard	Non-destructive hard
sample size	moderate	small	Very small	large
Sample type	Liquid, solid, particulate, granular	Liquid Semi-solid	Best for low loss and small sample	Best for flat sheet, powder, high temperature samples
Measurement at different temperatures	hard	easy	Hard	easy

Accuracy of low loss material	reasonable	bad	Good	reasonable
Accuracy of high loss material	Very good	good	poor	good

Unfortunately, even though there exist numerous methods to measure the dielectric properties of materials, most of the techniques are more appropriate for measurements under microwave frequency range rather than radio frequency. However, the frequency used in our research is 27.12 MHz, belonging to radio frequency range. Therefore, based on the knowledge about features of different measurement methods above, a modified transmission line which is suitable for the RF range measurement–open ended coaxial cell is used to obtain the salinity of potato samples.

4.2.2 Measurement developed in LAPLACE

Below is a picture about the coaxial cell. The yellow parts indicate the conductors while the dark green ones are gaps on the outer conductor. Since the slots are along the direction of surface current, the disturbance of these slots on the electromagnetic wave distribution is negligible. It is also confirmed by simulations that the electric field distributions are the same with and without gaps. The outer cylinder extends beyond the end of the inner conductor and in these regions acts as a circular waveguide below cutoff.

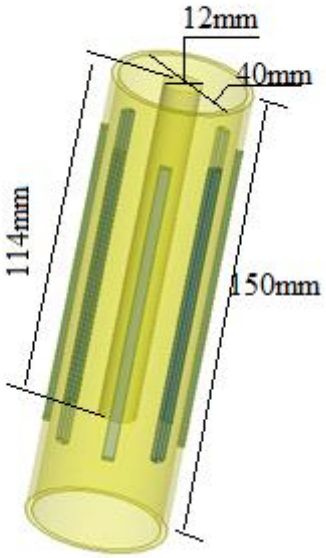


Figure 4.5 Schematic of coaxial cell

The main advantages of the coaxial cell are: 1) it can be used in large frequency band, including lower frequencies in radio frequency range; 2) potato is grouped under high loss material, the transmission line is good at the dielectric measurement of high loss materials; 3) the electromagnetic field between inner and outer conductor is isotropic on every section along ∅ direction. Since RF can propagate through the whole sample, the measured effective permittivity will be the average one of the whole sample; 4) even though the sample is not homogeneous, the measured data are supposed to be the same if sample is turned a random angle along inner conductor in multiple measurements.

The size of coaxial cell used in our research, however, is not standard. A conical transition is needed to connect the large size cell and standard N connector equipped with vector network analyzer, as shown in Figure 4.6. The conical transition employed is not a standard accessory, either. To obtain the parameters of potato sample more precisely, we decide to measure the characteristic parameters of the conical transition and then wipe off its effects on the measured dielectric parameters of the whole system. The process of how to wipe off the effects of conical transition is detailed below.

4.2.2.1 Determining the characterization of the conical transition

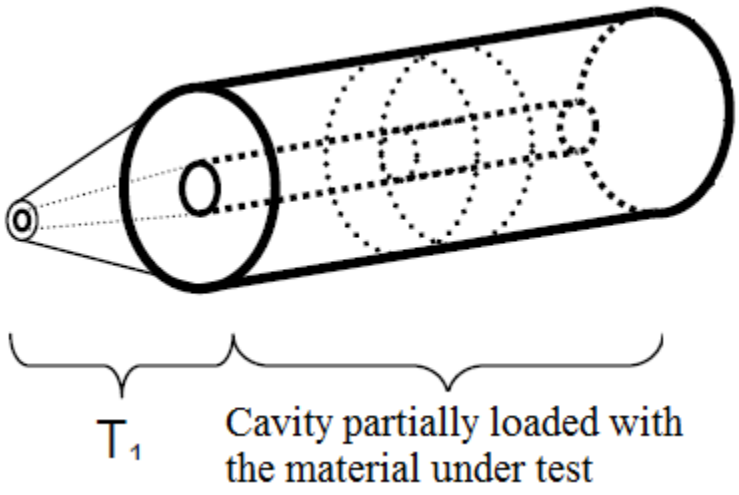


Figure 4.6 Schematic of coaxial cell connected with conical transition

Figure 4.6 is the coaxial cell partially loaded a sample mounting with conical transition by one end while the other one of the cell is open-ended. The measured S_{11} corresponds to the loaded cell and transition. To obtain the S parameter of the loaded cell, transmission matrix, i.e. ABCD matrix of each constituent is employed:

$$[ABCD]_{total} = [ABCD]_{cone}[ABCD]_{cavity} \tag{4-22}$$

$$[ABCD]_{cavity} = [ABCD]_{cone}^{-1}[ABCD]_{total} \tag{4-23}$$

Transmission matrix can be gotten by measurement. To simplify the work, the transition is replaced by the equivalent symmetric two ports circuit. Three options of equivalent circuits are available: T-form impedance, π-form admittance and a transformer.

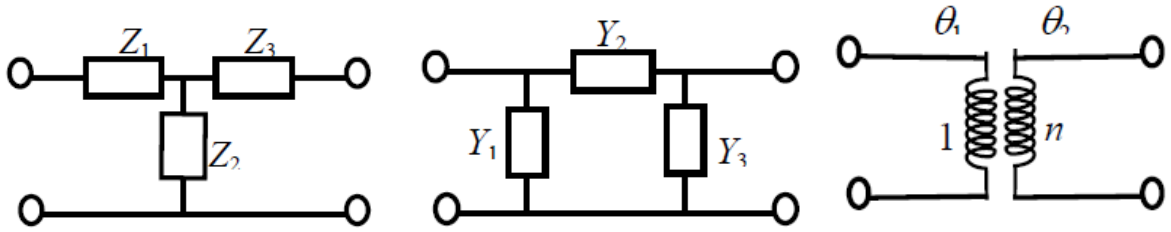


Figure 4.7 Equivalent circuits

In our work, the T-form impedance equivalent circuit is employed. To determine the value of each impedance, a set of original kit developed in our lab, which consists of three elements: a

short circuit (SC), an open circuit (OC) and a load resistance Z_l (LOAD) of $75\,\Omega$, is respectively used to connect the end of the conical transition. The corresponding input impedances of the whole system are measured, indicating as Z_{OC}, Z_{SC} and Z_{load}.

$$Z_{SC} = Z_1 + Z_2//Z_3 \tag{4-24}$$

$$Z_{OC} = Z_1 + Z_2 \tag{4-25}$$

$$Z_{load} = Z_1 + Z_2//(Z_3 + Z_{load}) \tag{4-26}$$

After subtracting equation (4-24) from (4-25) and (4-24) from (4-26), it is easy to know the value of each element.

$$Z_2 = \sqrt{(Z_l + K)(Z_{OC} - Z_{load})} \tag{4-27}$$

$$Z_3 = K - Z_2 \tag{4-28}$$

$$Z_1 = Z_{OC} - Z_2 \tag{4-29}$$

Where

$$\mathrm{K} = Z_l(Z_{load} - Z_{OC})/(Z_{SC} - Z_{load}) \tag{4-30}$$

To verify the former measurement and the deduced values for each element in the equivalent circuit, one can mount two identical transitions head to tail (Figure 4.8) and measure the reflection and transmission coefficients. Then the measured data are compared to those calculated by the T-form model elements values.



Figure 4.8 Picture of two transitions mounted head to tail

4.3 Estimate the salinities of researched material

After obtaining information about the conical transition, the input impedance of partially loaded cell is measured. Simulations to calculate the input impedances of the same system when using Landau and Lifshitz, Looyenga equation with different salinities are then implemented. The simulation results and measured ones are compared to obtain the estimated salinity. To further study the dielectric property of potato sample, the measured effective permittivity of Agata potato sample is then reversed using a code programming with COMSOL and Matlab. The reversed effective permittivity will be compared with those calculated by Landau and Lifshitz, Looyenga equation with the estimated salinity.

4.3.1 Measurement preparation

Potatoes Agata are bought from a market in Toulouse, France and stored in room temperature of about 16℃ for 24 hours. To shape the samples, a customized annular equipment is designed and fabricated to cut potatoes. It is made in metal and composed of two conductors which are assembled by screw spikes.

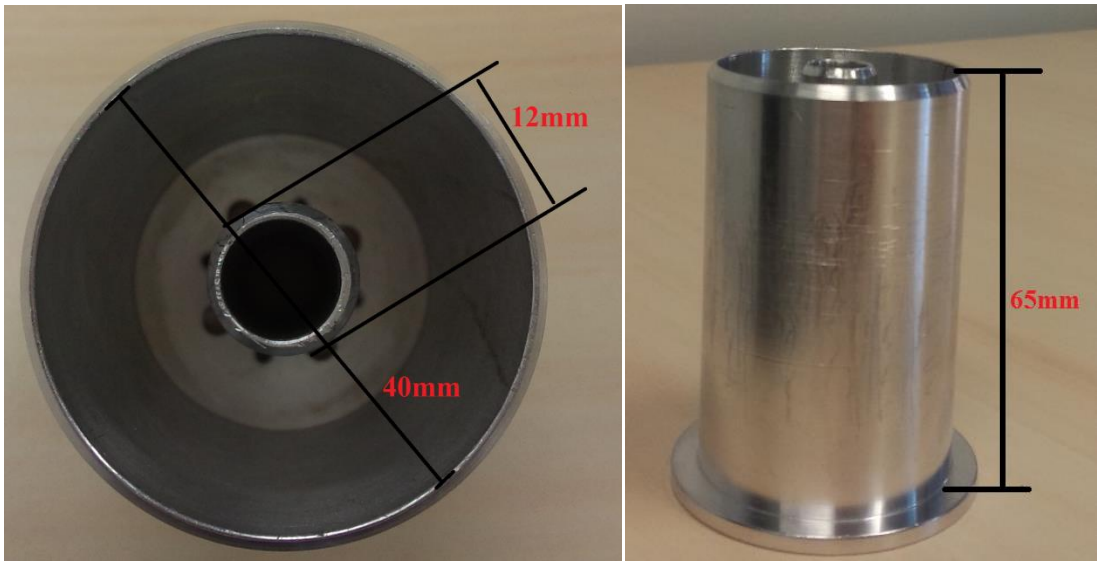


Figure 4.9 Photos of the cutting equipment



Figure 4.10 Photos of the cut sample

A vector network analyzer (ROHDE&SCHWARZ) is employed in the experiments to measure the S parameter of the whole system. Since the open-ended coaxial cell is very sensitive, the factors that may have impacts on the accuracy of measurement are analyzed before doing the experiments.

To check if the vertical location of samples in the cell has an impact on the measured results or not, two samples of 56mm and 54.2mm in height, placed at the location of 20mm and 30mm upper than the bottom of the inner conductor, are measured respectively. Small discrepancies exist in the input impedances among different measurements (Figure 4.11). To observe the difference more clearly, the wavy curves in Figure 4.11 are fitted by polynomials and presented in new graphs. It is obvious that the variations in imaginary part of input impedances are a little larger than those in real part. To invest this phenomena further, simulations for input impedances of potato samples with height of 54.2mm placed respectively 10mm, 20mm and 30mm upper the bottom of inner conductors are also done, revealing in Figure 4.13. The simulated results show the same change tendency in Figure 4.11, even though that the differences are bigger than the measured ones. The divergent phenomena still, however, can be explained: all the conditions are ideal in the simulation, while in the measurement, the experiment restrictions may import measured errors. One can conclude that the location of the sample has a small impact on the measured data.

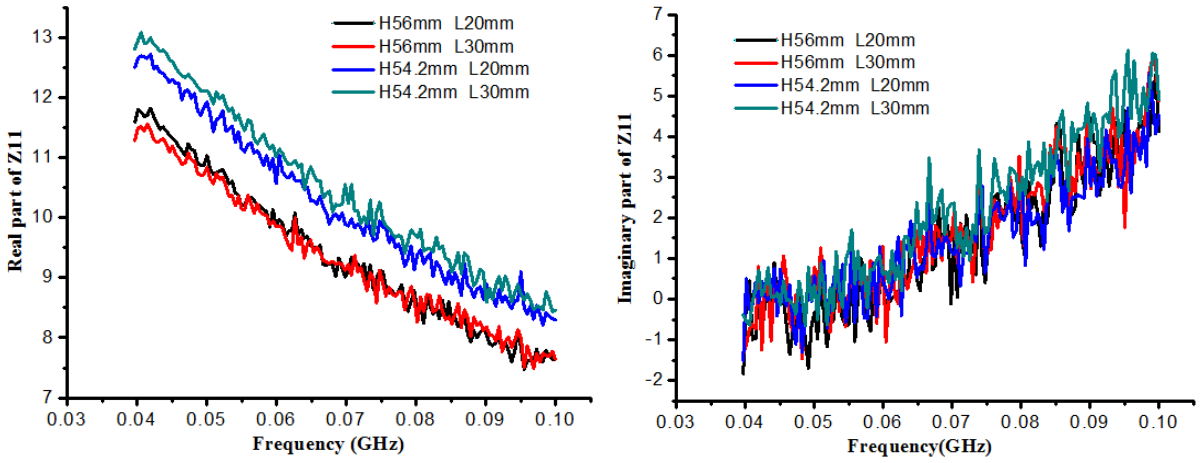


Figure 4.11 Comparisons of measured data of potato samples placed at different locations

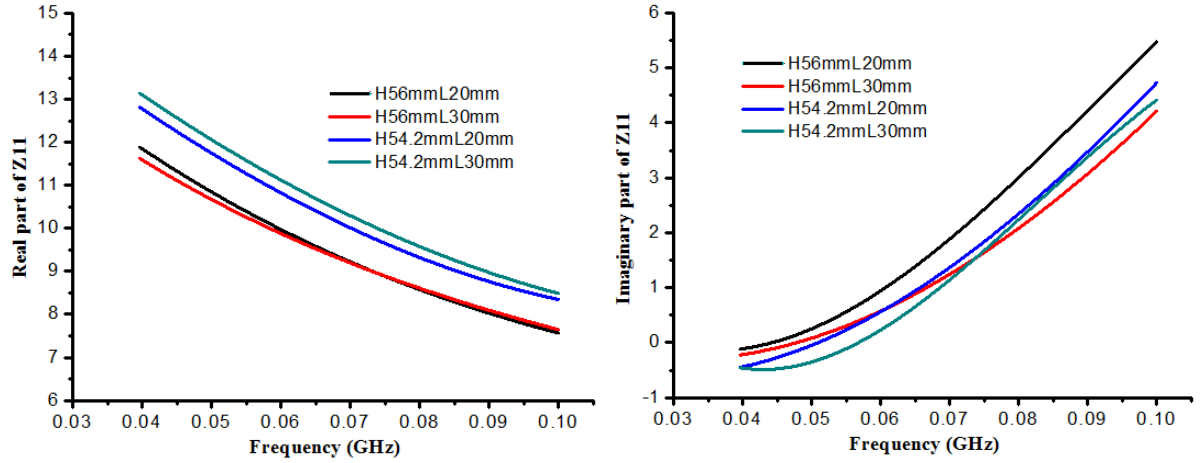


Figure 4.12 Comparisons of fitted measured data of potato samples placed at different locations

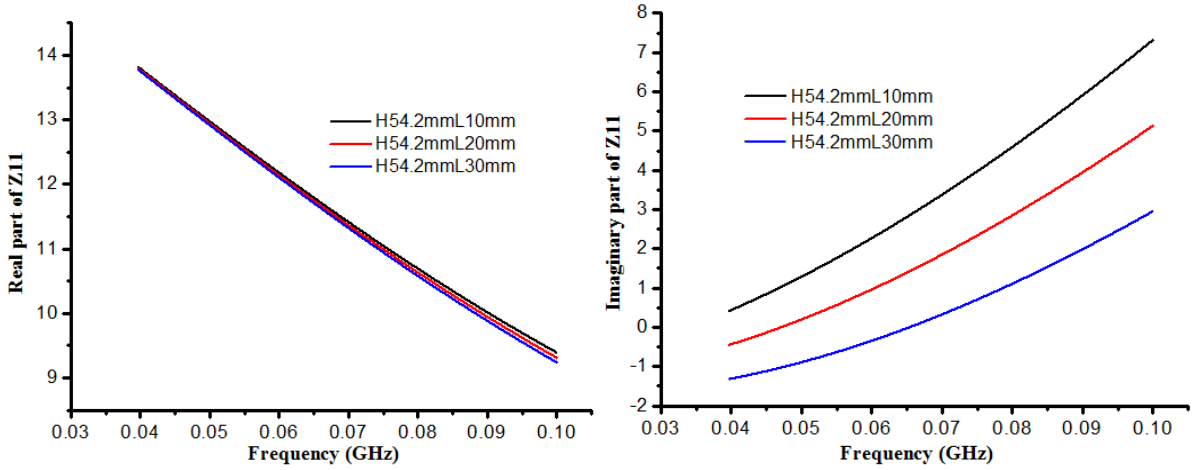


Figure 4.13 Comparisons of simulated data of potato samples placed at different locations

Figure 4.11 may be already capable to prove that height of sample affects measured data. However, those data are from two individual potatoes whose parameters are probably different, leading to different effective permittivities and input impedances. Therefore, to confirm the influence of sample's height, several annular samples are cut from a potato and measured. The measured results show that the greater difference of heights of samples, the larger the variations of measured data.

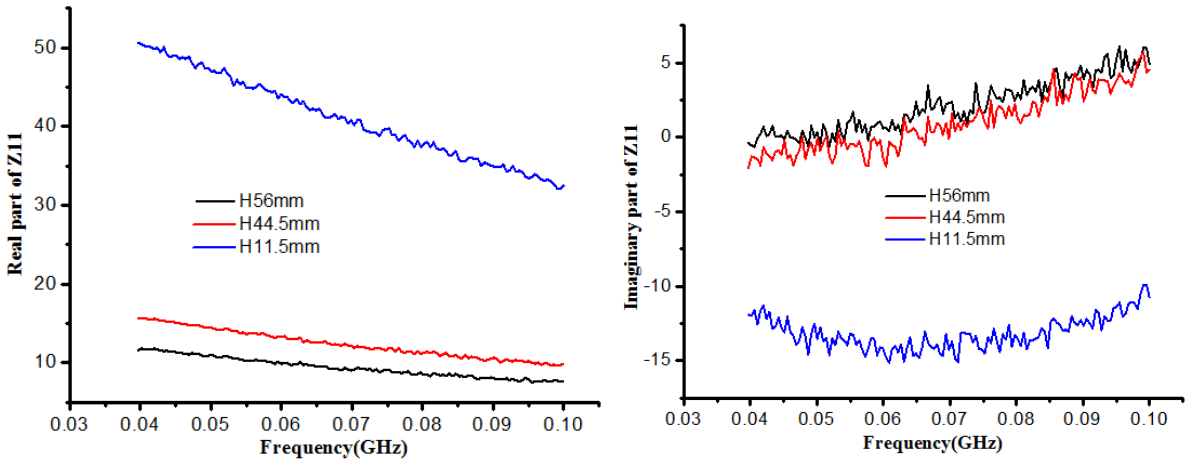


Figure 4.14 Comparison of measured data of potato samples with different height

During the experiment, we also notice that the potato sample had better touch the inner and outer conductors simultaneously. To find out the reason, simulations are conducted with different inner diameter of potato samples. The simulated data show that if there is space between the sample and conductors, the imaginary part of the input impedance will increase and the real part decreases. The wider the space between the sample and conductor becomes, the greater the change of the measured data is.

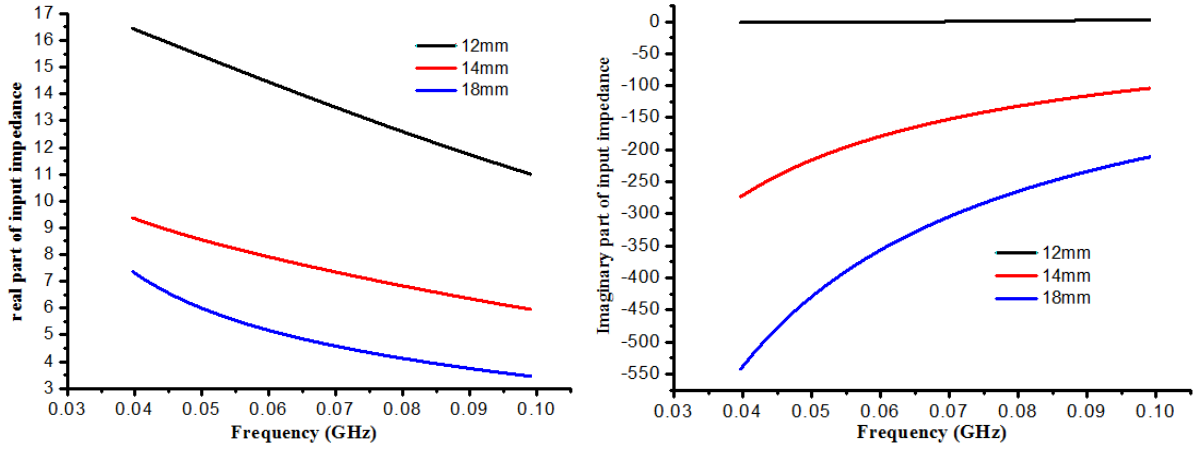


Figure 4.15 Simulated input impedances with different inner diameter of annular samples

Corresponding measurements are also taken and shown below.

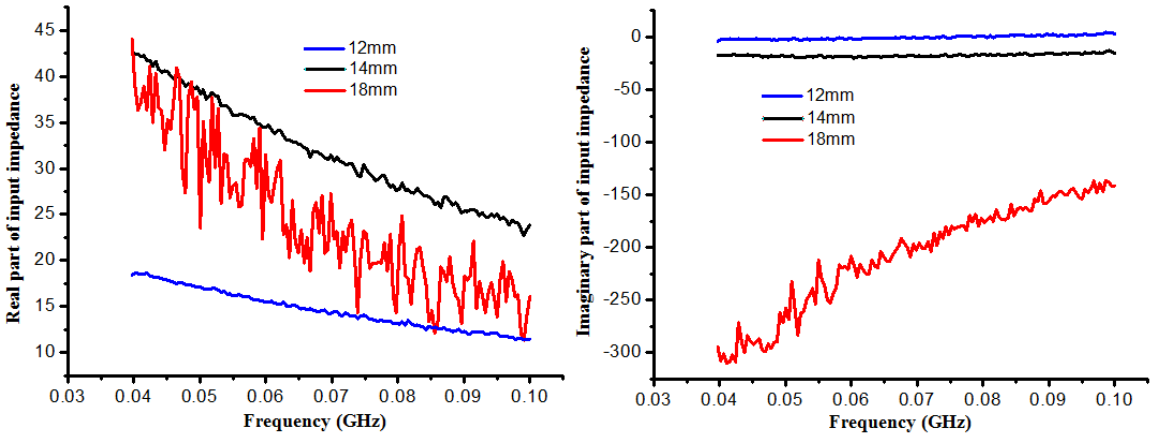


Figure 4.16 Measured input impedances with different inner diameter of annular samples

Comparing the measured input impedances with the simulated ones shown in Figure 4.15 and Figure 4.16, some discrepancies can be noticed. The measured change tendency and the values of real part of input impedances are different from those simulated. The reasons caused these conflicts may be: 1) the simulation conditions are ideal, while the experiments are afflicted with many restrictions; 2) when preparing the sample, potatoes are cut with an annular equipment first, and then enlarged the inner diameters by another individual equipment with diameters of 14mm and 18mm, respectively. Therefore, the inner and outer cylinders of the final sample are probably not concentric. The sample in the simulation, however, is perfectly concentric. In order to avoid importing more errors, all the samples touch both the conductors in our measurement.

4.3.2 Measuring the input impedance of partially loaded cell

Potatoes are shaped into rings that can fix between inner and outer conductors of the cell. All the potato samples indicated in this section are with height of 57mm. A conical transition introduced above is used to connect the loaded cell and Vector Network Analyzer. Measurements with the same potato are made under frequency of 40 MHz to 100 MHz. Because the range of S11 is very small--from -1 to 1, it is not easy to tell the differences among experimental measurements. Consequently, the input impedance of the whole system Z_{11} is chosen to be the compared parameter to help reverse the effective permittivity of potato sample. For one-port system, the relation of S11 and Z_{11} is simple,

$$Z_{11} = Z_0 \frac{1+S_{11}}{1-S_{11}} \tag{4-31}$$

After getting Z_{11} of the whole system, i.e. Z_{meas} the effect of the conical transition is wiped off to obtain the input impedance of the loaded cell Z_{ech}.

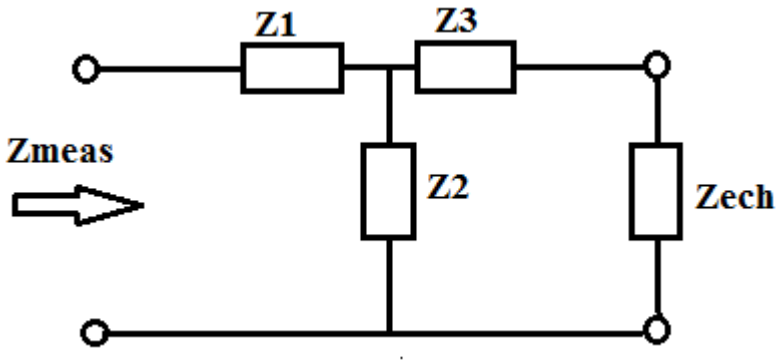


Figure 4.17 Equivalent circuit of the whole measured system



Figure 4.18 Picture of equipment for measurement

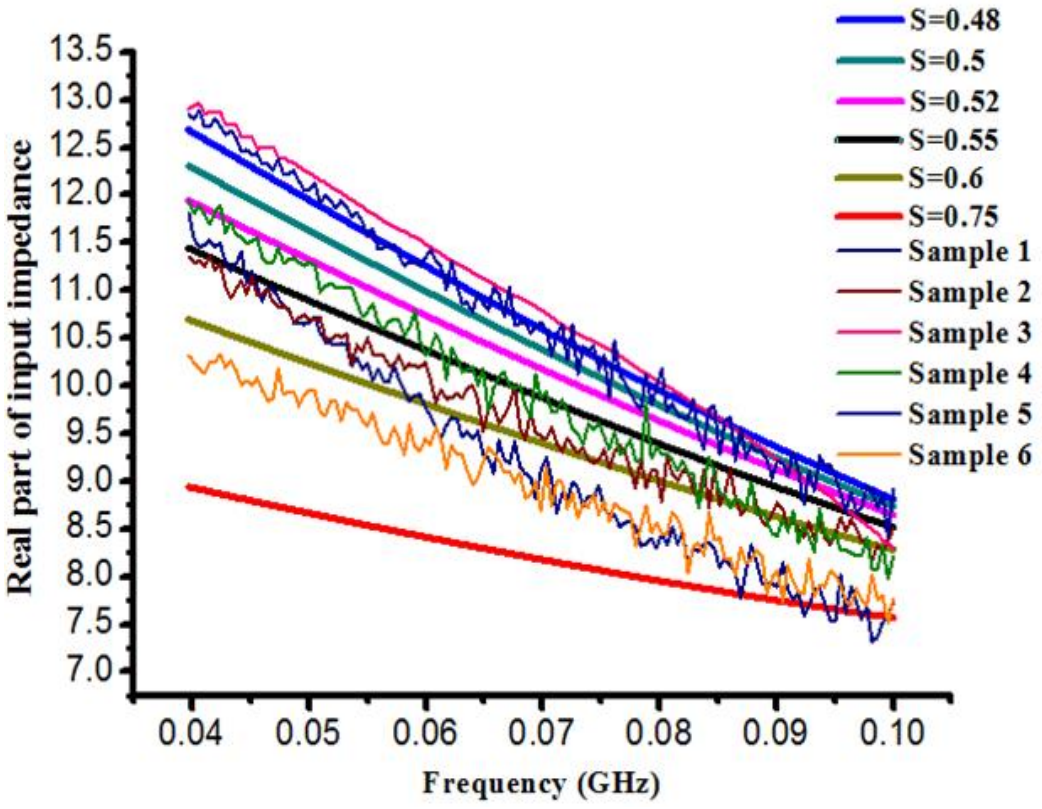
$$Z_{ech} = \frac{(Z_{meas}-Z_1)(Z_2+Z_3)-Z_2Z_3}{Z_2-(Z_{meas}-Z_1)} \quad (4\text{-}32)$$

4.3.3 Estimated results

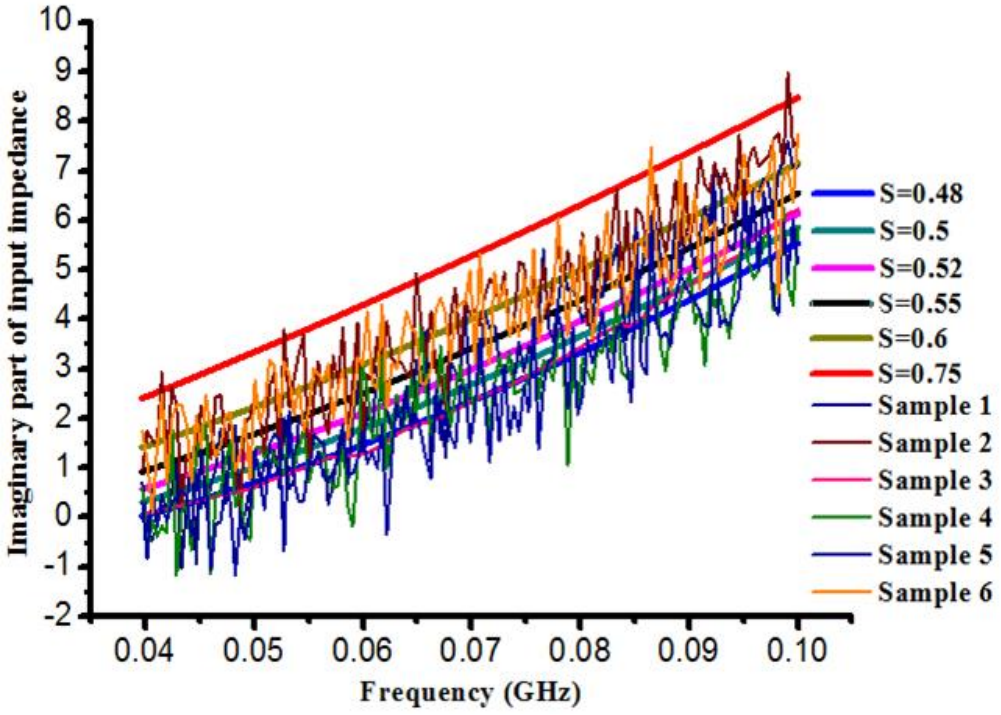
After doing the measurements, the input impedances of loaded cell are deduced according to the methods mentioned previously. Following the example of artificial neutral network method, we try to compare the measured input impedances and simulated ones to estimate the

salinity of potato Agata. Datta et al. has reported that the salinity of Russett Burbank potato produced in USA is about 0.75%. Therefore, a COMSOL combined Matlab code is developed to calculate the input impedances of loaded cell when the effective permittivity of sample is predicted by Landau and Lifshitz, Looyenga equation with different salinities around 0.75%. Comparisons of calculated and measured results are revealed in Figure 4.21. "Sample 1, 2, ..., 6" indicate the input impedance of each potato sample deduced by measured data, "$S = 0.48$, …, $S = 0.75$" present the calculated input impedance with different salinities: 0.48%, …, 0.75%. The measured data are not the same, but luckily, the discrepancy is not huge. This is normal because each potato is unique in the world. Its salinity, porosity and water saturation must be different from each other.

From the comparison of input impedances shown in Figure 4.19, it is obvious that the salinities of all the potato samples used in our measurement are not 0.75%, but rather in the range of 0.48% to 0.6%.



(a)



(b)

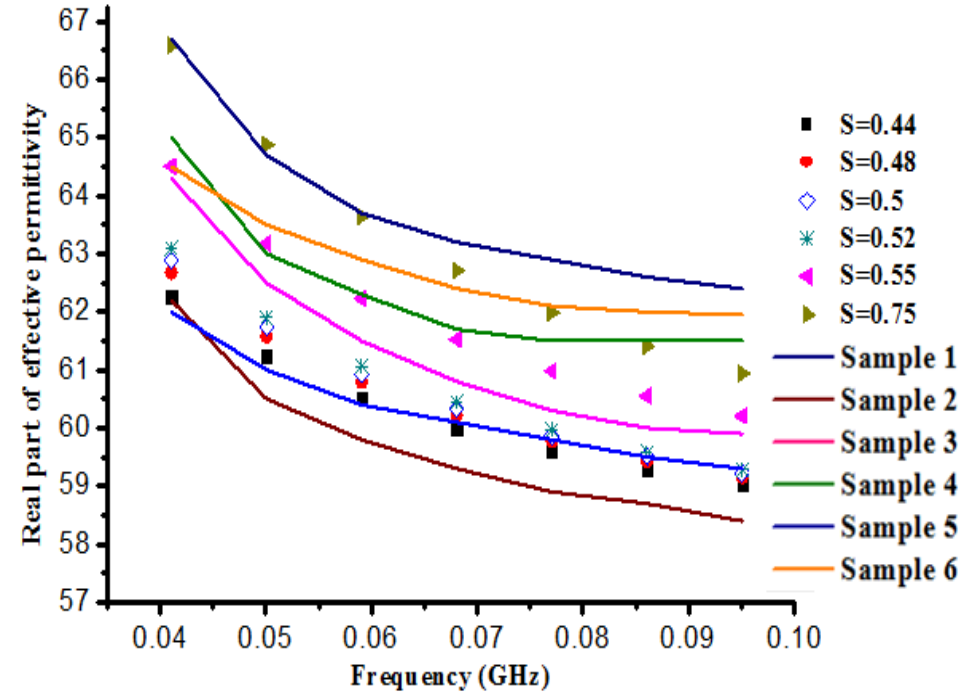
Figure 4.19 Comparison of measured and simulated input impedance: (a) real part, (b) imaginary part

To further study the effective permittivity of potato Agata, several data points of the measured input impedances for each potato sample are extracted and reversed into their corresponding effective permittivities by another COMSOL combined Matlab code. They are listed in table 4.3.

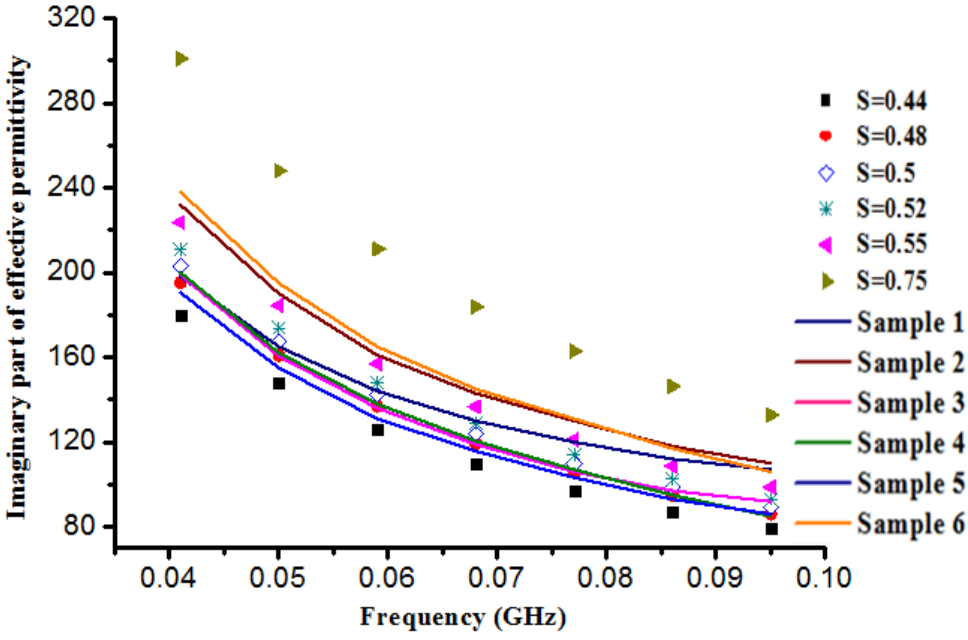
Table 4.3 Effective permittivities of measured samples

Freq	Sample 1		Sample 2		Sample 3		Sample 4		Sample 5		Sample 6	
(GHz)	Real	Imag.	Real	Imag.	Real	Imag.	Real	Imag.	Real	Imag.	Real	Imag.
0.0411	66.7	198.0	62.2	232.0	64.3	198.8	65.0	200.0	62.0	190.5	64.5	238.0
0.0501	64.7	165.0	60.5	190.0	62.5	160.5	63.0	162.0	61.0	155.0	63.5	195.0
0.0591	63.7	144.0	59.8	161.0	61.5	136.0	62.3	138.0	60.4	131.0	62.9	165.0
0.0681	63.2	130.0	59.3	143.0	60.8	119.0	61.7	120.5	60.1	115.8	62.4	145.0
0.0771	62.9	120.0	58.9	130.0	60.3	106.0	61.5	107.0	59.8	103.3	62.1	131.0
0.0860	62.6	112.0	58.7	118.0	60.0	97.0	61.4	95.0	59.5	93.0	62.0	117.0
0.0951	62.4	107.0	58.4	110.0	59.9	92.0	61.3	85.0	59.3	86.0	62.0	106.0

To double check estimated salinity range, the reversed effective permittivities will be compared with the theory ones calculated by Landau & Lifshitz, Looyenga equation with different salinities.



(a)



(b)

Figure 4.20 Comparison of measured and simulated effective permittivity: (a) real part, (b) imaginary part

Figure 4.20 shows clearly that the most of the solid lines of effective permittivity locates between the point lines when salinity equals 0.48% and 0.55%. This phenomenon is more obvious for the imaginary part of effective permittivity.

4.4 Discussion and conclusion

The reversed effective permittivities of our measurement in Figure 4.20 or in table 4.3 show the same change tendencies as those of Rusett Burbank potato measured by S. Nelson, with values in the same orders [3]. Even though that this is another kind of potato, the salinity and other parameters may be different, its values, however, are still consultative. This might prove that the estimated results are reasonable and receivable.

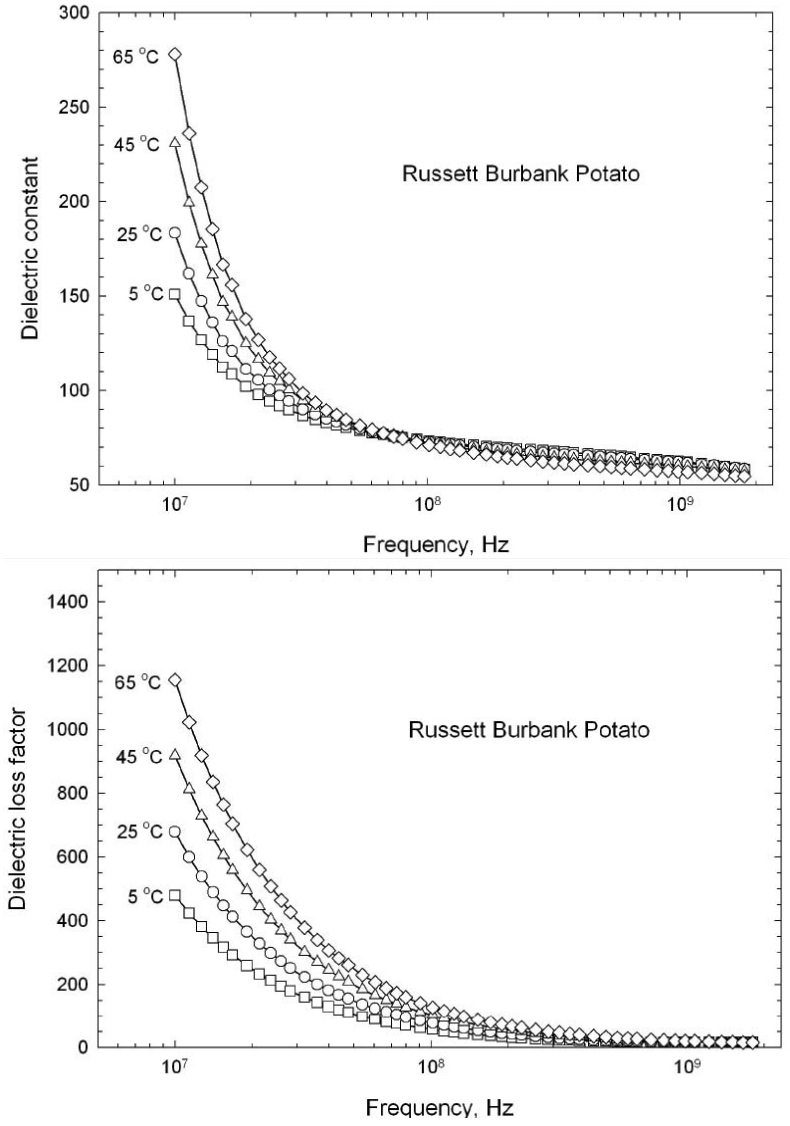


Figure 4.21 Measured data of Russett Burbank potato by Nelson

However, we should admit that the estimated range of salinity can not perfectly include all the cases of potato samples. Like the real part of input impedance of sample 6 in Figure 4.19 and the real part of effective permittivity of sample 1 and 2 in Figure 4.20, their lines do not locate

in this range. In fact, this phenomenon is explainable. As discussed in the section of measurement preparation, several factors would influence the measured results. In the experiments, it is impossible to shape the sample with the exact dimension as the one expected in the simulation. The surfaces of samples are not ideally smooth, leading to imperfectly touching the conductors of the coaxial cell. There are some variations of other parameters of potato samples in reality. But in the simulation, the parameters for all the potato samples are the same and ideal. All these factors will import the discrepancies between simulated and measured results.

To further test and verify the salinity range of samples of potato Agata, the averages of measured data at different frequencies are presented and compared with those calculated with salinities of 0.48% and 0.55% in table 4.4. It is obvious that the average salinity of potato samples is between 0.48% and 0.55%. In considering all the comparisons above and difficulties exist in the experiments, we can conclude that the salinity of Agata potato may be between 0.48% with 0.55%.

Table 4.4 Comparison of measured average and simulated effective permittivity

Freq	S=0.48%		S=0.55%		S=0.52%		Measure ave. data	
(GHz)	Real	Imag.	Real	Imag.	Real	Imag.	Real	Imag.
0.0411	62.7	195.2	64.5	223.8	63.1	210.9	64.1	209.6
0.0501	61.6	160.9	63.2	184.4	61.9	173.8	62.5	171.3
0.0591	60.8	136.9	62.2	157.0	61.1	147.9	61.8	145.8
0.0681	60.2	119.2	61.5	136.7	60.4	128.7	61.3	128.9
0.0771	59.8	105.6	61.0	121.1	60.0	114.1	60.9	116.2
0.0860	59.4	94.8	60.6	108.8	59.6	102.4	60.7	105.3
0.0951	59.2	86.0	60.2	98.7	59.3	92.9	60.6	97.7

It is also worth noticing that the average effective permittivity is very close to that calculated with salinity of 0.52%. Therefore, in the next heating section, the salinity of potato sample will take the average value of those of the measured samples--0.52%. Even though it may exist difference between this estimated value and the actual one, the average value is still acceptable and useful for dielectric heating Agata potatoes in the real world application. This will be proved in the chapter 5 by comparing the measured and simulated temperature distributions of RF heated samples.

Reference of chapter 4

[1] Nelson, S. O., "Microwave dielectric properties of fresh fruits and vegetables," *Transactions of the ASAE, vol.* 23, no.5, pp.1314-1317, 1980.

[2] Nelson, S. O., "Dielectric properties of agricultural products-Measurements and Applications," *IEEE Transactions on Electrical Insulation*, vol.26, no.5, pp. 845-869, 1991.

[3] Nelson, S. O., "Dielectric spectroscopy of fresh fruit and vegetable tissues from 10 to 1800 MHz," *Journal of microwave power &electromagnetic energy*, vol. 40, no. 1, pp.31-48, 2005

[4] Ari Sihvola, "Mixing Rules with Complex Dielectric Coefficients," *Subsurface Sensing Technologies and Applications*, vol. 1, no. 4, pp.393-415, 2000.

[5] A.W. Kraszewskl, S. Trabolsi and S.O.Nelson, "Grain permittivity measurements in free space," *25th European microwave conference*, vol.2, pp.840-844, 1995.

[6] FILIZ IçIER and TANER BAYSAL, "Critical reviews in food science and nutrition," vol.44, no.6, pp.465-471, 2004.

[7] Badaruzzaman Mohamad Noh, "Application of microwave sensors to potato products," *A thesis of university of Manchester for the degree of doctor of philosophy in the faculty of engineering and physical science*. 2010.

[8] Yifen Wang, Timothy D. Wig, Juming Tang, Linnea M. Hallberg, "Dielectric properties of foods relevant to RF and microwave pasteurization and sterilization," *Journal of food engineering*, vol. 57, pp.257-268.

[9] N. E. Bengtsson and P. O. Risman, "Dielectric properties of food at 3 GHz as determined by cavity perturbation technique. II Measurement in food materials," *Journal of microwave power &electromagnetic energy*, vol.6, pp.107-123,1971.

[10] R. K. Frank Daschner, "Determination of the Composition of Foodstuffs Using Microwave Dielectric Spectra," *Springer Berlin Heidelberg*, 2005.

[11] S. O. Nelson and A.K. Datta, "Dielectric Properties of Food Materials and Electric Field Interactions," in Handbook of Microwave Technology for Food Applications, A. K. Datta and R.C. Anantheswaran, Editors. *Marcel Dekker*: New York, 2001.

[12] D. C. Dube, “Study of Landau-Lifshitz-Looyenga's formula for dielectric correlation between powder and bulk,” *Journal of physics D: Applied physics*, vol. 3, no. 11, pp.1648-1652, 1970.

[13] E. M. Cheng1, F. Malek, M. Ahmed, K. Y. You, K. Y. Lee, and H. Nornikman, “The use of dielectric mixture equations to analyze the dielectric properties of a mixture of rubber tire dust and rice husks in a microwave absorber,” *Progress In Electromagnetics Research*, vol. 129, pp.559-578, 2012.

[14] Bottcher, C.J.F., “The dielectric constant of crystalline powders,” *Rec. Trav. Chim*. vol.64, pp.47-51,1945.

[15] Kraszewski, A., “Prediction of the dielectric properties of two-phase mixtures,” *Journal of microwave power*, vol. 12, no. 3, pp.215-222, 1977.

[16] Looyenga, H, “Dielectric constants of heterogeneous mixtures,” *Physica* vol.31, pp.401-406, 1965.

[17] S. O. Nelson and T.-S. You, “Relationships between microwave permittivities of solid and pulverized plastics,” *Journal of Physics D: Applied Physics*, vol. 23, pp. 346-353, 1990.

[18] S. O. Nelson, “Estimation of permittivities of solids from measurements on pulverized or granular materials,” in Dielectric Properties of Heterogeneous Materials, *Progress in Electromagnetics Research,* vol. 6, pp. 231-271, 1992,.

[19] S. O. Nelson, “Observations on the density dependence of the dielectric properties of particulate materials,” *Journal of Microwave Power*, vol. 18, no.2, pp. 143-152, 1983.

[20] S. O. Nelson, “Correlating dielectric properties of solids and particulate samples through mixture relationships,” *Transactions of the ASAE*, vol. 35, no.2, pp. 625-629, 1992.

[21] S. O. Nelson, “Determining dielectric properties of coal and limestone by measurements on pulverized samples,” *Journal of Microwave Power and Electromagnetic Energy*, vol. 31, no.4, pp. 215-220, 1996.

[22] S. O. Nelson, "Measurement and calculation of powdered mixture permittivities," *IEEE Transactions on Instrumentation and Measurement*, vol. 50, no.5, pp. 1066-1070, 2001.

[23] Enis Tuncer, “The Landau-Lifshitz/Looyenga dielectric mixture expression and its self-similar fractal nature,” *Cornell university library*, arXiv.org > cond-mat > arXiv: cond-mat/0503750v1, pp.1-13. 2005,

[24] Lawrence A. Klein and Calvin T. Swift, “An Improved Model for- the Dielectric Constant of Sea Water at Microwave Frequencies,” *IEEE Trans Antennas and Propagation*, vol. AP-25, no.1, pp.104-111, 1977.

[25] Ram Somaraju and Jochen Trumpf, “Frequency, temperature and salinity variation of the permittivity of Seawater,” *IEEE Trans Antennas and Propagation*, vol.54, no.11, pp.3441-3448, 2006,

[26] Stogryn A., “Equations for calculating the dielectric constant of saline water,” *IEEE transaction on microwave theory and techniques*, vol. 19, no.8, pp.733-736, 1971.

[27] D. H. Gadani, V. A. Rana, S. P. Bhatnagar, A. N. Prajapati, A. D. Vyas, “Effect of salinity on the dielectric properties of water,” *Indian journal of pure & applied physics*, vol. 50, pp.405-410, 2012.

[28] E. Grant, T. Buchanan, and H. Cook, “Dielectric behavior of water at microwave frequencies,” *J. Chcm. Phys.*, vol. 26, pp. 156-161,1957.

[29] Y. Shiinoki, Y. Motouri, and K. Ito, "On-line monitoring of moisture and salt contents by the microwave transmission method in a continuous salted butter-making process," *Journal of Food Engineering*, vol. 38, pp. 153-167, 1998.

[30] H. M. A. Al-Mattarneh, D. K. Ghodgaoankar, H. Abdul Hamid, A. A.-A.-F. Al-Fugara, A., and S. H. A.-A. B. Abu Bakar, S.H., "Microwave reflectometer system for continuous monitoring of water quality," Student Conference on Research and Development, SCORED 2002.

[31] M.S. Venkatesh, G.S.V. Raghavan, “An overview of dielectric properties measuring techniques,” *Canadian biosystems engineering*, vol. 47, 7.51-7.30, 2005.

[32] S. O. Nelson, “Fundamentals of dielectric properties measurements and agricultural applications,” *Journal of Microwave Power and Electromagnetic Energy*, vol.44, no.2, pp. 98-113. 2010,

[33] Udo Kaatze, “Techniques for measuring the microwave dielectric properties of materials,” *Metrologia*, vol. 47, pp.S91-S113, 2010.

[34] Measurement of dielectric material properties: application note, *ROHDE&SCHWARZ*, P3-9.

[35] H. S. Chua, A. D. Haigh, F. Thompson, and A. A. P. Gibson, “Measurement of the wet-mass, moisture content, volume and density of single wheat grain kernels,” *Science, Measurement and Technology, IEE Proceedings* -, vol. 151, pp. 384-388, 2004.

[36] Stuchly, M.A. and S.S. Stuchly., “Dielectric properties of biological substances – Tabulated,” *Journal of Microwave Power and Electromagnetic Energy,* vol.15, pp.19-26, 1980.

[37] V.Komarov, S.Wang and J.Tang, “Encyclopedia of RF and microwave engineering: Permittivity and measurement,” John Wiley & Son, Inc., New York, vol.4, pp.3693-3711, 2005.

[38] E. C. Burdette, F. L. Cain, and J. Seals, “In vivo probe measurement technique for determining dielectric properties at VHF through microwave frequencies,” *IEEE Transactions on Microwave Theory and Techniques*, vol. 28, pp. 414-427, 1980.

[39] D. K. Misra, “In situ electric probe method for determining the dielectric properties of materials,” *IEEE Transactions on Instrumentation and Measuremen*t, vol.37, pp.157-160, 1988.

[40] D. Misra, “On the measurement of the complex permittivity of materials by an open-ended coaxial probe,” *IEEE Microwave and Wireless Components Letters*, vol. 5, pp. 161-163,1995.

[41] Trabelsi, S., A.W. Kraszewski and S.O. Nelson. “A new density-independent function for microwave moisture content determination in particulate materials,” In *Proceedings of IEEE Instrumentation and Measurement Technology Conference*, 1997.

[42] G. Birnbaum and J. Franeau, "Measurement of the Dielectric Constant and Loss of Solids and Liquids by a Cavity Perturbation Method," *Journal of Applied Physics*, vol. 20, pp. 817-818, 1949.

[43] A. W. Kraszewski and S. O. Nelson, "Observations on resonant cavity perturbation by dielectric objects," IEEE Transactions on Microwave Theory and Techniques, vol.40, pp. 151-155, 1992.

Chapter 5 A 2D axisymmetric model of RF intermittently heating potato

After estimating the effective permittivity of potato Agata, simulations of RF heating potato are conducted in this chapter to further study the interaction between RF and porous media. To get more uniform temperature distributions, a coaxial cell is designed to periodically dry the potato sample with radio frequency. In simulation, the sample and coaxial cell are both simplified into a 2D axisymmetric model, which lowers the calculation requirement of computer but maintains the calculation accuracy. The parameters involved in this model are referred to a paper of Datta [1]. In order to check the accuracy of the simulation model of RF heating potato, experiments are also implemented.

This chapter will introduce the simulation model first, then present the governing equations of this model. Values of parameters used in the simulation are provided. The experiment implementation and comparisons of simulated and measured results are talked at the end of this chapter.

5.1 Schematic of 2D axisymmetric model

Figure 5.1 shows the schematic of 2D axisymmetric model for RF periodically heating potato. The outer cylinder extends beyond the ends of the inner conductor and in these regions acts as a circular waveguide below cutoff. The blue one indicates the potato sample which is shaped into a ring and fixed between the inner and outer conductor. RF power is inserted from the top surface with frequency of 27.12MHz. The bottom of the cell is open and set as scattering boundary.

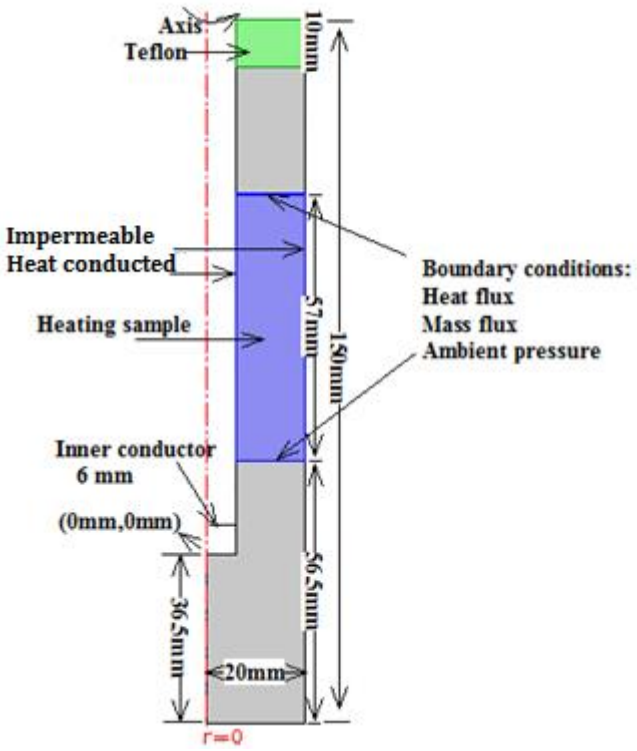


Figure 5.1 Schematic of 2D axisymmetric model

5.2 The governing equations

Electromagnetic wave drying of foodstuffs is a complex interplay of electromagnetics, mass, momentum and energy transport. During the heating process, since internal evaporation is dominant, distributed evaporation of liquid water to vapor should be included for a more consistent formulation of microwave drying problem. To better understand the MW/RF drying process and address the problems encountered therewith, this fundamentals-based multiphase model distinguishes the different phases (solid, liquid and gas) and builds formulas for each phase. Therefore, Maxwell' equations, mass conservation for each phase, momentum conservation equation and heat transfer equation are combined to describe the RF heating porous media model.

The computational process requires the solution of two different physics: electromagnetic distribution in heating cell and food material and, transport process (mass, momentum and heat transport) in the food material. Maxwell's equations are solved to obtain the electric field inside the oven cell and food and, is coupled with a multiphase porous media model (similar

to the 1D brick model) to obtain temperature and moisture distribution inside the sample. The two different sets of physics are discussed in detail in the following section.

5.2.1 Maxwell's equation

The behaviors of RF in the coaxial cell obey Maxwell's equations, from which the energy absorbed by potato sample can be obtained:

$$\nabla \times \vec{E} = -j\omega\mu_0\vec{H} \tag{5-1}$$

$$\nabla \times \vec{H} = j\omega\varepsilon_0\varepsilon_r\vec{E} \tag{5-2}$$

$$\nabla \cdot \varepsilon_r\vec{E} = 0 \tag{5-3}$$

$$\nabla \cdot \vec{H} = 0 \tag{5-4}$$

Where $\vec{E}$ is the electric field intensity, $\vec{H}$ is the magnetic field intensity. ω denotes the angular frequency, μ_0 and ε_0 are permeability and permittivity of free space, respectively. ε_r is the effective permittivity of potato, which can be expressed as:

$$\varepsilon_r = \varepsilon_r' - i\varepsilon_r'' \tag{5-5}$$

ε_r' represents the dielectric constant while ε_r'' is dielectric loss.

The dissipation power absorbed by the heated sample is calculated by:

$$Q = \frac{1}{2}\omega\varepsilon_0\varepsilon_r''(\vec{E}\cdot\vec{E}^*) \tag{5-6}$$

5.2.2 Momentum conservation equation

Darcy's law is valid for flow in the porous material that velocity is low. As mentioned previously in the assumptions, the Reynolds number is small. Therefore, the superficial velocity for each moving phase (liquid water, air and vapor) due to the total gas pressure gradient is given by:

$$\overrightarrow{u_i} = -\frac{k_{r,i}k_{in,i}}{\mu_i}\nabla P \tag{5-7}$$

Where i stands for water, air and vapor. The components of air and vapor share the same velocity. $k_{r,i}$ and $k_{in,i}$ are the relative and intrinsic permeability of corresponding phases, respectively. μ_i is the viscosity.

5.2.3 Mass conservation equation

The liquid water in the sample experiences the capillary pressure besides the total gas pressure.

Therefore, the net pressure of liquid is:

$$p_w = P - p_c \tag{5-8}$$

Substituting equation (5-8) into equation (5-7), the effective velocity of water is obtained:

$$\overrightarrow{u_{w,eff}} = -\frac{k_{r,w}k_{in,w}}{\mu_w}\nabla p_w = -\frac{k_{r,w}k_{in,w}}{\mu_w}\nabla P + \frac{k_{r,w}k_{in,w}}{\mu_w}\nabla p_c$$

$$= -\frac{k_{r,w}k_{in,w}}{\mu_w}\nabla P + \frac{k_{r,w}k_{in,w}}{\mu_w}\frac{\partial p_c}{S_w}\nabla S_w \tag{5-9}$$

Let $D_c = -\frac{k_{r,w}k_{in,w}}{\mu_w}\frac{\partial p_c}{S_w}$, the mass conservation equation for liquid water is

$$\frac{\partial}{\partial t}(\phi\rho_w S_w) + \nabla\cdot(\overrightarrow{u_w}\rho_w) - \nabla\cdot(D_c\nabla(\phi\rho_w S_w)) = -I \tag{5-10}$$

The continuous equation for gas phase is given by:

$$\frac{\partial}{\partial \mathrm{t}}\left(\phi\rho_{\mathrm{g}}\mathrm{S_g}\right) + \nabla\cdot\left(\rho_{\mathrm{g}}\overrightarrow{\mathrm{u_g}}\right) = I \tag{5-11}$$

The conservation equation for vapor should consider the bulk flow and binary diffusion:

$$\frac{\partial}{\partial t}\left(\phi\rho_g S_g\omega_v\right) + \nabla\cdot\left(\overrightarrow{u_g}\rho_g\omega_v\right) = \nabla\cdot\left(\phi S_g\frac{C_g^2}{\rho_g}M_a M_v D_{eff,g}\nabla x_v\right) + I \tag{5-12}$$

Where ϕ is the porosity, S_i, ρ_i are the saturation and density of different species, respectively. I is the phase change. ω_v is the mass fraction of vapor. The sum of mass fraction of vapor and air must equal unity, $\omega_v + \omega_a = 1$.

5.2.4 Heat conservation equation

The RF heating term is added as a source in the heat transfer equation, in which the convection due to moving phase, conduction and phase change are also included.

$$\frac{\partial}{\partial t}(\rho_{eff}C_{p,eff}T) + \nabla\cdot\left(\left(\rho C_p\vec{u}\right)_{fluid}T\right) = \nabla\cdot\left(k_{eff}\nabla T\right) - \lambda I + Q \tag{5-13}$$

$$\rho_{eff} = (1-\phi)\rho_s + \phi(S_w\rho_w + S_g\rho_g) \tag{5-14}$$

$$C_{p,eff} = x_s C_{p,s} + x_w C_{p,w} + x_g(\omega_v C_{p,v} + \omega_a C_{p,a} \quad (5\text{-}15)$$

$$k_{eff} = (1-\phi)k_{t,s} + \phi(S_w k_{t,w} + S_g(\omega_v k_{t,v} + \omega_a k_{t,a})) \quad (5\text{-}16)$$

λ is the latent heat of evaporation, x_i is the mass fraction of corresponding species.

5.2.5 Phase change

A phase change is the transformation of a thermodynamic system from one phase or state of matter to another one by heat transfer. It can be formulated in equilibrium and non-equilibrium ways. In the equilibrium formulation of evaporation, vapour is always assumed to be in equilibrium with the water in the solid, which has been used in the literature [2][3][4][5] [6]. The equilibrium vapour pressure, a function of moisture content and temperature, is given by the moisture isotherm equation [1][7]:

$$ln\left(\frac{p_{v,eq}}{p_{sat}}\right) = -0.0267M^{-1.656} + 0.0107e^{-1.287M}M^{1.513}ln(p_{sat}) \quad (5\text{-}17)$$

Where M is the dry basis moisture content. It is related to saturation by

$$M = \frac{\phi S_w \rho_w}{(1-\phi)\rho_s} \quad (5\text{-}18)$$

$p_{v,eq}$ is the equilibrium vapour pressure and p_{sat} indicates the vapour pressure of pure water, which is a function of temperature and given by Clausius–Clapeyron equation:

$$ln\left(\frac{p_{sat}(T)}{P_0}\right) = \frac{\Delta H_{vap}(T-T_0)}{RTT_0} \quad (5\text{-}19)$$

In the equilibrium formulation, p_v is always equal to $p_{v,eq}$ and given by equation (5-17).

However, there have been studies reported that evaporation is not instantaneous and non-equilibrium exists during rapid evaporation, even in still state, between water–vapour in gas phase and water in solid phase [8][9]. A discontinuity of temperature between the liquid surface and the water–vapour just above the surface has been observed through experiments on pure water [10]. An expression for predicting liquid evaporation flux of pure water surface is proposed by Ward and Fang 8, however, this expression is not suitable for hygroscopic solid. A more general expression of non-equilibrium evaporation rate for modeling phase change in porous media [11][12], which is consistent with studies on pure water, is given by

$$I = K(\rho_{v,eq} - \rho_v) \quad (5\text{-}20)$$

Where ρ_v is the vapour density at a location that comes from solution. K signifies the constant of evaporation rate that is the reciprocal of time in which phase change occurs. A large value of K means that phase change occurs in a small time. For the assumption of equilibrium, K is infinitely large or phase change occurs instantaneously. A very high value of K, however, makes the convergence of the numerical solution difficult. Independent ways of estimating K for a hygroscopic material are still unavailable but was recently estimated by a group to be of the order of 1 for evaporation of pure water [13].

In our model, the non-equilibrium formulation, given by equation (5-20), is used because it can express the evaporation rate explicitly and therefore would be preferred in the commercial software.

5.2.6 Initial and boundary conditions

The top of the sample is heated while the others are insulated and impermeable. The boundary conditions are then given by:

B.C. for equation (5-10): $\overrightarrow{n_{w,surf}} = h_m \varphi S_w (\rho_v - \rho_{v,cell}) + \rho_w \overrightarrow{u_w}$ (when $S_w = 1$) (5-21)

B.C. for equation (5-11): $P_{surf} = P_{amb}$ (5-22)

B.C. for equation (5-12): $\overrightarrow{n_{v,surf}} = h_m \varphi S_g (\rho_v - \rho_{v,cell}) + \rho_v \overrightarrow{u_v}$ (when $S_w = 1$) (5-23)

B.C. for equation (5-13):

$$q_{surf} = h_t (T_{cell} - T_{surf}) - \tau \overrightarrow{n_{w,surf}} - (\overrightarrow{n_{w,surf}} + \overrightarrow{n_{v,surf}}) C_{p,v} T - \rho_w \overrightarrow{u_w} C_{p,w} T \quad (5\text{-}24)$$

This is due to thermal energy equalization via conduction from hot to cold region during the power-off periods.

5.3 Input parameters

Input parameters are shown in table 5-1. All the physical and thermal properties are for raw potatoes. Actually, all the parameters of material under processing will change. However, it is difficult and unnecessary to measure all of their changes because not all of them will have a large impact on the simulated results. To try to conduct the simulation closer to the reality, some important parameters are discussed.

5.3.1 Specific heat capacity

The specific heat capacity of liquid water, vapor and air are functions of temperature. So is the thermal conductivity of water [13][14].

$$C_{p,w} = 4176.2 - 0.0909(T - 273) + 5.4731 \times 10^{-3}(T - 273)^2 \quad (5\text{-}25)$$

$$C_{p,v} = 1790 + 0.107(T - 273) + 5.856 \times 10^{-4}(T - 273)^2 - 1.997 \times 10^{-7}(T - 273)^3 \quad (5\text{-}26)$$

$$C_{p,a} = 1004.828 - 0.01185(T - 273) + 4.3 \times 10^{-4}(T - 273)^2 \quad (5\text{-}27)$$

$$k_{t,w} = 0.57109 + 1.762 \times 10^{-3}(T - 273) - 6.7036 \times 10^{-6}(T - 273)^2 \quad (5\text{-}28)$$

5.3.2 Capillary diffusivity of liquid water

Capillary action (sometimes capillarity, capillary motion) is the ability of a liquid to flow in narrow spaces without the assistance of, and in opposition to, external forces like gravity, which can be seen in porous media (Wikipedia). Capillary diffusivity of liquids is very important in convective drying as well as in RF or microwave heating. In convective heating, capillary force is the driving force for the liquid to move from wet region to dry region. In microwave heating, capillary force is also the only driving force for the liquid before the pressure gradient is developed large enough or after the pressure gradient is much reduced at the very dry stage. During the period of pressure gradient development, the capillary force can help the materials to maintain unsaturated state near the surface to some degree so that the governing equations described in this model are still valid.

It has been reported that capillary force is a function of water saturation and the relevant curve increases sharply when the saturation is very small [15]. The Leveret function is proposed to describe the capillary force and has been used for different materials [16][17].

$$\frac{p_c}{\sigma}\left(\frac{k_{in,w}}{\phi}\right)^{1/2} = J(S_w) \quad (5\text{-}29)$$

Where σ is the surface tension, ϕ is the porosity, $k_{in,w}$ the intrinsic permeability. This equation only considers the effect of water saturation without including the effects of porous structure and fluid properties. However, for the hygroscopic materials like food, the Leveret function is not general enough to be used. Numerous effective moisture diffusivity data have been reported in the publications. It represents the total moisture transport which is a

combination of capillary flow of liquid and diffusional flow of vapor. For the potato, its effective moisture diffusivity approximates the capillary diffusivity at the wet stage because the vapor diffusion is insignificant. However, when the sample becomes dry, the effective moisture diffusivity is quite different from the capillary diffusivity due to the increasing of the vapor diffusion. Fortunately, most of the effective moisture diffusivities of food were given in low moisture range. Therefore, combined all the information about the effective moisture diffusivity from very wet to very dry stages, Haitao Ni concluded that the liquid water diffusivity can be characterized as three regions [15]:

1) Constant rate region: $D_c > 1 \times 10^{-7}$
2) Falling rate region: $D_c < 1 \times 10^{-9}$
3) Transient region from constant to falling rate with diffusivity values between $1 \times 10^{-7}$and 1×10^{-9}.

He also proposed one equation to describe the water diffusivity for the entire region:

$$D_c = 1 \times 10^{-8} e^{-2.8+2M} \tag{5-30}$$

This formula has been employed in our research.

5.3.3 Permeability of water and gas

Permeability in the fluid mechanics is a measure of the ability of a porous medium to allow fluids to pass through it. The lager the permeability is, the faster the moisture transports and lower the internal pressure is. In opposite, the moisture will be hard to move through the sample and the inner pressure will accumulate, which can damage the potato sample.

Permeabilities k_w for hygroscopic materials are difficult to measure due to their low values and deformation of materials. Work on permeability is rare. Therefore, reasonable approximations need to be made. Bear proposed that the permeability of a material to a fluid is a product of intrinsic permeability $k_{in,w}$ and relative permeability $k_{r,w}$ [15].

$$k_w = k_{in,w} k_{r,w} \tag{5-31}$$

Intrinsic permeability

The intrinsic permeability $k_{in,w}$ is the permeability of a liquid or gas at fully saturated state, which corresponds to its maximum value. It depends on the structure of the material,

especially the porosity and pore size. The relative permeability $k_{r,w}$ represents how much fluid is in the pore volume.

For hygroscopic materials such as potato, there are additional complications in measuring its permeability. Materials deform during the heating process which changes the pore structures. The intrinsic and relative permeabilities are thus changed. To simplify the model and due to the unknown nature of variation of $k_{in,w}$ as a function of moisture content M, $k_{in,w}$ is assumed to be a constant and equal to $k_{in,w}$ at the raw state. This assumption is widely used by the researchers [1][14][16]. In this paper, the value of intrinsic permeability of liquid water is set as a constant of 1×10^{-15} [14].

For the gas intrinsic permeability $k_{in,g}$, there is less complexity. The permeability of gas k_g consistently increases with decreasing of liquid water and reaches its maximum value when there is no liquid left in the material. For the simplicity of the model and also due to the unknown variation of $k_{in,g}$ as a function of M, like $k_{in,w}$, $k_{in,g}$ is assumed as a constant. The value of $k_{in,g}$ of potato in our research is chosen as 2×10^{-15}.

Relative permeability

For the relative permeabilities, many expressions exist that represent the experimental data for different situations. A simpler analytical expression that represents the experimental data well was suggested by Jones and this formula is widely utilized in a lot of publications [1][14][16] and will be used in our research:

$$k_{r,w} = \begin{cases} [(S_w - 0.09)/0.91]^3, S_w > 0.09 \\ 0, S_w \leq 0.09 \end{cases} \quad (5\text{-}32)$$

$$k_{r,g} = \begin{cases} 1 - 1.1S_w, \ S_w < 1/1.1 \\ 0, S_w \geq 1/1.1 \end{cases} \quad (5\text{-}33)$$

5.3.4 The permittivity of potato during the processing

As discussed in the last chapter, the Landau and Lifshitz, Looyenga equation was used to predict changes in dielectric properties of the samples:

$$\varepsilon_{r,eff}^{1/3} = \sum_i v_i \, \varepsilon_{r,i}^{1/3} \quad (5\text{-}34)$$

Where i indicates each phase of constituent, v_i and $\varepsilon_{r,i}$ denote respectively its volume fraction and permittivity. The complex permittivity of the bulk matrix is 4-0.2j for potato and that of air phase is 1-0j. The dielectric property of saline water in potato sample is described by the Stogryn model.

$$\varepsilon_w = \varepsilon_\infty + \frac{\varepsilon_0 - \varepsilon_\infty}{(1+2j\pi\tau f)^{1-\alpha}} - \frac{i\sigma}{2\pi\varepsilon_0^* f} \tag{5-35}$$

Where ε_0 is the static dielectric constant of the solvent, τ is the relaxation time in seconds, σ denotes the ionic conductivity of the dissolved salts, ε_0^* the permittivity of free space. α is an empirical parameter that describes the distribution of relaxation times, which equals 0 in this paper. ε_∞ is the optical dielectric constant of the solvent, assumed as a constant of 4.9 [18] [19]. In our simulations of radio frequency heating potato, the salinity of sample is considered as 0.52%, according to the aforementioned measurements.

During the heating process, liquid water evaporates into vapor whose loss factor is 0, leading to a high salinity in the sample. The loss factor of the liquid increases and it becomes a better microwave absorber with rising temperature which increases the loss factor in turn [20]. Even though the volume fraction of the liquid water decreases with time, the imaginary part of effective permittivity of the sample will rise slightly at first, and then decrease gently while the dielectric constant varies in small reduction.

Table 5-1. Input parameters of potato in the simulation

Parameter	**Symbol**	**Value**	**Source**
Porosity	ϕ	0.88	[1]
Viscosity($P_a \cdot s$)			[1]
Water	μ_w	0.988e-3	
Vapor and air	μ_g	1.8e-5	
Intrinsic permeability(m^2)			[14]
Water	$k_{i,w}$	1e-15	
Vapor and air	$k_{i,g}$	2e-15	
Relative permeability			[14]
Water	$k_{r,w}$	Eq. (5-32)	
Vapor and air	$k_{r,g}$	Eq. (5-33)	
Binary diffusivity(m^2/s)	$D_{eff,g}$	2.6e-6	[14]
Capillary diffusivity (water)	D_c	Eq. (5-30)	[14]

Specific heat capacity($\mathbf{J/(kg \cdot K)}$)			[14]
Water	C_{pw}	Eq. (5-25)	
Solid	C_{ps}	1650	
Vapor	C_{pv}	Eq. (5-26)	
Air	C_{pa}	Eq. (5-27)	
Thermal conductivity($\mathbf{W/(m \cdot K)}$)			[14]
Water	k_w	Eq. (5-28)	
Solid	k_s	0.21	
Vapor	k_v	0.026	
Air	k_a	0.026	
Density($\boldsymbol{kg/m^3}$)			[14]
Water	ρ_w	1000	
Solid	ρ_s	1528	
Vapor	ρ_v	Ideal gas law	
Air	ρ_a	Ideal gas law	
Heat transfer coefficient($W/(m^2 \cdot K)$)	h_t	20	[1]
Mass transfer coefficient(m/s)	h_m	0.008	[1]
Evaporation rate constant(1/s)	K	20	
Latent heat of vaporization(J/kg)	λ	2.26e6	[1]
Vapor pressure(P_a)	p_v	Eq. (5-17)	[1]
Ambient pressure(P_a)	P_{amb}	101325	
Ambient temperature(K)	T_{amb}	299.65	
Initial condition			
Pressure(P_a)	P_0	101325	
Water saturation	S_0	0.95	
Temperature (K)	T_0	299.65	

In the chapter of introduction, the advantages of intermittent heating are talked and several application examples are provided. Therefore, to avoid hot spot and thermal runaway during RF/MW heating, intermittent heating is applied in our simulations to get more homogeneous temperature distribution.

In the simulation, the governing equations are partially coupled. That is: the Maxwell equation is employed to calculate the electric intensity field distribution first, which provide the heat energy. Then the mass conservation equation and heat transfer equation start to function with the calculated heat source to get the new temperature and mass distributions, which will in turn affect the effective permittivity of the researched sample in the Maxwell equation. The same loops are repeated. During the cooling process, the mass and heat conservation equations continue to do the calculation without the RF power.

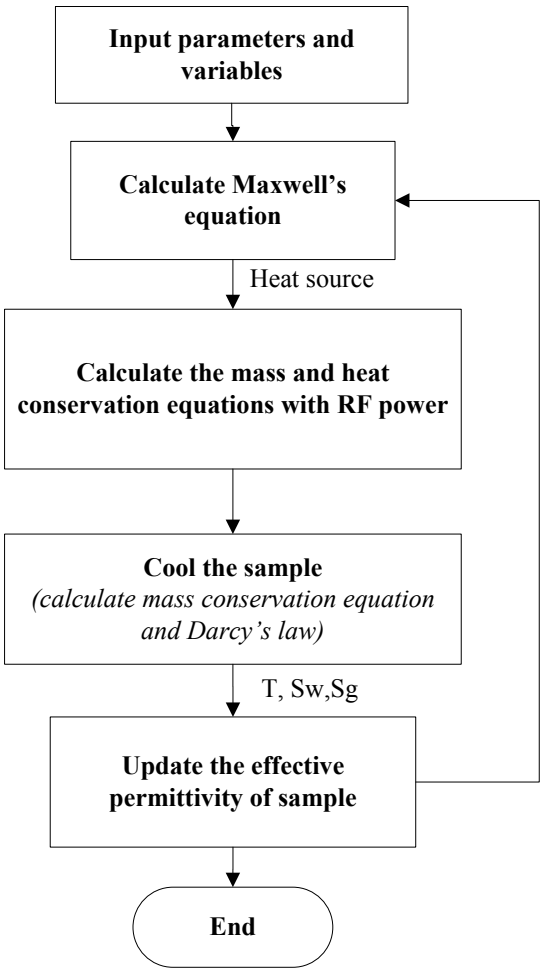


Figure 5.2 Simple flow chart of simulation

It is obvious from the flow chart that the effective permittivity is only updated at the end of each cycle, it is assumed to stay the same during each heating process. To make the update more clearly, a schematic diagram is offered in Figure 5.2. During each processing time Δt, the dielectric property in the sample is treated as constant. It will jump to another constant suddenly according to the temperature and each component's volume fraction after cooling and remains unchanged in the next loop. Therefore, the length of heating time in every loop is

significant for the quality of simulations. If the heating time is too long, then the effective permittivity will change a lot actually, which goes too far away from the assumption in the simulation. It will lead to inaccuracy of the predicted results. On the other side, if the sample is heated for very short time in each process period, there will be a lot of loops in the simulation and it will need more time to finish the experiments.

The dielectric loss at 27.12MHz and moisture in potato are both very high. In order to balance the simulated accuracy and total processing time, the parameters in the model must not change largely but each heating period can't be too short at the same time.

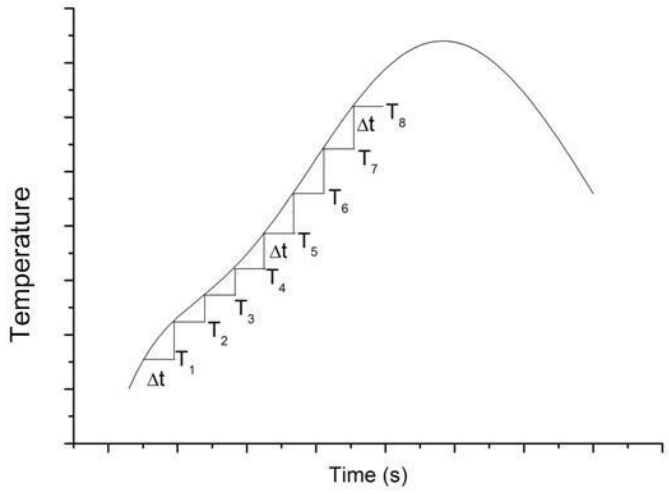


Figure 5.3 Schematic of effective permittivity updation

It is also worth noticing that, as mentioned in the previous chapter, the heated sample must touch both the conductors at the same time under frequency of 27.12MHz. Otherwise, the whole heating equipment will act as an open-ended system. It is difficult to match the heating system to 50 ohm cable, leading to a very low heating efficiency. To show this more directly, three heating simulations are conducted: sample doesn't touch the inner conductor; sample doesn't touch the outer conductor; sample touches both the conductors. All the samples are with height of 5.7 mm and heated for 1min and cooled for 2mins in per cycle by input power of 100W. The initial temperature is 295.15K. One can see that when the sample contacts either of conductors, its temperature increases only a little because tiny part of power is absorbed. Increasing frequency, the heating efficiency increases when the sample only touches one conductor.

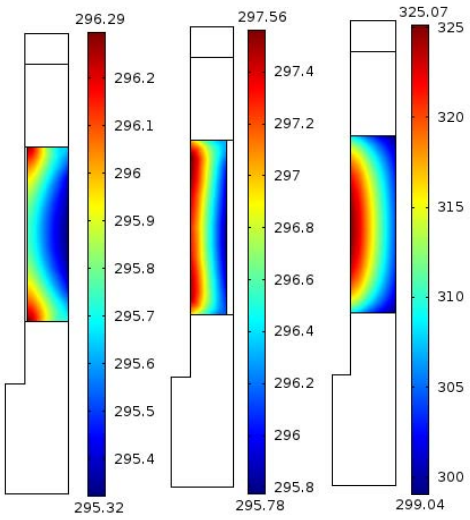


Figure 5.4 Temperature of cross-section after 12th heating: sample doesn't touch inner conductor (left); sample doesn't touch outer conductor (middle); sample touches both conductors (right)

5.4 The experiment

5.4.1 Material and preparation

Potatoes Agata are bought from the market of Jeanne d'Arc in Toulouse. They are stored in the room temperature for more than 24h before doing the experiments. The customized annular equipment shown in Figure 4.9 is again used to cut the samples.

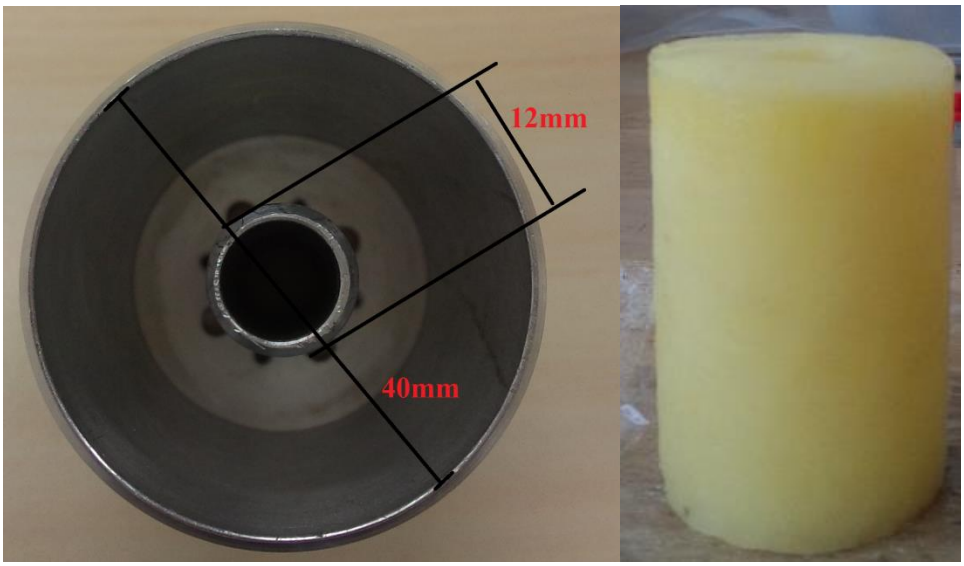


Figure 5.5 Photos of the cutting equipment and cut sample

Potato samples cut by this equipment can be fixed in the coaxial cell very well, even though that the surface of the sample is not perfectly smooth.

5.4.2 The implement of experiment

The schematic of the experiment setup is shown in Figure 5.6. A RF generator functioning at 27.12MHz is used for providing the power. It is easy-controlled but can not provide high power levels. A linear amplifier is employed next to the RF generator to magnify the generated power. A cone connects the coaxial cell and a 50 ohm cable. In order to make sure that most of the power produced by the RF generator is propagated into the cell, an adjustable impedance matching circuit is designed according to the simulated input impedance at different temperatures and moisture contents. It is a Pi type circuit with capacitors and inductors, added between the power source and heating cell to match their impedances during the heating experiments. A power directional coupler is designed with two coupled microstrips and connected before the impedance adaptation circuit to help to match the impedances during the experiments. The incident and reflected powers are also measured by the directional coupler at the same time.

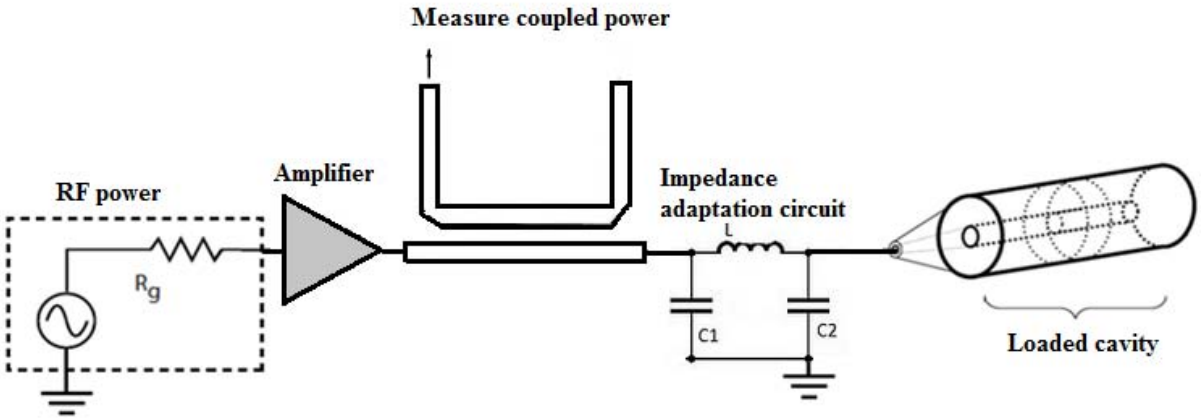


Figure 5.6 Schematic of the experiment setup

After setting up the experiment system, a potato sample is cut with the equipment aforementioned. The samples in all the experiments are placed 20mm upper than the bottom surface of inner conductor. To measure the temperature of certain points, two optical fiber temperature sensors (Polytec) are applied due to their immunity to electromagnetic environment and high accuracy. Both the sensors are inserted into the sample deeply from the side face horizontally to minimize the effect of gravity and avoid slipping or tilting during the process. The coordinates of the two points for measuring temperatures are shown in Figure

5.10. An infrared camera (FLIR) is also used to measure the temperature distribution of sample once stopping the experiment.

A photo of this experiment setup is revealed in Figure 5.7.

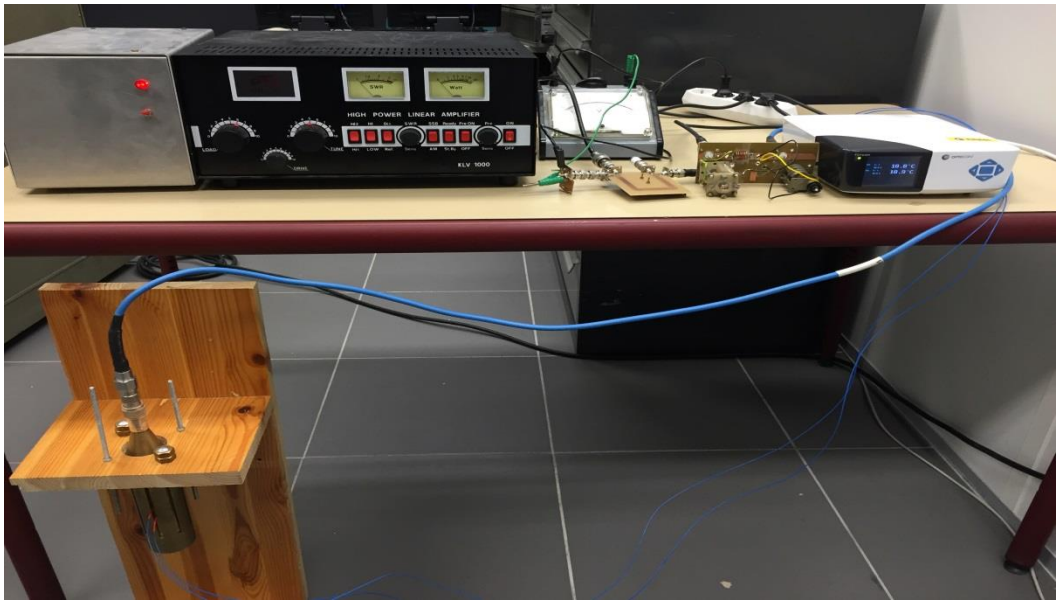


Figure 5.7 Photo of the experiment setup

5.5 Comparison of results and discussion

Before present the simulated and measured results of intermittent heating, a model of potato sample with height of 57mm being continuous heated for 450s by the power of 50W is simulated first. Another model with the same sample being periodically heated for 15 cycles is also conducted. In each time cycle, the sample is heated for 30s by 50W and cooled for 1min 30s. To justify the hypothesis that the intermittent heating is preferable with the same total input energy, their simulated temperature distributions, water contents and moisture losses are analyzed and compared.

5.5.1 Comparison of intermittent and continuous heating effects

From the consequences shown in Figure 5.8, it is clear that with the same total input energy, the intermittent heating can obtain more homogeneous temperature. The difference between the maximum and minimum temperatures in the intermittent heating model is 28℃ while that in the continuous heating model is 31℃. Even though that there is continuous power and the temperature gradient in the sample is larger, one still can observe from Figure 5.9 that less water is evaporated out for the continuous heating model. The reason cause this phenomenon is that the evaporation is restricted not only by the temperature difference but also the sizes of the surfaces through which the convection can

happen. Although the higher temperature can drive more water towards the surfaces, it cannot expel in time and accumulates on the surfaces, leading to the more moist boundaries in the continuous heating model. The water content on the top and bottom surfaces achieves 849.33 mol/m^3 and 819.44 mol/m^3 for the inner surface (the initial water content is 844 mol/m^3) while those in the intermittent heating model are 844.28 mol/m^3 and 805.41 mol/m^3.

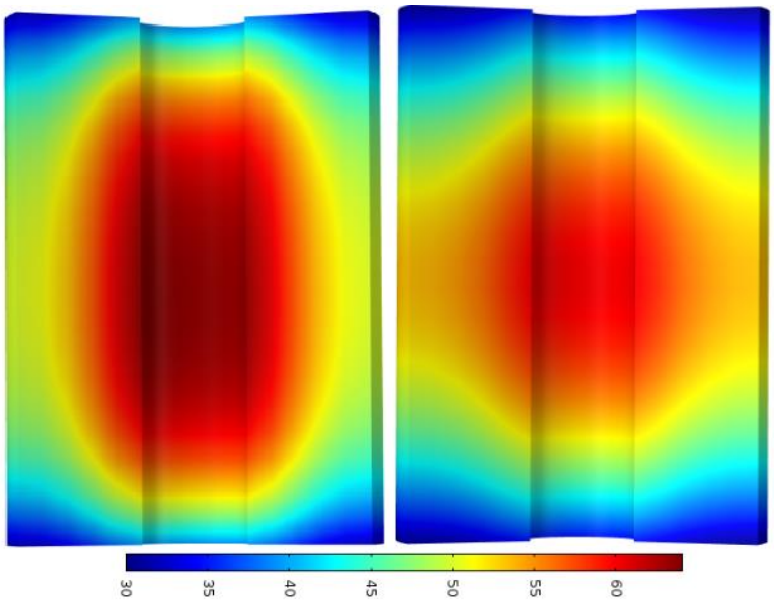


Figure 5.8 Temperature (℃) distributions of inner surface after processing with the same energy: (left) continuous heating; (right) intermittent heating

To make the drying effect more clearly, the changes of average water content and the moisture losses for the continuous and intermittent heating models are listed in Table 5-2.

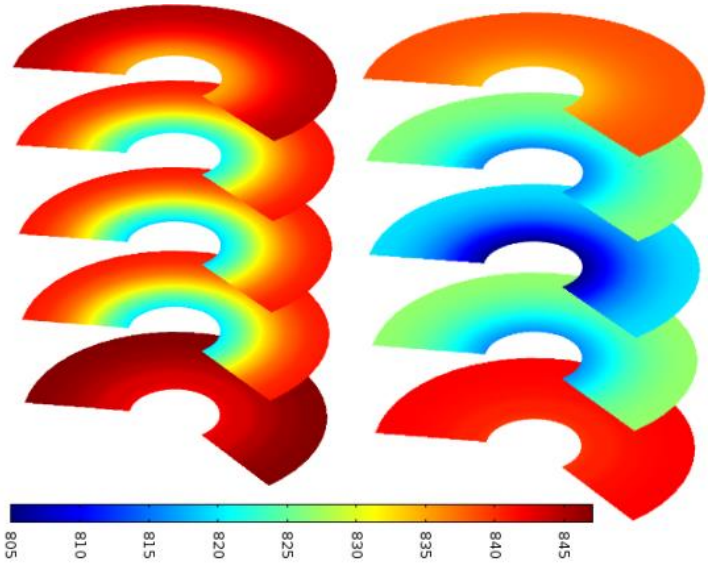


Figure 5.9 Water content (mol/m^3) distributions of inner surface after processing with the same energy: (a) continuous heating; (b) intermittent heating

Table 5-2. Comparison of water content changes and moisture losses for continuous and intermittent heating

Parameters	Intermittent heating	Continuous heating
Change of water content (mol/m^3)	18.76	7.15
Moisture loss (1)	0.11091	0.04333

The table shows evidently that consuming the same energy, intermittent heating model can obtain 160% more moisture loss than continuous heating. In summary, intermittent heating is preferable than continuous heating with the same total energy.

Besides the intermittent heating case presented above, other cases are also studied and analyzed to research the effects of different process periods, variations of heights of samples and power changes on the temperature distributions. The corresponding experiments are also conducted to measure the temperature changes during the heating process. The simulated and measured results are compared in this section. All the experiments in each case are repeated twice. Unfortunately, our balance can't take the weight of sample during the heating process because the sample has to contact both the conductors of the coaxial cell. We don't have the equipment to detect the change of pressures inside the heated potato. Therefore, the information of measured moisture content and pressure change during the process cannot be provided. The rationality of simulated moisture content and pressures, however, still can be addressed.

5.5.2 Comparison of temperature profiles of intermittent heating

Case 1: sample with height of 57mm, being heated 30s and cooled 1min 30s per cycle. The pure input power is 50w.

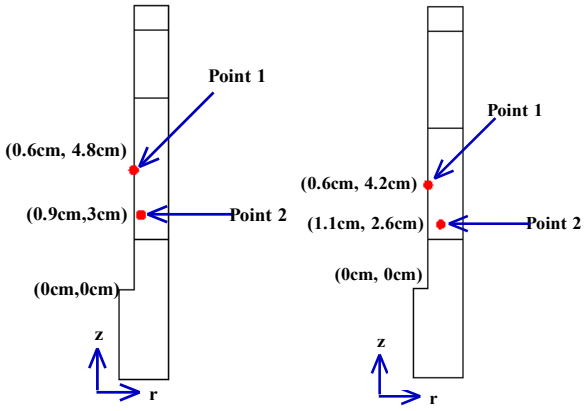


Figure 5.10 Positions of two points for measuring temperature: height of sample is 57mm (left); height of sample is 45mm (right)

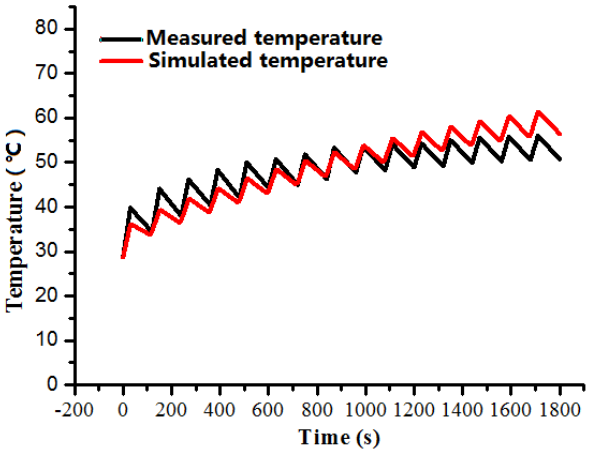


Figure 5.11 Temperature changes of point 1

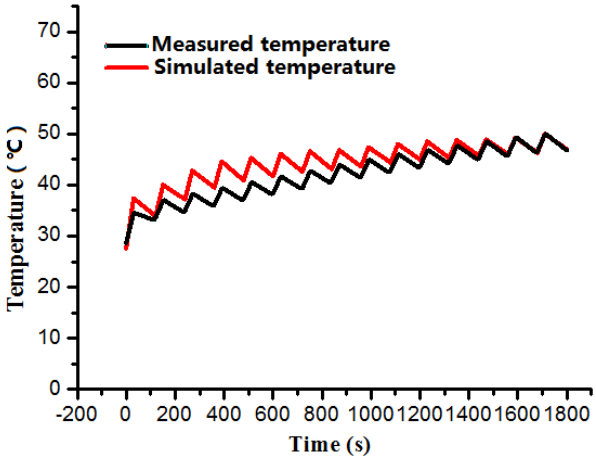


Figure 5.12 Temperature changes of point 2

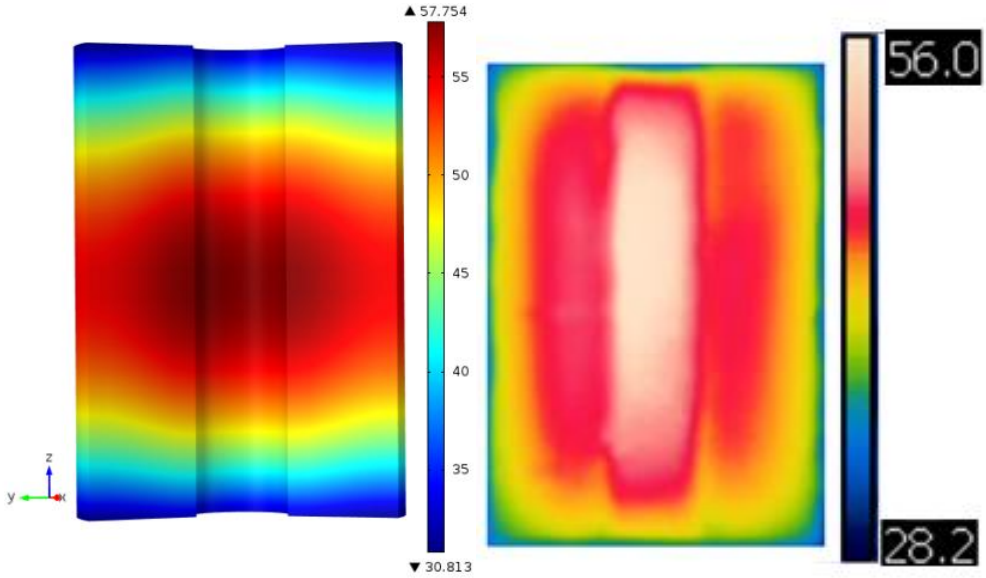


Figure 5.13 Comparison of temperatures of sample after processing 15 cycles (inside)

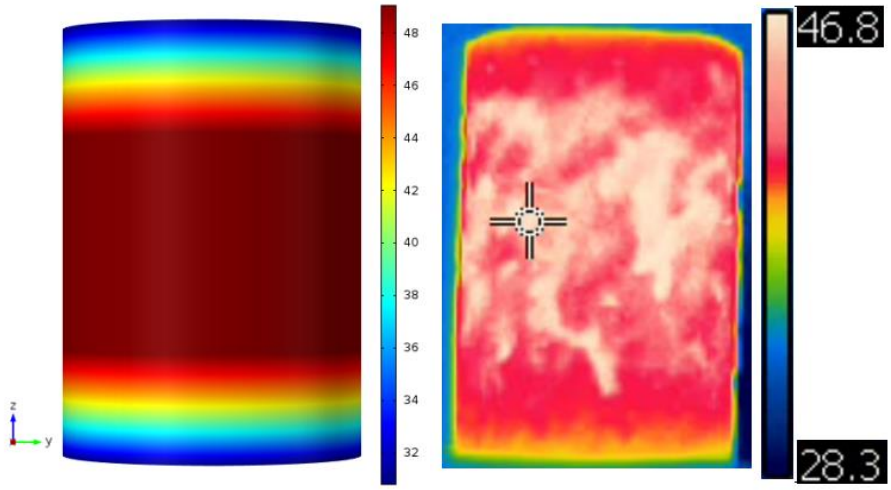


Figure 5.14 Comparison of temperatures of sample after processing 15 cycles (outside surface)

From the Figures 5.11, 5.12, it is observed that all the experimental results compare qualitatively with the simulated consequences. The cycling of radio frequency is clearly observed from the wavy nature of computed temperature. There has been papers reported the same change tendency under periodic microwave heating [21]. As shown in the figures, the temperature increases rapidly for about 30 seconds and then decays down for the next 1 min 30s due to thermal diffusion in each cycle.

The temperature climbs sharply for the first several heating cycles, then as time passing, the amplitude of augment reduces slowly. The higher temperature in our experiments approximately trend to be stable: the temperature in each case ends as changing in the similar range during the last cycles. This phenomenon is more evident for the temperature of point 1. That reason caused this phenomenon is that the moisture contents of the samples are highest at the beginning, which leads to the better absorption of RF power. The energy absorbed is much larger than that took away by the evaporation. After several heating cycles, more moisture is lost and the effective permittivity of sample decreases. The high temperature at that time contributes the stronger evaporation, which makes a smaller temperature increasing. Later, when the effective permittivity is further smaller and temperature higher, the intake of power is almost equal to that needed for evaporation during each cycle, resulting in only tiny temperature increase.

For the surface temperature distribution revealed in Figures 5.13 and 5.14, the simulated results are very close to the measured ones, with similar maximum and minimum temperature values. Obviously, the temperature near the inner boundary of coaxial cell is much higher than that near outer boundary, which corresponds to the theory that the electric intensity of coaxial structure declines with the distance from inner boundary. From the middle part to top and bottom surfaces, the temperature decreases. The outside surface has the similar temperature distribution. Because the vapor is evaporated through the upper and bottom surface, their temperatures are lowest. The temperature of heated sample is relatively homogeneous, with 28 degrees of difference between maximum and minimum temperatures.

To further check that if heating 30s in each cycle is too long and that this will import more difference between the simulated and measured results or not, other sets of experiments are done with the same height of sample and heated power but with different process cycle.

Case 2: sample with height of 57mm, being heated 15s and cooled 45s per cycle. The pure input power is 50w.

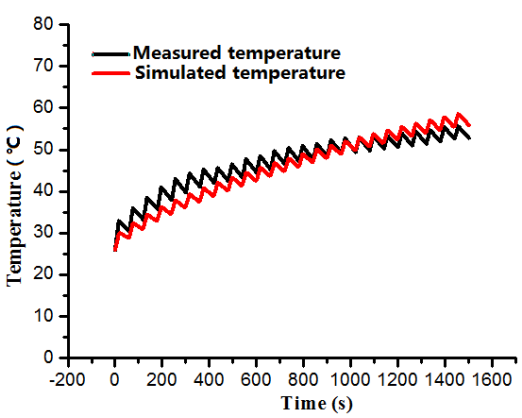


Figure 5.15 Temperature changes of point 1

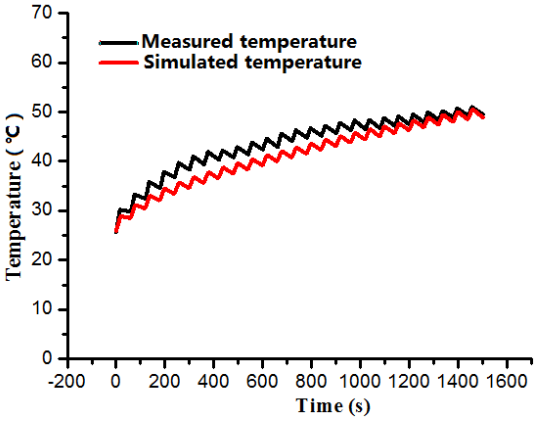


Figure 5.16 Temperature changes of point 2

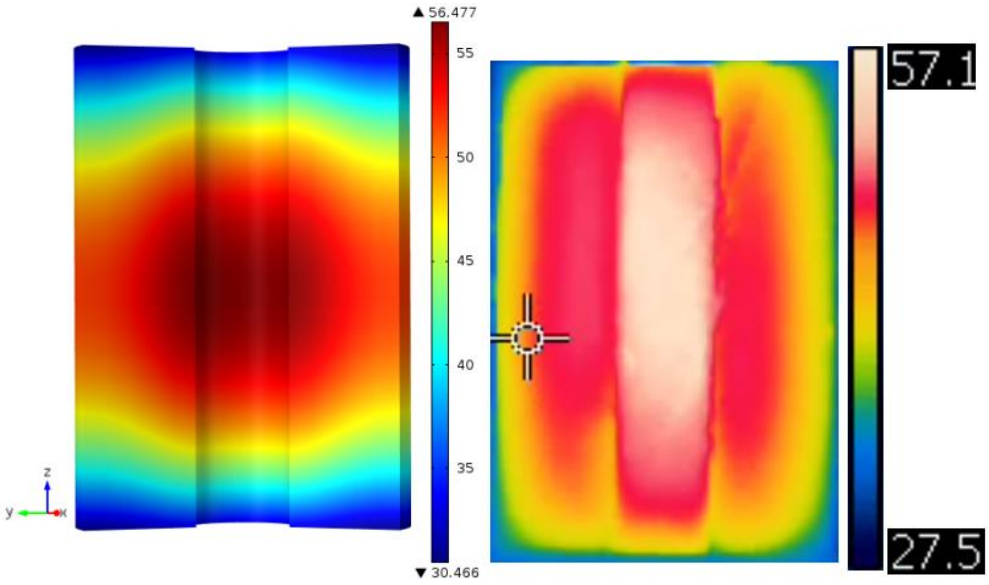


Figure 5.17 Comparison of temperatures of sample after processing 25 cycles (inside)

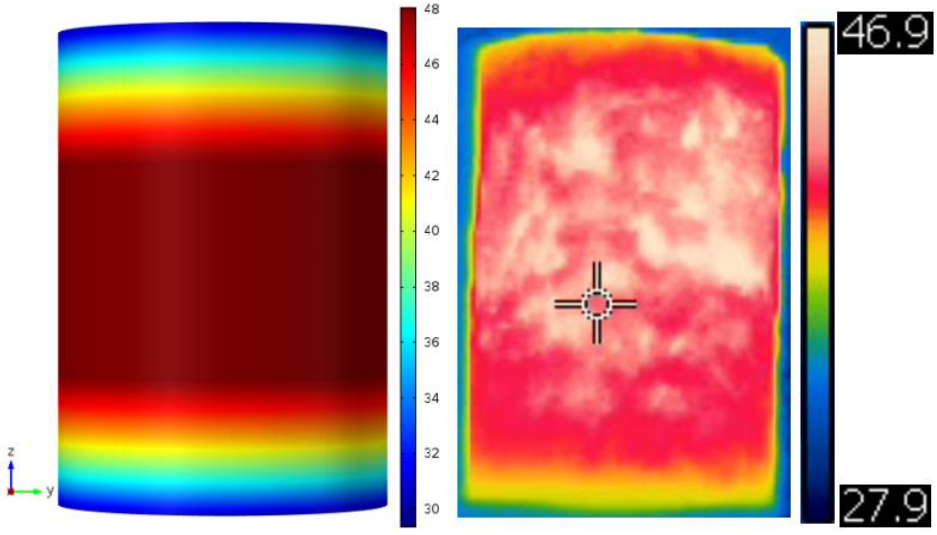


Figure 5.18 Comparison of temperatures of sample after processing 25 cycles (side surface)

Again, the experimental consequences are also close to each other. With the sample size and power but double shortening the time of each process cycle, we can observe that the temperature tendency as well as distribution in case 2 is similar to those of case 1. The point temperatures climb quickly at first, then the curves turn to be gentle after the temperature reaching about 53 degrees which is the same temperature value as in case1. It is also observed that the temperature in the end of each cycle of case 1 is similar to that of case 2, which indicates that assuming the effective permittivity of sample as a constant and sample being heated for 30s in each cycle is accepted for power of 50w. This may be still valid for lower powers and shorter samples.

For the two cases of experiments above, we can see that the enhancement of temperature declines as time increases. It is hard to get higher temperature. To research the effect of power on the temperature distribution and the behaviors of sample under higher temperatures, we decide to enlarge the inserted power.

Case 3: sample with height of 57mm, being heated 15s and cooled 45s per cycle. The pure input power is 100w.

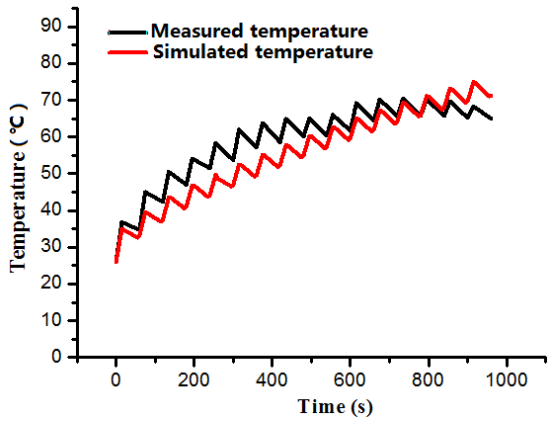


Figure 5.19 Temperature changes of point 1

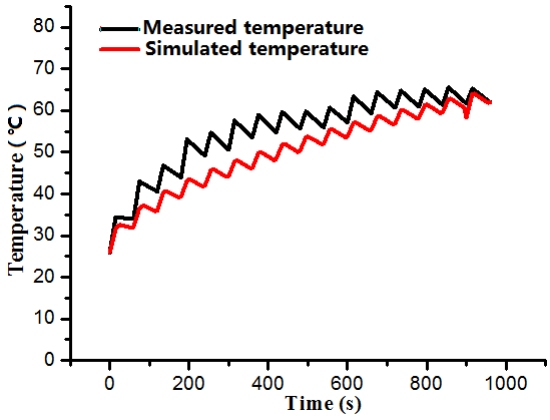


Figure 5.20 Temperature changes of point 2

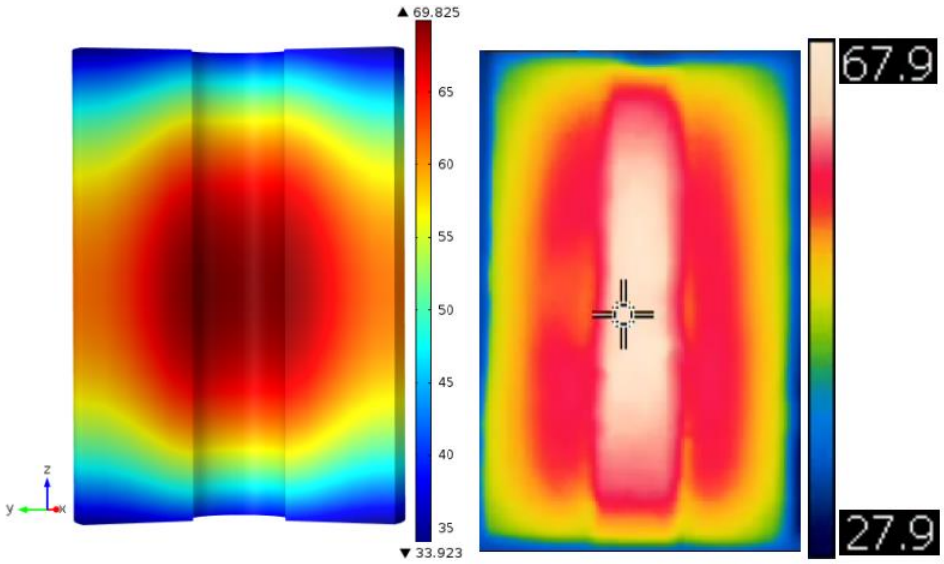


Figure 5.21 Comparison of temperatures of sample after processing 16 cycles (inside)

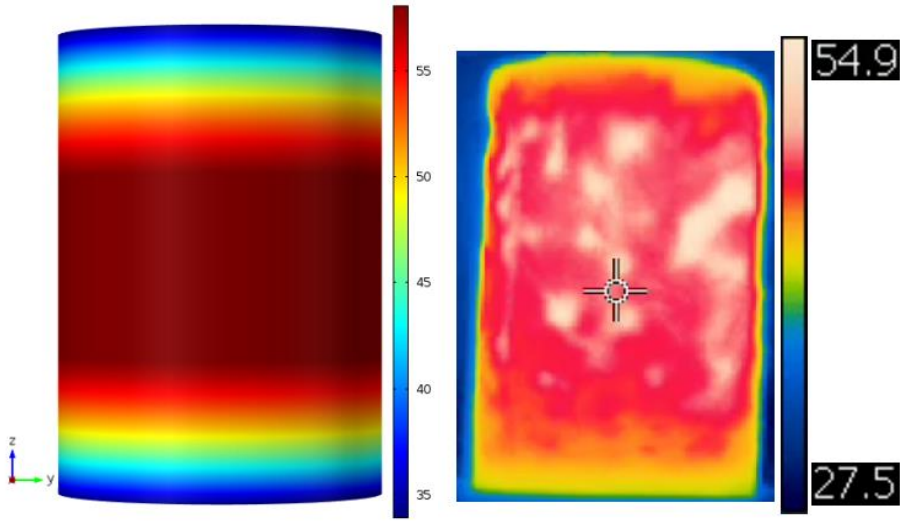


Figure 5.22 Comparison of temperatures of sample after processing 16 cycles (side surface)

It is clear that the temperatures in this case increase more sharply than those in case 1 and 2. However, the temperature change tendencies and distributions are the same. Figure 5.19 shows evidently that the augment of highest temperature becomes tiny when it reaches around 70 degrees. After being stable for 4 cycles, the temperature begins to decrease. Experiment is stopped. We find that the sample part near inner conductor is transformed. It becomes soft and very sticky, as shown in the picture below. To reveal the transformation more clearly, another periodically heated sample but without degeneration is posed as a comparison. Since the material is changed, the simulated model is not valid any more.

To further research the relation between temperature and transformation, experiments of samples being persistently heated are also conducted. It is found that the samples start to transform when their temperatures reach between 70 to74 degrees.

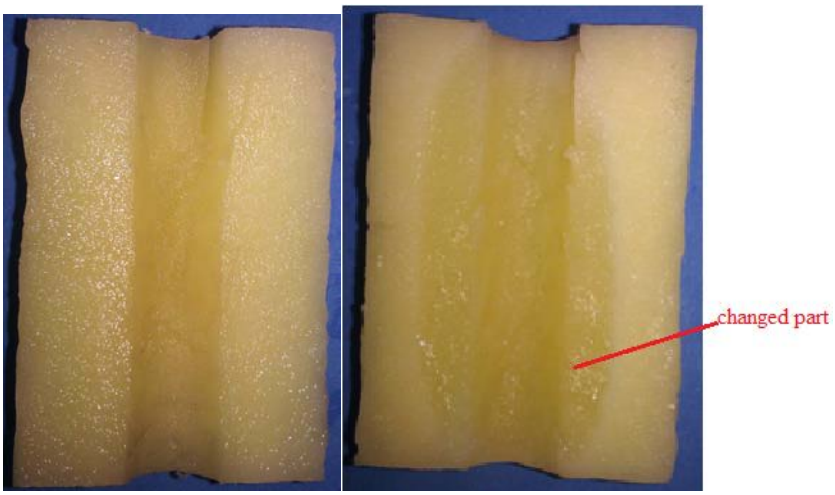


Figure 5.23 Samples without (left) and with (right) transformation

Comparing the simulated results in case 2 and case 3, double enlarging the input power, the increase of temperature of case 3 in each cycle is about twice as that in case 2. After processing for 16 cycles, the highest temperature for case 2 is 49.15 degrees, while that of case 1 is 71.2 degrees. The minimum temperatures for the two samples, however, are respectively about 29 and 33 degrees. Therefore, a 91% larger difference between the maximum and minimum temperatures is encountered for case 3.

The experiments with samples of different heights are done next to study the effect of change of height on temperatures. The samples are placed at the same location as those mentioned before. Two points are picked to measure the temperature change during the heating experiments and their coordinates are shown in Figure 5.10.

Case 4: sample with height of 47mm, being heated 15s and cooled 45s per cycle. The pure input power is 50w.

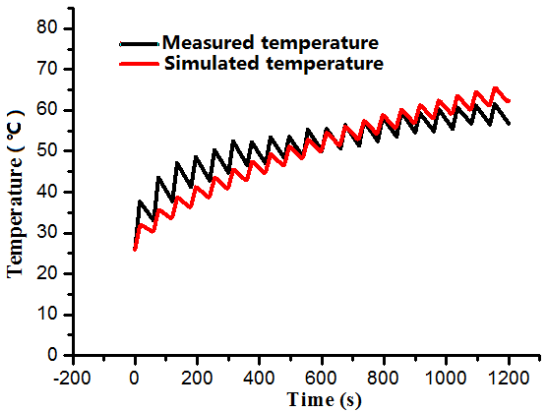


Figure 5.24 Temperature changes of point 1

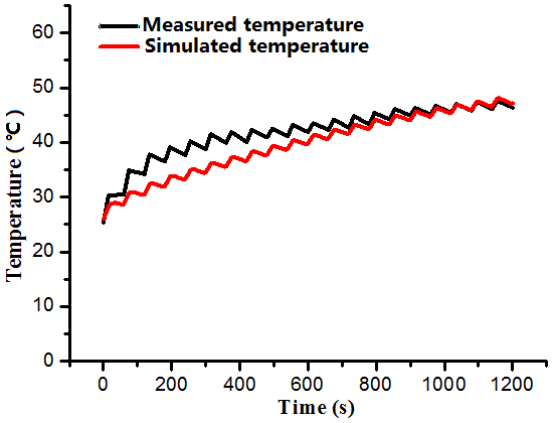


Figure 5.25 Temperature changes of point 2

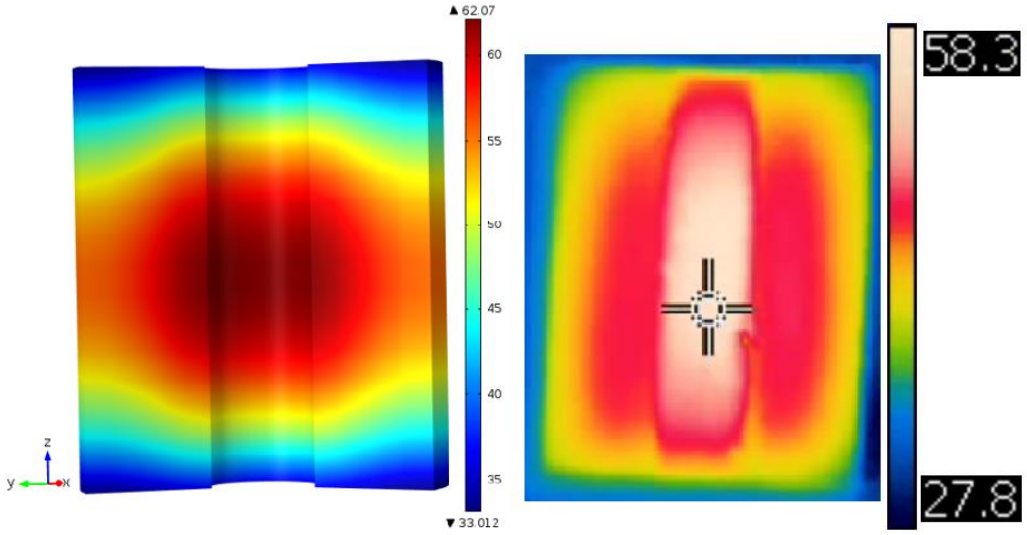


Figure 5.26 Comparison of temperatures of sample after processing 20 cycles (inside)

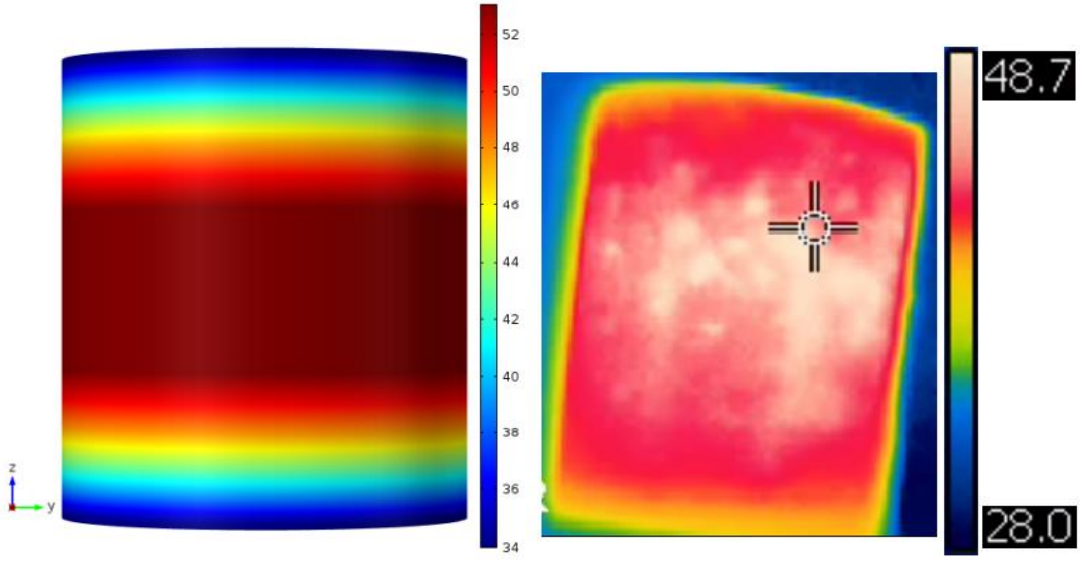


Figure 5.27 Comparison of temperatures of sample after processing 20 cycles (side surface)

Still, the simulated temperature changes agree very well with the measured ones. So do the temperature distributions of surfaces. For all the four cases, one can see that all the measured results compare qualitatively with the simulated consequences, given the complexity of experiments.

Meanwhile, we also notice that there still exist some discrepancies between the observed and predicted temperatures. Several factors may be responsible for the differences: 1) the effective permittivity of the simulated model are changed as steps, while in reality it changes all the time like a smooth curve; 2) several assumptions are utilized for the simulation which do not valid in reality; 3) the generated power is not perfectly fixed, which is shown evidently in the point temperature changes in case 3. The power is a little larger than the expected one, leading to lager difference between the simulated and measured temperatures; 4) in the simulation, the surface of the sample is ideally smooth, which can not be achieved in the experiments; 5) uncertainty and equipment errors may be imported during the experiments; 6) the probe may be slightly displaced from its initial location due to large pressure gradients that develop as heating proceeds; 7) last but not least, it takes decades of seconds to take the sample out of the cell and photograph the temperature distribution. During this time, the convective motion continues and makes the temperature distribution more uniform.

5.5.3 Simulated pressure tendency

With the model validated for temperature, to further analyze the interaction of radio frequency and porous media, the simulated pressure of point 1, average moisture content and their distributions during processing for the four cases are revealed here.

Case 1:

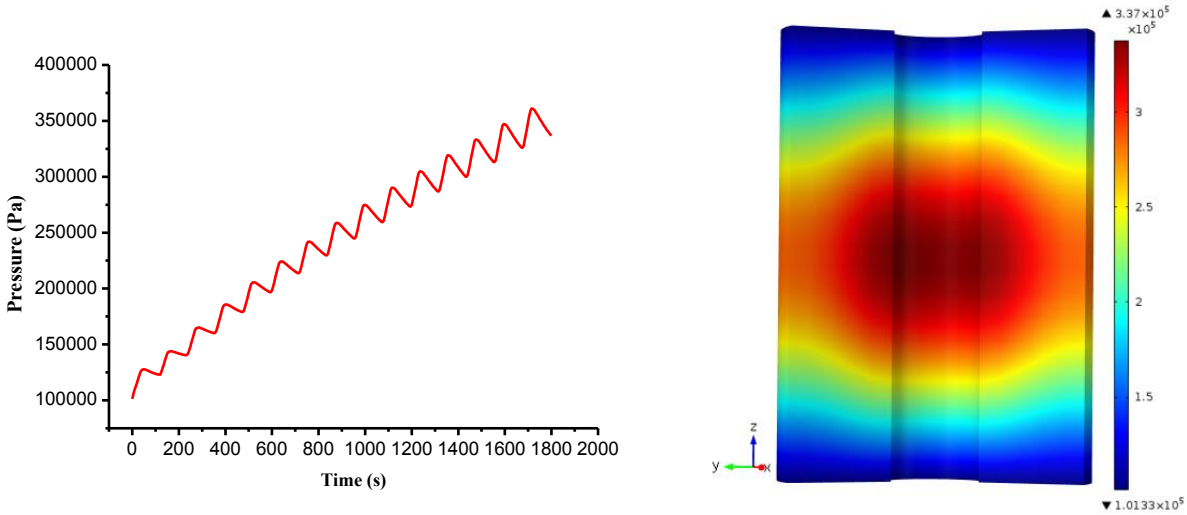


Figure 5.28 Pressure change of point 1(left) and distribution (right) after processing 15 cycles

Case 2:

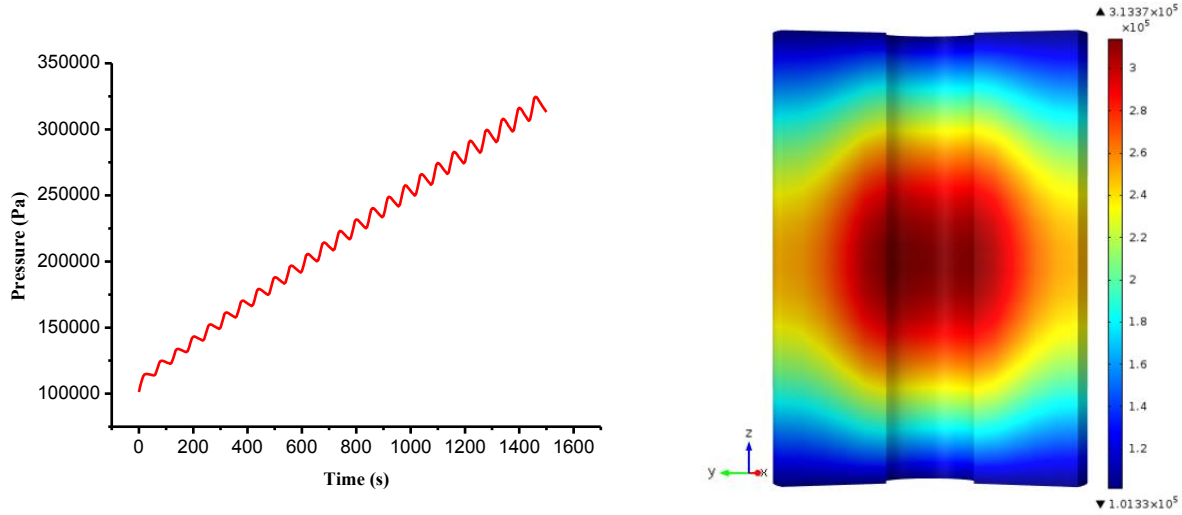


Figure 5.29 Pressure change of point 1(left) and distribution (right) after processing 25 cycles

Case 3:

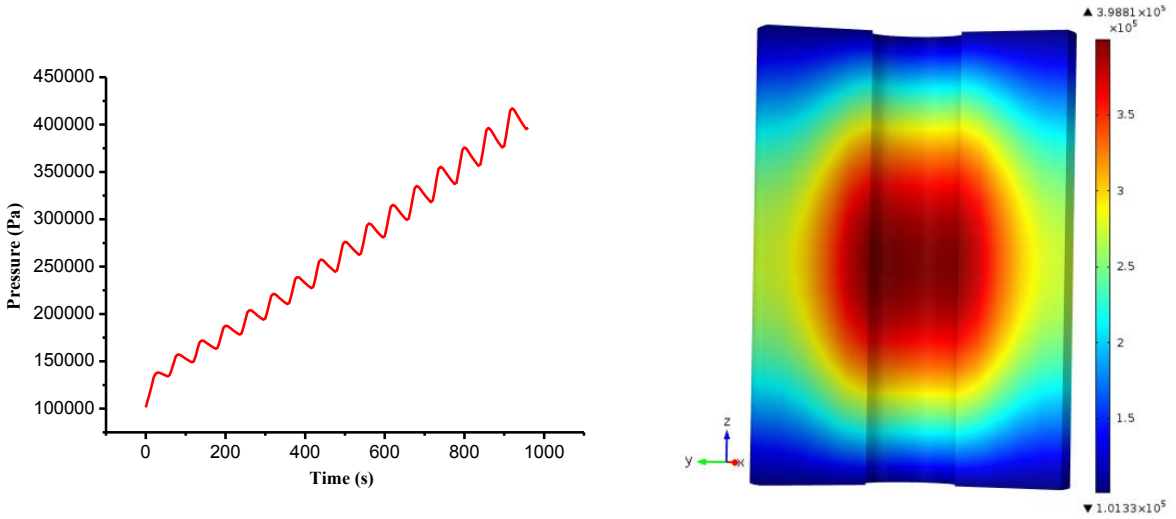


Figure 5.30 Pressure change of point 1(left) and distribution (right) after processing 16 cycles

Case 4:

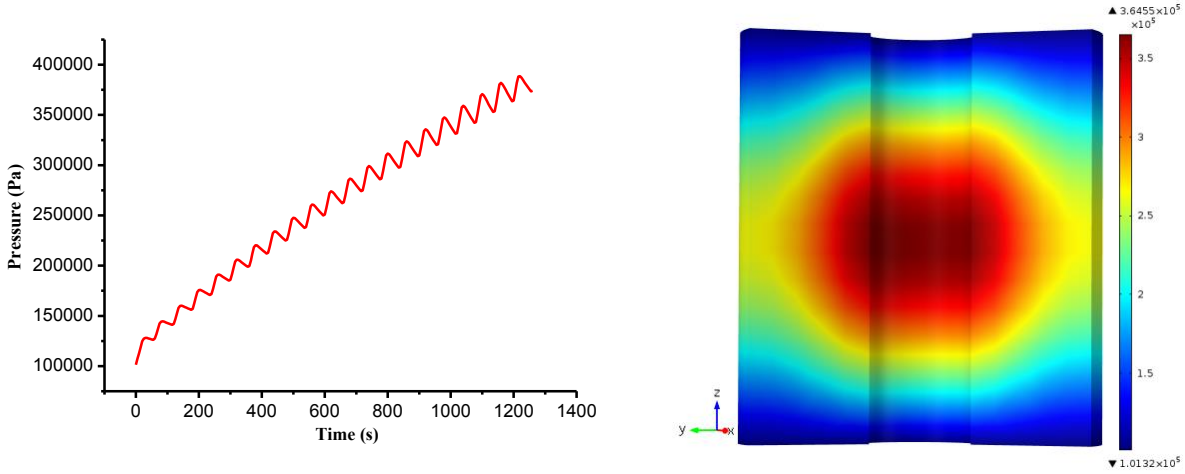


Figure 5.31 Pressure change of point 1(left) and distribution (right) after processing 20 cycles

From the curve graphs of Figure 5.28 to Figure 5.31, the cycling heating is obviously shown by the wavy curve of the point pressure for all the four cases. Because point 1 is near the inner conductor of the heating cell, the electric intensity is very strong there, leading to sharp increase of temperature. The high temperature gradient urges a lot of liquid to evaporate into vapor, arising the pressure of interior of heated sample. For the first several cycles, when the power is stopped, the convection with ambient environment cools the sample, along with the decline of pressure. However, the decreasing amplitude is relatively small because the generated vapor cannot be expelled quickly enough. Therefore, it is clear that the increasing magnitude of pressure at the first several cycles is larger comparing to the decreasing one

during cooling at the same process period. As time increasing, the wavy phenomenon is more obvious due to the vapor can be convected easier.

For the pressure distributions, they are all similar to their corresponding temperature distributions which are relatively homogeneous. The pressures around the inner center of the sample are higher. From the center to the side face, pressure deduces gently since the side face is set as isolated. The change of pressure between the center and top and bottom surfaces are much larger due to the gas only can convect out through the top and bottom surfaces and their pressures are both treated as the ambient pressure.

Comparing the pressures of all the cases, one can find that the pressure is higher if the input power is larger or sample is shorter. But the change of pressure is not proportional to that of power or sample height. Take case 2 and 3 for example, double the input power, the pressure of the sample just increases a little. Further information about the parameters relative to the pressure of the sample will be presented in next chapter.

In order to show the strong relation between temperature and pressure moreover, the distributions of temperature and pressure at different 5 cross-sections along z-axis are presented and compared for each case (Figure 5.32 to Figure 5.35). For case 1 to case 3, the coordinates of the cross-sections are respectively 2.2cm, 3.5cm, 4.8cm, 6.1cm and 7.2cm. Since the sample in case 4 is shorter, another set of coordinates is taken: 2.2cm, 3.2cm, 4.2cm, 5.2cm and 6.2cm. The cross-sectional distributions show clearer that temperature and pressure of each section is very uniform. The more the cross-section is close to the top or bottom surface, the more uniform the temperature or pressure distribution is. The temperature distributions of all the sections resemble their pressure distributions, just like the surfaces, which is expected according to the theory and the 1D model.

Case 1:

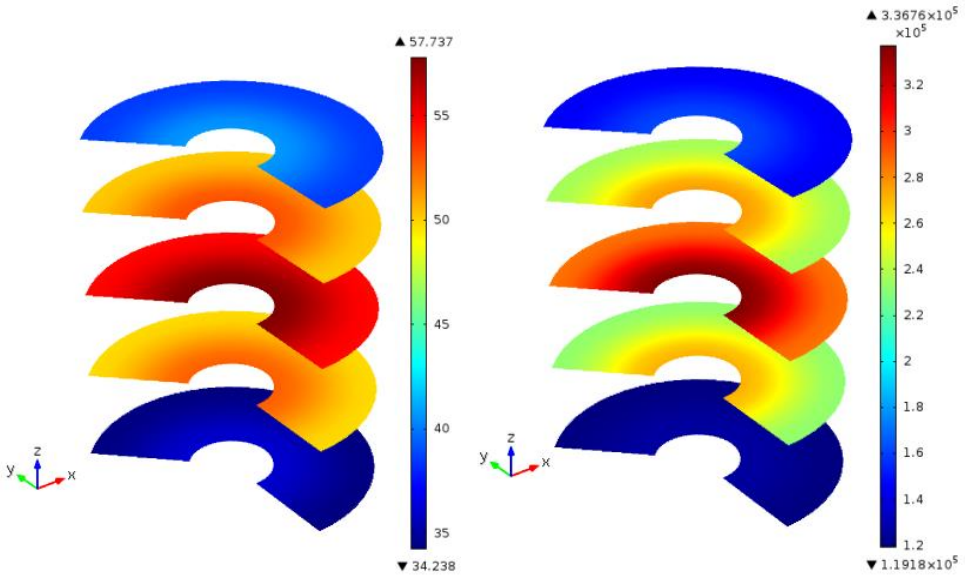


Figure 5.32 Cross-sectional distribution of temperature (left) and pressure (right) after processing 15 cycles

Case 2:

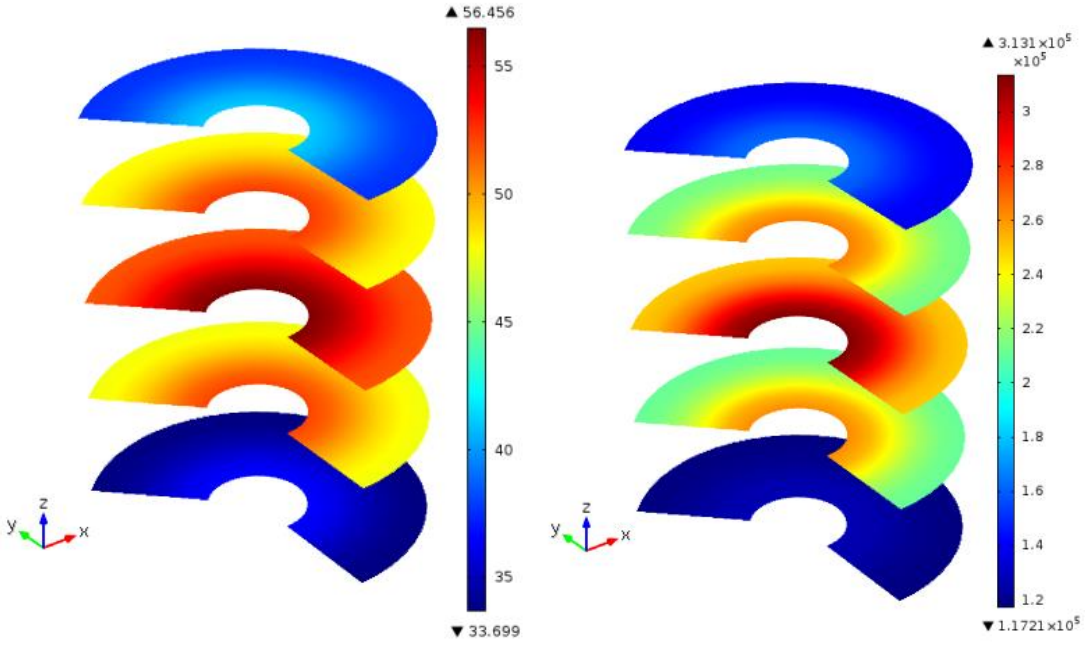


Figure 5.33 Cross-sectional distribution of temperature (left) and pressure (right) after processing 25 cycles

Case 3:

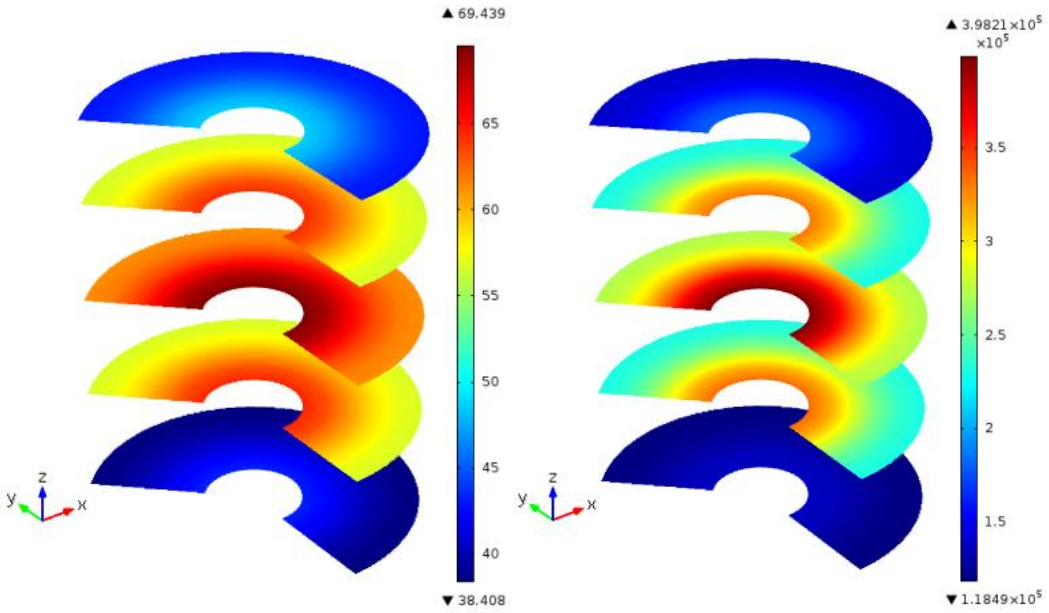


Figure 5.34 Cross-sectional distribution of temperature (left) and pressure (right) after processing 16 cycles

Case 4:

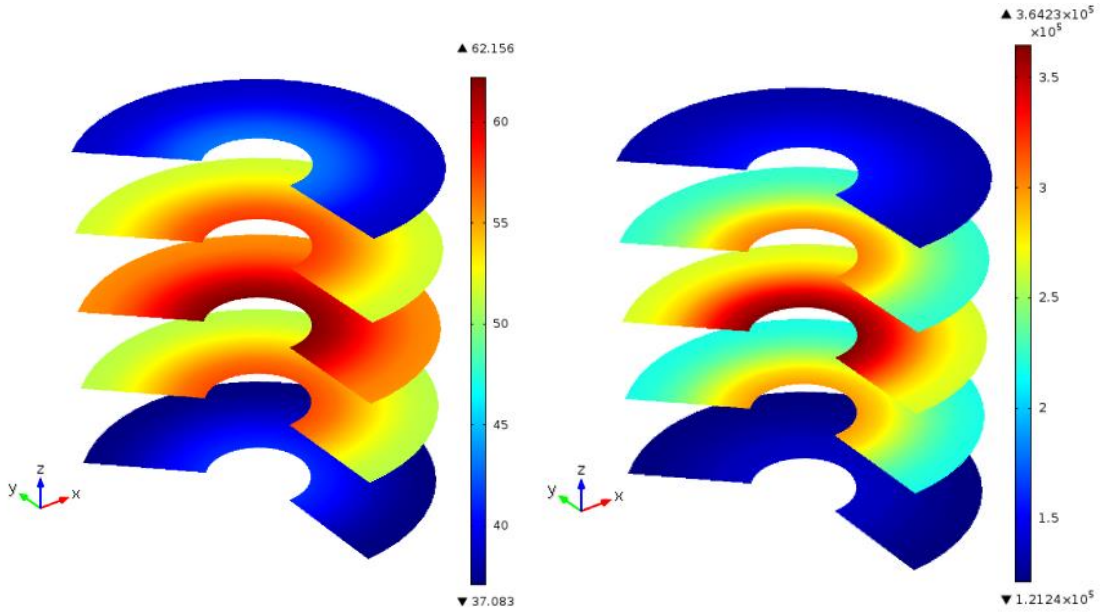


Figure 5.35 Cross-sectional distribution of temperature (left) and pressure (right) after processing 20 cycles

5.5.4 Simulated of moisture profiles

Case1:

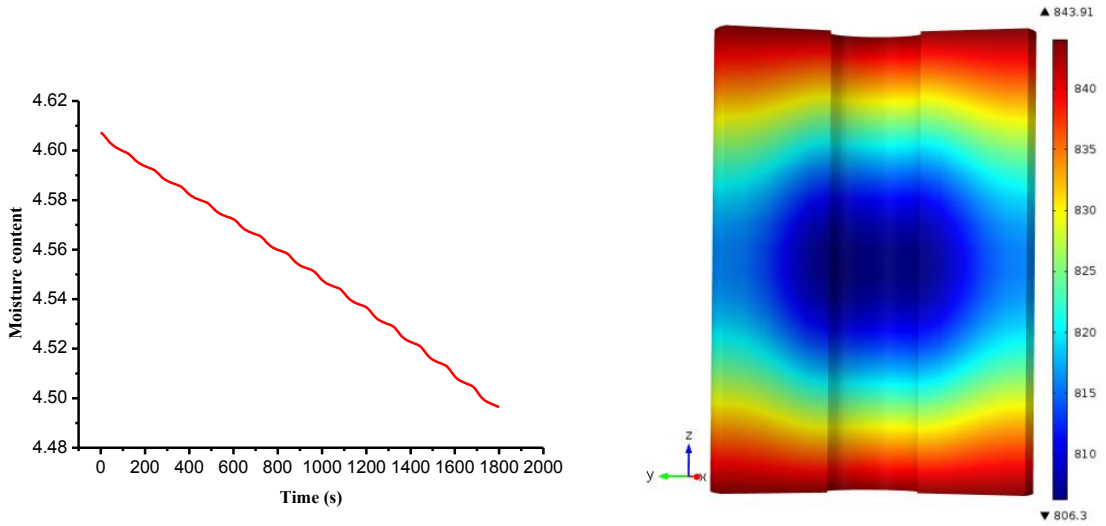


Figure 5.36 Average moisture content (left) and distribution (right) after processing 15 cycles

Case 2 :

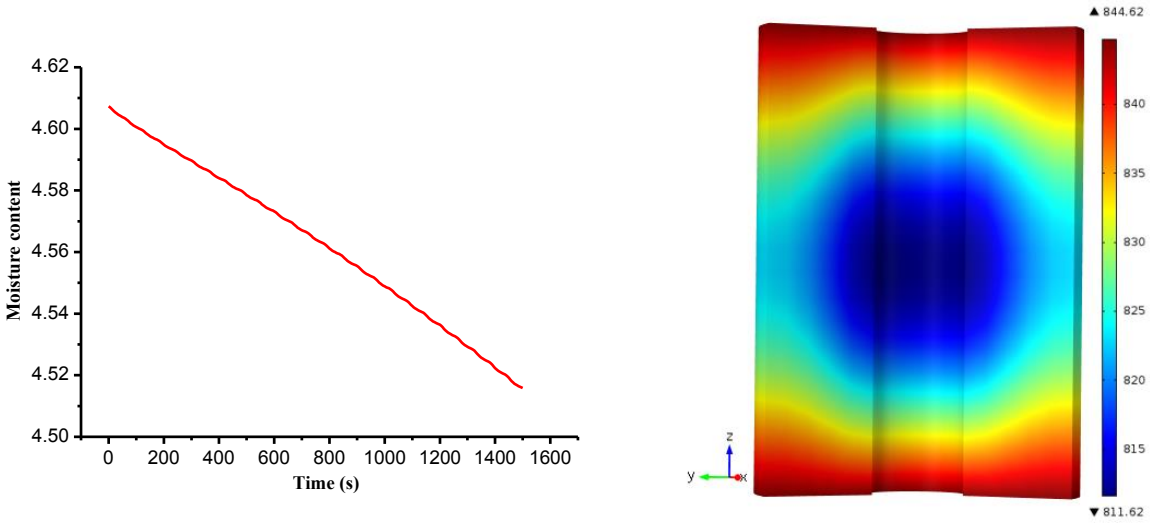


Figure 5.37 Average moisture content (left) and distribution (right) after processing 25 cycles

Case 3:

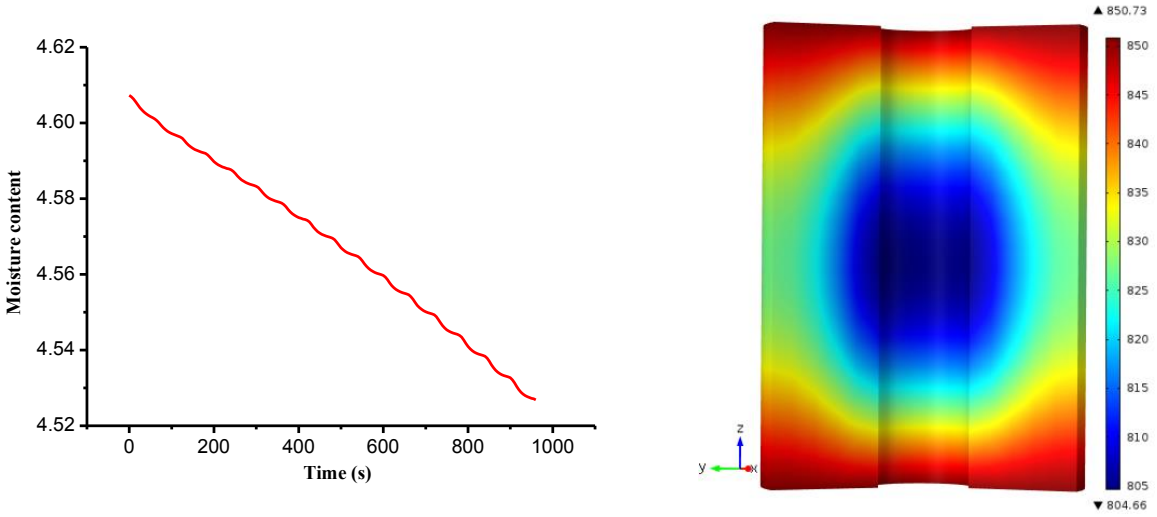


Figure 5.38Average moisture content (left) and distribution (right) after processing 16 cycles

Case 4 :

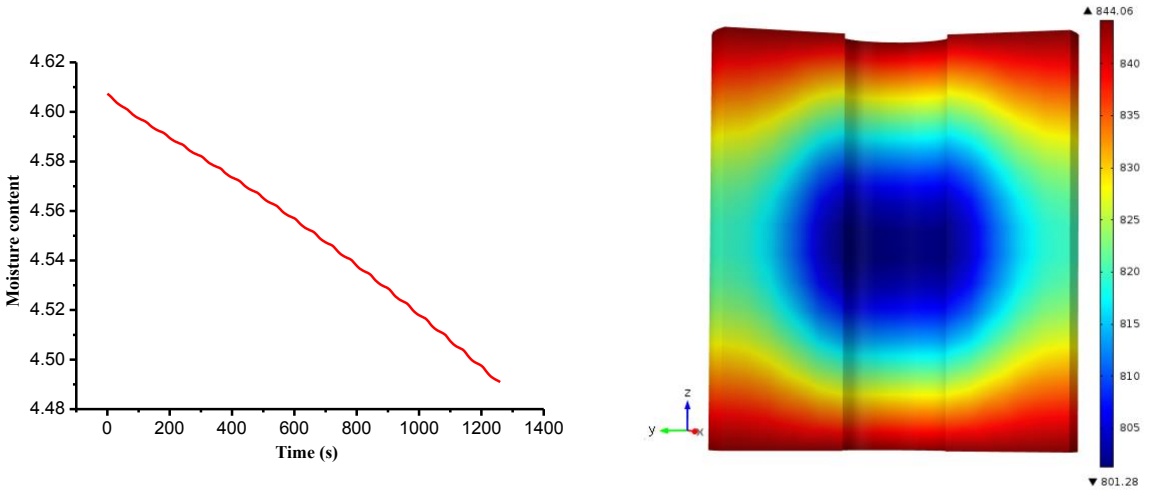


Figure 5.39 Average moisture content (left) and distribution (right) after processing 20 cycles

The average moisture contents of samples during heating and surface moisture distributions after processing are provided above from Figure 5.36 to 5.39. We can see that the curves indicating the change of average moisture content is rough. That is because the sample absorbed large quantities of RF power at the beginning of the heating, both the RF energy and convection work to dry the sample, leading to a larger loss of moisture. However, when the power is turned off, only convection still functions. Therefore, the moisture loses gently during cooling. As time goes on, the sample loses more and more moisture and its ability to absorb RF power declines. The moisture losses in the next periods also decrease. Thus, the

slopes of curve during each heating or cooling process are different from each other, which makes the whole curve not smooth but a little wavy. However, the fluctuant phenomenon is not obvious because the whole moisture loss during the heating process is too small and each processing time is too short.

For the moisture distributions, they are all opposite to their corresponding temperature and pressure distributions which are relatively homogeneous. According to the analysis aforementioned, the temperature and pressure are strongest around the inner center of samples. The great gradient of temperature and pressure push the vapor towards exterior of the samples. Therefore, the moisture contents around the inner center of the sample are the smallest. From the center to the side face, moisture content increases gently since side face is set as isolated and its temperature and pressure gradients are just a little smaller. Its moisture is also drive to the top or bottom due to they directly contact the ambient air. Thus, the change of moisture content between the center and top or bottom surface is much larger. It is also worth noticing that the moisture content at the top and bottom surfaces are larger than the original values. That is because the temperature and pressure at the top and bottom surfaces are not very large comparing to those of the ambient air, the convection between these two surfaces and ambient environment is very weak. The moisture driven from the other part of the sample cannot be expelled quickly enough and accumulates at these two surfaces.

The moisture content changes during the whole process of the four cases are also simply compared here. One can find that the moisture content loss is larger if the input power is larger or sample is shorter for the same processing time. But the change of moisture content is not proportional to that of power or sample height. Take case 2 and 3 for example, double the input power, the moisture content loss of the sample after processed for 960s (the whole processing time of case 3) just increases a little. Further information about the parameters relative to the moisture content of the sample will be also presented in next chapter.

5.6 Conclusion

In this chapter, a 2D axis-symmetric model of RF heating porous media is simulated under four different conditions. Corresponding experiments are also conducted and temperature changes in the samples are measured. All the simulated temperature distributions are homogeneous and very close to their corresponding experiment results, which indicates the accuracy of these models. However, when the temperature reaches about 70 -- 74 degrees, the

potato samples transform, making the simulation model invalid. Therefore, these models can only predict well the temperature of potatoes Agata under RF heating before the temperature reaches 70 degrees.

Unfortunately, the pressure change and moisture loss during the heating process cannot be measured. However, their simulated distributions are reasonable comparing to their corresponding temperature distributions. Their accuracies are theoretically addressed.

Reference of chapter

[1] Vineet Rakesh and Ashim K. Datta, Jeffrey H. Walton, Kathryn L. McCarthy and Michael J. McCarthy, "Microwave combination heating: coupled electromagnetics-multiphase porous media modeling and MRI experimentation," *AIChE Journal*, vol.58, no.4, pp.1262-1278, 2012.

[2] Crapsite, G.H.; Whitaker, S.; Rotstein, E. "Drying of cellular material-i a mass transfer theory," *Chemical Engineering Science*, vol.43, no.11, pp.2919–2928,1988.

[3] Ni, H.; Datta, K.A.; Torrance, K.E., "Moisture transport in intensive microwave heating of biomaterials: A multiphase porous media model," *Int. J. of Heat Mass Transfer*, vol.42, pp.1501–1512, 1999.

[4] Plumb, O.A.; Spolek, G.A.; Olmstead, B.A, "Heat and mass transfer in wood during drying," *Int. J. Heat Mass Transfer*, vol.28, no.9, pp.1669–1678, 1985.

[5] Stanish, M.A.; Schajer, G.S.; Kayihan, F. "A mathematical model of drying for hygroscopic porous media," *AIChE Journal*, vol.32, no.8, pp.1301–1311, 1986.

[6] H. Ni, A.K. Datta, K.E. Torrance, "Moisture transport in intensive microwave heating of biomaterials: a multiphase porous media model," *Int. J. Heat Mass Transfer*, vol.42, pp.1501-1512, 1999.

[7] Ratti, C., Crapiste, G.H. and Rotstein, E., "A new water sorption equilibrium expression for solid foods based on thermodynamic considerations," *J Food Sci*, vol.54, no.3, pp.738, 1989.

[8] Fang, G. and Ward, C.A., "Examination of the statistical rate theory expression for liquid evaporation rates," *Physical Review E*, vol.59, no.1, pp. 441–453, 1999.

[9] Minkowycz, W.J., Haji-Sheikh, A. and Vafai, K., "On departure from local thermal equilibrium in porous media due to a rapidly changing heat source: the Sparrow number," *Int. J. Heat Mass Transfer*, vol.42, no.18, pp. 3373–3385, 1999.

[10] Fang, G. and Ward, C.A., "Temperature measured close to the interface of an evaporating liquid," *Physical Review E*, vol.59, no.1, pp.417–428, 1999.

[11] Le, C.V., Ly, N.G. and Postle, R., "Heat and mass-transfer in the condensing flow of steam through an absorbing fibrous medium," *Int. J. Heat Mass Transfer*, vol.38, no.1, pp.81–89, 1995.

[12] Scarpa, F. and Milano, G., "The role of adsorption and phase change phenomena in the thermophysical characterization of moist porous materials," *International Journal of Thermophysics*, vol.23, no.4, pp.1033–1046, 2002.

[13] A. Halder, A. Dhall, A. K., Datta, "An improved, easily implementable, porous media based model for deep-fat frying — Part I: model development and input parameters," *Food Bioproducts Processing*, vol.85, pp. 209–219, 2007.

[14] Alexander Warning, Ashish Dhall, Diana Mitrea, Ashim K. Datta, "Porous media based model for deep-fat vacuum frying potato chips," *Journal of Food Engineering*, vol.110, pp.428–440, 2012.

[15] Haitao Ni, ""Multiphase moisture transport in porous media under intensive microwave heating," *A dissertation of Cornell University*, 1997.

[16] S. Ben Nasrallah and P. Perré, "Detailed study of a model of heat and mass transfer during convective drying of porous media," *Int. J. Heat Mass Transfer*, vol. 31, no. 5, pp.957-967, 1988.

[17] Ilic, M. and I. W. Turner., "Convective drying of a consolidated slab of wet porous material," *Int. J. Heat Mass Transfer*, vol.32, no.1, pp.2351-2362, 1989.

[18] A. Stogryn, "Equations for calculating the dielectric constant of saline water," *IEEE Trans. Microwave Theory Tech.*, vol.19, pp. 733-736, 1971.

[19] LAWRENCE A. KLEIN AND CALVIN T. SWIFT, "An improved model for the dielectric constant of sea water at microwave frequencies," *IEEE transaction on antennas and propagation*, vol.25, no.1, pp.104-111, 1977.

[20] Thomas .M and Frank J. W, http://www1.lsbu.ac.uk/water/microwave_water.html, 2004.

[21] N. N. Grinchik, P. V. Akulich, A. L. Adamovich, P. S. Kuts, and S. P. Kundas, "Modeling of nonisothermal heat and moisture transfer in capillary-porous media in periodic microwave heating," *Journal of Engineering Physics and Thermophysics*, vol.80, no.1, pp. 1-10, 2007.

Chapter 6 Sensitivity analysis and optimizations

In the previous chapter, the simulated temperatures, moisture contents and pressures are presented and analyzed, among which the simulated temperatures are experimentally verified. The corresponding parameters in the four cases are set not merely the same but also as constants. However, there is variation in values of most of the parameters in reality for potatoes. The properties such as permeability and diffusivity can vary tremendously for food materials, and little or no measured data is available. Also, with so many relevant parameters, it is important to know which ones are the most influential. Sensitivity analysis, where sensitivity of one parameter is studied while keeping other parameters constant, is one way to answer some of these questions. This chapter reports firstly the sensitivity of temperature, moisture loss and pressure to material parameters, like liquid and gas permeability, mass and heat transfer coefficients, power level, and RF frequency, and so on.

For this part of study, simulations are only run for heating potato samples with height of 57mm for 16 cycles. The process period is 15s for heating and 45s for cooling.

6.1 Sensitivity analysis

6.1.1 Effect of different RF power

Two different power levels are already employed to do the experiments in the last chapter. A simple comparison is also done. To further study the influence of power levels on the temperature, moisture and pressure distributions of the heated sample, more simulations are conducted and a wider and deeper discussion is carried out.

In this section, the power of 50W, 100W, 150W are respectively used to periodically heat the sample. The effectiveness of different power levels are revealed below.

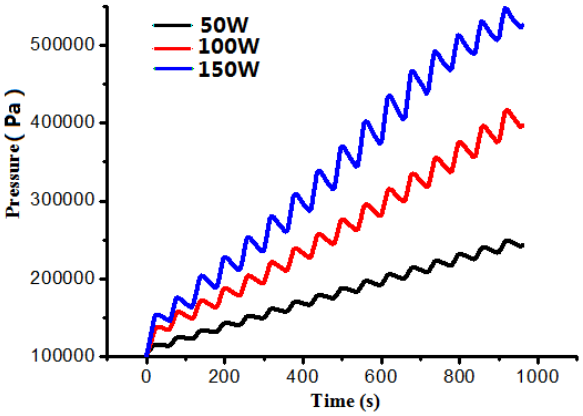


Figure 6.1 Comparison of pressures of point 1

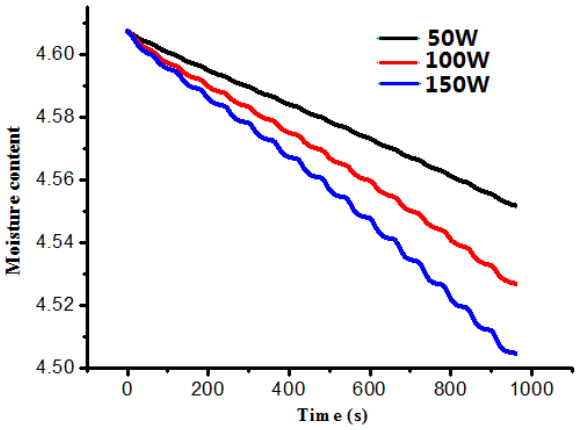


Figure 6.2 Comparison of moisture contents

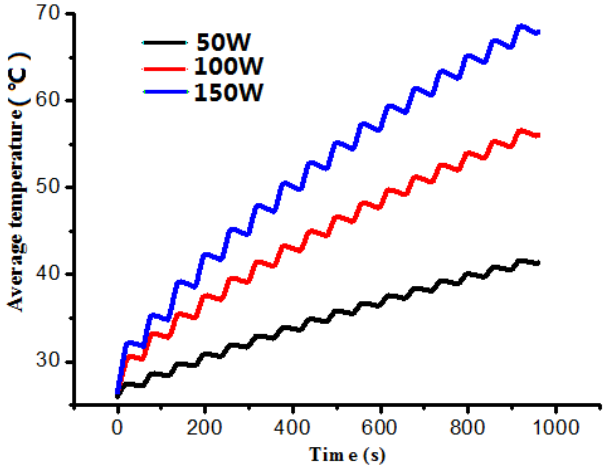


Figure 6.3Comparison of average temperatures

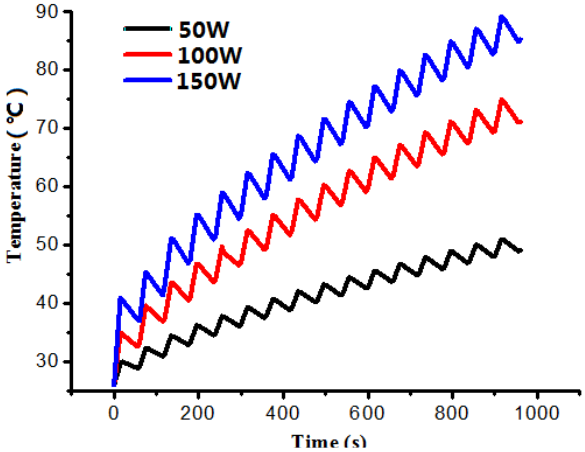


Figure 6.4Comparison of temperatures of point1

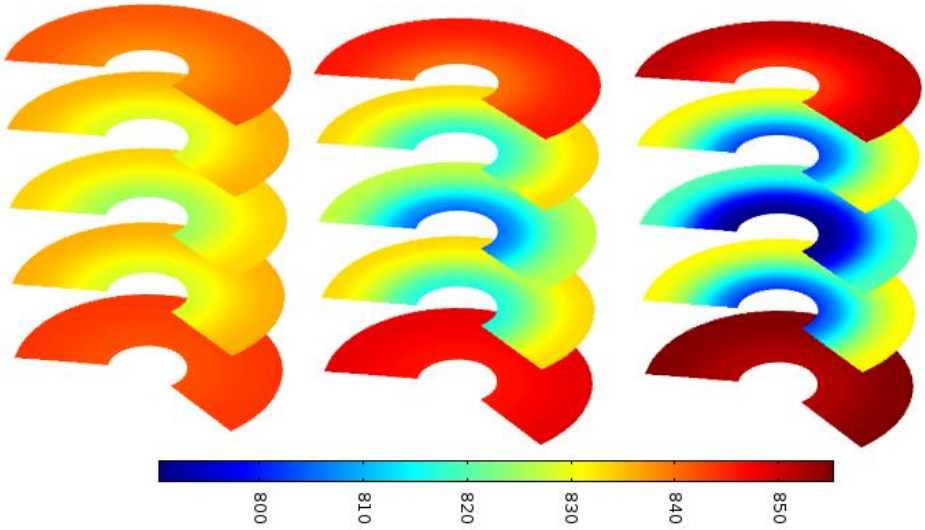


Figure 6.5 Comparison of water concentration distributions of different slices of samples heated by different powers: 50W (left), 100W (middle), 150W (right).

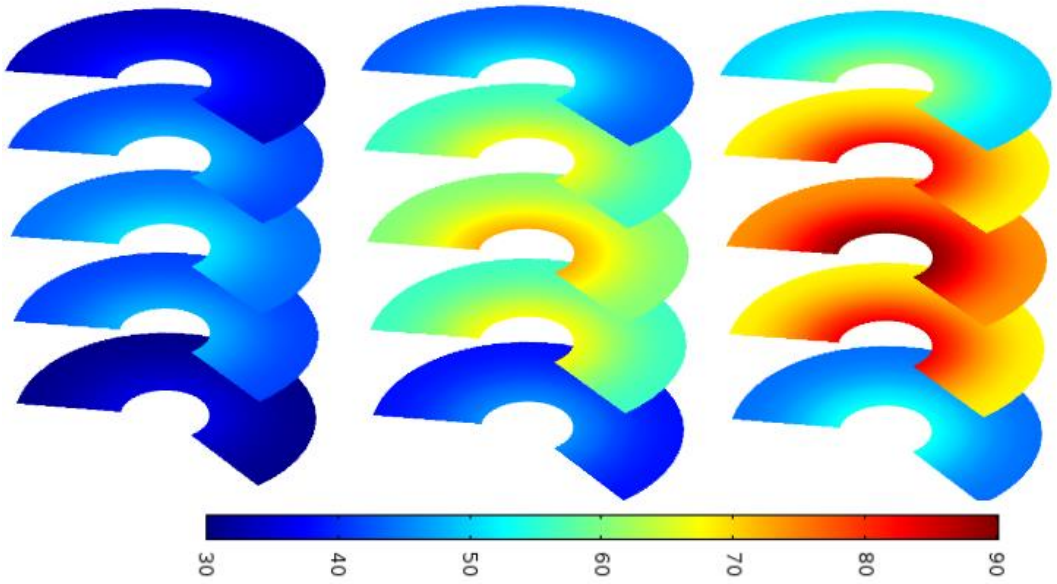


Figure 6.6 Comparison of temperature distributions of different slices of samples heated by different powers: 50W (left), 100W (middle), 150W (right).

From Figure 6.5 and 6.6, one can observe that the temperature distributions of the samples after being treated 16 cycles are similar. All of them have the highest temperature in the center and lowest temperature on the top and bottom surfaces.

It is very clear that increasing the input power, all the parameters in which we are interested raise. The more the input power, the higher the temperature, pressure and moisture loss. However, the increase is not proportional to that of the input power. To show the effects of different power levels more clearly, a table is presented below to reveal the change of each parameter after processing for 16 cycles under the three power levels.

Table 6.1 Increasing of temperature, pressure and moisture loss under different power levels

parameters	Point temperature	Point pressure	Moisture loss	Average temperature
50W	23.15	141409.374	0.05556	15.38468
100W	45.2	295322.42	0.08047	30.07614
150W	59.3	424642.537	0.10271	41.91129

We can see from the table that doubling the power, the temperature of point 1 and the average temperature increase twice. For the pressure of point 1, its augment is a little larger than

twofold of that of 50W. However, the moisture loss doesn't increase at the same magnitude. It may be because after the temperature and pressure gradients inside the sample push the liquid water to the surface, the liquid can not be expelled rather than "held" by the surface. It is reported that it is observed the liquid water driven from the interior accumulates on the surface and drops down directly when the surface can not "hold" the liquid any more [1]. When the power is enlarged three times, only the pressure of point 1 triples. The maximum temperature and average temperature increase respectively about 156% and 172.49%. The moisture loss only increases 84.86%. Therefore, according to our research, increasing the input power, the heating effect is certainly improved but not with the same amplitude of the incensement of energy. If one wants to dry the potatoes more quickly by enlarging the power, it is necessary to consider the balance of energy costs and drying effects.

6.1.2 Effect of mass transfer coefficient

Mass transfer coefficient h_m is directly relative to the moisture loss. The mass transfer coefficient for drying at an air temperature of 33℃ without the effects of forced convection is about 0.008. Considering the air temperature in the cell during the heating, we assume that the average temperature of air is 33℃ and the mass transfer coefficient of potato is 0.008 m/s. To study the impact of mass transfer coefficient on the drying effect, two other values-0.004 and 0.012 m/s are used in the simulated models. The simulated results are compared and analyzed below.

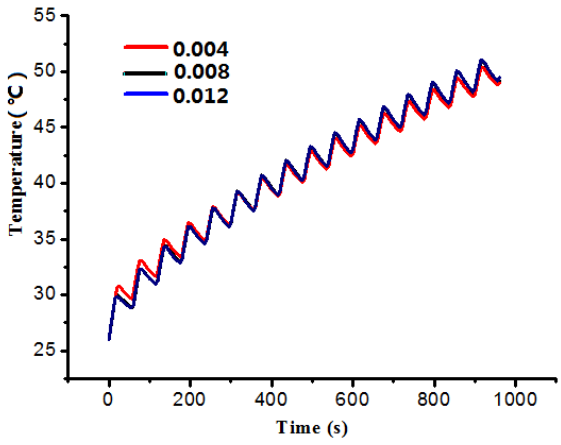


Figure 6.7Comparison of temperatures of point

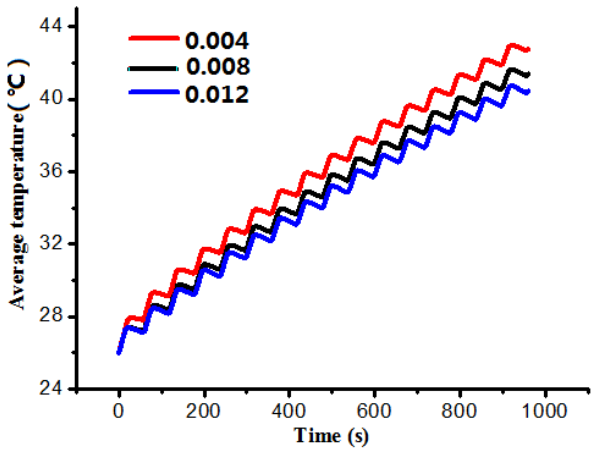


Figure 6.8 Comparison of average temperatures

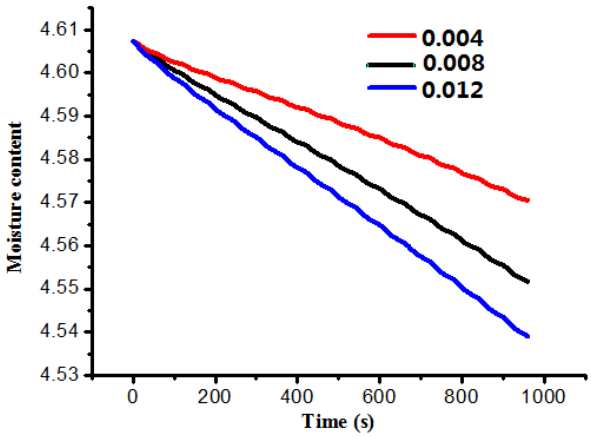


Figure 6.9 Comparison of moisture contents

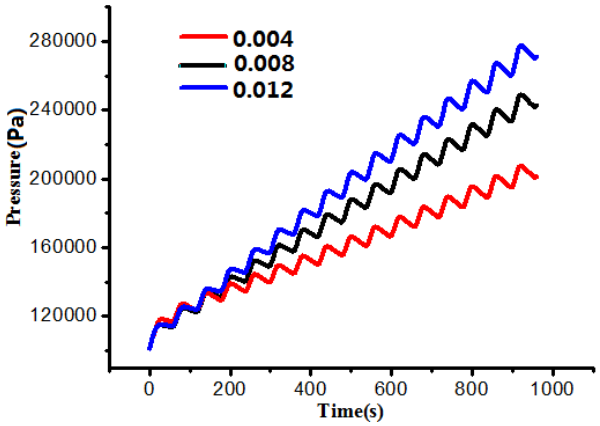


Figure 6.10 Comparison of pressures of point 1

It is obvious that the moisture losses of the three cases are very different from each other. The higher the mass transfer coefficient is, the more the moisture will lose. However, the change of mass transfer coefficient doesn't cause the same proportion of the moisture loss. At lower moisture transfer coefficient, less moisture is removed from the surface, increasing the surface wetness and RF absorption. This phenomenon is demonstrated more clearly by the moisture distributions in Figure 6.11. When the moisture transfer coefficient is smaller, the whole sample holds more liquid water inside, which enhances the energy absorption and decreases the temperature gradient between the inner and outer boundaries of the sample. Less removed moisture on the surface is also followed by less energy going into evaporation, leading to higher temperature on the surface. This is reflected by the average temperature profile in Figure 6.8 and shown clearly in Figure 6.12. The maximum temperatures shown by Figure 6.7 are not influenced much due to the surface effects do not penetrate much into the sample because the thermal conductivity and capillary diffusivity are both small. The difference exists in the temperature gradient in the sample causes the distinction of pressure in point 1.

The mass transfer coefficient can be manipulated by oven design or just simply change the air velocity around the heated sample. Since the mass transfer coefficient is so important in drying the porous media, one can modify the ambient environment to increase the mass transfer coefficient and improve the drying effect.

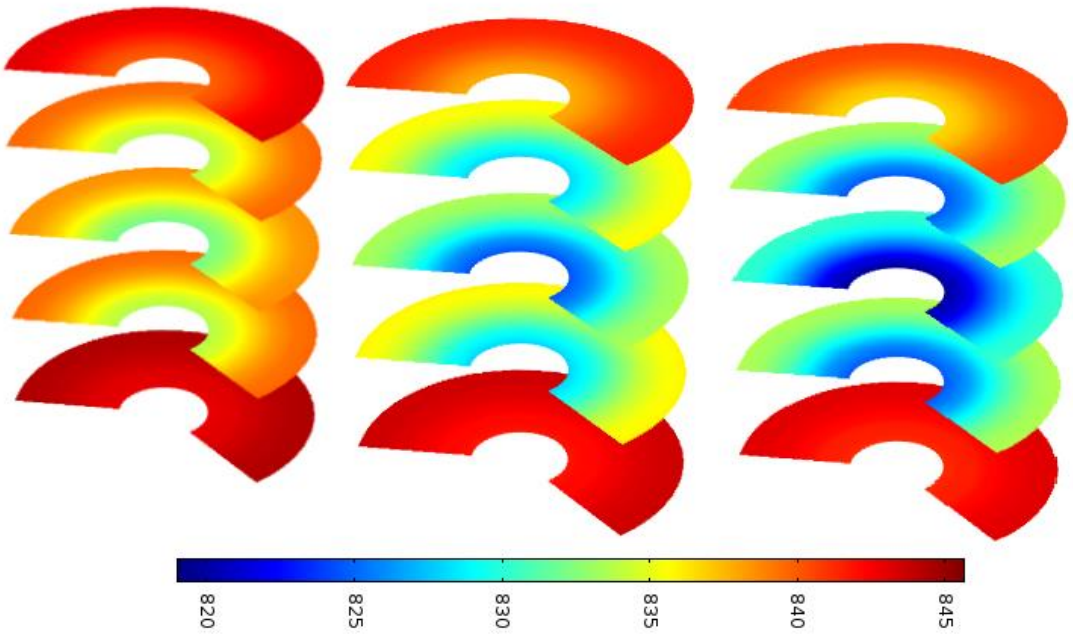


Figure 6.11 Comparison of water concentration distributions of different slices of samples heated by different values of h_m: 0.004m/s (left), 0.008m/s (middle), 0.012 m/s (right).

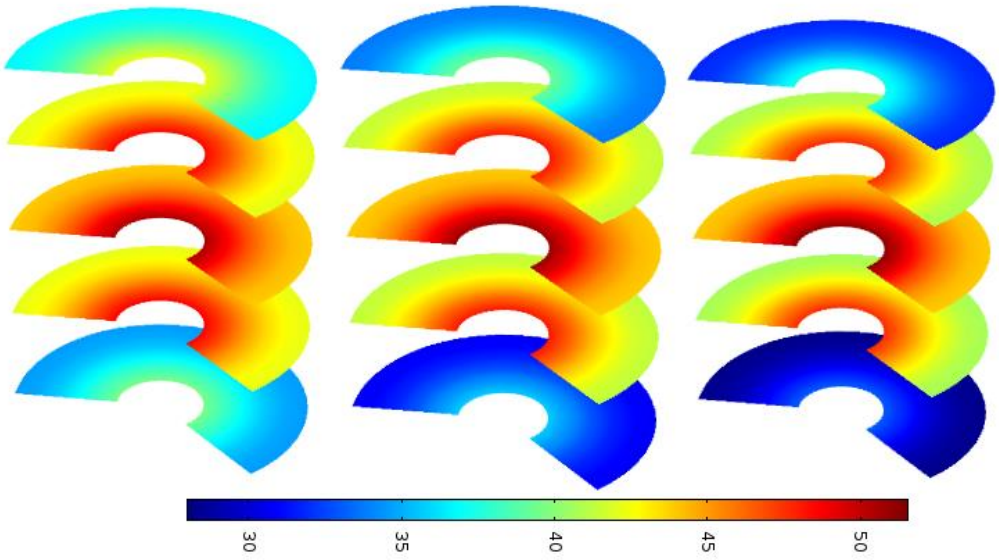
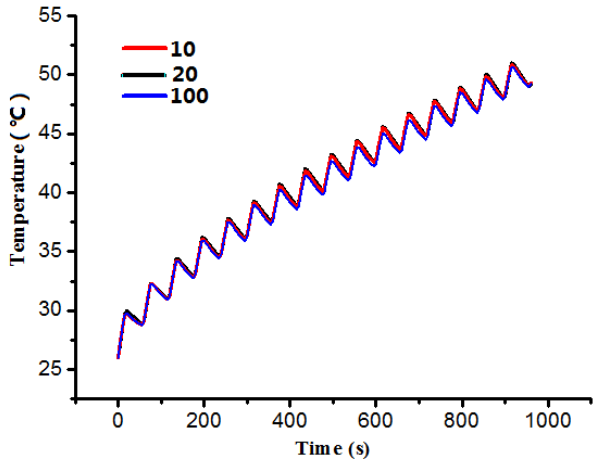


Figure 6.12 Comparison of temperature distributions of different slices of samples heated by different values of h_m: 0.004 (left), 0.008 (middle), 0.012 (right).

6.1.3 Effect of heat transfer coefficient

Heat transfer coefficient h_t is another important parameter for impacting the heat and mass transfer in the samples. Like the mass transfer coefficient, it can be changed by manipulating the environment around the sample. In our sensitivity analysis, another two values of heat transfer coefficients are implied in the model (10 and 100 $\mathrm{W}/(m^2 \cdot K)$). Their simulated results are then compared to those obtained with the original heat transfer coefficient--20 $\mathrm{W}/(m^2 \cdot K)$. The unit is omitted in the rest of this section.



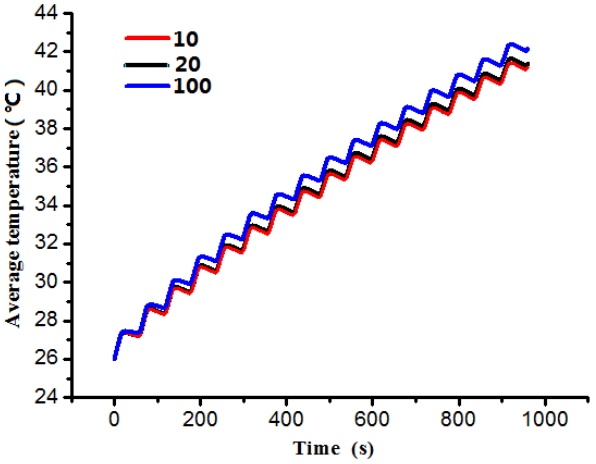
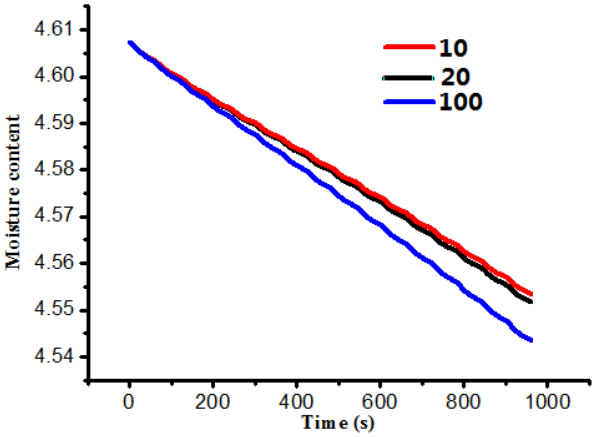


Figure 6.13Comparison of temperatures of point 1 Figure6.14Comparison of average temperatures



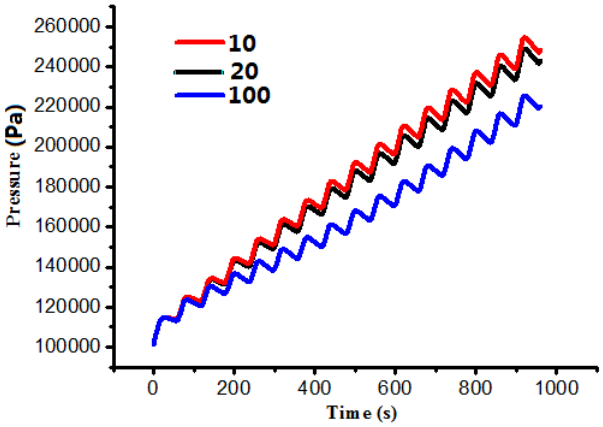


Figure 6.15 Comparison of moisture contents Figure 6.16 Comparison of pressures of point 1

At first glance, the effects of heat transfer coefficient on temperature, moisture content and pressure are similar to those of the mass transfer coefficient. Variation of heat transfer coefficient causes different heating effects. For the four parameters that we are interested in, it is obvious that the moisture losses of the three cases are different from each other. The higher the heat transfer coefficient is, the more the moisture will lose. However, the change of heat

transfer coefficient cannot bring the equivalent change amount of the moisture content loss. With lower heat transfer coefficient, heat loss from the surfaces to the ambient decreases, leading to the cooler surfaces. When the heat transfer coefficient is large enough, the heat interior is easier and quicker transferred to the surfaces. The energy from the interior is higher than that taken away by the evaporation on the surfaces, which leads to the surfaces with higher temperature and sample with higher average temperature. This phenomenon is shown very clearly by the maximum temperature and average temperature revealed respectively in Figure 6.13 and 6.14. In our research, the temperatures of the surfaces are very low and the evaporation on the surfaces is also weak. Therefore, the average temperature with larger heat transfer coefficient is greater. However, the difference in average temperature with different heat transfer coefficient is tiny, which is revealed in Figure 6.18. It may influence the temperature distribution of the heated sample only if the change of heat transfer coefficient is very large. The maximum temperatures shown by Figure 6.13 are not influenced much due to the surface effects do not penetrate much into the sample because the thermal conductivity and capillary diffusivity are both small.

When the heat transfer coefficient is bigger, the energy loss on the surfaces increases. Since the heat interior is easier to transfer though the sample, the temperature of middle part of the sample is quick to be heated. The temperature gradient between the surfaces and middle part drives the liquid to the surface to evaporate. This is reflected by the moisture content profile in Figure 6.15 and shown clearly in Figure 6.12. The smoothly flow of liquid water and smaller temperature gradient at higher heat transfer coefficient makes its pressure lower.

Therefore, like the mass transfer coefficient, one can try to change the ambient condition to modify the heat transfer coefficient and to improve the drying effect.

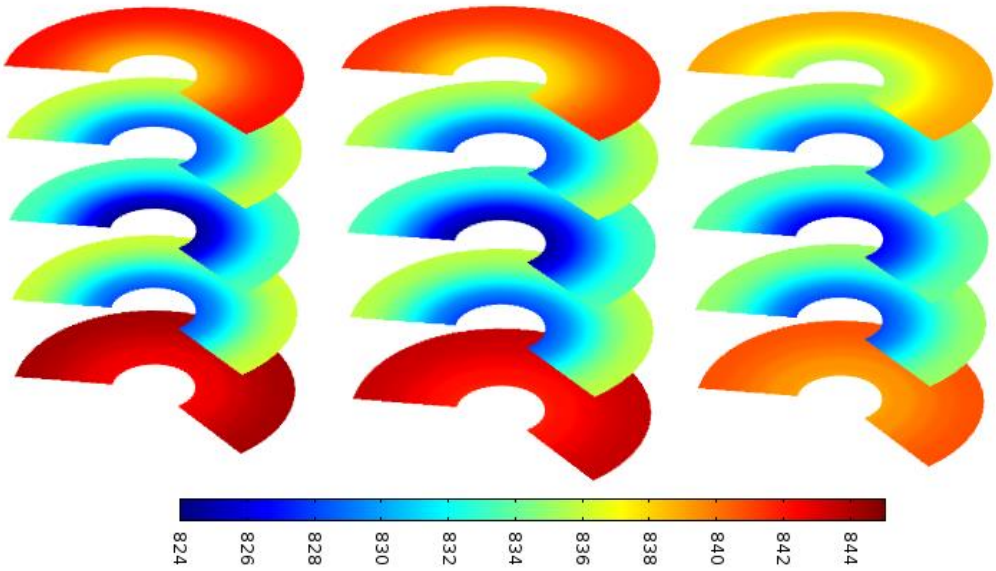


Figure 6.17 Comparison of water concentration distributions of different slices of samples heated by different values of h_t: 10 (left), 20 (middle), 100 (right).

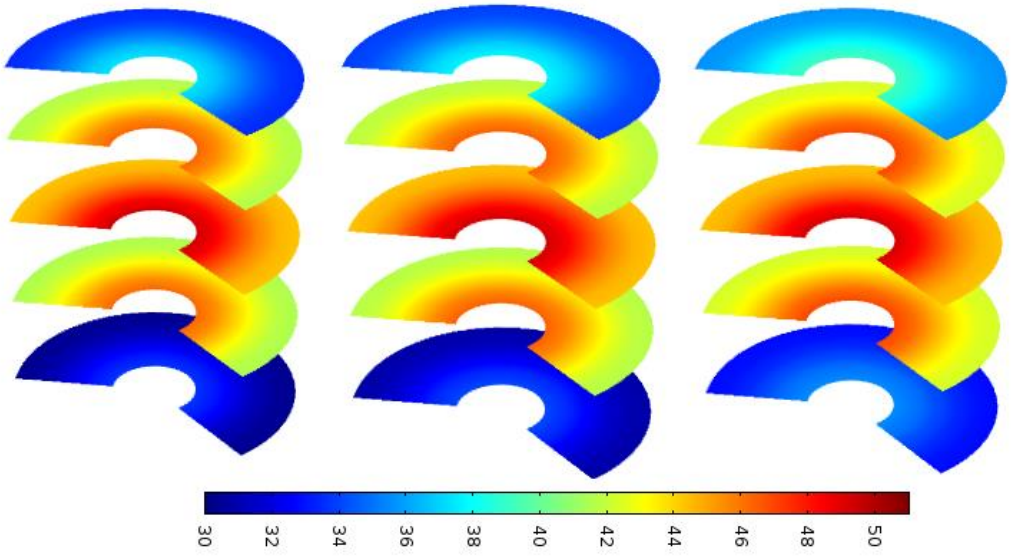


Figure 6.18 Comparison of temperature distributions of different slices of samples heated by different values of h_t: 10 (left), 20 (middle), 100 (right).

To understand whether a particular effect is contributed more due to the heat transfer coefficient than the mass transfer coefficient, a simple comparison is made here. Both the coefficients have an impact on the drying effect. However, by comparing the corresponding Figures, it is obvious that the mass transfer coefficient has a greater contribution to the temperature rising, moisture loss and pressure change, even though the variation of mass

transfer coefficient is much smaller than that of mass transfer coefficient. The heating effect of RF treating potato in our model is more sensitive to the mass transfer coefficient.

6.1.4 Effect of water intrinsic permeability

Permeability describes transport due to the gradient in total pressure and is perhaps the most important parameter in microwave heating. The intrinsic permeability $k_{in,w}$ is the vital component of permeability, which represents the permeability of a liquid at fully saturated state. It depends on the internal structure of the material, especially the porosity and pore sizes.

It is very hard to accurately measure the intrinsic permeability due to its small value and shrinkage during drying or heating. Usually, researchers estimate the intrinsic permeability to be a constant according to the existed experiments. Since these values are still somewhat arbitrary, sensitivity of the model to these parameters will be an important part of the analysis.

In this section, another two constants are set as the intrinsic permeability of liquid water and their corresponding models are run. Comparisons of the results are revealed below.

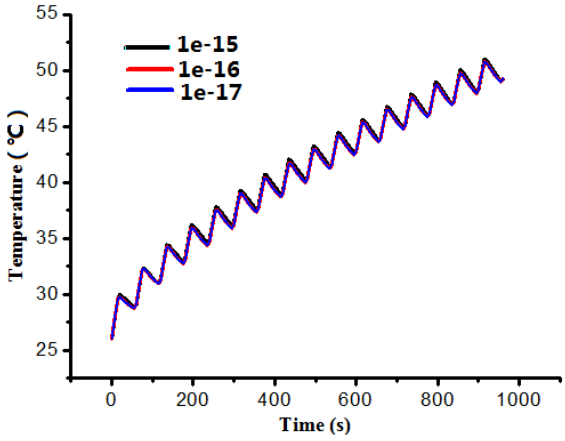


Figure 6.19 Comparison of temperatures of point 1

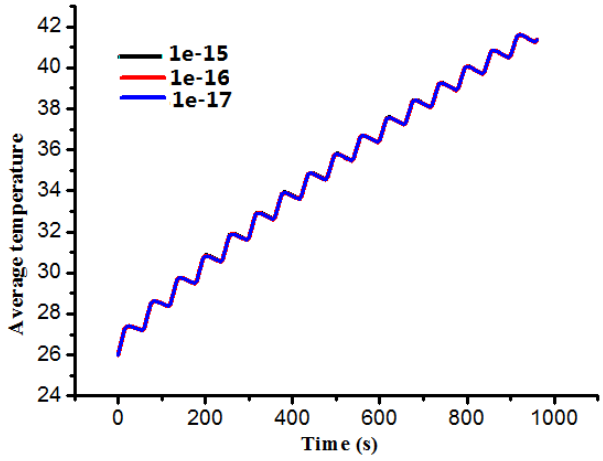


Figure6.20Comparison of average temperatures

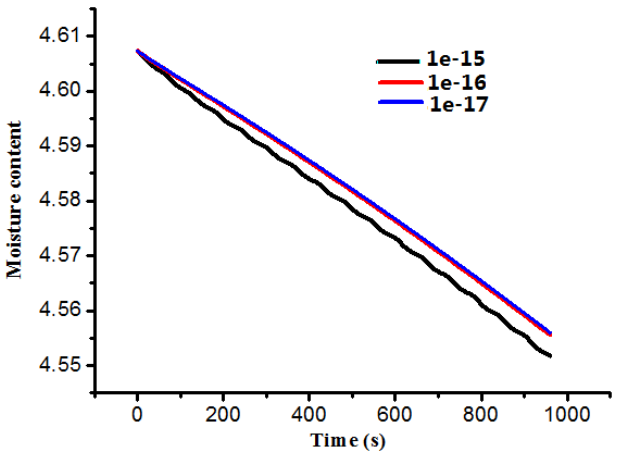


Figure 6.21Comparison of moisture contents

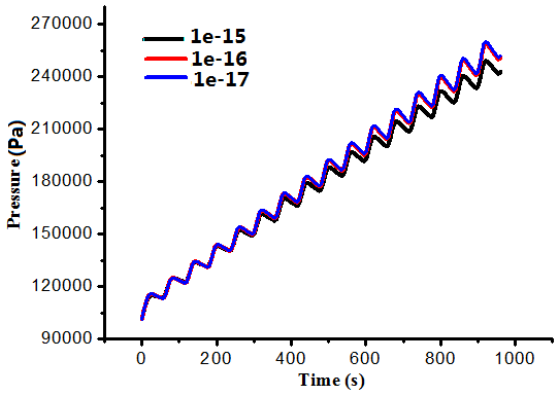


Figure 6.22 Comparison of pressures of point 1

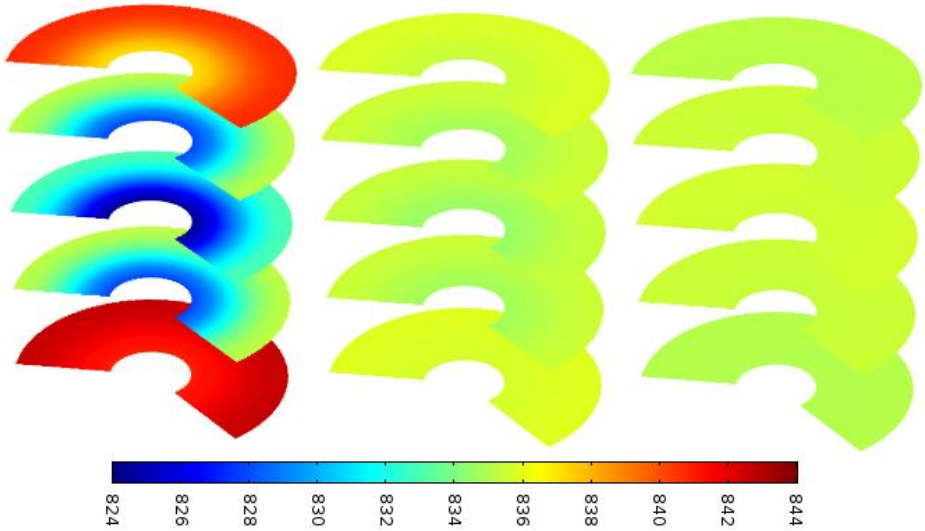


Figure 6.23 Comparison of water concentration distributions of different slices of samples heated by different values of $k_{in,w}$: 1e-15 (left), 1e-16 (middle), 1e-17 (right).

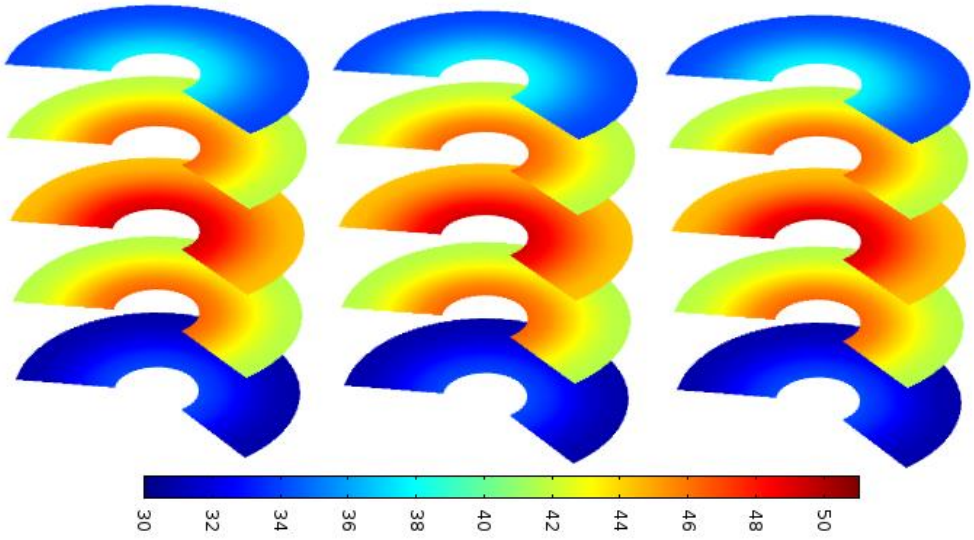


Figure 6.24 Comparison of temperature distributions of different slices of samples heated by different values of $k_{in,w}$: 1e-15 (left), 1e-16 (middle), 1e-17 (right).

As described above, the permeability is relative to the transport directly. The larger the permeability is, the more permeable the material. When $k_{in,w}$ is larger, the liquid migration from interior to outer surface is easier to happen. The smoother transport inside the sample leads to smaller pressure gradients, which is verified by Figure 6.22. Although the pressure gradient decreases with higher water intrinsic permeability, product of $k_{in,w}$ and the pressure gradient rises, increasing the flux of liquid toward the surface. Since the removal of liquid from surface would not change appreciably, liquid would accumulate near the surface, increasing surface saturation greatly, as shown by the left picture in Figure 6.23. There is no appreciable convective drying stage initially because very small overpressure can cause the liquid flow. The high saturation surfaces have a stronger ability to absorb the RF power. More water will be evaporated, expressing why the moisture loss is bigger when $k_{in,w}$ is larger (Figure 6.21).

As $k_{i,w}$increases, the maximum temperature tends to be a little lower because more liquid moves to the other part of the sample, taking away the heat at the same time. Lower water saturation inside leads to smaller microwave absorption. That is also the reason that the maximum pressure is a little lower. However, the differences of maximum temperature of these three cases are tiny, which can not be shown obviously in Figure 6.19. Even though the sample surfaces with higher $k_{in,w}$ can absorb more energy, the stronger evaporation also takes away large amount of heat. The amounts of these two powers determine the decreasing or

increasing of the surfaces temperature. In our case, temperature distributions are almost the same with different water intrinsic permeability due to their insignificant variation (Figure 6.24). On the other hand, when $k_{in,w}$ is smaller, the material is less permeable to the liquid. As a result, the pressure driven flow is less so that the surface can stay drier, as shown in Figure 6.23. It is much like convective drying.

Therefore, the water intrinsic permeability can affect the moisture loss and pressure of the sample. However, its impact on the temperature is much smaller. It is also worth noticing that if $k_{in,w}$ is already very small, the simulated results won't be changed when decreasing it.

6.1.5 Effect of water saturation

Water saturation S_w means fraction of water in a given pore space. It is expressed in volume/volume, percent or saturation units. The saturation relates directly the effective specific heat capacity and effective thermal conductivity in the heat transfer equation. If the water saturation is higher, the liquid water quantity existed in that region is larger, which follows by stronger RF power absorption ability. However, the effective specific heat capacity and thermal conductivity are also larger. It needs more energy for the temperature to increase. At the same time, the higher quantity of migration of liquid water to the cooler part of the sample will take away the heat, too. The general effect of these influences may make the temperature increase less. On the opposite, if the water saturation is smaller, even though the power absorbed is less, the temperature incensement is larger because the specific heat capacitor and thermal conductivity are smaller. It needs less energy to heat the sample. This phenomenon is clearly demonstrated in Figure 6.25 and 6.26.

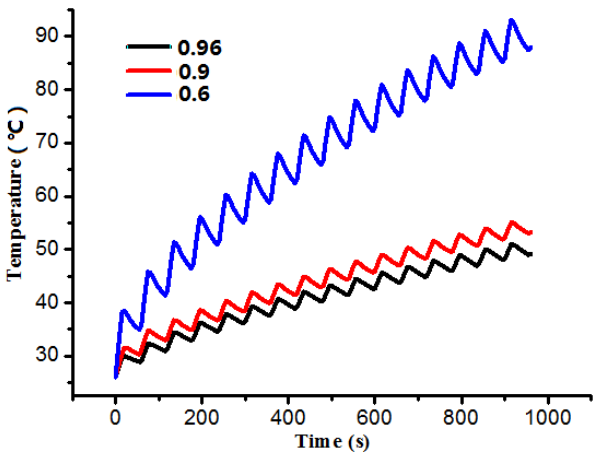


Figure 6.25 Comparison of temperatures of point 1

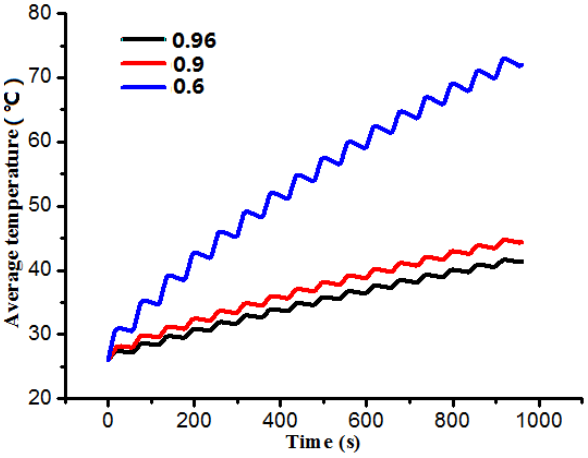


Figure6.26Comparison of average temperatures

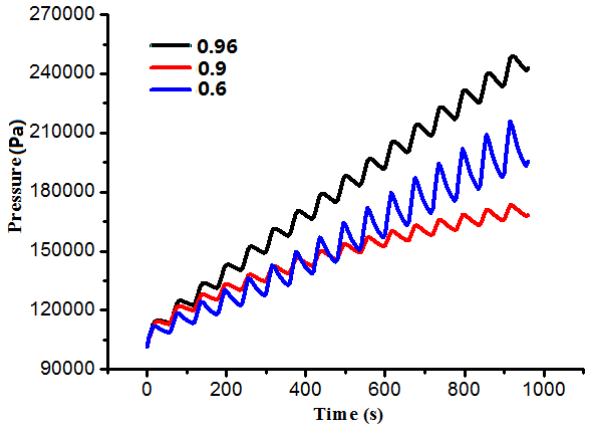


Figure 6.27 Comparison of pressures of point 1

From the comparison of temperature distributions of slices in Figure 6.29, it is more obvious that the temperature of sample is higher if the water saturation is smaller. The temperature gradient is also greater with low water saturation. Therefore, more liquid water is pushed towards surfaces to evaporate out. It is responsible for the higher moisture loss at lower water saturation which is listed in table 6.2. If the evaporation velocity at the surface is smaller than the migration of liquid water from interior, the surfaces will get wetter. In Figure 6.28, three legends are used respectively for the demonstration of three water concentration distributions due to their different original values. The maximum water concentration after being processed for 16 cycles reaches 530.31 mol/m^3 when the water saturation is 0.6. However, its original water concentration is only $528 mol/m^3$. For the higher S_w, less liquid water is driven to the surfaces, leading to the drier surfaces and more homogeneous moisture distribution (original water concentration is 792 $mol/m^3$when $S_w = 0.9$, $844 mol/m^3$ for $S_w = 0.96$).

Water saturation affects all most all the parameters of the sample, its variation may change some parameters regularly. However, some will be changed without laws, such as the pressure change shown in Figure 6.27.

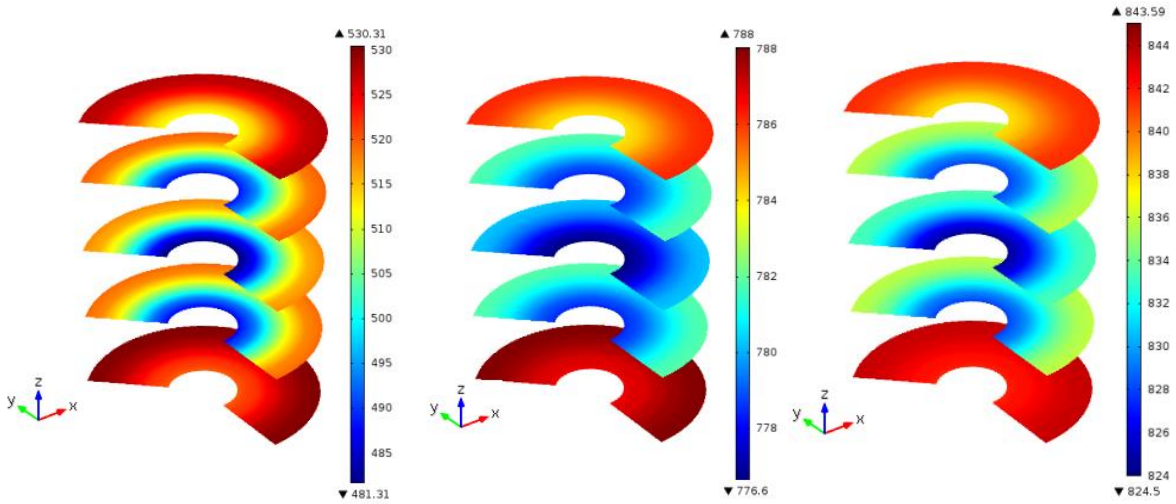


Figure 6.28 Comparison of water concentration distributions of different slices of samples heated by different values of S_w: 0.6 (left), 0.9 (middle), 0.96 (right).

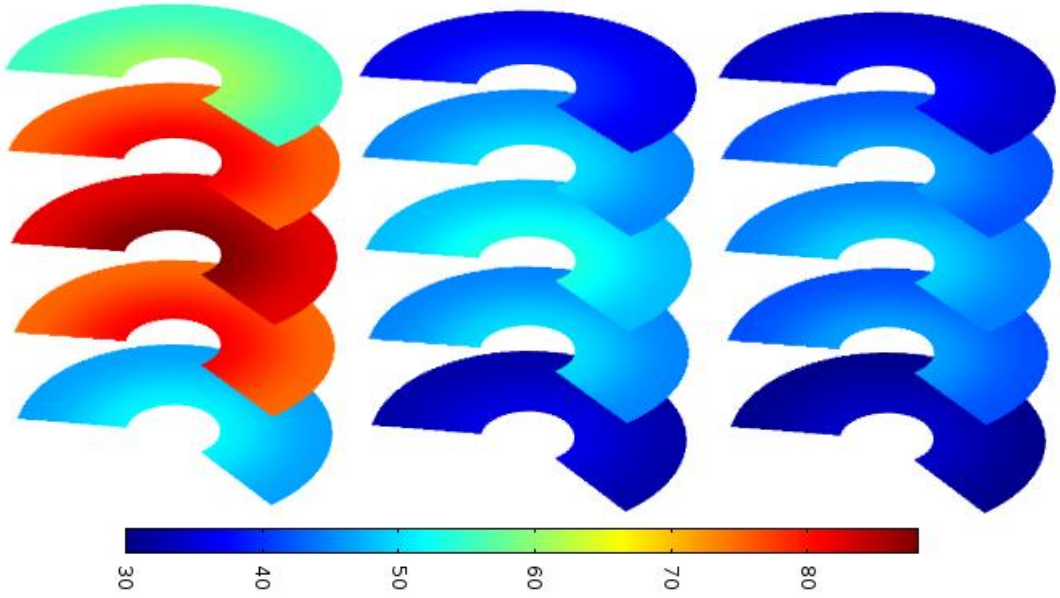


Figure 6.29 Comparison of temperature distributions of different slices of samples heated by different values of S_w: 0.6 (left), 0.9 (middle), 0.96 (right).

Table 6.2 Comparison of moisture content losses of different S_w

	$S_w = 0.96$	$S_w = 0.9$	$S_w = 0.6$
Moisture loss	0.05556	0.05567	0.09443

6.1.6 Effect of porosity

Another vital parameters in porous media which has impacts on almost all the other parameters is the porosity ϕ. Even though food materials are typically hygroscopic in which some water is tightly bound to the solid matrix, their porosities are defined as the analogous to those well-established in non-hygroscopic porous media. That is, the volume fraction of occupied by gas and liquid in the sample. In fact, each potato sample is unique. The porosity of each normal potato is different from those of others, although the difference is tiny. The sensitivity analysis of porosity change on the temperature, moisture content and pressure is very important. Therefore, small variation of potato's porosity and their corresponding simulations are conducted.

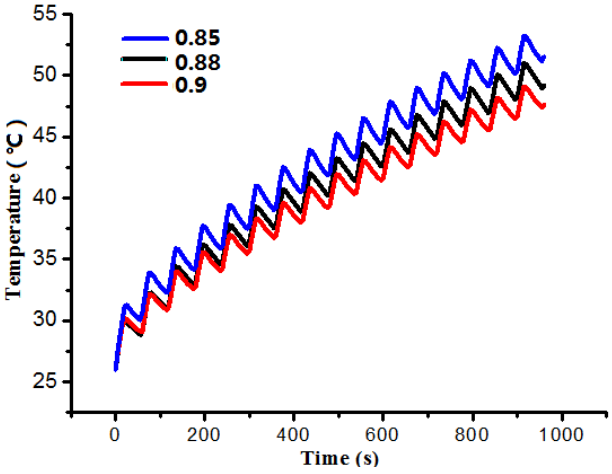


Figure 6.30 Comparison of temperatures of point 1

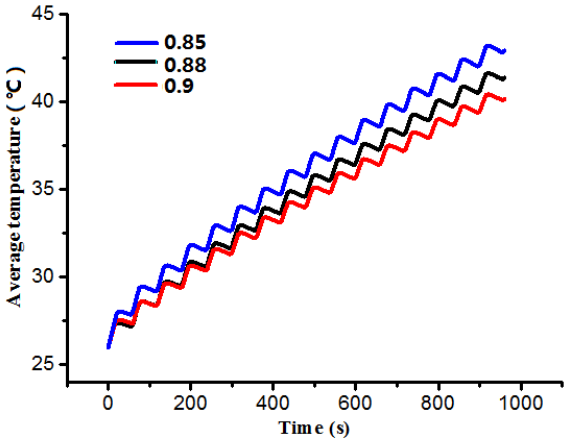


Figure6.31Comparison of average temperatures

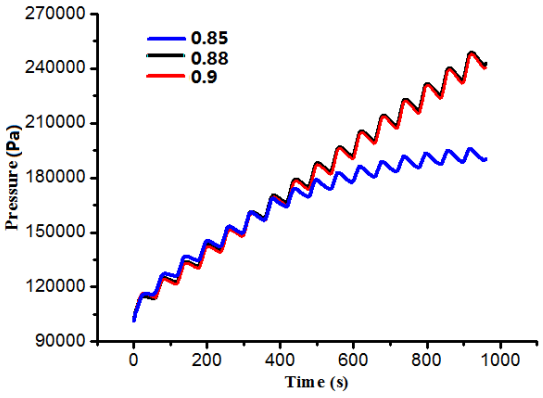


Figure 6.32 Comparison of pressures of point 1

Like water saturation, the porosity directly determines the effective specific heat capacity and effective thermal conductivity in the heat transfer equation. With higher porosity but the same

water saturation, more liquid water exists in that region, which increase the ability to absorb RF power. However, the effective specific heat capacity and thermal conductivity are also larger. It takes more energy for the temperature to increase. At the same time, the higher quantity of migration of liquid water to the cooler part of the sample will take away the heat, too. Under the action of these two opposite energies, the temperature still increases but with a small magnitude. On the contrary, if the water saturation is smaller, even though the power absorbed is less, the temperature increases larger because the specific heat capacitor and thermal conductivity are smaller. It needs less energy to heat the sample. From the Figure 6.30, 6.31 and 6.33, it is obvious that the effect of variation of porosity on temperature distribution is like that of water saturation.

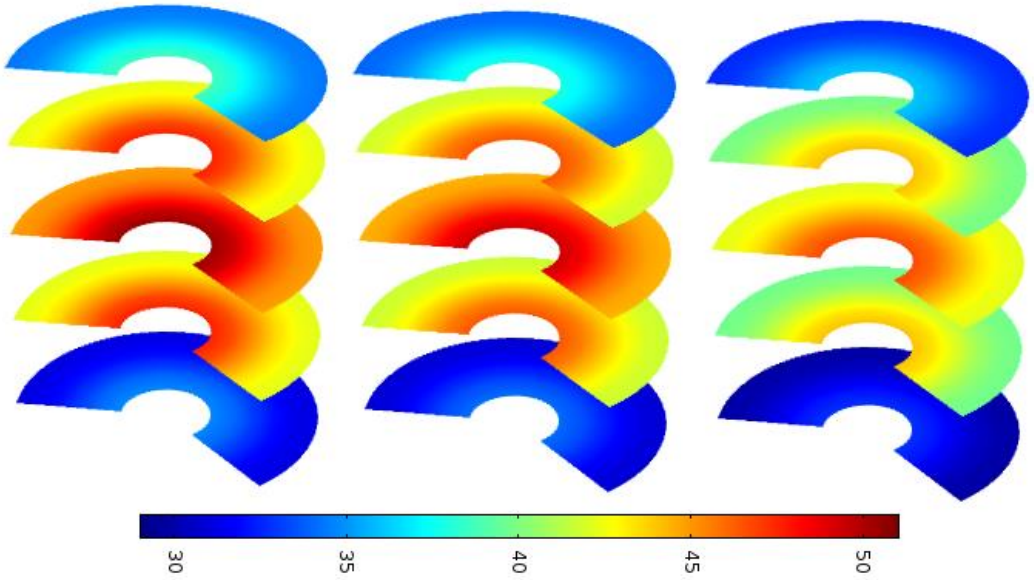


Figure 6.33 Comparison of temperature distributions of different slices of samples heated by different values of ϕ: 0.85(left), 0.88 (middle), 0.9 (right).

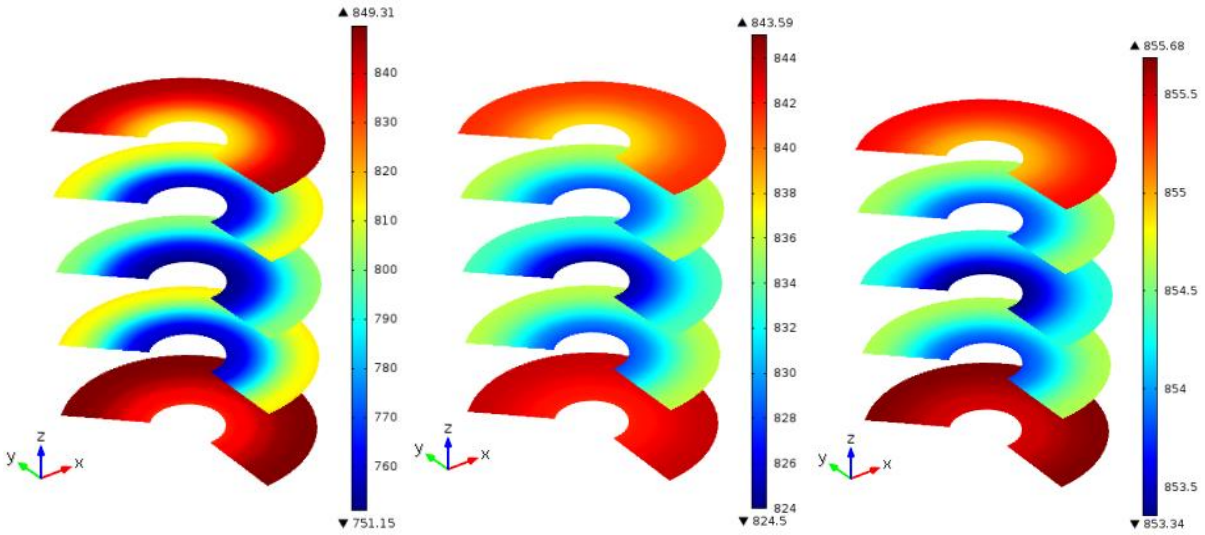


Figure 6.34 Comparison of water concentration distributions of different slices of samples heated by different values of ϕ: 0.85 (left), 0.88 (middle), 0.9 (right).

From the comparison of temperature distributions of slices in Figure 6.33, it is more obvious that the temperature of sample is higher if the porosity is smaller. The temperature gradient is also greater with low porosity. Therefore, more liquid water and gas is pushed towards surfaces to evaporate out. There is more space for the gas inside the sample, making the pressure decreasing, as in Figure 6.32. For the comparison of water distribution under these diverse porosities, in Figure 6.34, three legends are also used respectively for the demonstration of the water concentration distributions due to their different original values. When porosity is smaller, the higher temperature gradient drives more liquid water to the cooler surfaces. However, the evaporation on the surfaces depends on the temperature difference between the surface and ambient. If the evaporation velocity at the surface is smaller than the migration of liquid water from interior, the water accumulates on around the surfaces, like the case when $\phi = 0.85$ in Figure 6.34. Its maximum water concentration after being processed for 16 cycles reaches 849.31 mol/m^3. However, its original water concentration is only 816 mol/m^3. For the higher porosity, less liquid water is driven to the surfaces, leading to the drier surfaces and more homogeneous moisture distribution (original water concentration is 844 $mol/m^3$when $\phi = 0.88$, 864 mol/m^3 for $\phi = 0.9$).

It is also worth noticing that the temperature gradient when $\phi = 0.88$ is higher than that when $\phi = 0.9$, their pressures should have the same relation. However, the pressures of these two cases are almost the same. That may be because more water is evaporated from the sample in

the latter case, which leave more space for the gas and decreases the gas pressure. This reason is verified by the moisture loss listed in table 6.3.

From the discussion above, we can conclude that even though the small variation of porosity and water saturation don't affect the simulated results with large magnitude, their influence are still non-ignorable.

Table 6.3. Comparison of moisture losses of different ϕ

	$\phi = 0.85$	$\phi = 0.88$	$\phi = 0.9$
Moisture loss	0.06514	0.05556	0.06197

6.1.7 Effect of height of sample

The volume of the processed sample is a significant parameter to determine the heating rate. For the samples in our experiments, the surface area is fixed due to the material has to touch both the conductor at the same time. The only changeable one is the height of the heated sample. To make clear the effects of heights of samples, simulations with three different height values are conducted.

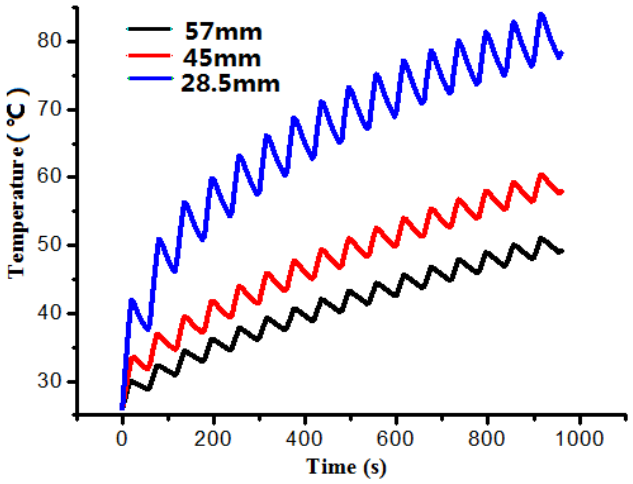


Figure 6.35 Comparison of temperatures of point 1

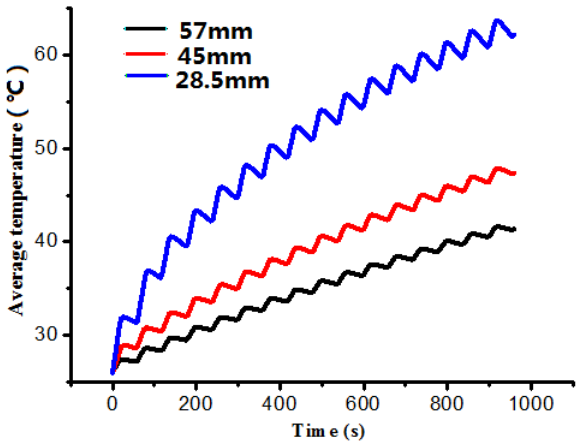
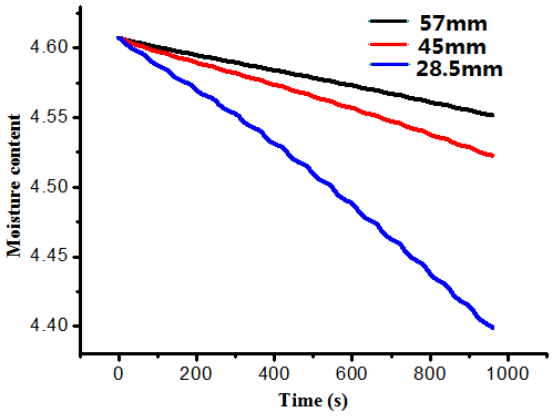


Figure6.36Comparison of average temperatures



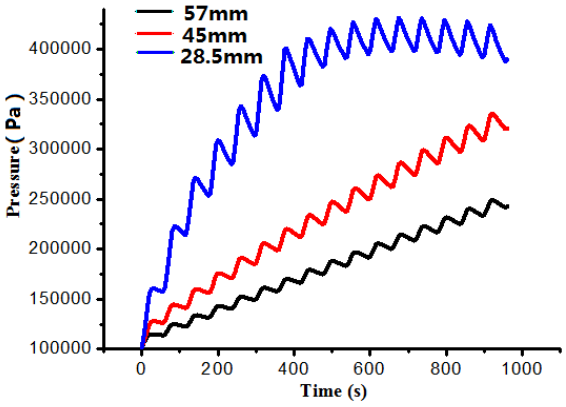


Figure 6.37 Comparison of moisture contents Figure 6.38 Comparison of pressures of point 1

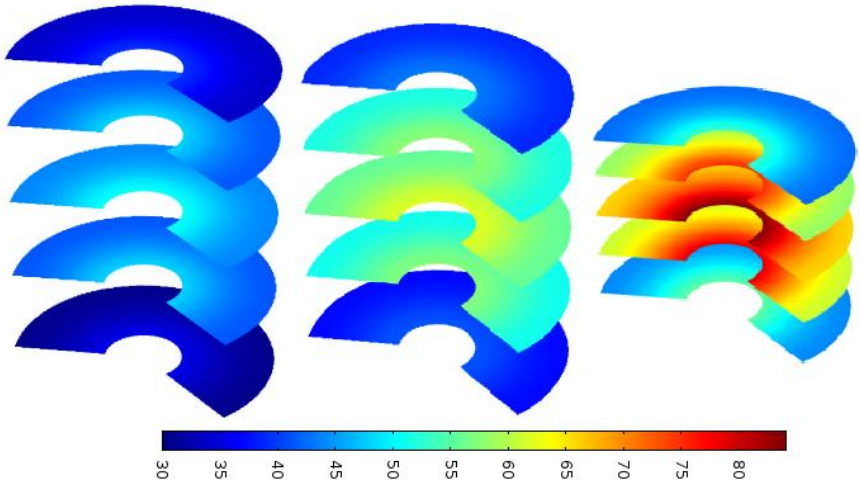


Figure 6.39 Comparison of temperature distributions of different slices of samples heated by different values of heights: 57mm (left), 45mm (middle), 28.5mm (right).

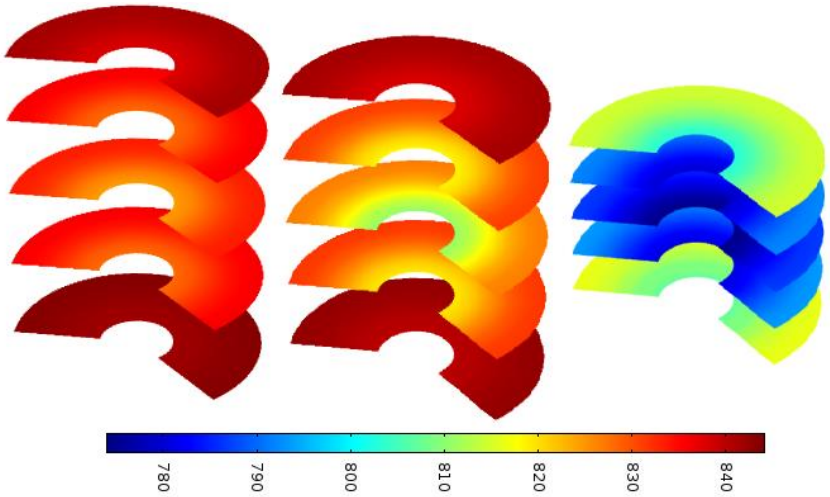


Figure 6.40 Comparison of water concentration distributions of different slices of samples heated by different values of heights: 57mm (left), 45mm (middle), 28.5mm (right).

The figures above show obviously that the variation of height changes all the profiles qualitatively. The more the height changes, the greater difference will emerge. In fact, shortening the height of the treated sample is kind of like enlarging the power. All the simulated results increase more. However, the same change of height or power may not bring the same improvement of heating effects. The simulated results of sample with height of 28.5mm and power of 50W is compared with those of sample with 57mm in height and heated by 100W. The comparison states clearly that the heating effect with smaller volume of sample is much better. Therefore, in the real world application, one can try to reduce the sizes of treated materials to improve its drying effect rather than purely increasing the heating power.

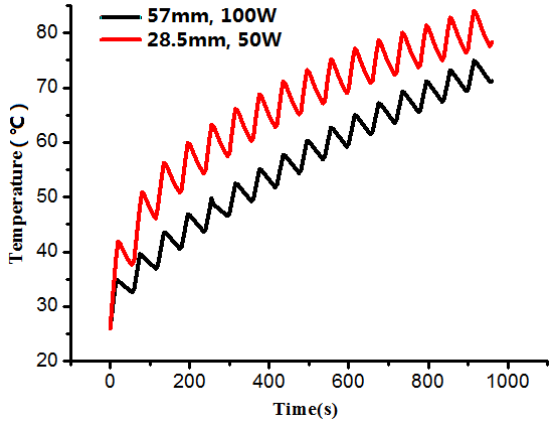


Figure 6.41 Comparison of temperatures of point 1

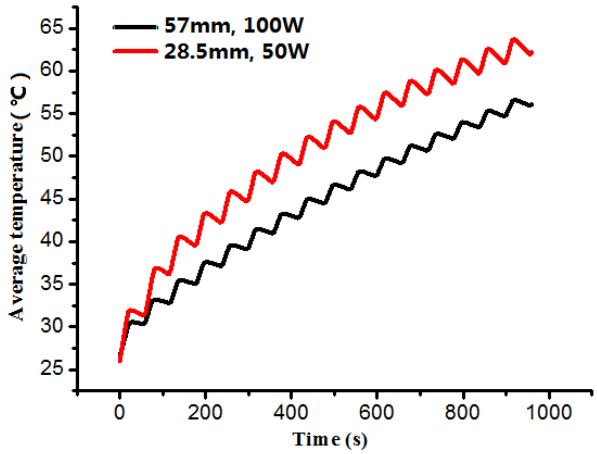


Figure6.42Comparison of average temperatures

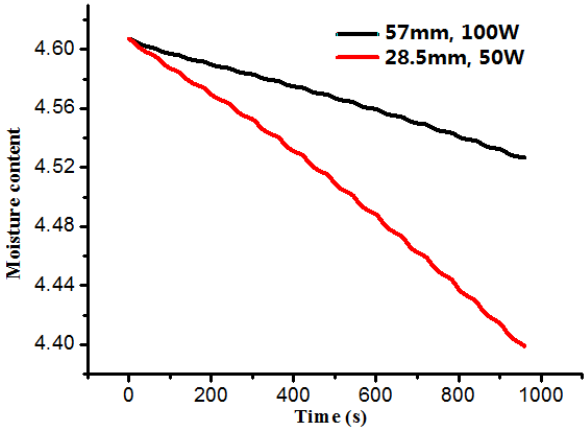


Figure 6.43 Comparison of moisture contents

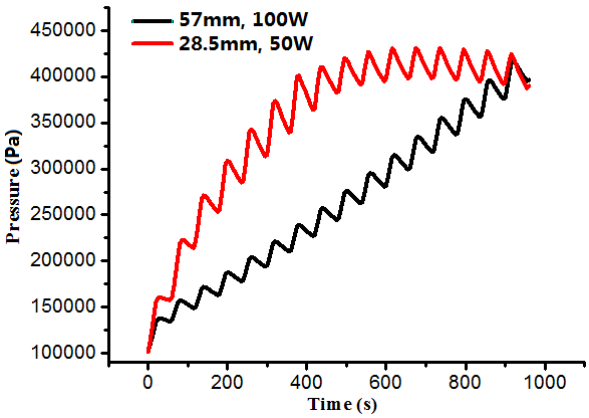


Figure 6.44 Comparison of pressures of point 1

6.1.7 Effect of different location of the potato sample

Chapter 4 already showed that the location of sample has an impact on the input impedance of the loaded coaxial cell, even though that the influence is not large. But tiny change of input impedance might raise big difference of heating efficiency. In this section, samples with height of 28.5mm are placed at three different positions—20mm, 40mm, and 60mm upper than the bottom surface of the inner conductor. Their simulations are done to study the influence of location of samples on the temperature, pressure distribution and moisture loss.

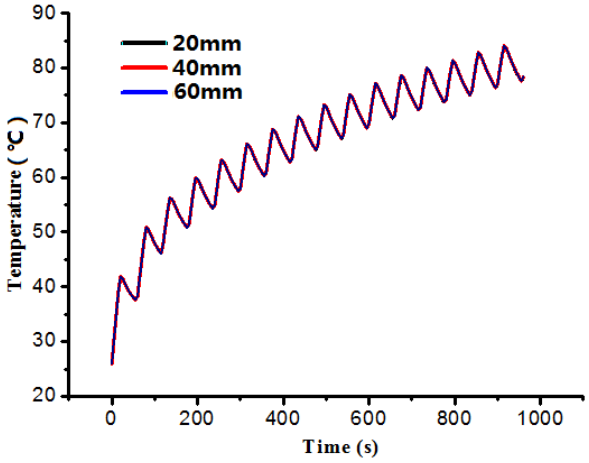


Figure 6.45 Comparison of temperatures of point 1

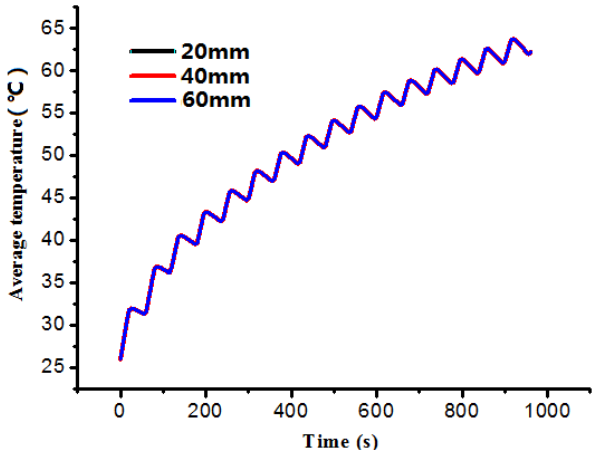


Figure6.46Comparison of average temperatures

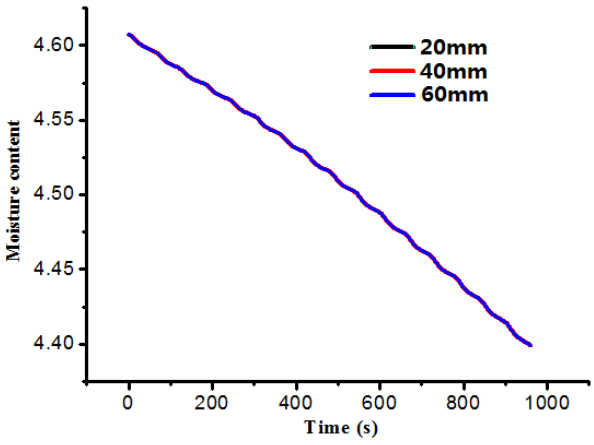


Figure 6.47 Comparison of moisture contents

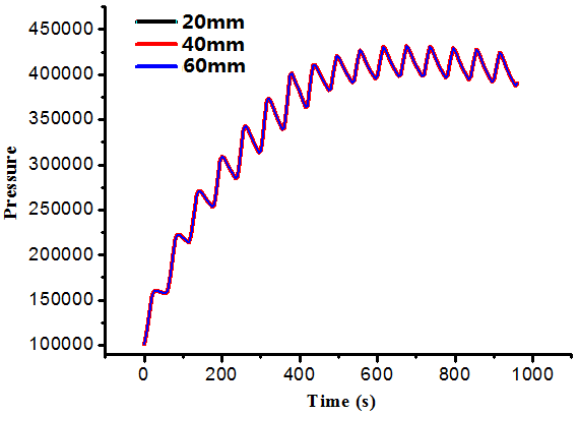


Figure 6.48 Comparison of pressures of point 1

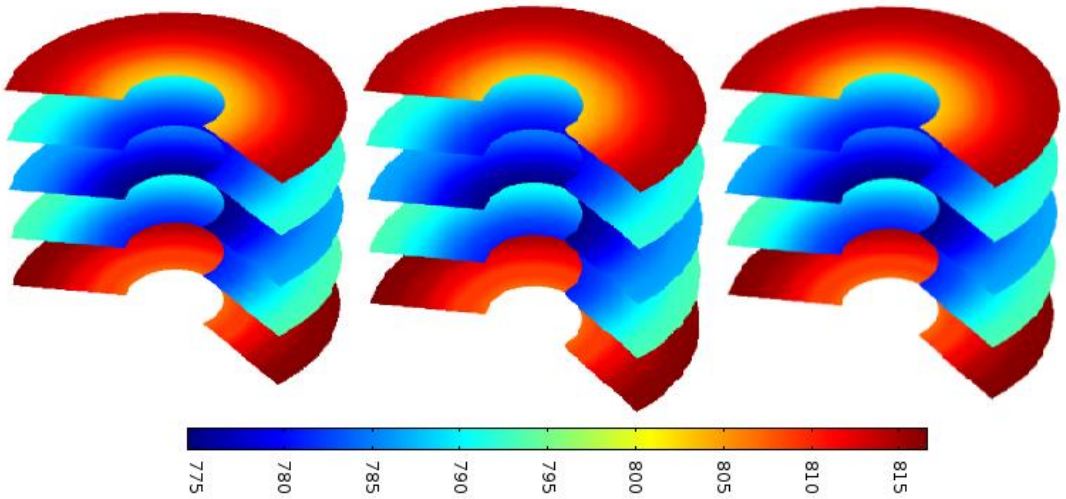


Figure 6.49 Comparison of water concentration distributions of different slices of samples heated by different values of positions: 20mm (left), 40mm (middle), 60mm (right).

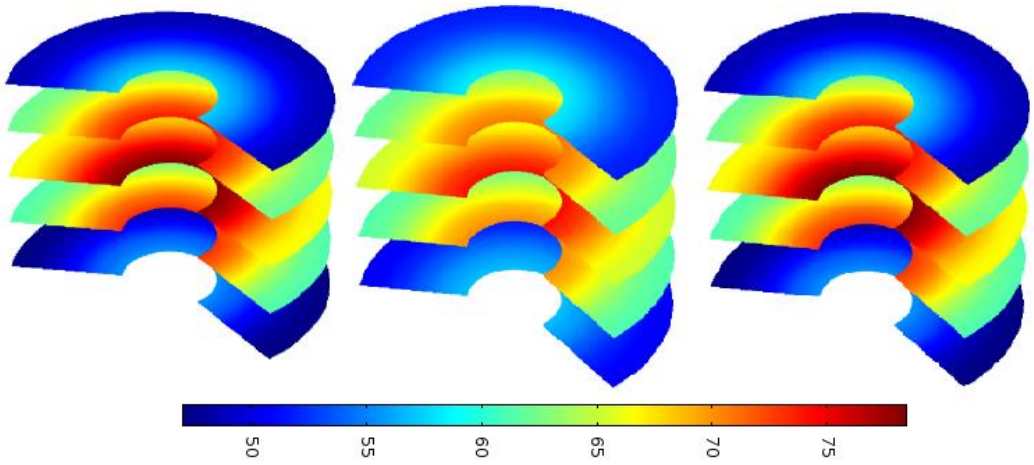


Figure 6.50 Comparison of temperature distributions of different slices of samples heated by different values of positions: 20mm (left), 40mm (middle), 60mm (right)

The figures shown above indicate the effects of locations of samples can be ignorable.

In this sensitivity analysis section, the effects of several important parameters on the simulated results are presented. In fact, the parameters of materials will change during the processing, however, it is very difficult to measure their changes and also unnecessary to take the exact values in the industrial application. In the simulated model, all of the parameters analyzed are set as constant. The controversial between the ideal simulation and reality in experiments may be the dominant reason for the difference of simulated and measured results.

6.2 The optimization of the RF heating model

Our RF heating model is detailed previously. The temperature of treated sample is homogeneous using the proposed model, which may provide an alternative trial to avoid the hot spot and thermal runaway that widely exist in the microwave and RF heating application. Unfortunately, the moisture loss of the heated sample can't be measured in the experiments since our sample has to touch both the conductors of the heating cell. The high-accuracy balance can not measure the total weight of the whole system. However, the moisture loss is the most vital parameter that we are interested in because our target is to dry the materials. Moreover, as mentioned before, the inner and outer surfaces of the potato sample have to contact the device directly, no energy and mass can convect with the ambient. The heat and vapor can be exchanged only through the top and bottom of the material, which limits the drying effect seriously. Therefore, improvements are need.

To obtain the weight of the sample during heating process, the treated material can not touch the conductors. We find that the sample would be heated when it doesn't contact the conductors if the frequency is high enough. However, the electronic field intensity in the sample focuses on a small part near the upper or bottom surfaces rather than generally decreasing from the inner conductor. This will lead to hot spot or thermal runaway easily. Thus, we try to design another model.

Since potatoes are not very large, the heating apparatus should not be very big. Therefore, the higher frequency we use, the smaller the cavity is. However, the equipment should not be very small either. Because the sample had better not touch the metal walls and there should be big enough space between the treated material and apparatus walls for better convection with the ambient environment. Then the working frequency should not be very high. Taking all these factors into consideration, a 800MHz ridge waveguide is chosen to be our new model.

Below is the schematic of the new model. A cut-off waveguide is set on the top surface of this apparatus. The heated sample is fixed in the center of the two ridges by being hung with Teflon wire through the cut-off waveguide. The other end of the wire is connected with a high-accuracy balance that is placed over the ridge waveguide. The power is inserted through a coaxial cable. On both sides of the waveguide, apertures are also installed. The optical fiber sensors can insert inside to measure the point temperature change via the apertures. If these

gaps are not very small, the infrared camera could be even employed to take the temperature distribution of the side face of heated material.

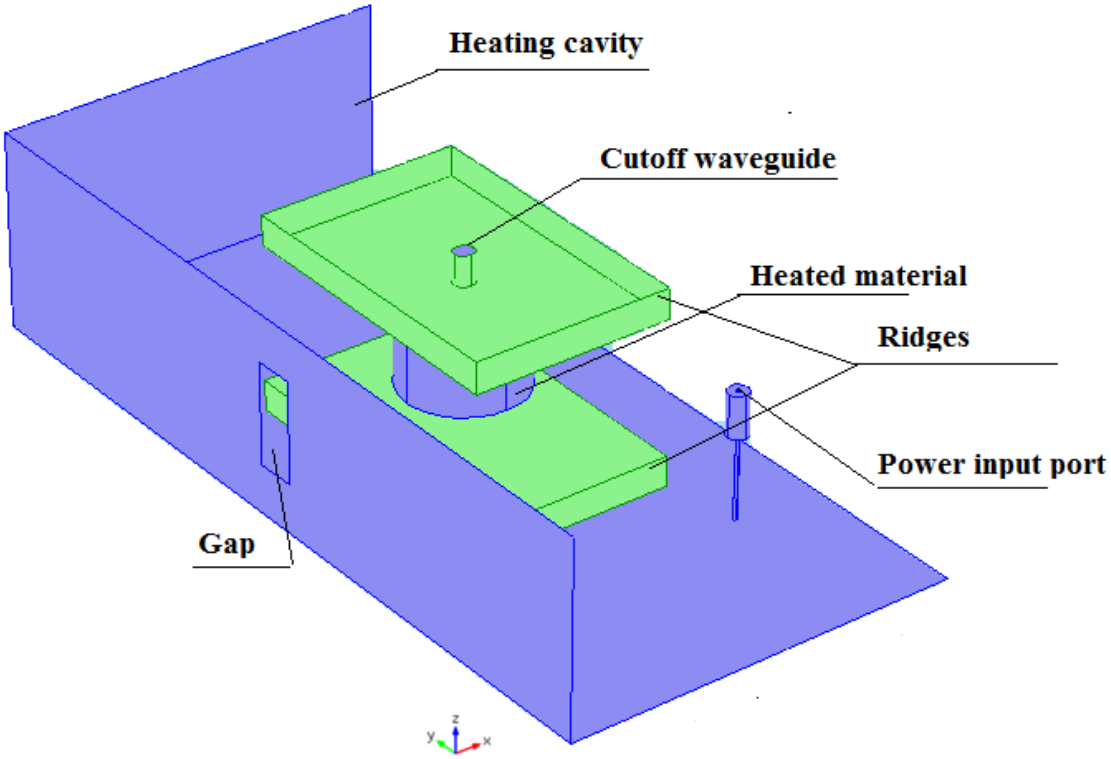


Figure 6.51 Schematic of new model

With this new model, several advantages are expected:

1) Both the moisture loss and temperature change can be measured during the heating process at the same time.

2) With potato sample located between the two ridges, stronger electronic field focuses around the treated material, leading to higher temperature rising.

3) Sample doesn't have to contact the metal walls to be heated. All the surfaces can convect with the ambient air in the cavity, which may lead to more moisture loss.

4) The gaps on the sides might create a free circulation between the air in the cavity and that in the free space. This might keep the air temperature around heated sample almost the same as the room temperature. It is closer to the settings in simulations and guarantee higher temperature gradient of the surfaces and their ambient. More and quicker evaporation may be achieved.

5) Since this model can cause more moisture loss, the integral temperature might be lower than that in our previous model due to the evaporated process consumes heat energy. Therefore, it needs longer to heat the sample up to 70℃. As presented in last chapter, the potato Agata transforms if its temperature reaches about 70℃, making the simulated model invalid. As this model may obtain lower temperature but higher moisture loss, we can predict the process for a longer time and get better drying effect.

6) If more liquid water inside the sample is evaporated out, more serious shrinkage may appear before the quality getting transformed. Therefore, the impact of shrinkage predicted in the simulation can be checked by experiments.

However, this model is just an idea now. It will be studied in the near future. Discontinuities imported by the ridges in the rectangular waveguide are studied now. Several papers [2][3][4] [5] will be referenced to try to remove the discontinuities and guarantee that higher electronic field will focus in the zone between two ridges.

6.3 Conclusion

In this chapter, the sensitivity analyses of 7 very important parameters on heating effects are studied first. We find that the heating effect is sensitive to almost all these parameters except the locations of samples. Although small variation of these parameters may not affect the simulated results with large magnitude, their influences are still non-ignorable. This may partially express the difference of simulated and measured results.

During the sensitivity analysis, we also find that shortening the height of heated sample or increasing the input power can improve the heating effect efficiently, with the former method having higher efficiency. By manipulating the oven design or just simply changing the air velocity around the heated sample, one can modify the mass transfer coefficient and heat transfer coefficient to mend the drying process. Based on this study, a new model is proposed to overcome the existed drawbacks in the previous model. This new design is just an idea now. More researches even realization of this model will be conducted later.

Reference of chapter 6

[1] Haitao Ni, Multiphase moisture transport in porous media under intensive microwave heating, *a dissertation of Cornell University*, 1997.

[2] Jun wu TAO, Contribution a la caracterisation des discontinuites en microondes et application a la sythese de filtre, *PhD thesis of nationa institute of polytechnique in toulouse*, 1988.

[3] Samuel Hopfer, The design of ridged waveguide, *IEEE Trans- MTT*, vol.3, pp. 20-19, 1955.

[4] J. R. Pyle, The cutoff wavelength of the TE_{10} mode in ridged rectangular waveguide of any aspect ratio, *IEEE Trans- MTT*, vol.14, pp. 175-183, 1966.

[5] Seymour B. Cohn, Properties of ridged waveguide, Proc. IEEE, vol. 35, pp 783-788, 1947.

Chapter 7 Conclusions and future work

The object of my dissertation is to study the interaction between RF and porous media and try to propose a model for RF homogeneous heating of porous materials. To achieve these goals, several steps are made.

The literature research is conducted first to learn about the mechanism of porous media like its definition, parameters and their relations. A lot of researchers have developed their models to describe the heat and mass transfer inside porous media. Among them, the mathematical model presented by S. Ben Nasrallah et al. is employed in my research to study heat and mass transfer of 1D brick in order to deepen understanding of the multiphase flow in porous media. Based on this 1D model, the mathematical equations are coupled with Maxwell's equations to investigate the interplay of RF and porous media. Before doing the RF heating simulation, salinity and effective permittivity of the researched sample are estimated due to few data existed in literatures. Experiments are carried out to check the accuracy of RF heating models. Sensitivity analysis are later operated to find the possible reasons to cause the difference between simulated and measured results, and more importantly, to find the improvements of the heating effect.

Several conclusions can be drawn from the study above:

1) Our calculated results of 1D brick are very close to those presented in the reference paper and another researcher's calculated consequences. The temperature, saturation and pressure profiles are theoretically analyzed.
2) Landau and Lifshitz, Looyenga equation is employed as an alternative to predict the effective permittivity change of potato Agata. To estimate a vital parameter in the mixing rule, several samples are shaped and loaded in a coaxial cell to measure the input impedances. Simulations of the corresponding model using Landau and Lifshitz, Looyenga equation with different salinities to update effective permittivities of the samples are also conducted. The salinity of Agata is estimated to be between 0.48% and 0.55% by comparing the measured and simulated data. To further verify the salinity range, a COMSOL combined Matlab code is developed to reverse the measured input impedances into the effective permittivity. The reversed effective permittivity compares qualitatively with those calculated by Landau and Lifshitz, Looyenga equation with salinities from 0.48% to 0.55%.

3) In the heating section, the salinity of potato sample will take the average value of those of the measured samples--0.52%.
4) Heated sample must contact both the inner and outer conductors of coaxial cell under 27.12MHz in our model. Otherwise, the sample won't be heated efficiently. The heating efficiency is better when sample only touches the inner conductor than that of sample only contacting outer conductor. The lager the distance between the sample and walls of coaxial cell, the weaker the heating effect.
5) All the simulated results of RF heating potato Agata compare qualitatively with their corresponding experimental consequences, which verify the accuracy of our RF heating model. Both the predicted and measured results are relatively homogeneous.
6) The location of the potato sample doesn't impact the heating results.
7) Both the variations of input power and height of sample can change the temperature, pressure distributions and moisture loss qualitatively. The more these two parameters vary, the bigger changes emerge. However, the improvements of parameters are not proportional to the changes of results. Comparing to the variation of input power, the same ratio change in height can bring better drying effect. Therefore, in the real world application, one can try to reduce the sizes of treated materials to improve its drying effect rather than purely increasing the heating power.
8) Even though the small variation of porosity and water saturation don't affect the simulated results with large magnitude, their influences are still non-ignorable.
9) The water intrinsic permeability can affect the moisture loss and pressure of the sample. However, its impact on the temperature is much smaller.
10) Both the heat transfer coefficient and mass transfer coefficient can influence the heating effect directly. However, the mass transfer coefficient has a greater contribution to the temperature rising, moisture loss and pressure change, even though the variation of mass transfer coefficient is much smaller than that of heat transfer coefficient. The heating effect of RF treating potato in our model is more sensitive to the mass transfer coefficient. Therefore, experimental measured moisture loss should be taken for better estimation of the mass transfer coefficient.
11) When the temperature reaches about 70 -- 74 degrees, the potato samples transform, making the simulation model invalid. Therefore, these models can only predict well the temperature of potatoes Agata under RF heating before the temperature reaches 70 degrees.

12) With the same total processing time but shorter heating cycles, the heating effects are similar in our model.

Perspective:

Some future works can be done:

1. Realize the new model proposed in chapter 6. Analyze the temperature, pressure distributions and moisture loss during the heating process. Compare the heating effects of the new model and previous model.
2. Implement experiments to measure the temperature and moisture profile. Compare the new simulated and measured results.
3. Take shrinkage into consideration during processing, check its impact on the theoretical results.

List of publications

Journal articles:

Li WU, Junwu TAO, Jean-Louis LACOUT, Tan-Hoa VUONG, Thermal analysis of RF intermittently heating porous media with coaxial cell. (reviewed)

International conference papers:

- Li Wu, Junwu Tao, Jean-Louis Lacout, Christian Chervin, Tan-Hoa Vuong, Jacques David, Comparison of two portable microwave sensors for measuring permittivity of tomatoes at different growth stages,14th international conference on microwave and high frequency heating, Nottingham, Great Britain, ISBN-13 9780853582939, pp,235-238, 2013.
- Li WU, Junwu TAO, Jean-Louis LACOUT, Tan-Hoa VUONG, A model of radio frequency heating potato with coaxial cell, 15th international conference on microwave and high frequency heating , Crakow, Poland, ISBN 987-83-928784-4-5, 2015.
- Li WU, Junwu TAO, Jean-Louis LACOUT, Estimating the salinity and effective permittivity of potato Agata under radio frequency, 15th international conference on microwave and high frequency heating, Crakow, Poland, ISBN 978-83-928784-4-5, 2015.

Vingtaine page de résumé français

1. Introduction

Un milieu poreux est caractérisé par un cloisonnement d'un volume total dans la matrice solide et l'espace des pores, ce dernier pouvant être rempli par une ou plusieurs fluides. Nombreuses substances naturelles telles que des roches et le sol (par exemple, des réservoirs pétroliers), des tissus biologiques (par exemple, des bois, des os), beaucoup d'aliments et des matériaux artificiels comme ciments et céramiques peuvent être considéré comme des milieux poreux. Ils peuvent être vus partout dans notre vie quotidienne, et ils jouent des rôles importants dans la recherche et les applications industrielles.

Avec l'explosion économique et démographique, le besoin en matériaux poreux tels que la nourriture, le bois ou la brique connait une croissance telle que leur commerce est très actif dans le monde entier. La déshydratation des milieux poreux étant l'une des méthodes la plus importante et stable pour leur préservation, elle est utilisé pour stocker, transporter au mieux ces matériaux parce que la plupart de l'eau à l'intérieur a été enlevé.

Avant, la plupart de séchage est basée sur le chauffage conventionnel tel que la vapeur, l'eau chaude, l'air chaud et leurs combinaisons, qui sont utilisés depuis que l'homme a appris l'usage du feu. Ces méthodes de chauffage sont très matures et appliquées partout si la déshydratation est nécessaire. Cependant, la source de l'énergie de chauffage classique ne peut chauffer directement que les surfaces de la matière traitée. Par conséquent des molécules alimentaires commence à réagir en grande partie à partir de la surface vers l'intérieur, de sorte que les couches successives soient chauffées à leurs tours, conduit à un gradient température qui peut brûler l'extérieur du matériau et rarement l'intérieur. Parce que les températures et l'humidité intérieure d'échantillons peuvent être modifiées que par la conduction de chaleur à partir des surfaces, ces processus de séchage exigent énormément de temps, d'énergie et de coût en raison de la chaleur latente de l'eau. En outre, les méthodes traditionnelles peuvent causer plus facilement des problèmes environnementaux. Aujourd'hui, le développement humain est confronté à une crise profonde des sources d'énergie et de l'environnement. Par conséquent, il est nécessaire de trouver des méthodes hautement efficaces pour le traitement de milieux poreux de très grandes dimensions. De nouvelles techniques de séchage sont donc nécessaires pour réduire la consommation d'énergie et de temps de séchage. Pour améliorer cette situation, beaucoup de nouvelles méthodes ont été étudié pour sécher les matériaux poreux : lyophilisation, four à l'air, le séchage sous vide, RF ou micro-ondes séchage….

L'avantage de chauffages par radio fréquence et micro-ondes par rapport aux autres techniques réside dans sa rapidité à atteindre la température désirée . Ceci est particulièrement vrai pour les aliments solides et semi-solides dans lesquels la diffusion thermique est lente par chauffage conventionnel. Il a été prouvé que les chauffages par radio fréquence ou par micro-ondes peuvent être plus homogènes que les chauffages classiques. Toutefois, l'uniformité de chauffage est difficile à prédire.

Nombreux chercheurs se sont concentrés sur le séchage micro-ondes sur une large gamme de milieux poreux dans différents domaines. Il y a jusqu'à présent beaucoup d'informations disponibles dans des articles publiés. Cependant, très peu d'informations disponible dans la littérature sur le chauffage en radio fréquence pour le séchage commercial des milieux poreux, et beaucoup moins installation commerciale en RF par rapport à celles en micro-ondes, malgré le fait que des applications de chauffage RF dans l'industrie alimentaire a été reconnu depuis les années 1940, et malgré les nombreux atouts qu'elle possède. Notre compréhension quantitative est encore limitée, même s'il existe périodiquement des articles de revue sur l'état de l'art du chauffage RF.

En outre, il a été rapporté que le chauffage par radio fréquence pourrait être une alternative intéressante sur le chauffage micro-ondes des milieux poreux en raison des avantages tels que meilleure pour les aliments volumineux et épais, des coûts d'investissement plus faibles, plus facile à comprendre et à contrôler, etc. Laycock, Piyasena et Mittal ont également signalé que le chauffage par radio fréquence à 27,12 MHz pourrait servir à réduire jusqu'à 90% le temps de cuisson de bœuf haché et broyé. Par conséquent, il est très intéressant et nécessaire à effectuer des recherches sur le traitement de matériaux poreux par radio fréquence. Pourtant, les chercheurs ont indiqué que le chauffage RF peut aussi conduire à la distribution inégale de la température avec l'existence de point chaud ou emballement thermique. Heureusement, ces problèmes pourraient être améliorés par un autre avantage du chauffage RF.

Cet autre avantage des systèmes de chauffage RF est qu'ils peuvent être activés ou désactivés immédiatement. Les mérites de chauffage intermittent sont connues pour une grande variété de matériaux avec ou sans l'énergie électromagnétique. Cela a été rapporté que le chauffage périodique abouti à une plus grande profondeur de chauffage que le chauffage continue avec le même apport d'énergie totale. En outre, le chauffage RF par intermittence conduit à une distribution de température plus homogène à l'intérieur de l'échantillon que le chauffage continue. Cela peut améliorer la qualité du produit, l'efficacité des processus et être une

solution alternative potentielle pour résoudre le problème des points chauds et l'emballement thermique.

Par conséquent, le chauffage radio fréquence présente un potentiel prometteur. Dans ma thèse, j'essaie de proposer un modèle de chauffage des milieux poreux par radio fréquence intermittent. Pour obtenir une distribution de température plus uniforme et de réduire l'exigence de calcul, une cellule coaxial a été utilisé comme l'équipement de chauffage. Comme mentionné ci-dessus, nombreux chercheurs se concentrent sur le chauffage micro-ondes. Les informations sur le paramètre essentiel qui détermine l'interaction entre des matériaux et radio fréquence –permittivité effective-est rare. Ainsi, un procédé d'estimation de la permittivité effective du milieu poreux est également proposé. Pomme de terre est choisie comme l'objet de recherche car ses paramètres structuraux sont disponibles dans des littératures.

Les objets de ma thèse sont les suivants :

1) Proposer un modèle multi-physique pour chauffer des milieux poreux par radio fréquence avec une cellule coaxial.
2) Etudier l'interaction de radio fréquence et des milieux poreux. Analyser comment la masse et la chaleur transportent à l'intérieur de l'échantillon pendant le chauffage de radio fréquence.
3) Développer un système expérimental pour mesurer la distribution de la température et changement de l'humidité de vérifier les résultats de la simulation.
4) Etudier et analyser quels sont les paramètres ayant une forte incidence sur les effets de chauffage.
5) Essayer d'améliorer le système de chauffage radio fréquence.

L'interaction entre énergie radio fréquence et des milieux poreux est très compliquée. Pour comprendre mieux le mécanisme d'énergie radio fréquence chauffant des milieux poreux, les principes décrivant le transfert de la masse et de chaleur dans les matériaux sous le chauffage par convection sont étudiés les premiers.

2. L'étude numérique sur le transfert multi-phase sous chauffage convectif

2.1 Modèle mathématique

Plusieurs chercheurs ont développé des équations de transfert de la chaleur et de la masse pour des matériaux poreux à partir des équations de conservation et des modèles de la mécanique de fluide. Dans cette section, les formules présentées dans l'article de S. Ben

Nasrallah sont employées pour étudier le transfert de la masse et de la chaleur dans le modèle de brique unidimensionnel avec chauffage par convection.

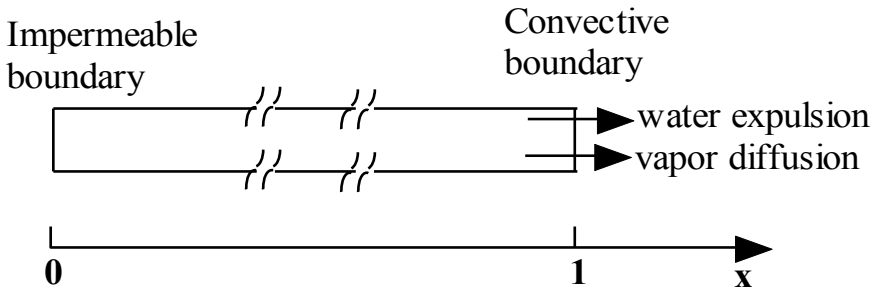


Figure 1 Schéma du modèle de brique 1D

Un schéma de modèle de brique 1D est montré dans la figure 1, sous forme d'une plaque plate poreuse. Le côté gauche de la plaque est exposé à un flux d'air avec la vitesse, température et l'humidité relative fixe. L'échange d'énergie et d'humidité entre l'échantillon et l'espace extérieur aura lieu de ce côté. L'autre côté est adiabatique et imperméable, où des fluxes de l'énergie et l'humidité sont égal à zéro.

Les équations de conservation pour la vapeur, l'eau liquide, mélange gazeux et la chaleur dans le milieu poreux sont écrites, respectivement, comme:

$$\frac{\partial \rho_v}{\partial t} + \frac{\partial}{\partial x}\left(\rho_v \overrightarrow{u_v} - \rho_g D_{eff,g} \frac{\partial}{\partial x}\left(\frac{\rho_v}{\rho_g}\right)\right) = I \tag{1}$$

$$\frac{\partial \rho_w}{\partial t} + \frac{\partial}{\partial x}\left(\rho_w \overrightarrow{u_w}\right) = -I \tag{2}$$

$$\frac{\partial \rho_g}{\partial t} + \frac{\partial}{\partial x}\left(\rho_g \overrightarrow{u_g}\right) = I \tag{3}$$

$$\frac{\partial}{\partial t}\left(\overline{\rho C_p} T\right) + \frac{\partial}{\partial x}\left(\rho_w C_{p,w} \overrightarrow{u_w} T + \sum_{j=v,a} \rho_j C_{p,j} \overrightarrow{u_j} T\right) = \frac{\partial}{\partial x}\left(k_{eff} \frac{\partial T}{\partial x}\right) - \Delta h_{vap}^{\circ} I \tag{4}$$

Où

$$\Delta h_{vap}^{\circ} = \Delta h_{vap} + (C_{p,w} - C_{p,v})T \tag{5}$$

$$\overline{\rho C_p} = \rho_s C_{p,s} + \rho_w C_{p,w} + \rho_v C_{p,v} + \rho_a C_{p,a} \tag{6}$$

L'équation (1) est ajoutée à (2), ce qui élimine le changement de phase I. La nouvelle équation et l'équation (3) et (4) peuvent être réorganisés et simplifiés dans les formules des variables de saturation d'eau S_w, de la température T et pression totale de gaz P.

$$K_4 \frac{\partial S_w}{\partial t} + K_5 \frac{\partial T}{\partial t} + K_6 \frac{\partial P}{\partial t} = \nabla(K_1 \nabla S_w) + \nabla(K_2 \nabla T) + \nabla(K_3 \nabla P) \tag{6}$$

$$K_{10}\frac{\partial S_w}{\partial t}+K_{11}\frac{\partial T}{\partial t}+K_{12}\frac{\partial P}{\partial t}=\nabla(K_7\nabla S_w)+\nabla(K_8\nabla T)+\nabla(K_9\nabla P) \quad (7)$$

$$K_{16}\frac{\partial S_w}{\partial t}+K_{17}\frac{\partial T}{\partial t}+K_{18}\frac{\partial P}{\partial t}=-\nabla\cdot\left(\left(\rho C_p\vec{u}\right)_{fluid}T\right)+\nabla(K_{13}\nabla S_w)+\nabla(K_{14}\nabla T)+\nabla(K_{15}\nabla P) \quad (8)$$

Les relations suivantes définissent les conditions aux limites de type convectif à droite et de type isolé à gauche :

Limite isolé :

$$-K_1\nabla S_w-K_2\nabla T-K_3\nabla P=0 \quad (9)$$

$$-K_7\nabla S_w-K_8\nabla T-K_9\nabla P=0 \quad (10)$$

$$-k_{eff}\nabla T=0 \quad (11)$$

Limite convectif :

$$-K_1\nabla S_w-K_2\nabla T-K_3\nabla P=\phi\left(\frac{p_vM_v}{RT}-\rho_{v0}\right)h_m \quad (12)$$

$$P=P_{amb} \quad (13)$$

$$-K_{13}\nabla S_w-K_{14}\nabla T-K_{15}\nabla P=(T-T_{amb})h_t \quad (14)$$

La méthode des différences finies a été utilisée pour discrétiser le système d'équations différentielles (6)-(8) avec différence centrale dans l'espace et le schéma de Crank-Nicolson dans le temps. Nos résultats calculés avec une discrétisation de 60 éléments uniformes sont comparés avec ceux de même modèle calculés par autres chercheurs.

2.2 Résultats et discussion

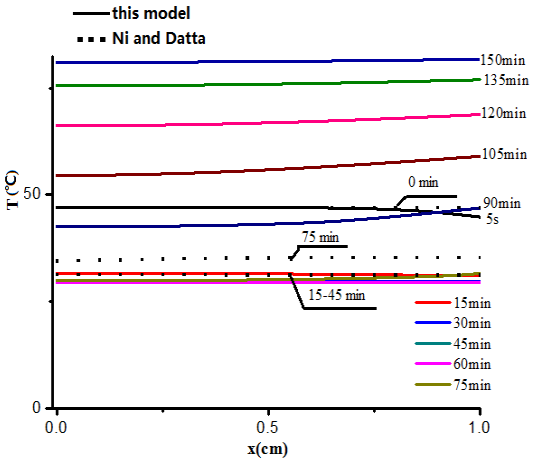


Figure 2 Températures calculés par Matlab

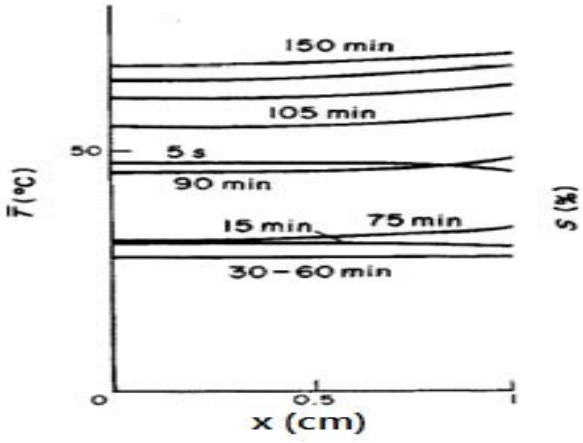


Figure 3 Températures selon Nasrallah

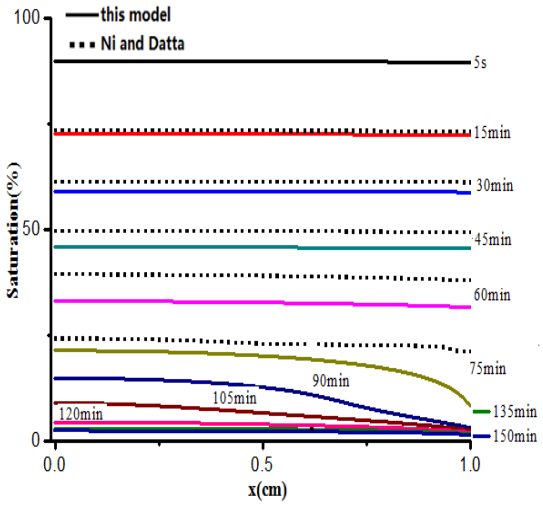


Figure 4 Saturations calculés par Matlab

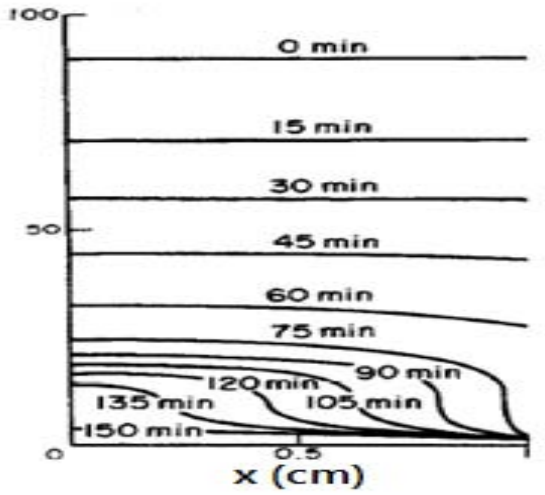


Figure 5 Saturations selon Nasrallah

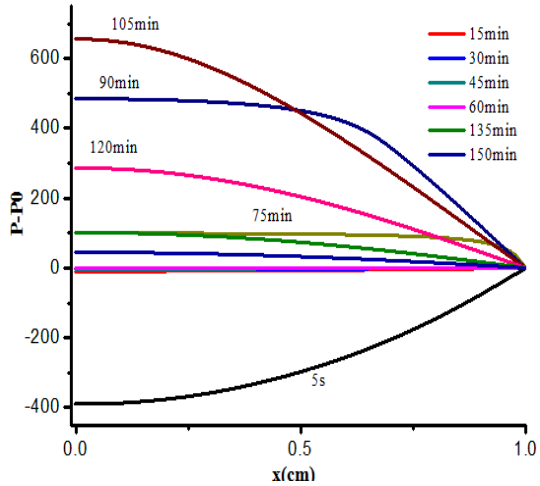


Figure 6 Pressions calculés par Matlab

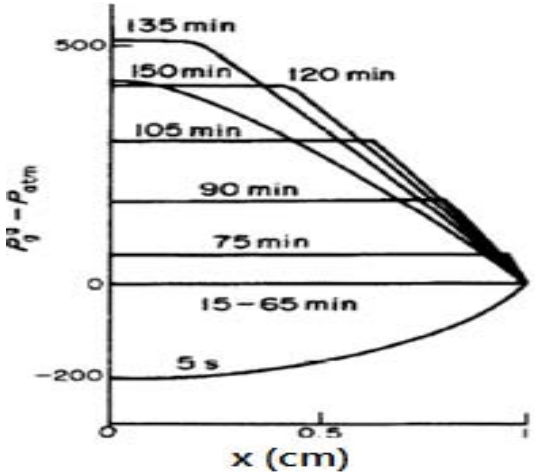


Figure 7 Pressions selon Nashrallah

Les figures ci-dessus montrent nos résultats numériques sur la variation dans l'espace et dans le temps des 3 variables d'état : température, saturation et pression totale, ainsi que la comparaison avec des résultats de références. Il est évident que les résultats calculés sont accord qualitatifs avec ceux figurés dans le document de référence ; la tendance de changement et les valeurs étant très comparables. Ni et Datta ont travaillé sur le même problème avec un système d'équations similaire que le notre, et ont publié leurs résultats dans un article. Pour réaliser une double validation les résultats obtenus par Ni er Datta sont également montré dans les figures 2 et 4 en trait pointillé. On peut observer que les résultats dans ces deux figures sont très proches. Il convient de noter que nos résultats numériques sont plus proches de ceux présentés par Nasrallah comparant les résultats présentés par Ni et Datta.

Cependant, nous devrions également remarquer qu'il existe encore des différences entre nos résultats et ceux de Nasrallah. La saturation de l'eau près de la surface prédit par notre modèle est plus progressive que la leur et il existe des divergences dans les pressions. Les raisons qui causent la différence entre nos résultats et ceux référencés sont peut-être: 1) la différence des schémas de discrétisation. Nous utilisons des différences finies uniformes alors que Nasrallah a développé une différence finie non uniforme de façon à avoir des maillages denses près de la frontière ouverte ; 2) le document référencé a utilisé différence centrée dans l'espace et une formulation totalement implicite de la différenciation dans le temps; notre recherche, cependant, n'a pas utilisé une autre méthode particulière mais la méthode de Crank-Nicolson pour discrétiser le terme convectif ; 3) lors du calcul des coefficients des équations, les traitements des termes futures de coefficients entre nous et Nasrallah durant le processus de résolution peut être différentes, ce qui conduit à des écarts minuscules pour les résultats calculés et celle de référence.

Dans cette section, les milieux poreux sont traités comme des compositions de trois phases : gaz, liquide et solide. Un modèle unidimensionnel du chauffage d'un matériau poreux tel que brique a été étudié par le transfert convectif de masse et de chaleur. Les résultats numériques montrent un accord qualitatif avec ceux publiés par S. Ben Nasrallah et Haitao Ni. La précision sur les rapports entre différents paramètres ainsi que des hypothèses a été vérifiée. Les équations de Maxwell seront ajoutées aux théories déjà utilisées dans le précédent modèle 1D, et couplés avec ces dernières pour étudier l'interaction des RF et des milieux poreux. Parce qu'il n'est pas facile à préparer le brique dans des formes imposées et ses paramètres sous chauffage RF ne sont pas entièrement connus, nous décidons d'utiliser la pomme de terre pour poursuivre notre recherche.

Les propriétés diélectriques des matériaux sont très importants dans la détermination du mécanisme d'interaction entre l'énergie d'électromagnétique et les matériaux dans la gamme des fréquences RF ou micro-ondes. En partant de l'objectif de chauffage RF des milieux poreux tel que pomme de terre, il est nécessaire de disposer des données précises sur la permittivité de celle-ci. Jusqu'à présent, nombreux chercheurs ont réalisé des mesures des permittivités effectives sur un grand nombre de matériaux. Toutefois, la plupart des mesures ont été effectuées dans des gammes micro-ondes. Il existe seulement de nombres limités de données dans la littérature sur la permittivité de la pomme de terre en fréquences RF. En plus, ces données mesurées sont essentiellement celles de pomme de terre de Russett Burbank produit aux Etats-Unis, et rien sur les pommes de terre de type Agata, disponible sur le

marché de Toulouse et utilisé dans notre recherche. Il est par conséquent nécessaire d'obtenir la permittivité effective d'Agata.

3. Mesure de la permittivité effective de la pomme de terre Agata

Le terme permittivité implique la permittivité relative complexe, i.e. la permittivité d'un matériau par rapport à l'espace libre. Elle est souvent appelée la constante diélectrique complexe, qui est exprimée en $\varepsilon_r = \varepsilon_r' - i\varepsilon_r''$, où ε_r' est la constante diélectrique, et ε_r'' est le facteur de perte diélectrique. La constante diélectrique est associé à la capacité de stockage de l'énergie dans le champ électrique dans les matériaux. Le facteur de perte présente une dissipation d'énergie dans le matériau ou la conversion d'énergie électrique en l'énergie thermique. Ici, tous les mécanismes de perte, celles dues aux relaxations dipolaires et à la conduction ionique, sont inclus dans le facteur de perte diélectrique.

La permittivité du milieu poreux est supposée être une fonction de la température, de la fréquence et de la teneur en humidité qui sont en corrélation les unes aux autres. La variation d'un paramètre va influencer sur les autres. Il est presque impossible de vérifier la relation entre un facteur et la permittivité effective sans modifier les autres facteurs. En plus, même si certaines mesures pourront être effectuées, la déduction des propriétés diélectriques exactes pour les matériaux poreux est une entreprise difficile voire impossible. Il est par exemple très difficile d'obtenir la température et la distribution de l'humidité uniforme dans l'échantillon poreuse en raison de sa structure non homogène, ce qui conduit à une mesure inexacte. Pour certains matériaux, l'usinage des échantillons aux dimensions exactes requises pour la mesure des propriétés diélectriques est également difficile. Par conséquent, les règles de mélange semblent être une approche alternative intéressante car il a été rapporté que les règles de mélange approchent des propriétés dans une certaine mesure d'être utilisé dans le travail du monde réel.

3.1 L'équation de Laudau, Lifshitz et Looyenga

Jusqu'à présent, beaucoup d'équations de mélanges diélectriques différentes ont été proposées pour prévoir la permittivité effective de mélanges, tels que l'équation d'indice de réfraction complexe, l'équation de Landau et Lifshitz, Looyenga, l'équation Bottcher, l'équation de Rayleigh et ainsi de suite. Nombreux chercheurs ont évalué les performances de ces différentes méthodes pour estimer la permittivité effective de mélange. Il a été conclu que l'équation de Landau et Lifshitz, Looyenga semble être le choix recommandés pour une utilisation pratique avec des mélanges. Par conséquent, nous décidons d'utiliser l'équation de

Landau et Lifshitz, Looyenga pour prédire le changement de permittivité effective dans notre modèle.

L'échantillon de pomme de terre se compose de l'eau salé, solide et gaz. Sa propriété diélectrique est donnée par :

$$\varepsilon_{r,eff}^{1/3} = \upsilon_w \varepsilon_{r,w}^{1/3} + \upsilon_s \varepsilon_{r,s}^{1/3} + \upsilon_g \varepsilon_{r,g}^{1/3} \quad (15)$$

Où $\varepsilon_{r,eff}$ est la permittivité effective de la pomme de terre, $\varepsilon_{r,w}$, $\varepsilon_{r,s}$, $\varepsilon_{r,g}$ représentent respectivement la permittivité de l'eau salé, solide et gaz. υ_w, υ_s, υ_g sont les fractions volumiques correspondant. Stogryn modèle est choisi pour décrire la propriété diélectrique de l'eau salé dans l'échantillon de pomme de terre.

Malheureusement, la salinité de pomme de terre Agata, qui joue un rôle critique dans la détermination de la permittivité du mélange, est inconnue. Donc, nous devons trouver un moyen pour estimer la salinité de l'échantillon de pomme de terre.

Des chercheurs ont prédit la salinité de plusieurs types de matériaux par des mesures de la propriété diélectrique de ces échantillons et par la recherche de la corrélation entre la teneur en sel et la permittivité. Inspiré par ces articles, nous décidons de mesurer les paramètres S de l'ensemble du système sous différentes fréquences et d'obtenir les impédances d'entrées correspondantes. La salinité de la pomme de terre Agata est estimée plus tard par comparant les impédances d'entrées mesurés et simulés.

Il existe beaucoup de méthodes de mesure des propriétés diélectriques. Les techniques les plus couramment utilisés pour la mesure de la permittivité à des fréquences micro-ondes comprennent des méthodes de sondes en guide ouvert, des méthodes de ligne de transmission, des méthodes de cellules résonantes, celle d'espace libre à l'aide d'antenne cornet, des méthodes de réflectométrie dans le domaine temporelle, et ainsi de suite. Chacune de ces techniques de mesure peuvent être conçue pour fonctionner dans une gamme spécifique de fréquences micro-ondes. Sur la base des techniques existantes, une cellule coaxiale a été développée pour la mesure de pomme de terre Agata.

3.2 Méthode de mesure développée par LAPLACE

Voici une image sur le système de mesure avec la cellule coaxiale (Figure 8). La taille de la cellule coaxiale utilisée dans notre recherche n'est pas standard. Une transition conique est nécessaire pour connecter la cellule de grande taille et de connecteur standard de type N équipé avec l'analyseur de réseau vectoriel. La transition conique employée n'est pas non plus

un accessoire standard. Pour obtenir les paramètres des échantillons de pommes de terre plus précisément, nous décidons de mesurer les paramètres caractéristiques de la transition conique et puis d'éliminer ses effets des paramètres diélectriques mesurés de l'ensemble de système. Le processus de la façon d'éliminer les effets de transition conique est adressé ci-dessous.



Figure 8 L'image d'équipement de mesure

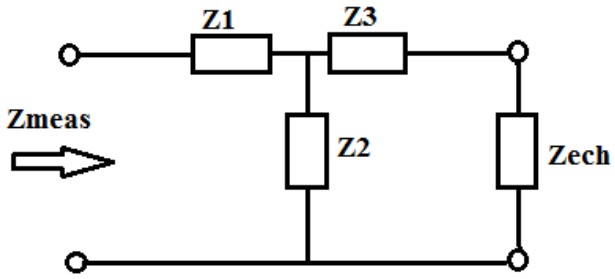


Figure 9 Circuit équivalent du système de mesure

$$Z_{ech} = \frac{(Z_{meas}-Z_1)(Z_2+Z_3)-Z_2Z_3}{Z_2-(Z_{meas}-Z_1)} \quad (16)$$

Après avoir effectué les mesures, les impédances d'entrées de la cellule chargée sont déduites selon l'équation 16. Nous essayons de comparer les impédances d'entrées mesurées et celles simulées pour estimer la salinité de la pomme de terre Agata. Datta et al. a rapporté que la salinité de pomme de terre Russett Burbank produite aux Etats-Unis est d'environ 0,75%. Par conséquent, une code combiné Matlab et COMSOL est développée pour calculer les impédances d'entées de la cellule chargée lorsque la permittivité effective de l'échantillon est prédite par l'équation Landau, Lifshitz et Looyenga avec différentes salinités d'environ 0,75%.

3.3 Résultats et discussion

La comparaison des résultats calculés et mesurés sont montrées dans la Figure 10. "Sample 1, 2,...6" indique l'impédance d'entrée de chaque échantillon de pomme de terre déduite des données mesurées, " $S = 0.48$, …, $S = 0.75$ " présentent les impédances d'entrées avec différents salinités: 0.48%, …, 0.75%. Les données mesurées ne sont pas les mêmes, mais

heureusement, la différence n'est pas énorme. Ceci est normal car chaque pomme de terre est unique dans le monde. Sa salinité, la porosité et la saturation en eau d'une pomme de terre doivent être différentes que celles d'autres.

De la comparaison des impédances d'entrées représentées sur la Figure 10, il est évident que les salinités de tous les échantillons de pommes de terre utilisées dans la mesure ne sont pas 0,75%, mais plutôt dans la gamme de 0,48% à 0,6%.

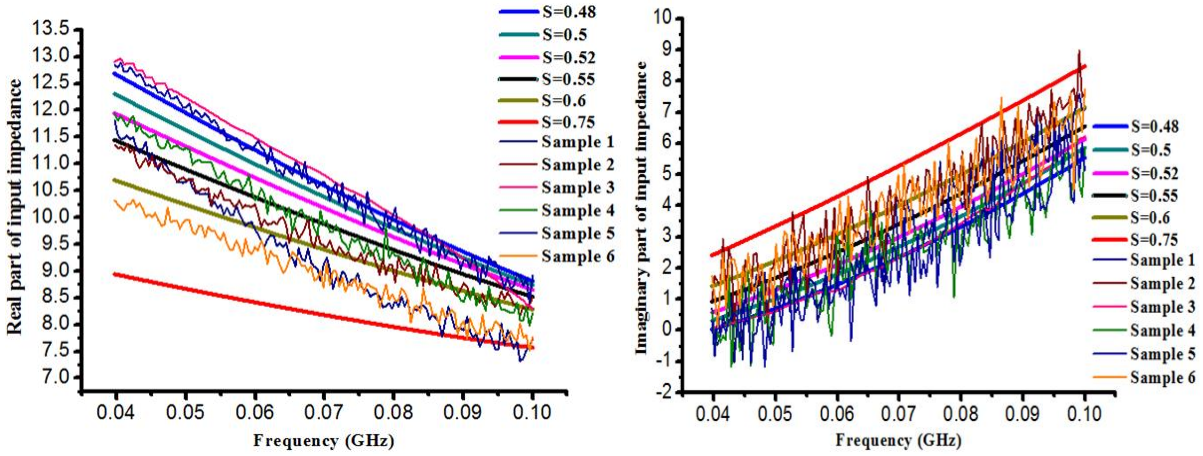


Figure 10 Comparaison des impédances d'entrées mesurées et simulées:

(à gauche) partie réelle, (à droite) partie imaginaire

Pour étudier la permittivité effective de la pomme de terre Agata, une modélisation inverse a été réalisée en comparant les impédances d'entrées mesurées sur plusieurs points de fréquences pour chaque échantillon et celles simulées à l'aide du logiciel COMSOL. La procédure d'optimisation a été implantée sous MATLAB en lien avec COMSOL. Les résultats extraits sont énumérés dans le tableau 1.

Tableau 1. Les permittivités effectives des échantillons mesurées

Freq	Sample 1		Sample 2		Sample 3		Sample 4		Sample 5		Sample 6	
(GHz)	Real	Imag.	Real	Imag.	Real	Imag.	Real	Imag.	Real	Imag.	Real	Imag.
0.0411	66.7	198.0	62.2	232.0	64.3	198.8	65.0	200.0	62.0	190.5	64.5	238.0
0.0501	64.7	165.0	60.5	190.0	62.5	160.5	63.0	162.0	61.0	155.0	63.5	195.0
0.0591	63.7	144.0	59.8	161.0	61.5	136.0	62.3	138.0	60.4	131.0	62.9	165.0
0.0681	63.2	130.0	59.3	143.0	60.8	119.0	61.7	120.5	60.1	115.8	62.4	145.0
0.0771	62.9	120.0	58.9	130.0	60.3	106.0	61.5	107.0	59.8	103.3	62.1	131.0
0.0860	62.6	112.0	58.7	118.0	60.0	97.0	61.4	95.0	59.5	93.0	62.0	117.0
0.0951	62.4	107.0	58.4	110.0	59.9	92.0	61.3	85.0	59.3	86.0	62.0	106.0

Les permittivités effectives de notre mesure dans le tableau 1 montrent les mêmes tendances de variation en fréquence que celles de la pomme de terre Rusett Burbank mesurées par S.

Nelson, avec des valeurs dans les mêmes ordres de grandeur. Même si que cela est un autre type de la pomme de terre, la salinité et d'autre paramètres peuvent être différents, ses valeurs, cependant, sont encore consultatives. Cela pourrait prouver que les résultats estimés sont raisonnables et recevables.

Pourtant, nous devons admettre que la gamme estimée de la salinité ne peut pas comprendre parfaitement tous les cas d'échantillons de pommes de terre. Comme la partie réelle de l'impédance d'entrée de l'échantillon 6 dans la figure 10, la courbe se situe clairement en dehors de celles mesurées des échantillons. En fait, ce phénomène est explicable parce que plusieurs facteurs pourraient influencer les résultats de mesures. Dans les expériences, il est impossible de réaliser l'échantillon avec la dimension exacte que celle prévue dans la simulation. Les surfaces des échantillons ne sont pas idéalement lisses, ce qui conduit à des contacts imparfaits entre l'échantillon et les conducteurs de la cellule coaxial. Il y a certainement des variations d'autre paramètres au sein d'échantillons de pommes de terre utilisés; Mais dans la simulation, les paramètres de toutes les échantillons de pommes de terre sont les mêmes et idéals. Tous ces facteurs vont introduire des écarts entre les résultats simulés et mesurés.

Pour estimer la gamme de salinité des échantillons des pommes de terre Agata, les moyennes des données mesurés sont présentées et comparées avec celles calculées avec des salinités de 0,48% à 0.55% dans le tableau 2. Il est évident que la moyenne des salinités des échantillons des pommes de terre est entre 0,48% et 0,55%. En tenant compte de toutes les comparaisons ci-dessus et des difficultés existent dans les expériences, nous pouvons conclure que la salinité de la pomme de terre Agata peut être comprise entre 0,48% et 0,55%.

Tableau 2 Comparaison de moyenne de permittivité effective mesurée et celles simulées

Freq	S=0.48%		S=0.55%		S=0.52%		Measure ave. data	
(GHz)	Real	Imag.	Real	Imag.	Real	Imag.	Real	Imag.
0.0411	62.7	195.2	64.5	223.8	63.1	210.9	64.1	209.6
0.0501	61.6	160.9	63.2	184.4	61.9	173.8	62.5	171.3
0.0591	60.8	136.9	62.2	157.0	61.1	147.9	61.8	145.8
0.0681	60.2	119.2	61.5	136.7	60.4	128.7	61.3	128.9
0.0771	59.8	105.6	61.0	121.1	60.0	114.1	60.9	116.2
0.0860	59.4	94.8	60.6	108.8	59.6	102.4	60.7	105.3
0.0951	59.2	86.0	60.2	98.7	59.3	92.9	60.6	97.7

Il est également intéressant de remarquer que la moyenne de la permittivité effective est très proche de celle calculée avec la salinité de 0,52%. Par conséquent, dans la section suivante sur le chauffage, la salinité de l'échantillon de pomme de terre prendra la valeur moyenne de celles des échantillons mesurés—0,52%. Même s'il peut exister des différences entre la valeur estimée et celle réelle, la valeur moyenne est encore acceptable et utile pour le chauffage des pommes de terre Agata dans des applications réelles. Cela sera prouvé dans la section suivante en comparant les distributions de température mesurées et simulées sur des échantillons chauffées par radiofréquence.

4. Un modèle 2D axisymétrique de radiofréquence chauffant des pommes de terre par intermittence

4.1 Modèle de la simulation

La figure 11 montre le schéma de modèle 2D axisymétrique de radiofréquence chauffant des pommes de terre par intermittence. Le cylindre extérieur se prolonge au delà d'extrémité du conducteur interne et dans la région il agit comme le mode TM_{01} d'un guide d'onde circulaire sous coupure. Le bleu indique l'échantillon de pomme de terre qui est façonnée dans la forme annulaire et fixée entre le conducteur interne et externe. La puissance RF est appliquée à l'entrée supérieure avec une fréquence de 27,12MHz. Le fond de la cellule est ouvert, modélisé avec des conditions aux limites de type diffusion.

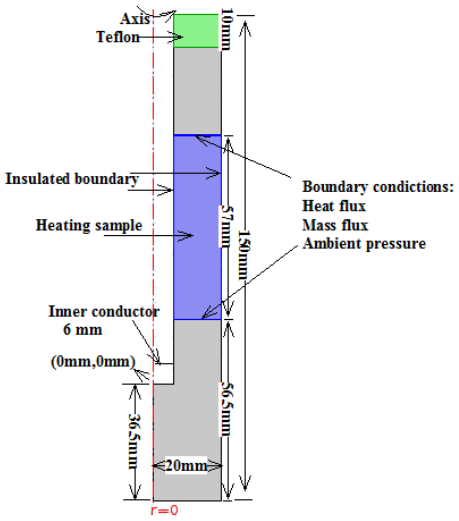


Figure 11 Le schéma de modèle 2D axisymétrique

$$\nabla \times \mu_r^{-1}\left(\nabla \times \vec{E}\right) - k_0^2 \varepsilon_r \vec{E} = 0 \qquad (17)$$

$$\frac{\partial}{\partial t}(\varphi\rho_w S_w) + \nabla\cdot(\overrightarrow{u_w}\rho_w) - \nabla\cdot\left(\mathrm{D_c}\nabla(\varphi\rho_w S_w)\right) = -I \tag{18}$$

$$\frac{\partial}{\partial t}\left(\varphi\rho_g S_g\right) + \nabla\cdot\left(\rho_g\overrightarrow{u_g}\right) = I \tag{19}$$

$$\frac{\partial}{\partial t}\left(\varphi\rho_g S_g\omega_v\right) + \nabla\cdot\left(\overrightarrow{u_g}\rho_g\omega_v\right) = \nabla\cdot\left(\varphi S_g\frac{C_g^2}{\rho_g}M_a M_v D_{eff,g}\nabla x_v\right) \tag{20}$$

$$\frac{\partial}{\partial t}(\rho_{eff}C_{p,eff}T) + \nabla\cdot\left(\left(\rho C_p\vec{u}\right)_{fluid}T\right) = \nabla\cdot\left(k_{eff}\nabla T\right) - \lambda I + Q \tag{21}$$

B.C. pouréqu.18: $\overrightarrow{n_{w,surf}} = h_m\varphi S_w\left(\rho_v - \rho_{v,cell}\right) + \rho_w\overrightarrow{u_w}$ (when $S_w = 1$) (22)

B.C. pouréqu.19: $P_{surf} = P_{amb}$ (23)

B.C. pouréqu.20: $\overrightarrow{n_{v,surf}} = h_m\varphi S_g\left(\rho_v - \rho_{v,cell}\right) + \rho_v\overrightarrow{u_v}$ (when $S_w = 1$) (24)

B.C. pouréqu.21:

$$q_{surf} = h_t\left(T_{cell} - T_{surf}\right) - \tau\overrightarrow{n_{w,surf}} - \left(\overrightarrow{n_{w,surf}} + \overrightarrow{n_{v,surf}}\right)C_{p,v}T - \rho_w\overrightarrow{u_w}C_{p,w}T \tag{25}$$

4.2 Des expériences

Des pommes de terre Agata sont achetées sur le marché de Jeanne d'arc à Toulouse. Ils sont stockés en la température ambiante pendant plus de 24 heures avant de faire des expériences. Un équipement annulaire personnalisé est à nouveau utilisé pour couper des échantillons.

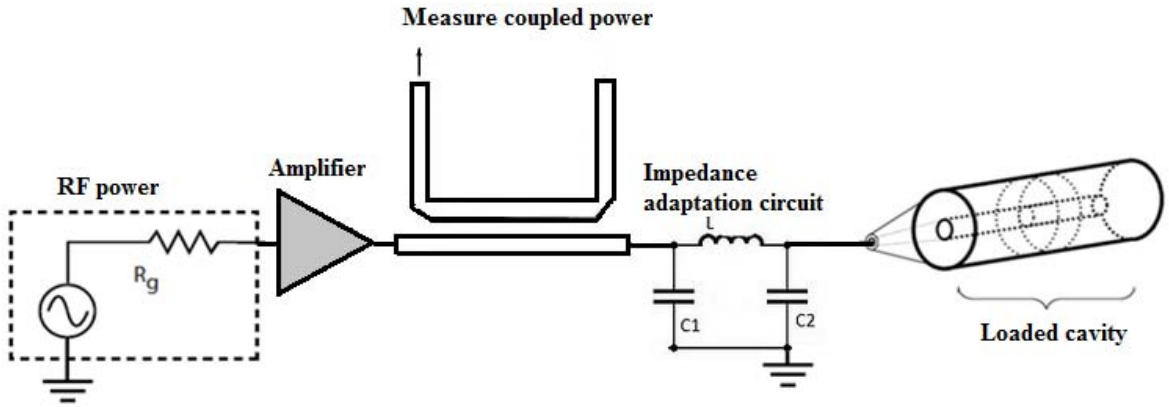


Figure 12 Schéma d'équipement expérimental

Ont été étudiés et analysés les effets de variation sur la période de processus, la hauteur de l'échantillon et de la puissance sur les distributions de température. Les expériences correspondantes sont également menées pour mesurer la variation de température pendant le

processus de chauffage. Les comparaisons des résultats simulées er mesurées sont faites dans cette section. Toutes les expériences dans chaque cas sont répétées deux fois.

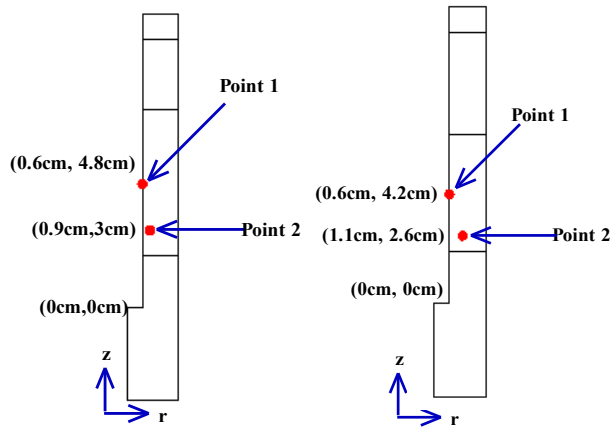
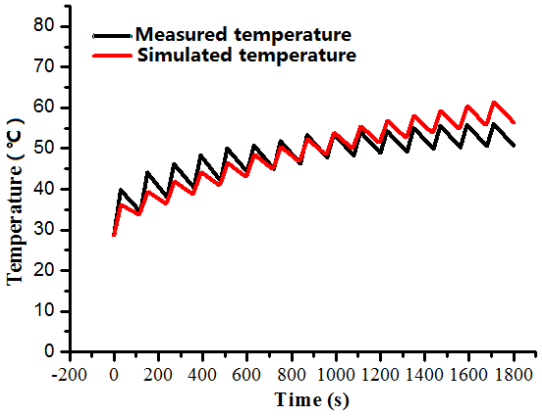


Figure 13 Positions des deux points pour mesurer la température : hauteur de l'échantillon est de 57mm (à gauche); la hauteur de l'échantillon est de 45mm (à droite)

4.3 Résultats et discussion

Quatre cas de simulations sont effectués et comparées avec les résultats expérimentaux:

Cas 1: échantillon avec hauteur 57mm; cycle de chauffage 30s puis de refroidissement 1min 30s. La puissance du générateur est 50W.



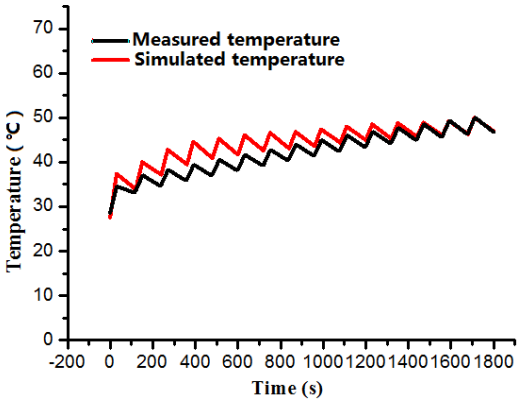


Figure 14 Changement de température du point 1 Figure 15 Changement de température du point 1

Cas 2: échantillon de hauteur 57mm; cycle de chauffage 15s puis refroidissement 45s. La puissance est 50W.

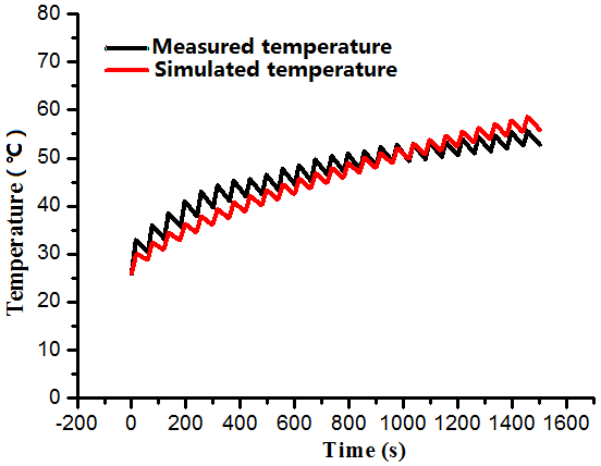


Figure 16 Changement de température du point 1

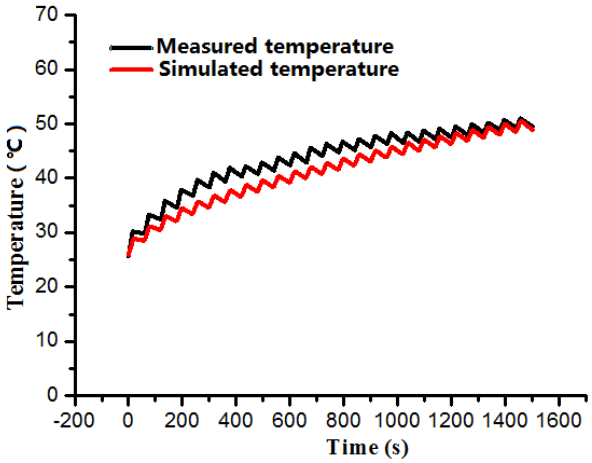


Figure 17 Changement de température du point 2

Cas 3: échantillon de hauteur 57mm; cycle de chauffage 15s puis refroidissement 45s. La puissance est 100W.

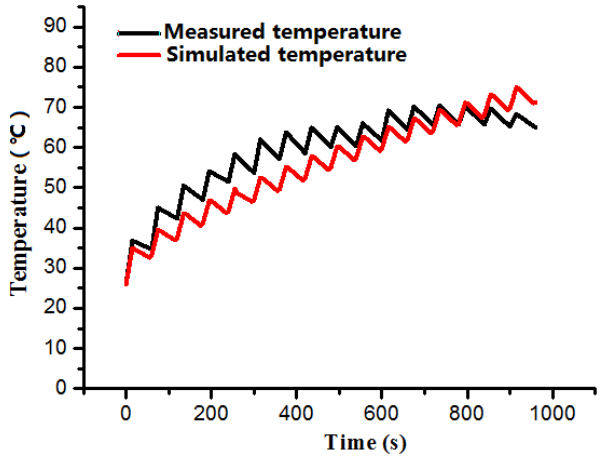


Figure 18 Changement de température du point 1

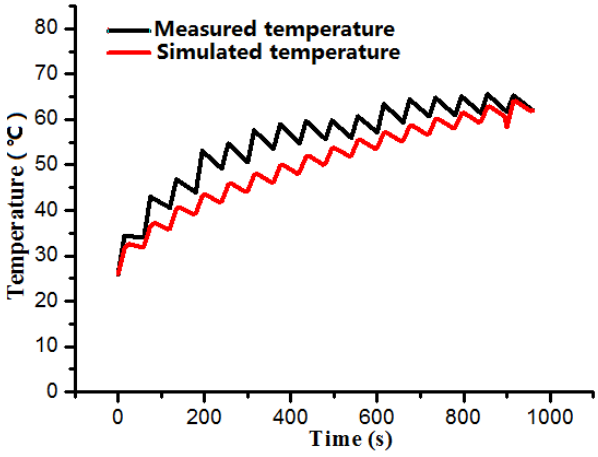
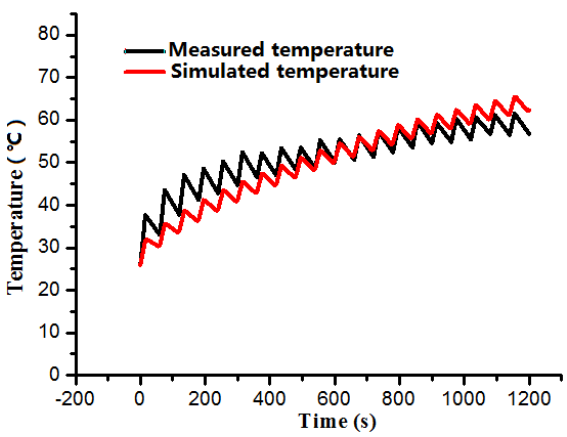


Figure 19 Changement de température du point 2

Cas 4: échantillon de hauteur 45mm; cycle de chauffage 15s puis refroidissement 45s. La puissance est 50W.



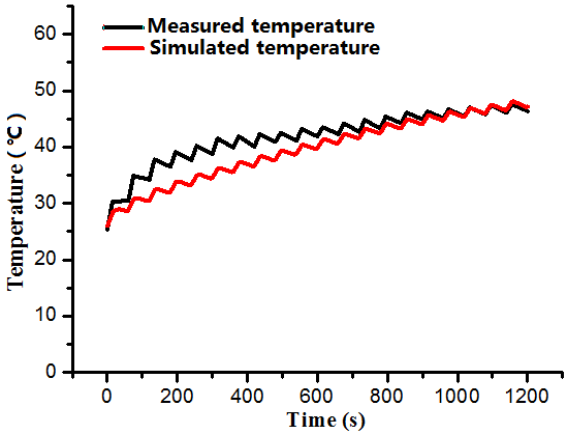


Figure 20 Changement de température du point 1 Figure 21 Changement de température du point 2

Pour tous les quatre cas, on peut observer les mêmes tendances de variation entre résultats mesurés et simulés, montrant que les mesures valident qualitativement les simulations.

Cependant, nous remarquons également qu'il existe encore des écarts parfois importants entre les températures observés et celles prédites. Plusieurs facteurs peuvent être responsables pour ces écarts : 1) La permittivité effective du modèle simulé est modifiée par palier dans le temps, alors qu'en réalité elle change tout le temps comme une courbe lisse ; 2) Plusieurs hypothèses sont utilisées pour la simulation qui ne sont pas valables dans la réalité ; 3) La puissance générée n'est pas parfaitement connue, ce qui est représenté évidemment dans les changements de la température du point 1 dans le cas 3. La puissance est un peu plus grande que celle attendue, ce qui conduit à la plus grand différence entre les températures simulées et mesurées; 4) Dans la simulation, les surfaces de l'échantillon sont idéalement lisses, qui ne peut être obtenues dans les expériences; 5) Les erreurs d'incertitude et de l'équipement peuvent être importés au cours des expériences; 6) La sondes peut être légèrement déplacées de ses positions initiales en raison de forts gradients de pression qui se développent pendant le chauffage ; 7) Enfin et surtout, il faut des dizaines de secondes pour prendre l'échantillon hors de la cellule et de photographier la distribution de température. Pendant ce temps, le mouvement de convection se poursuit et fait la distribution de température plus uniforme.

Durant l'expérience, on constate que si la température de l'échantillon de pomme de terre atteint à 70 à74 degrés, la géométrie commence à déformer.

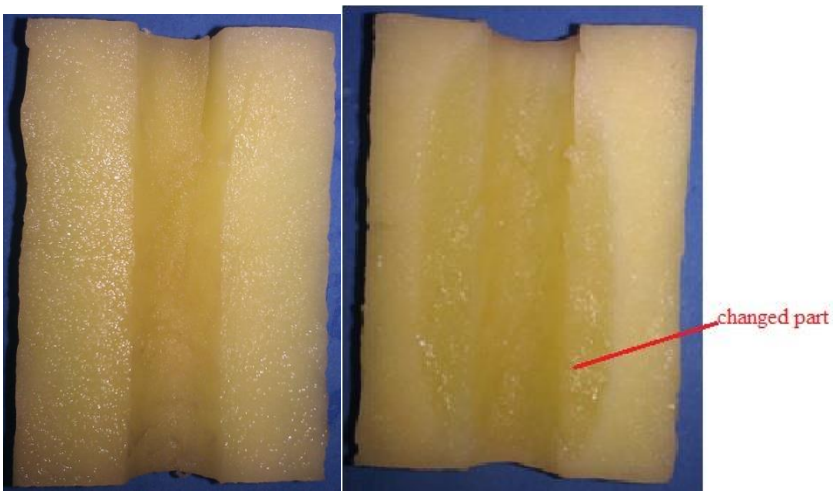


Figure 22 L'échantillon sans (à gauche) et avec (à droite) la transformation

4.4 Analyse de sensibilité

Dans les quatre cas étudiés nous avons travaillé avec des paramètres des structures identiques et constants. Pourtant, il existe en réalité des variations dans les valeurs de la plupart des paramètres de pomme de terre. Les propriétés telles que la perméabilité et la diffusivité peuvent varier énormément pour les produits alimentaires. Très peu ou pas de données mesurées sont disponible. Avec autant de paramètres pertinents, il est important de savoir quels sont ceux les plus influents. L'analyse de sensibilité, où la sensibilité d'un paramètre est étudiée en gardant les autres paramètres constants, est une façon de répondre à certaines de ces questions. Cette section rapporte la sensibilité de la température, de la perte de l'humidité et de la pression vis à vis des paramètres importants, tels que le niveau de puissance, la perméabilité liquide, le coefficient de transfert de masse, le coefficient de transfert de chaleur, la hauteur de l'échantillon, la porosité, la saturation, et la position de l'échantillon traitée. Nous constatons que l'effet de chauffage est sensible à presque tous ces paramètres, sauf la position d'échantillon. Bien que petite variation de ces paramètres ne puisse pas affecter les résultats simulés avec grande ampleur, leurs influences sont négligéables. Cela peut partiellement exprimer la différence des résultats simulés et mesurés.

D'après nos études, augmentant la puissance d'entrée, l'effet de chauffage est certainement amélioré, mais pas dans la même proportion que l'augmentation de puissance. Si l'on veut sécher des pommes de terre plus rapidement en augmentant la puissance, il est nécessaire de considérer l'équilibre des coûts d'énergie et les effets de séchage. Les effets des variations de porosité et de saturation en l'eau ne sont pas négligeables. Lors de l'analyse de sensibilité, nous constatons également que le raccourcissement de la hauteur de l'échantillon chauffée ou

l'augmentation de la puissance d'entrée peut améliorer le chauffage ; cependant la première solution est plus efficace. Par conséquent, dans l'application dans le monde réel, on peut essayer de réduire la taille des matériaux traités pour améliorer l'effet de chauffage plutôt que d'augmenter purement la puissance. En manipulant la conception du four ou tout simplement changeant la vitesse de l'air autour de l'échantillon chauffée, on peut modifier des coefficients de transferts de masse et de chaleur durant le procédé de séchage.

4.5 L'optimisation du modèle de chauffage par radiofréquence

Notre modèle de chauffage par radiofréquence est détaillé précédemment. La température de l'échantillon traité est homogène en utilisant le modèle proposé, ce qui peut fournir un essai pour éviter le point chaud et l'emballement thermique qui existent dans les applications de chauffage par micro-ondes et radiofréquence. Malheureusement, la perte de l'humidité de l'échantillon chauffée ne peut pas être mesurée dans les expériences parce que notre échantillon doit toucher les deux conducteurs de la cellule de chauffage. La balance de haute précision ne peut pas mesurer le poids total de l'ensemble du système. Cependant, la perte de l'humidité est le paramètre le plus important parce que notre objectif est le séchage des matériaux. En outre, comme mentionné précédemment, les surfaces intérieure et extérieure de l'échantillon de pomme de terre doivent toucher directement l'appareil, bloquant ainsi l'échange de masse avec l'air ambiant. La chaleur et la vapeur échangent uniquement à travers le haut et le bas de l'échantillon, ce qui limite sérieusement l'effet de séchage. Par conséquent, des améliorations sont nécessaires.

Pour obtenir le poids d'échantillon pendant le processus de chauffage, l'échantillon ne doit pas toucher des conducteurs. Nous constatons que l'échantillon pourrait être chauffé lorsqu'il n'y pas de contact avec les conducteurs si la fréquence est suffisamment élevée. Cependant, l'intensité du champ électronique dans l'échantillon se concentre sur une petite partie à proximité des surface supérieure ou inférieure, plutôt que se diminuer de conducteur intérieur à celui extérieur. Cela conduira à point chaud ou l'emballement thermique facilement. Ainsi, nous essayons de concevoir un autre modèle.

Comme les pommes de terre ne sont pas très grandes, l'appareil de chauffage ne doit pas être très grand non plus. Cependant, l'équipement ne doit pas non plus être très petit. Parce qu'il vaut mieux que l'échantillon ne touche pas les conducteurs et il devrait y avoir assez grand espace entre des matières traitées et les parois de l'appareil pour une meilleure convection avec l'air ambiant. Donc, la fréquence de travail ne devrait pas être très élevée. En

considérant tous ces facteurs, un guide d'onde nervuré qui fonctionne à 800MHz est choisi comme base de notre nouvelle cellule.

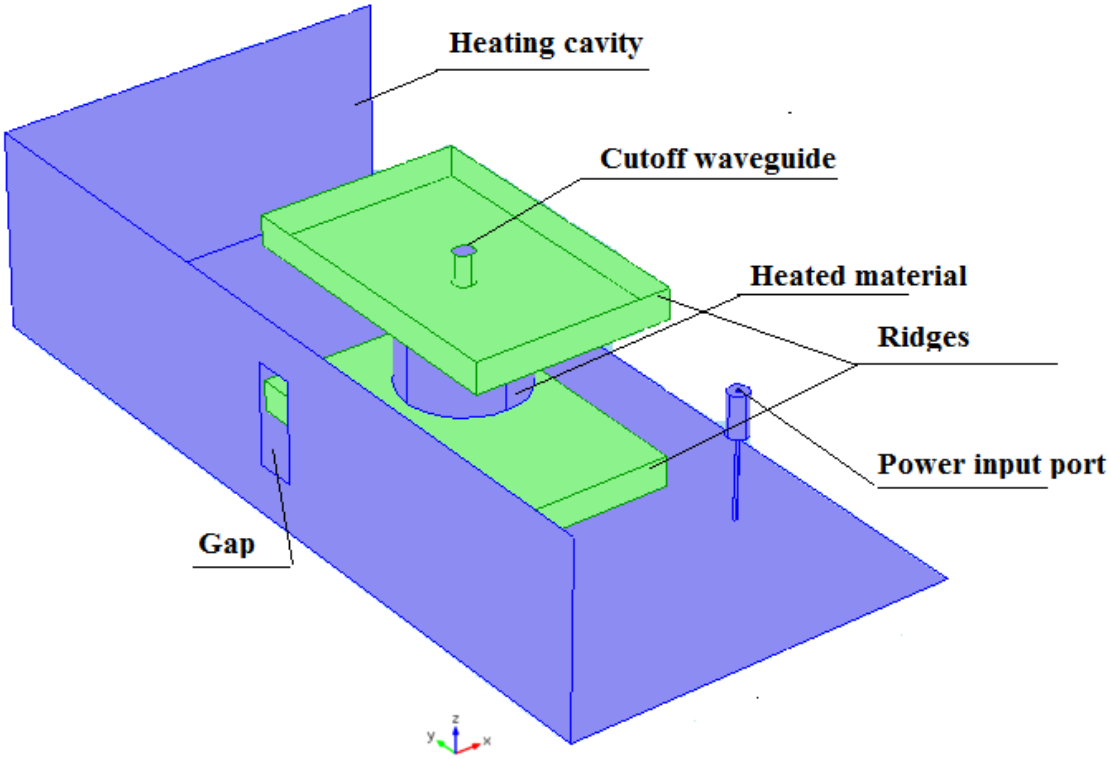


Figure 23Schéma de nouveau modèle

Cette nouvelle conception est juste une idée maintenant. Plus de recherches, même la réalisation de ce modèle seront effectuées plus tard.

5. Conclusions

Durant mon travail de thèse j'ai étudié l'interaction entre l'énergie radiofréquence et les milieux poreux, et proposé un modèle chauffant des milieux poreux uniquement par radiofréquence. Pour atteindre ces objectifs, plusieurs mesures ont été effectuées.

Basé sur le modèle 1D, les équations de transfert de chaleur et de masse sont couplées avec celles de Maxwell pour étudier l'interaction entre la radiofréquence et les milieux poreux. Avant de simuler le chauffage par radiofréquence, la salinité et la permittivité effective de l'échantillon étudié sont estimées afin de remédier aux manques de données publiées dans la littérature. Des expériences sont effectuées pour vérifier la précision des modèles de chauffage radiofréquence. L'analyse de sensibilité est ensuite exploité pour trouver les

raisons possibles qui provoquent des différences entre les résultats simulés et mesurés, et plus important, pour trouver les améliorations de l'effet de chauffage.

Plusieurs conclusions peuvent être tirées de l'étude ci-dessus :

1) Nos résultats calculés de brique 1D sont très proches que ceux présentés dans deux articles de référence. Les profils de saturation, de température et de pression sont analysés.
2) L'équation de Landau et Lifshitz, Looyenga est employée comme une alternative pour prédire le changement de la permittivité effective de pomme de terre Agata. Pour estimer un paramètre essentiel dans la règle de mélange, plusieurs échantillons sont fabriqués et chargés dans une cellule coaxiale pour mesurer les impédances d'entrée. Les simulations des modèles correspondants utilisant l'équation de Landau, Lifshitz et Looyenga avec différentes salinités pour la mise à jour des permittivités effectives des échantillons sont également menées. La salinité d'Agata est estimée entre 0,48% et 0,55% en comparant les données mesurées et simulées. Pour revérifier la gamme de salinité, un code Matlab combinant COMSOL est développé pour une modélisation inverse des impédances d'entrées mesurées dans les permittivités effectives. Les permittivités effectives extraites des mesures sont en relativement bon accord avec celles calculées par l'équation de Landau, Lifshitz et Looyenga utilisant des salinités de 0,48% à 0,55%.
3) Dans la section de chauffage, la salinité d'échantillon de pomme de terre prend la valeur moyenne de celles des échantillons mesurés—0,52%.
4) L'échantillon chauffé doit toucher les conducteurs intérieur et extérieur de cellule coaxiale à la fréquence 27.12MHz dans notre modèle. Sinon, l'échantillon ne sera pas chauffé efficacement. L'efficacité de chauffage lorsque l'échantillon ne touche que le conducteur intérieur est meilleure que celle quand l'échantillon touche seulement le conducteur extérieur. Plus la distance est large entre l'échantillon et les parois de la cellule coaxiale, plus l'effet de chauffage est faible.
5) Il existe un accord qualitatif entre tous les résultats simulés de pommes de terre Agata chauffés par radiofréquence et ceux de mesures, ce qui vérifie l'exactitude de notre modèle de chauffage par radiofréquence. Les résultats attendus et mesurés sont relativement homogènes.
6) L'emplacement de l'échantillon n'affecte pas les résultats de chauffage.

7) Des variations de puissance d'entrée et de hauteur d'échantillon peuvent changent la température, la perte de l'humidité et la pression qualitativement. Une plus grande variation de l'un de ces deux paramètres produit un plus grand changement. Cependant, des améliorations de l'effet de chauffage ne sont pas proportionnelles aux variations des paramètres. En comparant à la variation de puissance d'entrée, le même changement en hauteur peut apporter un meilleur effet de séchage. Par conséquent, dans l'application dans le monde réel, il est préférable de réduire la taille des matériaux traités plutôt que d'augmenter purement la puissance pour améliorer l'effet de chauffage.
8) Bien que petites variations de porosité et de saturation en l'eau ne puisse pas affecter les résultats simulés avec grande ampleur, leurs influences ne sont pas négligeables.
9) La perméabilité intrinsèque de l'eau peut influencer la perte d'humidité et la pression de l'échantillon. Toutefois, cet effet sur la température est beaucoup plus faible.
10) Le coefficient de transfert de mass et celui de transfert de chaleur peuvent affecter directement l'effet de chauffage. Cependant, le coefficient de transfert de masse a une plus grande contribution à l'élévation de la température, de la perte de l'humidité et de pression, même si la variation du coefficient de transfert de masse est beaucoup plus petite que celle du coefficient de transfert de chaleur. L'effet de chauffage de pomme de terre traitée par radiofréquence dans notre modèle est plus sensible au coefficient de transfert de masse. Par conséquent, la perte d'humidité mesurée doit être prise pour une meilleure estimation du coefficient de transfert de masse.
11) Lorsque la température atteint environ 70-74 degrés, les échantillons des pommes de terre se transforment, ce qui rend le modèle de simulation invalide. Par conséquent, ce modèle peut seulement prédire la température de pomme de terre Agata chauffant par radiofréquence avant que la température atteint 70 degrés.
12) Avec la même durée totale de traitement mais des cycles de chauffage plus courts, des effets de chauffage sont similaires dans notre modèle.

La perspective :

La suite de ces travaux peuvent consister à :

1. Réaliser 1e nouveau modèle proposé dans la section 4.5. Analyser des distributions de la température et de la pression et la perte d'humidité pendant le processus de

chauffage. Comparer les effets de chauffage du nouveau modèle et du modèle précédent.

2. Conduire des expériences pour mesurer le profil de température et d'humidité du nouveau modèle. Comparer les résultats simulés et mesurés.

3. Prendre le retrait de l'échantillon en considération au cours du traitement et contrôler son impact sue les résultats théorique.